

150311

**MODELING AND SIMULATION OF
WIND ENERGY CONVERSION SYSTEM
USING PWM CONVERTERS**



by

Tolga SÜRGEVİL

January, 2004

İZMİR

150311

MODELING AND SIMULATION OF WIND ENERGY CONVERSION SYSTEM USING PWM CONVERTERS

**A Thesis Submitted to the
Graduate School of Natural and Applied Sciences of
Dokuz Eylül University
In Partial Fulfillment of the Requirements for
the Degree of Doctor of Philosophy in Electrical and Electronics Engineering,
Electrical and Electronics Program**

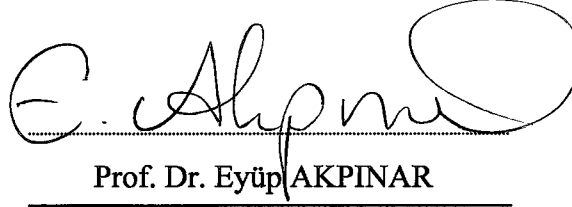
**by
Tolga SÜRGEVİL**

January, 2004


İZMİR

Ph.D. THESIS EXAMINATION RESULT FORM

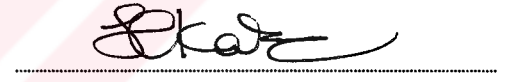
We certify that we have read the thesis, entitled “**Modeling and Simulation of Wind Energy Conversion System Using PWM Converters**” completed by **Tolga SÜRGEVİL** under supervision of **Prof. Dr. Eyüp AKPINAR** and that in our opinion it is fully adequate, in scope and in quality, as a thesis for the degree of Doctor of Philosophy.


Prof. Dr. Eyüp AKPINAR


Supervisor


Prof. Dr. Erol UYAR

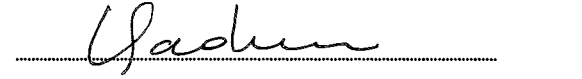
Jury Member


Assoc. Prof. Dr. Haldun Karaca

Jury Member


Prof. Dr. Mustafa Gündüzalp

Jury Member


Doç. Dr. Işık Gaderce

Jury Member

Approved by the
Graduate School of Natural and Applied Sciences


Prof. Dr. Cahit HELVACI
Director

ACKNOWLEDGMENTS

The research in the scope of this thesis has been conducted at the Department of Electrical and Electronics Engineering of Dokuz Eylül University under the supervision of Prof. Dr. Eyüp Akpınar. First, I would like to express my gratitude to him for his guidance and support during this work. I would also like to thank the members of the Electrical Machines and Power Electronics Laboratory Group and other staff of the Department for their assistance.

This thesis was carried out as a part of project, ‘Wind energy conversion system with induction generator using PWM converters’ sponsored by Turkish Scientific and Research Council (TÜBİTAK) under contract no. 101E004. I would like to thank them for their financial support.

I would like to thank Prof. Dr. Erol Uyar, Assoc. Prof. Dr. Haldun Karaca, and Assist. Prof. Dr. Erginer Urgan for their comments and support to this work during their presence in my Ph.D. Thesis Committee. I would also like to thank Assist. Prof. Dr. Sinan Pravadalıoğlu for his help during fuzzy logic control programming.

Last, but not the least, I feel deeply indebted to my family and friends, who above all else deserves respect and gratitude, for their patience and support.

Tolga SÜRGEVİL

ABSTRACT

In this thesis, a DSP based pulse-width-modulated dual voltage source converter double-cage induction machine drive for wind energy conversion system is presented. The detailed modeling of the double-cage induction machine is obtained with hybrid abc/qd and qd/abc models as well as the conventional qd/qd model. The determination of the equivalent circuit parameters of the induction machine is achieved by applying genetic algorithm. The converters are designed and implemented with a single fixed-point DSP to control the power flow in a wind energy conversion system. In the implementation of the system, two digital PI controllers are used in dc link voltage regulation and rotor speed control. The methods rely on hysteresis current control and slip regulation technique on the line-side converter and machine-side converter, respectively. The results obtained from computer simulations of the complete mathematical model of the drive circuit and double cage induction machine are compared to experimental work carried in laboratory. Finally, the implemented system is tested with a 5kW wind turbine in the campus.

Keywords : Wind Energy Conversion System, Double-Cage Induction Machine, PWM Voltage Source Converter

ÖZET

Bu tezde DSP tabanlı darbe genişlik bindirimi tekniğini kullanan çeviricilerin çift-kafes asenkron makina sürücüsü olarak rüzgar enerjisi dönüşümü sisteminde uygulanması amaçlanmıştır. Çift kafesli asenkron makinanın detaylı matematiksel modelleri yapılmış, qd/qd modelinin yanı sıra hibrid abc/qd ve qd/abc modelleri çıkarılmıştır. Asenkron makinanın eşdeğer devre parametreleri genetik algoritma yöntemi uygulanarak bulunmuştur. Rüzgar enerjisi dönüşüm sisteminde güç akışını denetlemek etmek amacıyla çeviriciler tek bir sayısal işaret işlemci kullanılarak tasarlanmış ve uygulanmıştır. Sistemin uygulamasında dc link gerilimini ve mil hızını denetlemek için iki adet sayısal PI denetleyici tasarlanmıştır. Şebeke tarafı ve jeneratör tarafı çeviricilerde sırasıyla histeresis akım denetimi ve kayma faktörü regülasyonu yöntemlerinden yararlanılmıştır. Sürücü devresi ve asenkronun makina modelleri kullanılarak elde edilen bilgisayar benzetimleri sonuçları laboratuvarında uygulanan sistemden elde edilen deneysel sonuçlarla karşılaştırılmıştır. Son olarak gerçekleştirilen sistem kampüs içerisinde kurulan 5kW gücünde rüzgar türbini ile test edilmiştir.

Anahtar Sözcükler : Rüzgar Enerjisi Dönüşüm Sistemi, Çift Kafes Asenkron Makina, PWM Çevirici

CONTENTS

	Page
Contents.....	VI
List of Tables	X
List of Figures.....	XI

Chapter One

Introduction	1
---------------------	----------

Chapter Two

Modeling of Double-Cage Induction Machine	11
--	-----------

2.1 Voltage Equations in Machine Variables.....	13
2.2 Voltage Equations in Arbitrary Reference Frame.....	31
2.3 Voltage Equations in abc/qd Reference Frame.....	39
2.4 Voltage Equations in qd/abc Reference Frame.....	43
2.5 Torque Expressions.....	49
2.6 Steady-state Equivalent Circuit.....	51
2.6.1 Analysis of the Equivalent Circuit.....	53
2.7 Determination of Machine Parameters.....	55
2.7.1 Genetic Algorithm Approach.....	55
2.7.2 Motor Equations for Genetic Algorithm.....	58
2.7.3 Machine Parameters.....	60
2.8 Simulation and Experimental Results.....	61
2.8.1 Load Test.....	62
2.8.2 Free Acceleration Test.....	65
2.8.3 Steady-state Characteristics.....	67

Chapter Three

Modeling and Control of Three-Phase PWM

AC-DC-AC Voltage Source Converters 69

3.1 Modeling of Line-Side PWM Voltage Source Converter.....	69
3.1.1 Current Control of Line-Side PWM Voltage Source Converter.....	74
3.1.2 Closed-loop Voltage Control.....	75
3.1.3 Design Considerations of Line-Side PWM VSC.....	76
3.1.4 Determination of DC link Capacitor.....	78
3.2 Modeling of Machine-Side PWM Voltage Source Inverter.....	79
3.2.1 Closed-loop Speed Control.....	81
3.3 Fuzzy Logic Control.....	82
3.3.1 Structure of Fuzzy Logic Control.....	83
3.3.2 Fuzzy Sets and Membership Functions.....	84
3.3.2.1 Fuzzy Set Operations.....	87
3.3.2.2 Fuzzy Relations.....	87
3.3.2.3 Linguistic Variable.....	88
3.3.2.4 Fuzzy Rules.....	89
3.3.2.5 Aggregation of Rules.....	90
3.3.2.6 Inference Process.....	91
3.3.2.7 Defuzzification Methods.....	92
3.4 Digital Proportional-Integral Controller.....	95
3.5 DC Link Voltage Control.....	96
3.5.1 DC Link Voltage Control with PI Controller.....	96
3.5.2 DC Link Voltage Control with FLC.....	97
3.5.3 PI Speed Controller.....	100
3.6 System Parameters and Simulation Results.....	101
3.6.1 Instrumentation Gains for Simulation.....	101
3.6.2 Determination of Digital PI Parameters of Voltage Controller.....	103
3.6.3 Determination of Digital PI Parameters of Speed Controller.....	104
3.6.4 Simulation Results.....	104
3.6.4.1 Motor Operation.....	105

3.6.4.2 Generator Operation.....	106
----------------------------------	-----

Chapter Four

Implementation of Three-Phase PWM AC-DC-AC

Voltage Source Converters	111
4.1 Gate Drive Interface.....	112
4.2 Voltage and Current Sensing Circuits.....	113
4.3 Speed Feedback.....	114
4.4 Power Supply Circuits.....	115
4.5 Experimental Setup.....	115
4.6 Software Programming.....	117
4.6.1 Sinusoidal PWM Waveform Generation.....	118
4.6.2 Maximum Power Point Tracking Routine.....	120
4.7 Simulation and Experimental Results.....	121
4.7.1 No-load Operation as Motor.....	122
4.7.2 Load Tests.....	123
4.7.2.1 Motor Operation.....	125
4.7.2.2 Generator Operation.....	128
4.7.3 Maximum Power Point Tracking Test.....	132
4.7.3.1 Analysis of DC Motor for Maximum Power Point Operation.....	134

Chapter Five

Wind Energy Conversion Systems	136
5.1 Torque and Power Characteristics of a Wind Turbine.....	136
5.2 Classification of Wind Energy Conversion Systems.....	138
5.2.1 Constant-speed Constant-frequency (CSCF) Systems.....	138
5.2.2 Variable-speed Constant-frequency (VSCF) Systems.....	140
5.2.3 Variable-speed Variable-frequency (VSVF) Systems.....	145
5.3 Wind Turbine Modeling.....	146
5.3.1 Efficiency Analysis of Double-cage Induction Machine.....	148
5.3.2 Effect of Gearbox on the Machine Efficiency.....	151
5.4 Speed Control of DCIM Driven by the Wind Turbine.....	152

5.4.1 Simulation Results of Variable-Speed Drive with Wind Turbine.....	153
5.5 Experimental Results.....	160

Chapter Six

Conclusions	167
References.....	170
Furtherwork.....	177
Appendix A.....	178
Appendix B.....	189
Appendix C.....	205
Notes.....	216



LIST OF TABLES

Table 2.1	Test on star-connected motor	61
Table 2.2	The DCIM parameters obtained from GA	61
Table 2.3	Locked rotor test under different supply voltages	66
Table 3.1	Rule matrix for PI based fuzzy controller	99
Table 4.1	Measured quantities during MPPT	135
Table 5.1	CSCF operation under varying gear ratios ($R = 2.75m$, $\lambda_{opt} = 4.3$)	153
Table 5.2	Wind turbine parameters	154
Table 5.3	Electrical circuit and control parameters	155

LIST OF FIGURES

Figure 1.1	Variable speed wind generation system	8
Figure 2.1	Winding diagram of a 2-pole, 3-phase, Y-connected double-cage induction machine	14
Figure 2.2	Flux lines in a DCIM	18
Figure 2.3	Equivalent circuit of double-cage induction machine	53
Figure 2.4	Equivalent single rotor circuit	58
Figure 2.5	Circuit diagram for loading tests of DCIM	62
Figure 2.6	Speed response of the machine during transition from light load to normal load (upper trace-simulation, lower trace-experimental)	63
Figure 2.7	Torque response of the machine during transition from light load to normal load (simulation)	64
Figure 2.8	Phase current of the machine during transition from light load to normal load (dotted lines-simulation, continuous lines-experimental)	64
Figure 2.9	Rotor speed for free acceleration test (simulation)	65
Figure 2.10	Rotor speed for free acceleration test (experiment, 750 rpm/div, time-base:0.05s/div)	65
Figure 2.11	Electromagnetic torque for free acceleration test (simulation)	66
Figure 2.12	Phase current of the machine during free acceleration test (dotted lines-simulation, continuous lines-experiment)	67
Figure 2.13	Steady-state torque-slip curves at rated and reduced armature terminal voltage. Continuous lines show the curve obtained from estimated parameters while the dots show measured values	68
Figure 3.1	Electrical circuit of 3-phase PWM ac-dc-ac converter	70
Figure 3.2	Block representation of line-side PWM voltage source converter model	73
Figure 3.3	Closed-loop control scheme of 3-phase PWM ac-to-dc converter	76
Figure 3.4	Unity power factor operation of the converter (a) rectifier (b) regenerative	77
Figure 3.5	Block representation of machine-side PWM voltage source inverter model	81

Figure 3.6	Closed-loop speed control scheme of the DCIM	82
Figure 3.7	Structure of a fuzzy logic controller	84
Figure 3.8	Commonly used membership functions	85
Figure 3.9	Fuzzy set operations	87
Figure 3.10	Representation of error as a linguistic variable	89
Figure 3.11	Graphical representation of inference	92
Figure 3.12	Graphical representations of defuzzification methods (a) Max-membership (b) centroid (c) weighted average (d) max-min membership	95
Figure 3.13	Block scheme of PI controlled line-side PWM VSC	97
Figure 3.14	Block scheme of fuzzy controlled line-side PWM VSC	98
Figure 3.15	Membership functions for error and change of error	99
Figure 3.16	Membership functions for change of output	100
Figure 3.17	Closed-loop scheme of PI speed controller	100
Figure 3.18	Open-loop responses for determination PI parameters on the line-side converter (a) error (b) change of error	104
Figure 3.19	Simulation results for motor operation with digital PI controller on the line-side converter (a) dc link voltage (V) (b) rotor speed (rpm)	106
Figure 3.20	Simulation results for rectifier operation of the line-side converter at steady-state with digital PI controller (a) ac line voltage (V) (b) ac line current (A)	107
Figure 3.21	Simulation results for motor operation with fuzzy controller on the line-side converter (a) dc link voltage (V) (b) rotor speed (rpm)	107
Figure 3.22	Simulation results for rectifier operation of the line-side converter at steady-state with fuzzy controller (a) ac line voltage (V) (b) ac line current (A)	108
Figure 3.23	Simulation results for generator operation with digital PI controller on the line-side converter (a) dc link voltage (V) (b) rotor speed (rpm)	109
Figure 3.24	Simulation results for regenerative operation of the line-side converter at steady-state with digital PI controller (a) ac line voltage (V) (b) ac line current (A)	109
Figure 3.25	Simulation results for generator operation with fuzzy controller on the line-side converter (a) dc link voltage (V) (b) rotor speed (rpm)	110
Figure 3.26	Simulation results for regenerative operation of the line-side converter at steady-state with fuzzy controller (a) ac line voltage (V) (b) ac line current (A)	110
Figure 4.1	Block diagram of the implemented drive system	112
Figure 4.2	Optocoupler drive interface for gating signals of IGBTs	113

Figure 4.3	Voltage sensing circuit	114
Figure 4.4	Current sensing circuit	114
Figure 4.5	Filter circuit for tacho feedback signal	115
Figure 4.6	Power supply circuit	115
Figure 4.7	Ward-Leonard system	116
Figure 4.8	Flow-chart of the developed control software	120
Figure 4.9	MPPT algorithm	121
Figure 4.10	Experimental results during free acceleration of DCIM (upper trace: dc link voltage-160V/div, lower trace: rotor speed-375rpm/div, time/div: 0.5s)	122
Figure 4.11	Simulation results during free acceleration of DCIM (a) dc link voltage, (b) rotor speed-375rpm/div, time/div: 0.5s	123
Figure 4.12	Machine phase current transient during closing at set rotor speed (trace-5A/div, time/div: 20ms)	124
Figure 4.13	Simulation results of transient during closing at set rotor speed (a) machine phase current (A) (b) electromagnetic torque (Nm), time/div: 50ms	124
Figure 4.14	Motor operation at steady-state observed at motor load test (upper trace: line-to-line DCIM voltage-320V/div, lower trace: DCIM phase current: 5A/div, time/div: 5ms)	125
Figure 4.15	Simulation results for motor operation at steady-state (a) line-to-line voltage of DCIM (V) (b) DCIM phase current (A)	126
Figure 4.16	Rectifier operation of the line-side converter observed at motor load test (upper trace: phase voltage-110V/div, lower trace: phase current-4A/div, time/div: 10ms)	126
Figure 4.17	Simulation results for rectifier operation of the line-side converter (a) phase voltage (V) (b) phase current (A)	127
Figure 4.18	Simulation results for transient response under step load change for motoring operation (a) dc link voltage (V) (b) rotor speed (rpm), time/div: 1s	127
Figure 4.19	Experimental results under step load change for motoring operation (upper trace: dc link voltage-160V/div, lower trace: rotor speed-375rpm/div, time/div: 0.5s)	128
Figure 4.20	Generator operation at steady-state observed at generator load test (upper trace: DCIM line-to-line voltage-320V/div, lower trace DCIM phase current: 2A/div, time/div: 10ms) ...	129
Figure 4.21	Simulation results for generator operation at steady-state (a) DCIM line-to-line voltage (V) (b) DCIM phase current (A) ..	129
Figure 4.22	Regenerative operation of the line-side converter observed at generator load test (upper trace: phase voltage-110V/div, phase current-4A/div, time/div: 10ms)	130
Figure 4.23	Simulation results for regenerative operation of the line-side converter (a) DCIM phase voltage (V) (b) phase current (A) .	130

Figure 4.24	Simulation results for transient response under step load change for generator operation (a) dc link voltage (V) (b) rotor speed (rpm), time/div: 1s	131
Figure 4.25	Experimental results under step load change for generator operation (upper trace: dc link voltage-160V/div, lower trace: rotor speed-375rpm/div, time/div: 0.5s)	131
Figure 4.26	Variation of dc link power with respect to rotor speed	133
Figure 4.27	Experimental results during maximum power point tracking operation (upper trace: dc link voltage-160V/div, lower trace: rotor speed-375rpm/div, time/div-10s)	134
Figure 5.1	Power coefficient characteristics	137
Figure 5.2	Torque coefficient characteristics	138
Figure 5.3	CSCF system with field excited synchronous generator	140
Figure 5.4	VSCF system with pitch blade angle control	141
Figure 5.5	VSCF system with a slip ring induction machine	142
Figure 5.6	VSCF system with fuzzy controlled PWM converters	143
Figure 5.7	VSCF system with brushless doubly-fed induction generator	144
Figure 5.8	VSCF system with slip-energy recovery drive	145
Figure 5.9	VSVF system with a field excited synchronous generator	146
Figure 5.10	VSVF system with a capacitor excited induction generator ...	146
Figure 5.11	Power coefficient of the wind turbine versus tip-speed ratio ..	148
Figure 5.12	Torque coefficient of the wind turbine versus tip-speed ratio ..	148
Figure 5.13	Equivalent circuit of double-cage induction machine	151
Figure 5.14	Direct grid connection scheme	151
Figure 5.15	Free acceleration of the DCIM to 375 rpm when the turbine is directed out of wind (top: electromagnetic torque of DCIM, bottom: DCIM rotor speed)	156
Figure 5.16	Free acceleration of the DCIM to 1500 rpm when the turbine is directed out of wind (top: electromagnetic torque of DCIM, bottom: DCIM rotor speed)	157
Figure 5.17	Supply voltage and current at the line-side converter at the rotational speed of 1500 rpm when the turbine is directed out of wind	157
Figure 5.18	DCIM phase voltage and current at the rotational speed of 1500 rpm when the turbine is directed out of wind	158
Figure 5.19	Supply voltage and current at the line-side converter at the wind speed of 8m/s and the rotational speed of 1500 rpm	159
Figure 5.20	DCIM phase voltage and current at the wind speed of 8m/s and the rotational speed of 1500 rpm	159

Figure 5.21	Recorded rms values of the ac line current at a rotor speed of 940 rpm	161
Figure 5.22	Recorded rotor speed of the DCIM (188 rpm/div)	161
Figure 5.23	Recorded dc link current at a rotor speed of 940 rpm	162
Figure 5.24	Recorded wind speed at a rotor speed of 940 rpm (3.2m/s/div)	162
Figure 5.25	Recorded dc link current at a rotor speed of 865 rpm.....	163
Figure 5.26	Recorded wind speed at a rotor speed of 865 rpm (3.2m/s/div)	163
Figure 5.27	Grid voltage and current on the line side when the rotor speed is fixed at 940 rpm (upper trace: grid voltage-125V/div, lower trace: grid current-4A/div)	164
Figure 5.28	Grid voltage and current on the line side when the rotor speed is fixed at 865 rpm (upper trace: grid voltage-125V/div, lower trace: grid current-4A/div)	165
Figure 5.29	DCIM phase current and wind speed when the rotor speed is fixed at 940 rpm (upper trace: wind speed-3.2 m/s/div, lower trace: DCIM phase current-2A/div)	165
Figure 5.30	DCIM phase current and wind speed when the rotor speed is fixed at 865 rpm (upper trace: wind speed-3.2 m/s/div, lower trace: DCIM phase current-2A/div)	166

CHAPTER ONE

INTRODUCTION

The use of wind power has been in existence for over 3000 years, especially in mechanical systems for water pumping and grain grinding. The utilization of wind power for electricity generation is not a new concept and this idea was first realized in 1891. Since then, step by step improvements were made in this technology, but it is not considered to be the consistent source for providing electric power. In 1970s, the researches on the wind power systems are encouraged by the oil price shock and the improvements of power electronics applications on power control. The fact of that fossil fuel resources are not renewable and have harmful impacts on environment prompted the researches to focus on clean and safe energy resources as an alternative. During last decades, an increasing interest has emerged on wind energy technology and it is considered to be one of the most important renewable energy resources (Hansen et al, 2001), (Ackermann & Söder, 2000), (Walker & Jenkins 1997). Today, it is one of the rapidly growing technologies and markets. By the end of 2003, the total installed capacity of wind energy is estimated to be more than 35,000 MW all around the world (WEB_1).

With increasing attention on renewable energy resources, wind energy conversion systems (WECS) are today's one of the most popular subject that the researches are intensively carried on. Many applications of wind power can be found in a wide power range from a few kilowatts to several megawatts in small scale off-grid stand-alone systems or large scale grid-connected wind farms. The status and issues in many different wind power applications such as power grid integration, power quality, economic aspects, environmental impacts, turbine aerodynamics, technology, and applications have been researched and discussed in publications (Hansen et al, 2001), (Walker & Jenkins 1997), (Ackermann & Söder, 2000).

The conversion of wind power into electrical form is achieved by means of wind turbines driving generators. The wind turbines used in these systems are mostly three-bladed, horizontal-axis or propeller type and they dominate the wind turbine applications. The wind turbine is mounted on a nacelle on the top of a tower. The nacelle contains the generator, gearbox, and nacelle rotor. The shaft of the generator is coupled to the wind turbine through a gearbox. The nacelle is oriented into the wind with a tail vane on small turbines, while it is yawed into or out of the wind by electrical control of the nacelle rotor on large turbines. The modern wind turbines with two or three blades are designed to operate at higher tip-speed ratio. This allows the use of a smaller and lighter gearbox. But, their starting torque is low and might need to be started when the wind speed reaches the operation range (Ackermann & Söder, 2000). As another type, the vertical-axis wind turbines are still being investigated and developed, but so far they have not proved as cost-effective as horizontal-axis types (Walker, 1997).

The selection of the generator type depends on many factors such as application type, machine characteristics, maintenance, price etc. Currently, induction machines dominate the commercial wind turbine generators. The well-known advantages of induction generators are their robustness, low cost, and ease of maintenance (Bansal et al, 2003). In wind energy applications, they are also preferred since they provide some flexibility against fluctuating wind due to asynchronous operation. The major disadvantage is that they need excitation through supply terminals (Hansen et al, 2001). Various application types with induction generators, such as squirrel cage (Simoes et al, 1997), wound-rotor (Çadırcı & Ermiş, 1992), and brushless doubly-fed (Brune et al, 1994), are proposed for wind power systems.

Induction machines used in high power industrial applications mostly have double squirrel cage rotor. The rotor designs of the induction machines produce a large variety of torque-speed characteristics. Induction machines having double-cage rotor structure fall under the Class C in standard design classes defined by NEMA and IEC. These are preferred to single-cage induction machines because of their

improved starting torque and reduced starting current capabilities in applications that require high-starting torque, such as loaded pumps, compressors, and conveyors (Chapman, 2002). The torque-speed characteristics of the induction machines are highly dependent upon the variation of the voltage level at the armature terminals. Such a variation causes a significant change on the performance of the induction machine because the developed torque is proportional to the square of the voltage. As a result, this drawback has prompted some of the manufacturers to design the induction machines rated more than 5 kW as double cage.

In order to simulate the systems such as WECS consisting of induction machines, a precise modeling and the parameters of the induction machine are required. Lack of machine data and inappropriate choice of the machine equivalent circuit will yield to incorrect results in the analysis (Waters & Willoughby, 1982). The modeling of single-cage induction machines in system studies is well-known and their parameters can be determined through a set of standard test procedures (IEEE Standard no.112-1996, 1997). However, this is somewhat complicated in the modeling and parameter determination of the double-cage induction machines. Since the extra rotor circuit in the construction of the double-cage induction machines causes nonlinearity in the analysis of the equivalent circuit, the machine parameters cannot be directly determined from standard tests and needs to be estimated. The success of conventional optimization techniques relies on initial guess of the parameters due to convergence problem to a local minimum instead of global minimum (Nangsue et al, 1999). Recently, an optimization technique called genetic algorithm (GA), is applied to the parameter determination problem of induction machines to overcome this convergence difficulty (Nangsue et al, 1999), (Shahalami & Saadate, 1998).

Due to the advances in power electronics technology, the use of power electronic converters in wind energy conversion systems has rapidly been growing. With the improved reliability, higher power ratings, and lower price per kilowatts of the power electronic components, the techniques used in torque and speed control of synchronous and induction machines are mostly applied in wind energy conversion systems. The main advantages of employing power electronic converters are that

they allow the variable-speed operation in order to maximize the power production of the wind turbine and enhanced control (Zinger & Muljadi, 1997), (Hansen et al, 2001). A well known fact is that a good matching of the coupled energy conversion devices (i.e. wind turbine and generator) is essential since the conversion efficiency is determined through the interaction of these devices (Buehring & Freris, 1981). Power electronic converters provide an interface between the generator terminals and the utility grid line or autonomous loads. Hence, various control techniques that employ different power electronic converter topologies are proposed depending on the system and generator types as well as the required conversion and control purpose (Khater, 1996).

Many different power electronic converters are used in wind energy conversion systems. These are used for converting power from one ac system to another; typically, from the constant voltage constant frequency ac grid line to variable voltage variable frequency generator in such systems. There are many circuit topologies for ac to ac power conversion. In such converters, two common approaches can be used. These are direct conversion, such as in cycloconverters or matrix converters (Skvarenina, 2002) and dc link conversion, also called ac-dc-ac conversion (Kassakian et al, 1991). Two back to back three-phase voltage source converters (VSCs) using pulse width modulation (PWM) technique fall under the second category. An intermediate dc link is provided between two converters via a capacitor. This intermediate stage provides energy storage and filtering function. Since the converters on the line-side and machine-side are decoupled by a dc link capacitor, the two converters can be controlled separately (Hansen et al, 2001). These active converters can provide bidirectional power flow between two ac systems. The use of back to back PWM VSCs in wind energy applications is widespread because of this bidirectional power flow ability and various control strategies have been proposed (Simoes et al, 1997), (Pena et al, 2001). Moreover, due to the advantages of adjustable power factor and low total harmonic distortion of the ac mains currents of the back to back PWM converters, this circuit topology is considered to be an ideal frequency changer and solution to the problems of conventional diode or thyristor based drives (Singh et al, 1999). Due to the standards limiting the harmonic pollution

of electrical mains, it becomes necessary to modify power electronic equipments interfacing to power supply lines. Hence, PWM converters are being considered to be the prime candidates as a reliable power electronic interface in applications that require bidirectional power flow (Liserre, 2001). This converter topology provides sinusoidal ac line currents at a desired power factor at the ac grid or line-side. Hence, this feature of adjustable power factor in these converters also allows their use as active filters for minimizing current harmonics of the polluting loads in ac power systems or VAR compensation (Akagi et al, 1990).

Many publications deal with the ac current control of the line-side PWM VSCs such as predicted current control with fixed switching frequency (Wu et al, 1990), (Wu et al, 1991), hysteresis current control (Ooi et al, 1987), indirect current control (Dixon & Ooi, 1988) for dc link voltage regulation and sinusoidal line current waveforms at the desired power factor. Predicted current control with a fixed switching frequency (PCFF) relies on the prediction of line currents from dc link voltage variations. In indirect current control (ICC), a standard sinusoidal PWM switching pattern is provided without needing current transducers. In PCFF and ICC, system parameters are required for obtaining sinusoidal PWM switching patterns and stability of the converter is dependent upon the parameter variations. Hysteresis current control (HCC) is a simple and robust method that keeps the line current errors within a defined hysteresis band. This method is quite robust to the parameter variations in the system and easy to implement. The main disadvantage of HCC is the varying switching frequency depending on the load conditions. (Zargari & Joos, 1995).

The cascaded PWM voltage source inverter (VSI) at the machine-side is used for dc to ac conversion and provides variable voltage variable frequency at the stator terminals of DCIM. The magnitude and frequency of its ac output voltage or current can be controlled electronically using sinusoidal PWM technique in such inverters, which is commonly used in most induction motor drives (Ong, 1998). The principle of adjusting voltage or current magnitude and frequency is referred to as scalar control. The simplicity of the scalar control systems with respect to vector controlled

systems are their advantages. The common scalar control techniques are the constant volts per hertz (CVH) control that relies on the principle of adjustment of the magnitude of the stator voltage in proportion to its frequency in order to maintain approximately constant stator flux and torque control (TC) technique, in which the magnitude and frequency of the stator currents are adjusted so that the steady-state torque of the machine is controlled. The CVH is a simpler speed control scheme since it requires only speed feedback, while the TC is more complicated since the speed feedback has to be supplemented by a current feedback (Trzynadlowski, 1994).

The typical speed control scheme for PWM VSI fed induction machine drive using CVH scalar control method relies on slip regulation technique. Adjustment of the slip at positive and negative values allows the operation of the induction machine for both motoring and generating (Ong, 1998). The circuit topology with active converters on both line and machine sides allows four-quadrant operation of the DCIM. The main advantage of using the slip regulation technique is to achieve a simpler speed control scheme that requires only speed feedback as discussed above. Also, since limiting the slip within a defined range provides the machine currents be controlled indirectly, the requirement for an inner current control loop is not needed (Dubey, 1989).

In addition to the circuit topology and control methods mentioned above, appropriate controller logic is also required for a reliable conversion operation of the system. The solutions for controller requirements are based on classical control theory that includes proportional-integral-derivative (PID) and modern control theory including self-tuning controllers, model reference adaptive controllers etc., which require precise mathematical models. Recently, fuzzy logic controllers (FLC) have received more interest due to their advantages over conventional controllers, such as not requiring precise mathematical models, robustness, handling nonlinearities, and being closer to human thinking etc. (Raviraj & Sen, 1997), (Ross, 1995). Due to nonlinear and time varying structure of the power electronic systems, FLC seems to be a suitable solution in the control of these systems (Liserre, 2001).

With emerging of fast computing digital signal processors (DSPs), the analog control systems for electric motor drives are being replaced by digital controllers. The well-known disadvantages of analog controllers are derating, aging, noise sensitivity etc. and they are being replaced by digital controllers due to these problems. The DSPs allow the implementation of sophisticated control algorithms and offer significant advantages such as fast processing of vast data, high operational flexibility. As a result of these benefits, they attract increased attention and widely used in implementations in control of electric motor drives. For example, Texas Instruments offers C24x series of DSP controllers for a wide range of digital motor control applications. Prices of these DSP controllers are low and they provide a better solution that meets the signal processing requirements in electric motor drives (WEB_2).

The purpose of this thesis is to design the DSP based PWM voltage source converters (VSCs) feeding a double-cage induction machine (DCIM) in a grid-connected wind energy conversion system. The modeling and implementation of the proposed system will be given in this thesis. The block scheme of the proposed system is given in Figure 1.1. The system consists of two back to back PWM VSCs, which provides a power electronic interface between the DCIM terminals and the utility grid line. The wind turbine is a propeller type, three-bladed turbine and coupled to the DCIM shaft through a gearbox. The generator is a 3-phase 4-pole induction machine with double-cage rotor. Since the starting torque of the wind turbine is low, the DCIM should satisfy the torque required for the startup of the system. The system can be started by driving the DCIM as motor via PWM converters, which allow both generator and motor operation of the DCIM. The PWM VSC at the line-side is connected to the ac grid through series inductors. These series inductors on each phase of the ac line are required for line current harmonic filtering and boost operation of the PWM VSC at the line-side. The control of both line current and dc link voltage can be achieved in these converters. The ac currents of the line-side converter and dc link voltage are controlled by hysteresis current control (HCC). The speed control of the DCIM is achieved by employing the slip regulation

technique because it provides inherent current limiting and reduces the amount of measurement devices. The complete control of the system is carried out by the software developed on the TMS320F240 DSP, which is a fixed-point processor of Texas Instruments C24X family. Required computations and generation of switching signals based on the proposed control logic are performed on DSP. In closed-loop control schemes, the digital proportional-integral (PI) and fuzzy logic control (FLC) approaches are implemented. A detailed analysis and mathematical modeling of the parts in the drive system are obtained. The implementation of the drive system was tested in the laboratory and employed in the wind turbine built in the university campus. The results obtained from computer simulations and experiments are compared. The rest of the chapters are organized as follows:

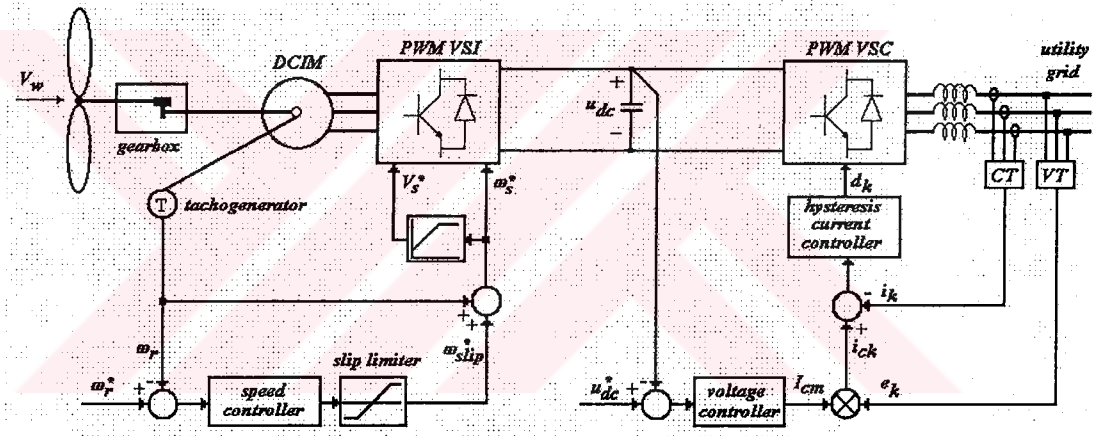


Figure 1.1 Variable speed wind generation system

In Chapter 2, the mathematical modeling of the double-cage induction machine will be given. The derivations of the commonly used qd/qd model (Adkins & Harley, 1975), and the hybrid abc/qd and qd/abc models of the machine will be given. The qd/qd model of the DCIM has been derived in some papers (Khalil et al, 1982), (Richards, 1988), (Richards & Sarma, 1994) from the universal machine model. However, this approach for the modeling of the DCIM is not correct in. The mistake made in the derivation of this model from the universal machine model is recognized and reported (Sürgevil & Akpınar, 2003) after deriving the hybrid abc/qd and qd/abc models, which are obtained first time in this study, and comparing their results to the ones obtained from the qd/qd model given by (Adkins & Harley, 1975). The off-line

parameters of the single-cage and deep bar induction machines were determined by using GA in the paper proposed by (Nangsue et al, 1999). The equivalent circuit parameters of the DCIM have been obtained using GA approach first time in this study and verification is performed by experimental tests.

In Chapter 3, the mathematical models of both PWM converters will be given in order to predict the steady-state and transient response of the drive system using computer simulations. The derived models will be combined with the DCIM models, which are given in Chapter 2. The closed-loop dc link voltage and speed control schemes will also be included into the models. The conventional proportional-integral (PI) and fuzzy logic controller (FLC) schemes for closed-loop voltage and speed control will be presented. The performances of the fuzzy logic and PI controllers in the drive system will be compared in computer simulations. The proposed system in this thesis differs from the systems that use the same power electronic converter topology given in the papers (Simoes et al, 1997), (Pena et al, 2001) from the viewpoint of control methods applied. The control of the converters in these papers relies on vector control method on both converters employing fuzzy logic controllers in WECS application. The applied control methods in this thesis employ hysteresis current controller on the line-side converter and slip regulation on the DCIM side with digital PI controllers. These control methods in the design of the converters in this thesis are chosen such that they eliminate the need for system parameters and reduce the requirements for measurement as well as the computational burden. Hence, the proposed system suggests a simpler solution in a WECS application, which has not been reported in the literature so far.

In Chapter 4, the DSP based design of the PWM VSCs for DCIM drive in the laboratory will be presented. The control logic of the PWM converters proposed in Chapter 3 is implemented on Texas TMS320F240 DSP by employing digital PI controller on both closed-loop dc link voltage and DCIM speed control. The dedicated control program flowcharts and auxiliary electronic circuits that are used in the drive system will be given. By including the models of the controllers in Z-domain, the inclusion of the sampling rate and execution time of the DSP into the

complete model is achieved. The detailed simulation model is used to compare the digital PI and fuzzy PI controllers that are employed in the WECS first time in the study. The experimental results obtained from laboratory test setup of the system will be compared with computer simulations.

In Chapter 5, the classification of the wind energy conversion systems will be briefly introduced. Different application types of WECS are investigated and presented. The modeling of the wind turbine characteristics for computer simulations will be given. The simulations of the implemented drive system with wind turbine model are performed. The actual moment of inertia of the turbine is also included into the model in this part. The effect of varying wind conditions is carefully recorded during experiments. The excluded effects of actual wind conditions on the emulation system are clearly reported in this study. The implemented system in the campus is the first horizontal axis wind turbine at the power level of 5kW designed in Turkey. Finally, the experimental results obtained from the implemented wind energy conversion system will be presented and discussed.

CHAPTER TWO

MODELING OF DOUBLE-CAGE INDUCTION MACHINE

The stator of a double-cage induction machine (DCIM) is the same as that of a conventional induction machine and its rotor has two cages: The outer cage of the rotor has a small cross sectional area that provides a high resistance and owing to its higher permeance, it provides a low leakage inductance. On the contrary, the inner cage has greater cross sectional area with a lower permeance, which in effect provides a low resistance and high leakage inductance. The outer and inner cages are short circuited by a common or separate end rings (Kostenko & Piotrovsky, 1977).

The effect of each cage on the performance of the machine can be evaluated separately. DCIM uses the skin-effect principle in order to obtain a variable rotor resistance with respect to rotor speed. At low rotor speeds of the machine, the frequency of the rotor current is high and the current mostly flows in outer cage because of its lower reactance. However, when the machine is operating at small slips near the synchronous speed, the frequency of the rotor current is low. The effect of the reactances can be neglected and the current mostly flows in the inner cage. Hence, the effective rotor resistance decreases from a higher value to a lower value as the speed of the machine increases from standstill to synchronous speed. As a consequence, machine can develop higher starting torque with reduced armature currents and during steady-state, can operate at small slips (Fitzgerald et al, 1993).

While studying on the induction motor transients, it is convenient to represent the machine variables in q_d/q_d reference frame, since the time-varying inductances between stator and rotor of the induction machine are transformed into time invariant

form using generalized reference frame theory (Krause et al, 1994). However, it has some advantages in the applications to express the machine variables in abc/qd or qd/abc reference frames, such as using the soft starting drive connected to the stator (Çadırcı et al, 1999); bus transfer of induction motors (Akpınar & Ungan, 1999); and slip energy recovery drive connected to the rotor sides (Akpınar & Pillay, 1990). The selection of the reference frame may change depending on the application in order to take the effects of specific variables into account.

In the modeling of the DCIM, three more equations are needed in addition to single-cage machine model in order to represent the second rotor circuit in terms of machine variables. The dq/dq model of a double-cage induction motor includes the mutual inductance between top and bottom rotor slots (Adkins & Harley, 1975). Also, the reduced order models have been obtained from the qd/qd model of the machine deduced from the universal machine model (Khalil et al, 1982), (Richards, 1988), (Richards & Sarma, 1994). But, the inductance L_{23} does not exist in these models, since the field and damper windings of a synchronous machine are being interpreted as the upper and bottom cages for the DCIM.

The machine inductances can be predicted by using magnetic field solver packages if the manufacturers provide the motor dimensions. The parameters of a double-cage machine including L_{23} have been obtained by using the finite element method by (Nabeta et al, 1997). Also, analytical methods have been proposed to determine the DCIM parameters depending on the assumption that the rotor starting cage leakage reactance is equal to zero (Chalmers & Mulki, 1970), (Waters & Willoughby, 1983), (Alger, 1965).

Many numerical equation solvers fail to solve all the machine parameters from the no-load, locked rotor, full-load and breakdown test results although the number of equations is equal to the number of unknown machine parameters because of highly non-linearity of the equations obtained from the exact equivalent circuit model. Therefore, recently there have been published papers (Nangsue et al, 1999), (Shahalami & Saadate, 1998) to overcome this difficulty by using the genetic

algorithm, which is an optimization technique. This optimization procedure provides incorrect results and sometimes does not converge to feasible solution, if the equations in the cost function are not consistent (i.e., some equations are written from approximate equivalent circuit and some of them are from exact equivalent circuit) to represent the real and reactive power flow in the practical machine. The genetic algorithm is applied to estimate the motor parameters for the DCIM from the no-load, locked rotor, breakdown and full-load tests in the paper proposed by (Nangsue et al, 1999), but the mutual inductance between top and bottom part of the rotor slot L_{23} is not considered.

In this chapter, the derivation of the mathematical models of the double-cage induction machine will be introduced. First, the derivation of the equations in terms of machine variables is given in Section 2.1. The qd/qd , abc/qd , and qd/abc models, which are obtained using generalized reference frame theory, are given in Sections 2.2, 2.3, and 2.4, respectively. The derivation of torque expressions for all models is given in Section 2.5 for complete modeling of DCIM. Steady-state equivalent circuit is derived in Section 2.6. In Section 2.7, the motor parameters in the exact equivalent circuit are estimated from the genetic algorithm, and used for transient and steady state analysis of the machine. The results of digital simulation using dynamic models are compared to the experimental results and discussed in Section 2.8.

2.1 Voltage Equations in Machine Variables

The winding diagram of a 2-pole 3-phase Y-connected, symmetrical double-cage induction machine is given in Figure 2.1. It is assumed that the stator windings of the machine (denoted by 1) are identical and have sinusoidal distribution with 120° displacement. Each stator winding has N_1 turns and resistance r_1 . The rotor part of the machine is represented by two equivalent 3-phase windings connected in parallel. Each upper-cage or starting-cage winding (denoted by 2) has N_2 turns and resistance r_2 , while each lower-cage or running-cage windings (denoted by 3) have N_3 turns and resistance r_3 . Also, the rotor windings are assumed to be identical and sinusoidally distributed with 120° displacement. The magnetic axes of both rotor

windings (a2, a3) are the same and the angular displacement between the rotor and stator magnetic axis (a1) is depicted by θ_r .

The winding inductances of the double-cage induction machine can be obtained from the relationship between the flux and current. By definition, the self inductance of a winding is the ratio of the flux linked by that winding to the winding current of itself, while all other winding currents are zero for a magnetically linear system. The mutual inductance between two windings is the ratio of the flux linked by one winding to the current flowing in the other winding while all other winding currents are zero.

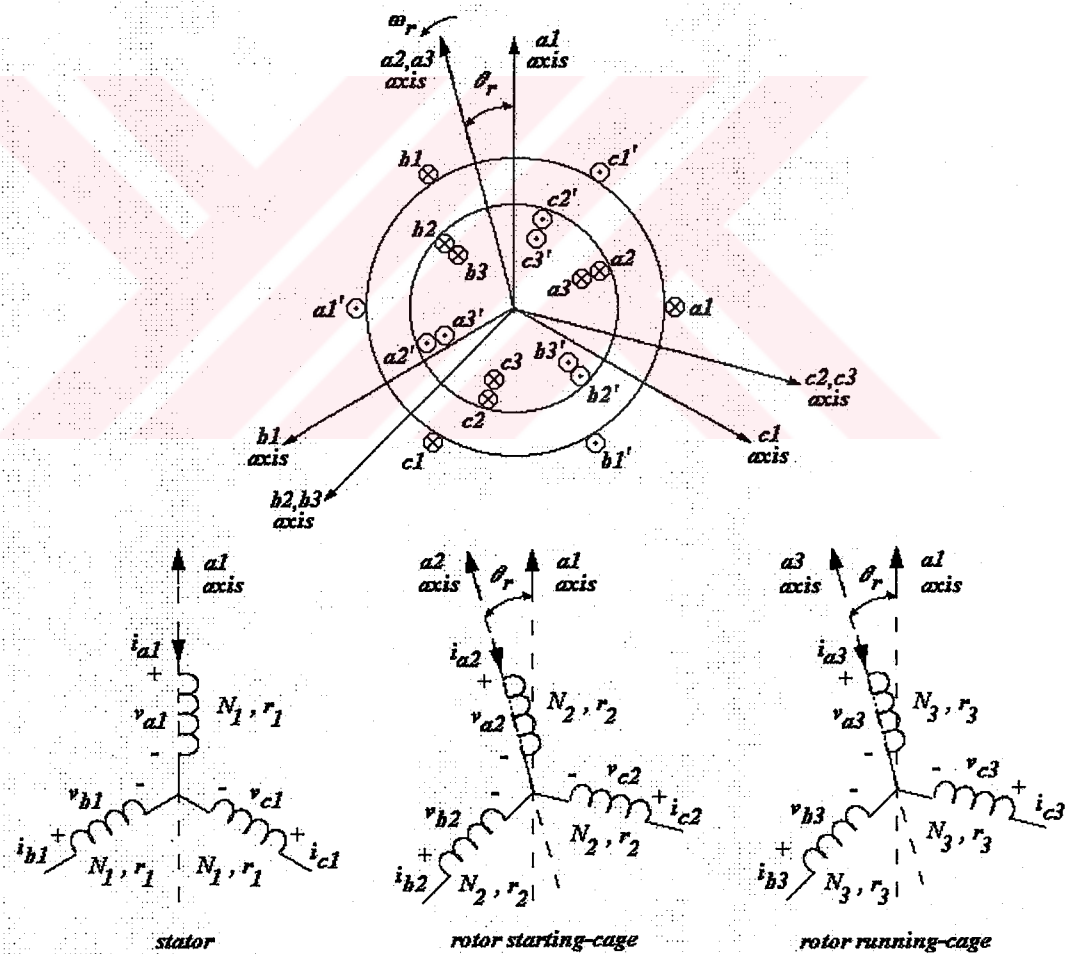


Figure 2.1 Winding diagram of a 2-pole, 3-phase, Y-connected double-cage induction machine

In order to obtain a linear model of the machine, mmf drops and saturation in the magnetic core of the machine are neglected. Since the rotor of the machine is cylindrical, the air gap of the machine is assumed to be uniform. Under these assumptions, the total flux linking stator a1 winding due to the current flowing only in a1 winding can be written as

$$\lambda_{a1a1} = L_{l1} i_{a1} + \left(\frac{N_1}{2} \right)^2 \frac{\pi \mu_o r l}{g} i_{a1} \quad (2.1)$$

where L_{l1} is stator leakage inductance due to leakage flux. l is the axial length of air gap and r is the radius of the inside circumference of stator. μ_o is the permeability of free space and g is the air-gap length. Hence, the self inductance of the stator a1 winding is obtained as

$$L_{a1a1} = L_{l1} + \left(\frac{N_1}{2} \right)^2 \frac{\pi \mu_o r l}{g} = L_{l1} + L_{m1} \quad (2.2)$$

Similarly, the self inductances of other stator windings b1 and c1 can be obtained as

$$L_{b1b1} = L_{l1} + \left(\frac{N_1}{2} \right)^2 \frac{\pi \mu_o r l}{g} = L_{l1} + L_{m1} \quad (2.3)$$

$$L_{c1c1} = L_{l1} + \left(\frac{N_1}{2} \right)^2 \frac{\pi \mu_o r l}{g} = L_{l1} + L_{m1} \quad (2.4)$$

In order to determine the mutual inductance between the stator a1 and b1 windings, the flux linking a1 winding due to the current flowing only in b1 winding is computed as

$$\lambda_{a1b1} = -\frac{1}{2} \left(\frac{N_1}{2} \right)^2 \frac{\pi \mu_o r l}{g} i_{b1} \quad (2.5)$$

and the mutual inductance between these windings is

$$L_{a1b1} = -\frac{1}{2} \left(\frac{N_1}{2} \right)^2 \frac{\pi \mu_o r l}{g} = -\frac{1}{2} L_{m1} \quad (2.6)$$

Similarly, the mutual inductances between the stator a1-c1 and b1-c1 windings are

$$L_{a1c1} = -\frac{1}{2} \left(\frac{N_1}{2} \right)^2 \frac{\pi \mu_o r l}{g} = -\frac{1}{2} L_{m1} \quad (2.7)$$

$$L_{b1c1} = -\frac{1}{2} \left(\frac{N_1}{2} \right)^2 \frac{\pi \mu_o r l}{g} = -\frac{1}{2} L_{m1} \quad (2.8)$$

The mutual inductance between the stator a1 and rotor a2 windings is determined by computing the flux linking stator a1 winding due to the current flowing only in rotor a2 winding as follows

$$\lambda_{a1a2} = \left(\frac{N_1}{2} \right) \left(\frac{N_2}{2} \right) \frac{\pi \mu_o r l}{g} i_{a2} \quad (2.9)$$

and the mutual inductance is

$$L_{a1a2} = \left(\frac{N_1}{2} \right) \left(\frac{N_2}{2} \right) \frac{\pi \mu_o r l}{g} \cos \theta_r = L_{12} \cos \theta_r \quad (2.10)$$

It is clear that the mutual inductance between the stator a1 and rotor a3 windings is

$$L_{a1a3} = \left(\frac{N_1}{2} \right) \left(\frac{N_3}{2} \right) \frac{\pi \mu_o r l}{g} \cos \theta_r = L_{13} \cos \theta_r \quad (2.11)$$

Since the rotor windings are displaced by 120° , the mutual inductances between other stator and rotor starting-cage windings are

$$L_{a1b2} = L_{b1c2} = L_{c1a2} = \left(\frac{N_1}{2}\right)\left(\frac{N_2}{2}\right)\frac{\pi\mu_o rl}{g}\cos\theta_r = L_{12}\cos(\theta_r + 120^\circ) \quad (2.12)$$

and

$$L_{a1c2} = L_{b1a2} = L_{c1b1} = \left(\frac{N_1}{2}\right)\left(\frac{N_2}{2}\right)\frac{\pi\mu_o rl}{g}\cos\theta_r = L_{12}\cos(\theta_r - 120^\circ) \quad (2.13)$$

Similarly, the mutual inductances between other stator and rotor running-cage windings are obtained as

$$L_{a1b3} = L_{b1c3} = L_{c1a3} = \left(\frac{N_1}{2}\right)\left(\frac{N_3}{2}\right)\frac{\pi\mu_o rl}{g}\cos\theta_r = L_{13}\cos(\theta_r + 120^\circ) \quad (2.14)$$

and

$$L_{a1c3} = L_{b1a3} = L_{c1b3} = \left(\frac{N_1}{2}\right)\left(\frac{N_3}{2}\right)\frac{\pi\mu_o rl}{g}\cos\theta_r = L_{13}\cos(\theta_r - 120^\circ) \quad (2.15)$$

Hence, the flux linkages of the stator a1, b1, c1 windings can be written in expanded form as follows

$$\begin{aligned} \lambda_{a1} &= L_{a1a1}i_{a1} + L_{a1b1}i_{b1} + L_{a1c1}i_{c1} + L_{a1a2}i_{a2} + L_{a1b2}i_{b2} + L_{a1c2}i_{c2} \\ &\quad + L_{a1a3}i_{a3} + L_{a1b3}i_{b3} + L_{a1c3}i_{c3} \\ &= (L_{l1} + L_{m1})i_{a1} - \frac{1}{2}L_{m1}i_{b1} - \frac{1}{2}L_{m1}i_{c1} \\ &\quad + L_{12}\cos\theta_r i_{a2} + L_{12}\cos(\theta_r + 120^\circ)i_{b2} + L_{12}\cos(\theta_r - 120^\circ)i_{c2} \\ &\quad + L_{13}\cos\theta_r i_{a3} + L_{13}\cos(\theta_r + 120^\circ)i_{b3} + L_{13}\cos(\theta_r - 120^\circ)i_{c3} \end{aligned} \quad (2.16)$$

$$\begin{aligned}
\lambda_{b1} &= L_{b1a1}i_{a1} + L_{b1b1}i_{b1} + L_{b1c1}i_{c1} + L_{b1a2}i_{a2} + L_{b1b2}i_{b2} + L_{b1c2}i_{c2} \\
&\quad + L_{b1a3}i_{a3} + L_{b1b3}i_{b3} + L_{b1c3}i_{c3} \\
&= -\frac{1}{2}L_{m1}i_{a1} + (L_{l1} + L_{m1})i_{b1} - \frac{1}{2}L_{m1}i_{c1} \\
&\quad + L_{12} \cos(\theta_r - 120^\circ)i_{a2} + L_{12} \cos \theta_r i_{b2} + L_{12} \cos(\theta_r + 120^\circ)i_{c2} \\
&\quad + L_{13} \cos(\theta_r - 120^\circ)i_{a3} + L_{13} \cos \theta_r i_{b3} + L_{13} \cos(\theta_r + 120^\circ)i_{c3}
\end{aligned} \tag{2.17}$$

$$\begin{aligned}
\lambda_{c1} &= L_{c1a1}i_{a1} + L_{c1b1}i_{b1} + L_{c1c1}i_{c1} + L_{c1a2}i_{a2} + L_{c1b2}i_{b2} + L_{c1c2}i_{c2} \\
&\quad + L_{c1a3}i_{a3} + L_{c1b3}i_{b3} + L_{c1c3}i_{c3} \\
&= -\frac{1}{2}L_{m1}i_{a1} - \frac{1}{2}L_{m1}i_{b1} + (L_{l1} + L_{m1})i_{c1} \\
&\quad + L_{12} \cos(\theta_r + 120^\circ)i_{a2} + L_{12} \cos(\theta_r - 120^\circ)i_{b2} + L_{12} \cos \theta_r i_{c2} \\
&\quad + L_{13} \cos(\theta_r + 120^\circ)i_{a3} + L_{13} \cos(\theta_r - 120^\circ)i_{b3} + L_{13} \cos \theta_r i_{c3}
\end{aligned} \tag{2.18}$$

The flux linkage in a DCIM is shown in Figure 2.2. In equations (2.16)-(2.18), the leakage inductance L_{l1} is due to the leakage flux of the stator winding, which is shown by ϕ_{l1} , and the mutual inductances L_{m1} , L_{12} , L_{13} are due to mutual flux shown by ϕ_m in Figure 2.2.

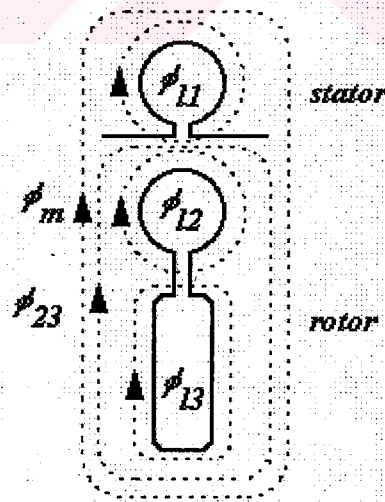


Figure 2.2 Flux lines in a DCIM

In a similar way given in the determination of stator winding inductances above, both rotor winding inductances can be determined. The rotor starting-cage and running-cage self inductances are

$$L_{a2a2} = L_{b2b2} = L_{c2c2} = L_{l2} + \left(\frac{N_2}{2}\right)^2 \frac{\pi\mu_o r l}{g} + L_{23} = L_{l2} + L_{m2} + L_{23} \quad (2.19)$$

$$L_{a3a3} = L_{b3b3} = L_{c3c3} = L_{l3} + \left(\frac{N_3}{2}\right)^2 \frac{\pi\mu_o r l}{g} + L_{23} = L_{l3} + L_{m3} + L_{23} \quad (2.20)$$

where L_{l2} and L_{l3} are the rotor starting-cage leakage inductance and rotor running-cage leakage inductances due to leakage flux of each winding, respectively. L_{23} is the inductance due to flux linking both rotor windings as shown in Figure 2.2.

The flux linking any two of different rotor windings is the magnetizing flux also linking the stator windings. So, the mutual inductances between rotor starting-cage windings a2-b2, a2-c2, and b2-c2 are determined as

$$L_{a2b2} = L_{a2c2} = L_{b2c2} = -\left(\frac{N_2}{2}\right)^2 \frac{\pi \mu_o r l}{2g} = -\frac{1}{2} L_{m2} \quad (2.21)$$

and the mutual inductances between rotor running-cage windings a2-b2, a2-c2, and b2-c2 are

$$L_{a3b3} = L_{a3c3} = L_{b3c3} = -\left(\frac{N_3}{2}\right)^2 \frac{\pi \mu_o r l}{2g} = -\frac{1}{2} L_{m3} \quad (2.22)$$

In order to find the mutual inductance between the same windings of rotor-starting cage and rotor running-cage, the total flux linking a2 winding due to the current flowing only in a3 winding is computed as

$$\lambda_{a2a3} = L_{23}i_{a3} + \left(\frac{N_2}{2}\right)\left(\frac{N_3}{2}\right)\frac{\pi\mu_o r l}{g}i_{a3} \quad (2.23)$$

which yields to

$$L_{a2a3} = L_{23} + \left(\frac{N_2}{2}\right)\left(\frac{N_3}{2}\right)\frac{\pi\mu_o r l}{g} = L_{23} + L_{m23} \quad (2.24)$$

Similarly, the mutual inductances of other windings of the rotor

$$L_{b2b3} = L_{23} + \left(\frac{N_2}{2}\right)\left(\frac{N_3}{2}\right)\frac{\pi\mu_o r l}{g} = L_{23} + L_{m23} \quad (2.25)$$

$$L_{c2c3} = L_{23} + \left(\frac{N_2}{2}\right)\left(\frac{N_3}{2}\right)\frac{\pi\mu_o r l}{g} = L_{23} + L_{m23} \quad (2.26)$$

Since the flux path linking rotor a2-b3, a2-c3, b2-c3 windings is associated with the magnetizing flux path, the mutual inductances between these windings are

$$L_{a2b3} = L_{a2c3} = L_{b2c3} = -\left(\frac{N_2}{2}\right)\left(\frac{N_3}{2}\right)\frac{\pi}{2}\frac{\mu_o r l}{g} = -\frac{1}{2}L_{m23} \quad (2.27)$$

Hence, the flux linkages of rotor starting-cage can be written in expanded form as follows

$$\begin{aligned} \lambda_{a2} &= L_{a2a1}i_{a1} + L_{a2b1}i_{b1} + L_{a2c1}i_{c1} + L_{a2a2}i_{a2} + L_{a2b2}i_{b2} + L_{a2c2}i_{c2} \\ &\quad + L_{a2a3}i_{a3} + L_{a2b3}i_{b3} + L_{a2c3}i_{c3} \\ &= L_{12} \cos \theta_r i_{a1} + L_{12} \cos(\theta_r - 120^\circ) i_{b1} + L_{12} \cos(\theta_r + 120^\circ) i_{c1} \\ &\quad + (L_{12} + L_{m2} + L_{23})i_{a2} - \frac{1}{2}L_{m2}i_{b2} - \frac{1}{2}L_{m2}i_{c2} \\ &\quad + (L_{m23} + L_{23})i_{a3} - \frac{1}{2}L_{m23}i_{b3} - \frac{1}{2}L_{m23}i_{c3} \end{aligned} \quad (2.28)$$

$$\begin{aligned}
\lambda_{b2} &= L_{b2a1}i_{a1} + L_{b2b1}i_{b1} + L_{b2c1}i_{c1} + L_{b2a2}i_{a2} + L_{b2b2}i_{b2} + L_{b2c2}i_{c2} \\
&\quad + L_{b2a3}i_{a3} + L_{b2b3}i_{b3} + L_{b2c3}i_{c3} \\
&= L_{12} \cos(\theta_r + 120^\circ)i_{a1} + L_{12} \cos \theta_r i_{b1} + L_{12} \cos(\theta_r - 120^\circ)i_{c1} \\
&\quad - \frac{1}{2}L_{m2}i_{a2} + (L_{l2} + L_{m2} + L_{23})i_{b2} - \frac{1}{2}L_{m2}i_{c2} \\
&\quad - \frac{1}{2}L_{m23}i_{a3} + (L_{m23} + L_{23})i_{b3} - \frac{1}{2}L_{m23}i_{c3}
\end{aligned} \tag{2.29}$$

$$\begin{aligned}
\lambda_{c2} &= L_{c2a1}i_{a1} + L_{c2b1}i_{b1} + L_{c2c1}i_{c1} + L_{c2a2}i_{a2} + L_{c2b2}i_{b2} + L_{c2c2}i_{c2} \\
&\quad + L_{c2a3}i_{a3} + L_{c2b3}i_{b3} + L_{c2c3}i_{c3} \\
&= L_{12} \cos(\theta_r - 120^\circ)i_{a1} + L_{12} \cos(\theta_r + 120^\circ)i_{b1} + L_{12} \cos \theta_r i_{c1} \\
&\quad - \frac{1}{2}L_{m2}i_{a2} - \frac{1}{2}L_{m2}i_{b2} + (L_{l2} + L_{m2} + L_{23})i_{c2} \\
&\quad - \frac{1}{2}L_{m23}i_{a3} - \frac{1}{2}L_{m23}i_{b3} + (L_{m23} + L_{23})i_{c3}
\end{aligned} \tag{2.30}$$

The flux linkages of rotor running-cage windings in expanded form are written as

$$\begin{aligned}
\lambda_{a3} &= L_{a3a1}i_{a1} + L_{a3b1}i_{b1} + L_{a3c1}i_{c1} + L_{a3a2}i_{a2} + L_{a3b2}i_{b2} + L_{a3c2}i_{c2} \\
&\quad + L_{a3a3}i_{a3} + L_{a3b3}i_{b3} + L_{a3c3}i_{c3} \\
&= L_{13} \cos \theta_r i_{a1} + L_{13} \cos(\theta_r - 120^\circ)i_{b1} + L_{13} \cos(\theta_r + 120^\circ)i_{c1} \\
&\quad + (L_{m23} + L_{23})i_{a2} - \frac{1}{2}L_{m23}i_{b2} - \frac{1}{2}L_{m23}i_{c2} \\
&\quad + (L_{l3} + L_{m3} + L_{23})i_{a3} - \frac{1}{2}L_{m3}i_{b3} - \frac{1}{2}L_{m3}i_{c3}
\end{aligned} \tag{2.31}$$

$$\begin{aligned}
\lambda_{b3} &= L_{b3a1}i_{a1} + L_{b3b1}i_{b1} + L_{b3c1}i_{c1} + L_{b3a2}i_{a2} + L_{b3b2}i_{b2} + L_{b3c2}i_{c2} \\
&\quad + L_{b3a3}i_{a3} + L_{b3b3}i_{b3} + L_{b3c3}i_{c3} \\
&= L_{13} \cos(\theta_r + 120^\circ)i_{a1} + L_{13} \cos \theta_r i_{b1} + L_{13} \cos(\theta_r - 120^\circ)i_{c1} \\
&\quad - \frac{1}{2}L_{m23}i_{a2} + (L_{m23} + L_{23})i_{b2} - \frac{1}{2}L_{m23}i_{c2} \\
&\quad - \frac{1}{2}L_{m3}i_{a3} + (L_{l3} + L_{m3} + L_{23})i_{b3} - \frac{1}{2}L_{m3}i_{c3}
\end{aligned} \tag{2.32}$$

$$\begin{aligned}
\lambda_{c3} &= L_{c3a1}i_{a1} + L_{c3b1}i_{b1} + L_{c3c1}i_{c1} + L_{c3a2}i_{a2} + L_{c3b2}i_{b2} + L_{c3c2}i_{c2} \\
&\quad + L_{c3a3}i_{a3} + L_{c3b3}i_{b3} + L_{c3c3}i_{c3} \\
&= L_{13} \cos(\theta_r - 120^\circ)i_{a1} + L_{13} \cos(\theta_r + 120^\circ)i_{b1} + L_{13} \cos \theta_r i_{c1} \\
&\quad - \frac{1}{2}L_{m23}i_{a2} - \frac{1}{2}L_{m23}i_{b2} + (L_{m23} + L_{23})i_{c2} \\
&\quad - \frac{1}{2}L_{m3}i_{a3} - \frac{1}{2}L_{m3}i_{b3} + (L_{13} + L_{m3} + L_{23})i_{c3}
\end{aligned} \tag{2.33}$$

Once the flux linkages are expressed in terms of machine variables, the voltage equations of the machine can be obtained as follows

$$v_{a1} = r_1 i_{a1} + p \lambda_{a1} \tag{2.34}$$

$$v_{b1} = r_1 i_{b1} + p \lambda_{b1} \tag{2.35}$$

$$v_{c1} = r_1 i_{c1} + p \lambda_{c1} \tag{2.36}$$

$$v_{a2} = r_2 i_{a2} + p \lambda_{a2} \tag{2.37}$$

$$v_{b2} = r_2 i_{b2} + p \lambda_{b2} \tag{2.38}$$

$$v_{c2} = r_2 i_{c2} + p \lambda_{c2} \tag{2.39}$$

$$v_{a3} = r_3 i_{a3} + p \lambda_{a3} \tag{2.40}$$

$$v_{b3} = r_3 i_{b3} + p \lambda_{b3} \tag{2.41}$$

$$v_{c3} = r_3 i_{c3} + p \lambda_{c3} \tag{2.42}$$

where $p = \frac{d}{dt}$ is the derivative operator

The above voltage equations (2.34)-(2.42) of the machine can be rewritten in matrix form as follows

$$\begin{bmatrix} \mathbf{v}_{abc1} \\ \mathbf{v}_{abc2} \\ \mathbf{v}_{abc3} \end{bmatrix} = \begin{bmatrix} \mathbf{r}_1 & \mathbf{0} & \mathbf{0} \\ \mathbf{0} & \mathbf{r}_2 & \mathbf{0} \\ \mathbf{0} & \mathbf{0} & \mathbf{r}_3 \end{bmatrix} \begin{bmatrix} \mathbf{i}_{abc1} \\ \mathbf{i}_{abc2} \\ \mathbf{i}_{abc3} \end{bmatrix} + p \begin{bmatrix} \boldsymbol{\lambda}_{abc1} \\ \boldsymbol{\lambda}_{abc2} \\ \boldsymbol{\lambda}_{abc3} \end{bmatrix} \quad (2.43)$$

where $\mathbf{r}_1, \mathbf{r}_2, \mathbf{r}_3$ are the diagonal stator, rotor starting-cage, and rotor running-cage resistance matrices, respectively. From the flux linkage equations derived above, the matrix form of the flux linkages can be written as

$$\begin{bmatrix} \boldsymbol{\lambda}_{abc1} \\ \boldsymbol{\lambda}_{abc2} \\ \boldsymbol{\lambda}_{abc3} \end{bmatrix} = \begin{bmatrix} \mathbf{L}_{11} & \mathbf{L}_{12} & \mathbf{L}_{13} \\ (\mathbf{L}_{12})^T & \mathbf{L}_{22} & \mathbf{L}_{23} \\ (\mathbf{L}_{13})^T & (\mathbf{L}_{23})^T & \mathbf{L}_{33} \end{bmatrix} \begin{bmatrix} \mathbf{i}_{abc1} \\ \mathbf{i}_{abc2} \\ \mathbf{i}_{abc3} \end{bmatrix} \quad (2.44)$$

The inductance matrices in equation (2.44) are expressed as follows

$$\mathbf{L}_{11} = \begin{bmatrix} L_{l1} + L_{m1} & -\frac{1}{2}L_{m1} & -\frac{1}{2}L_{m1} \\ -\frac{1}{2}L_{m1} & L_{l1} + L_{m1} & -\frac{1}{2}L_{m1} \\ -\frac{1}{2}L_{m1} & -\frac{1}{2}L_{m1} & L_{l1} + L_{m1} \end{bmatrix} \quad (2.45)$$

is the stator self inductance matrix. Here, L_{l1} is the leakage inductance and L_{m1} is the magnetizing inductance of the stator windings.

$$\mathbf{L}_{12} = L_{12} \begin{bmatrix} \cos \theta_r & \cos(\theta_r + 120^\circ) & \cos(\theta_r - 120^\circ) \\ \cos(\theta_r - 120^\circ) & \cos \theta_r & \cos(\theta_r + 120^\circ) \\ \cos(\theta_r + 120^\circ) & \cos(\theta_r - 120^\circ) & \cos \theta_r \end{bmatrix} \quad (2.46)$$

is the stator to rotor starting-cage mutual inductance matrix and L_{12} is the amplitude of the mutual inductances between these windings.

$$\mathbf{L}_{13} = L_{13} \begin{bmatrix} \cos \theta_r & \cos(\theta_r + 120^\circ) & \cos(\theta_r - 120^\circ) \\ \cos(\theta_r - 120^\circ) & \cos \theta_r & \cos(\theta_r + 120^\circ) \\ \cos(\theta_r + 120^\circ) & \cos(\theta_r - 120^\circ) & \cos \theta_r \end{bmatrix} \quad (2.47)$$

is the stator to rotor running-cage mutual inductance matrix and L_{13} is the amplitude of the mutual inductances between these windings.

$$\mathbf{L}_{22} = \begin{bmatrix} L_{l2} + L_{m2} + L_{23} & -\frac{1}{2}L_{m2} & -\frac{1}{2}L_{m2} \\ -\frac{1}{2}L_{m2} & L_{l2} + L_{m2} + L_{23} & -\frac{1}{2}L_{m2} \\ -\frac{1}{2}L_{m2} & -\frac{1}{2}L_{m2} & L_{l2} + L_{m2} + L_{23} \end{bmatrix} \quad (2.48)$$

is the rotor starting-cage self-inductance matrix. Here, L_{l2} is the leakage inductance and L_{m2} is the magnetizing inductance of the rotor starting-cage windings. L_{23} is the inductance due to flux linking two rotor windings.

$$\mathbf{L}_{33} = \begin{bmatrix} L_{l3} + L_{m3} + L_{32} & -\frac{1}{2}L_{m3} & -\frac{1}{2}L_{m3} \\ -\frac{1}{2}L_{m3} & L_{l3} + L_{m3} + L_{32} & -\frac{1}{2}L_{m3} \\ -\frac{1}{2}L_{m3} & -\frac{1}{2}L_{m3} & L_{l3} + L_{m3} + L_{32} \end{bmatrix} \quad (2.49)$$

is the rotor running-cage self inductance matrix. Here, L_{l3} is the leakage inductance and L_{m3} is the magnetizing inductance of the rotor running-cage windings.

$$\mathbf{L}_{23} = \begin{bmatrix} L_{23} + L_{m23} & -\frac{1}{2}L_{m23} & -\frac{1}{2}L_{m23} \\ -\frac{1}{2}L_{m23} & L_{23} + L_{m23} & -\frac{1}{2}L_{m23} \\ -\frac{1}{2}L_{m23} & -\frac{1}{2}L_{m23} & L_{23} + L_{m23} \end{bmatrix} \quad (2.50)$$

is the rotor starting-cage to rotor running-cage mutual inductance matrix. L_{m23} is the inductance of both rotor windings associated with main magnetizing flux path.

Hence, the machine equations of each circuit are obtained. The rotor variables of the machine are referred to the stator side by the turns ratios as follows

$$\mathbf{i}'_{abc2} = \frac{N_2}{N_1} \mathbf{i}_{abc2}, \mathbf{i}'_{abc3} = \frac{N_3}{N_1} \mathbf{i}_{abc3} \quad (2.51)$$

$$\mathbf{v}'_{abc2} = \frac{N_1}{N_2} \mathbf{v}_{abc2}, \mathbf{v}'_{abc3} = \frac{N_1}{N_3} \mathbf{v}_{abc3} \quad (2.52)$$

$$\lambda'_{abc2} = \frac{N_1}{N_2} \lambda_{abc2}, \lambda'_{abc3} = \frac{N_1}{N_3} \lambda_{abc3} \quad (2.53)$$

The flux path of the magnetizing inductances of each winding is the same. Also, the mutual inductances between rotor and stator windings are defined over the same magnetic flux path. So, the following expression can be written:

$$L_{m1} = \frac{N_1^2}{R_m} \quad (2.54)$$

$$L_{12} = \frac{N_1 N_2}{R_m} = \frac{N_2}{N_1} L_{m1} \quad (2.55)$$

$$L_{13} = \frac{N_1 N_3}{R_m} = \frac{N_3}{N_1} L_{m1} \quad (2.56)$$

where the reluctance of main flux path (R_m) is defined by

$$R_m = \frac{g}{\pi \mu_o r l} \quad (2.57)$$

The stator to rotor mutual inductance matrices referred to the stator side are expressed as

$$\mathbf{L}'_{12} = \frac{N_1}{N_2} \mathbf{L}_{12} \quad (2.58)$$

$$\mathbf{L}'_{13} = \frac{N_1}{N_3} \mathbf{L}_{13} \quad (2.59)$$

Substituting equations (2.46) and (2.47) into (2.58) and (2.59) yields to

$$\mathbf{L}'_{12} = L_{m1} \begin{bmatrix} \cos \theta_r & \cos(\theta_r + 120^\circ) & \cos(\theta_r - 120^\circ) \\ \cos(\theta_r - 120^\circ) & \cos \theta_r & \cos(\theta_r + 120^\circ) \\ \cos(\theta_r + 120^\circ) & \cos(\theta_r - 120^\circ) & \cos \theta_r \end{bmatrix} \quad (2.60)$$

$$\mathbf{L}'_{13} = L_{m1} \begin{bmatrix} \cos \theta_r & \cos(\theta_r + 120^\circ) & \cos(\theta_r - 120^\circ) \\ \cos(\theta_r - 120^\circ) & \cos \theta_r & \cos(\theta_r + 120^\circ) \\ \cos(\theta_r + 120^\circ) & \cos(\theta_r - 120^\circ) & \cos \theta_r \end{bmatrix} \quad (2.61)$$

Since the stator and rotor magnetizing inductances are defined over the same magnetic flux path, the following expression can be written

$$L_{m1} = \left(\frac{N_1}{N_2} \right)^2 L_{m2} = \left(\frac{N_1}{N_3} \right)^2 L_{m3} \quad (2.62)$$

The rotor self inductance matrices are referred to the stator side by the square of the turns ratios as follows

$$\mathbf{L}'_{22} = \left(\frac{N_1}{N_2} \right)^2 \mathbf{L}_{22} \quad (2.63)$$

$$\mathbf{L}'_{33} = \left(\frac{N_1}{N_3} \right)^2 \mathbf{L}_{33} \quad (2.64)$$

Substituting equations (2.48) and (2.49) into (2.63) and (2.64) yields to

$$\mathbf{L}'_{22} = \begin{bmatrix} L'_{l2} + L_{m1} + L'_{23} & -\frac{1}{2}L_{m1} & -\frac{1}{2}L_{m1} \\ -\frac{1}{2}L_{m1} & L'_{l2} + L_{m1} + L'_{23} & -\frac{1}{2}L_{m1} \\ -\frac{1}{2}L_{m1} & -\frac{1}{2}L_{m1} & L'_{l2} + L_{m1} + L'_{23} \end{bmatrix} \quad (2.65)$$

$$\mathbf{L}'_{33} = \begin{bmatrix} L'_{l3} + L_{m1} + L'_{23} & -\frac{1}{2}L_{m1} & -\frac{1}{2}L_{m1} \\ -\frac{1}{2}L_{m1} & L'_{l3} + L_{m1} + L'_{23} & -\frac{1}{2}L_{m1} \\ -\frac{1}{2}L_{m1} & -\frac{1}{2}L_{m1} & L'_{l3} + L_{m1} + L'_{23} \end{bmatrix} \quad (2.66)$$

where

$$L'_{l2} = \left(\frac{N_1}{N_2} \right)^2 L_{l2} \quad (2.67)$$

$$L'_{l3} = \left(\frac{N_1}{N_3} \right)^2 L_{l3} \quad (2.68)$$

$$L'_{23} = \frac{N_1^2}{N_2 N_3} L_{23} \quad (2.69)$$

The relationship between the stator magnetizing inductance and the mutual inductance between the two rotor windings can be expressed as

$$L_{m1} = \frac{N_1^2}{N_2 N_3} L_{m23} \quad (2.70)$$

The mutual inductance matrix between the two rotor windings is referred to the stator side as follows

$$\mathbf{L}'_{23} = \frac{N_1^2}{N_2 N_3} \mathbf{L}_{23} \quad (2.71)$$

and substituting equation (2.50) into (2.71) yields to

$$\mathbf{L}'_{23} = \begin{bmatrix} L'_{23} + L_{m1} & -\frac{1}{2}L_{m1} & -\frac{1}{2}L_{m1} \\ -\frac{1}{2}L_{m1} & L'_{23} + L_{m1} & -\frac{1}{2}L_{m1} \\ -\frac{1}{2}L_{m1} & -\frac{1}{2}L_{m1} & L'_{23} + L_{m1} \end{bmatrix} \quad (2.72)$$

Finally, the resistances of the rotor windings are referred to the stator side as follows

$$r'_2 = \left(\frac{N_1}{N_2} \right)^2 r_2 \quad (2.73)$$

$$r'_3 = \left(\frac{N_1}{N_3} \right)^2 r_3 \quad (2.74)$$

The flux linkages referred to the stator side in compact form are expressed as

$$\begin{bmatrix} \lambda_{abc1} \\ \lambda'_{abc2} \\ \lambda'_{abc3} \end{bmatrix} = \begin{bmatrix} \mathbf{L}_{11} & \mathbf{L}'_{12} & \mathbf{L}'_{13} \\ (\mathbf{L}'_{12})^T & \mathbf{L}'_{22} & \mathbf{L}'_{23} \\ (\mathbf{L}'_{13})^T & (\mathbf{L}'_{23})^T & \mathbf{L}'_{33} \end{bmatrix} \begin{bmatrix} \mathbf{i}_{abc1} \\ \mathbf{i}'_{abc2} \\ \mathbf{i}'_{abc3} \end{bmatrix} \quad (2.75)$$

Thus, the voltage equations of the double-cage induction machine referred to the stator side can be written in compact form as

$$\begin{bmatrix} \mathbf{v}_{abc1} \\ \mathbf{v}_{abc2} \\ \mathbf{v}_{abc3} \end{bmatrix} = \begin{bmatrix} \mathbf{r}_1 + p\mathbf{L}_{11} & p\mathbf{L}'_{12} & p\mathbf{L}'_{13} \\ p(\mathbf{L}'_{12})^T & \mathbf{r}_2' + p\mathbf{L}'_{22} & p\mathbf{L}'_{23} \\ p(\mathbf{L}'_{13})^T & p(\mathbf{L}'_{23})^T & \mathbf{r}_3' + p\mathbf{L}'_{33} \end{bmatrix} \begin{bmatrix} \mathbf{i}_{abc1} \\ \mathbf{i}_{abc2} \\ \mathbf{i}_{abc3} \end{bmatrix} \quad (2.76)$$

The voltage equations in the matrix form are obtained and given in equation (2.80). Here, the self inductances are expressed as the sum of their leakage and mutual inductances as follows

$$L_{11} = L_{l2} + L_{m1} \quad (2.77)$$

$$L'_{22} = L'_{l2} + L_{m1} \quad (2.78)$$

$$L'_{33} = L'_{l3} + L_{m1} \quad (2.79)$$

$$\begin{bmatrix} v_{e1} \\ v_{b1} \\ v_{e1} \\ v_{e2} \\ v_{b2} \\ v_{e2} \\ v_{e3} \\ v_{b3} \\ v_{e3} \end{bmatrix} = \begin{bmatrix} r_1 + L_{11}p & -\frac{1}{2}L_{m1}p & pL_{m1}\cos\theta_r & pL_{m1}\cos(\theta_r + 120^\circ) & pL_{m1}\cos(\theta_r - 120^\circ) & pL_{m1}\cos\theta_r & pL_{m1}\cos(\theta_r + 120^\circ) & pL_{m1}\cos(\theta_r - 120^\circ) & pL_{m1}\cos\theta_r \\ -\frac{1}{2}L_{m1}p & r_1 + L_{11}p & pL_{m1}\cos(\theta_r - 120^\circ) & pL_{m1}\cos\theta_r & pL_{m1}\cos(\theta_r + 120^\circ) & pL_{m1}\cos\theta_r & pL_{m1}\cos(\theta_r - 120^\circ) & pL_{m1}\cos\theta_r & pL_{m1}\cos(\theta_r + 120^\circ) \\ -\frac{1}{2}L_{m1}p & -\frac{1}{2}L_{m1}p & r_1 + L_{11}p & pL_{m1}\cos\theta_r & pL_{m1}\cos(\theta_r - 120^\circ) & pL_{m1}\cos\theta_r & pL_{m1}\cos(\theta_r + 120^\circ) & pL_{m1}\cos\theta_r & pL_{m1}\cos(\theta_r - 120^\circ) \\ pL_{m1}\cos\theta_r & pL_{m1}\cos(\theta_r - 120^\circ) & pL_{m1}\cos(\theta_r + 120^\circ) & -\frac{1}{2}L_{m1}p & -\frac{1}{2}L_{m1}p & -\frac{1}{2}L_{m1}p & -\frac{1}{2}L_{m1}p & -\frac{1}{2}L_{m1}p & -\frac{1}{2}L_{m1}p \\ pL_{m1}\cos(\theta_r + 120^\circ) & pL_{m1}\cos\theta_r & pL_{m1}\cos(\theta_r - 120^\circ) & -\frac{1}{2}L_{m1}p & -\frac{1}{2}L_{m1}p & -\frac{1}{2}L_{m1}p & -\frac{1}{2}L_{m1}p & -\frac{1}{2}L_{m1}p & -\frac{1}{2}L_{m1}p \\ pL_{m1}\cos(\theta_r - 120^\circ) & pL_{m1}\cos(\theta_r + 120^\circ) & pL_{m1}\cos\theta_r & -\frac{1}{2}L_{m1}p & -\frac{1}{2}L_{m1}p & -\frac{1}{2}L_{m1}p & -\frac{1}{2}L_{m1}p & -\frac{1}{2}L_{m1}p & -\frac{1}{2}L_{m1}p \\ pL_{m1}\cos\theta_r & pL_{m1}\cos(\theta_r - 120^\circ) & pL_{m1}\cos(\theta_r + 120^\circ) & -\frac{1}{2}L_{m1}p & -\frac{1}{2}L_{m1}p & -\frac{1}{2}L_{m1}p & -\frac{1}{2}L_{m1}p & -\frac{1}{2}L_{m1}p & -\frac{1}{2}L_{m1}p \\ pL_{m1}\cos(\theta_r + 120^\circ) & pL_{m1}\cos\theta_r & pL_{m1}\cos(\theta_r - 120^\circ) & -\frac{1}{2}L_{m1}p & -\frac{1}{2}L_{m1}p & -\frac{1}{2}L_{m1}p & -\frac{1}{2}L_{m1}p & -\frac{1}{2}L_{m1}p & -\frac{1}{2}L_{m1}p \\ pL_{m1}\cos(\theta_r - 120^\circ) & pL_{m1}\cos(\theta_r + 120^\circ) & pL_{m1}\cos\theta_r & -\frac{1}{2}L_{m1}p & -\frac{1}{2}L_{m1}p & -\frac{1}{2}L_{m1}p & -\frac{1}{2}L_{m1}p & -\frac{1}{2}L_{m1}p & -\frac{1}{2}L_{m1}p \end{bmatrix} \begin{bmatrix} i_{a1} \\ i_{b1} \\ i_{c1} \\ i'_{a2} \\ i'_{b2} \\ i'_{c2} \\ i'_{a3} \\ i'_{b3} \\ i'_{c3} \end{bmatrix}$$

(2.80)

2.2 Voltage Equations in Arbitrary Reference Frame

In the voltage equations expressed in terms of machine variables, the inductances are time-varying and introduce difficulty in the analysis of the machine. In order to eliminate these time-varying inductances, transformations are applied to stator and rotor variables of the machine. Hence, the time-varying inductances of the machine are transformed into time-invariant form as described in reference-frame theory.

Let \mathbf{f} be the variable representing the quantities voltage, current, and flux linkage. The stator variables, which are expressed in machine variables and denoted by abc , are transformed into $qd0$ variables by applying the transformation as follows

$$\mathbf{f}_{qd01} = \mathbf{K}_s \mathbf{f}_{abc1} \quad (2.81)$$

The transformation matrix \mathbf{K}_s is defined as

$$\mathbf{K}_s = \frac{2}{3} \begin{bmatrix} \cos \theta & \cos(\theta - 120^\circ) & \cos(\theta + 120^\circ) \\ \sin \theta & \sin(\theta - 120^\circ) & \sin(\theta + 120^\circ) \\ \frac{1}{2} & \frac{1}{2} & \frac{1}{2} \end{bmatrix} \quad (2.82)$$

where

$$\theta = \int_0^t \omega(\xi) d\xi + \theta(0) \quad (2.83)$$

and ξ is dummy integration variable. $\omega(\xi)$ defines the angular speed of the reference frame and may have any arbitrary value. The inverse transformation matrix \mathbf{K}_s^{-1} can be obtained as

$$\mathbf{K}_s^{-1} = \begin{bmatrix} \cos \theta & \sin \theta & 1 \\ \cos(\theta - 120^\circ) & \sin(\theta - 120^\circ) & 1 \\ \cos(\theta + 120^\circ) & \sin(\theta + 120^\circ) & 1 \end{bmatrix} \quad (2.84)$$

Similarly, the transformations applied to the rotor variables of the machine are as follows

$$\mathbf{f}'_{qd02} = \mathbf{K}_r \mathbf{f}'_{abc2} \quad (2.85)$$

$$\mathbf{f}'_{qd02} = \mathbf{K}_r \mathbf{f}'_{abc3} \quad (2.86)$$

where

$$\mathbf{K}_r = \frac{2}{3} \begin{bmatrix} \cos \beta & \cos(\beta - 120^\circ) & \cos(\beta + 120^\circ) \\ \sin \beta & \sin(\beta - 120^\circ) & \sin(\beta + 120^\circ) \\ \frac{1}{2} & \frac{1}{2} & \frac{1}{2} \end{bmatrix} \quad (2.87)$$

In equation (2.87), $\beta = \theta - \theta_r$ and the angular displacement of rotor is expressed as

$$\theta_r = \int_0^t \omega_r(\xi) d\xi + \theta_r(0) \quad (2.88)$$

where $\omega_r(\xi)$ is the angular speed of the rotor. The inverse transformation matrix \mathbf{K}_r^{-1} can be expressed as

$$\mathbf{K}_r^{-1} = \frac{2}{3} \begin{bmatrix} \cos \beta & \sin \beta & 1 \\ \cos(\beta - 120^\circ) & \sin(\beta - 120^\circ) & 1 \\ \cos(\beta + 120^\circ) & \sin(\beta + 120^\circ) & 1 \end{bmatrix} \quad (2.89)$$

Applying the transformations to stator and rotor abc variables of the induction machine as given in equations (2.81), (2.85), and (2.86), the expression of flux linkages given in equation (2.78) can be written as

$$\begin{bmatrix} \mathbf{K}_s^{-1} \lambda_{qd01} \\ \mathbf{K}_r^{-1} \lambda'_{qd02} \\ \mathbf{K}_r^{-1} \lambda'_{qd03} \end{bmatrix} = \begin{bmatrix} \mathbf{L}_{11} & \mathbf{L}'_{12} & \mathbf{L}'_{13} \\ (\mathbf{L}'_{12})^T & \mathbf{L}'_{22} & \mathbf{L}'_{23} \\ (\mathbf{L}'_{13})^T & (\mathbf{L}'_{23})^T & \mathbf{L}'_{33} \end{bmatrix} \begin{bmatrix} \mathbf{K}_s^{-1} \mathbf{i}_{qd01} \\ \mathbf{K}_r^{-1} \mathbf{i}'_{qd02} \\ \mathbf{K}_r^{-1} \mathbf{i}'_{qd03} \end{bmatrix} \quad (2.90)$$

The expression of flux linkages in terms of $qd0$ variables can be rewritten by using the properties of matrix multiplication as follows

$$\begin{bmatrix} \lambda_{qd01} \\ \lambda'_{qd02} \\ \lambda'_{qd03} \end{bmatrix} = \begin{bmatrix} \mathbf{K}_s \mathbf{L}_{11} \mathbf{K}_s^{-1} & \mathbf{K}_s \mathbf{L}'_{12} \mathbf{K}_r^{-1} & \mathbf{K}_s \mathbf{L}'_{13} \mathbf{K}_r^{-1} \\ \mathbf{K}_r (\mathbf{L}'_{12})^T \mathbf{K}_s^{-1} & \mathbf{K}_r \mathbf{L}'_{22} \mathbf{K}_r^{-1} & \mathbf{K}_r \mathbf{L}'_{23} \mathbf{K}_r^{-1} \\ \mathbf{K}_r (\mathbf{L}'_{13})^T \mathbf{K}_s^{-1} & \mathbf{K}_r (\mathbf{L}'_{23})^T \mathbf{K}_r^{-1} & \mathbf{K}_r \mathbf{L}'_{33} \mathbf{K}_r^{-1} \end{bmatrix} \begin{bmatrix} \mathbf{i}_{qd01} \\ \mathbf{i}'_{qd02} \\ \mathbf{i}'_{qd03} \end{bmatrix} \quad (2.91)$$

The elements of the transformed impedance matrix given in equation (2.91) are defined and obtained as follows

$$\begin{bmatrix} \lambda_{qd01} \\ \lambda'_{qd02} \\ \lambda'_{qd03} \end{bmatrix} = \begin{bmatrix} \mathbf{a}_{11} & \mathbf{a}_{12} & \mathbf{a}_{13} \\ \mathbf{a}_{21} & \mathbf{a}_{22} & \mathbf{a}_{23} \\ \mathbf{a}_{31} & \mathbf{a}_{32} & \mathbf{a}_{33} \end{bmatrix} \begin{bmatrix} \mathbf{i}_{qd01} \\ \mathbf{i}'_{qd02} \\ \mathbf{i}'_{qd03} \end{bmatrix} \quad (2.92)$$

$$\mathbf{a}_{11} = \mathbf{K}_s \mathbf{L}_{11} \mathbf{K}_s^{-1} = \begin{bmatrix} L_{l1} + M & 0 & 0 \\ 0 & L_{l1} + M & 0 \\ 0 & 0 & L_{l1} \end{bmatrix} \quad (2.93)$$

$$\mathbf{a}_{22} = \mathbf{K}_r \mathbf{L}'_{22} \mathbf{K}_r^{-1} = \begin{bmatrix} L_{l2} + M + L'_{23} & 0 & 0 \\ 0 & L_{l2} + M + L'_{23} & 0 \\ 0 & 0 & L_{l2} + L'_{23} \end{bmatrix} \quad (2.94)$$

$$\mathbf{a}_{33} = \mathbf{K}_r \mathbf{L}'_{33} \mathbf{K}_r^{-1} = \begin{bmatrix} L_{l3} + M + L'_{23} & 0 & 0 \\ 0 & L_{l3} + M + L'_{23} & 0 \\ 0 & 0 & L_{l3} + L'_{23} \end{bmatrix} \quad (2.95)$$

$$\mathbf{a}_{12} = \mathbf{a}_{13} = \mathbf{K}_s \mathbf{L}'_{12} \mathbf{K}_r^{-1} = \mathbf{K}_s \mathbf{L}'_{13} \mathbf{K}_r^{-1} = \begin{bmatrix} M & 0 & 0 \\ 0 & M & 0 \\ 0 & 0 & 0 \end{bmatrix} \quad (2.96)$$

$$\mathbf{a}_{21} = \mathbf{a}_{31} = \mathbf{K}_r (\mathbf{L}'_{12})^T \mathbf{K}_s^{-1} = \mathbf{K}_r (\mathbf{L}'_{13})^T \mathbf{K}_s^{-1} = \begin{bmatrix} M & 0 & 0 \\ 0 & M & 0 \\ 0 & 0 & 0 \end{bmatrix} \quad (2.97)$$

$$\mathbf{a}_{23} = \mathbf{a}_{32} = \mathbf{K}_r \mathbf{L}'_{23} \mathbf{K}_r^{-1} = \mathbf{K}_r (\mathbf{L}'_{23})^T \mathbf{K}_r^{-1} = \begin{bmatrix} L'_{23} + M & 0 & 0 \\ 0 & L'_{23} + M & 0 \\ 0 & 0 & L'_{23} \end{bmatrix} \quad (2.98)$$

where

$$M = \frac{3}{2} L_{m1} \quad (2.99)$$

The derivation of the matrices given in equations (2.93)-(2.98) is obtained using the trigonometric relations, which are given in Appendix A.

Once the flux linkages are obtained, the voltage equations of stator windings are written in terms of qd0 variables for an RL circuit as follows

$$\mathbf{v}_{abc1} = \mathbf{r}_1 \mathbf{i}_{abc1} + p \boldsymbol{\lambda}_{abc1} \quad (2.100)$$

$$\mathbf{v}_{qd01} = \mathbf{K}_s \mathbf{r}_1 \mathbf{K}_s^{-1} \mathbf{i}_{qd01} + \mathbf{K}_s p [\mathbf{K}_s^{-1} \boldsymbol{\lambda}_{qd01}] \quad (2.101)$$

The transformed stator resistance matrix is the same as in machine variables, hence equation (2.101) becomes

$$\mathbf{v}_{qd01} = \mathbf{r}_1 \mathbf{i}_{qd01} + \mathbf{K}_s p[\mathbf{K}_s^{-1}] \boldsymbol{\lambda}_{qd01} + \mathbf{K}_s \mathbf{K}_s^{-1} p \boldsymbol{\lambda}_{qd01} \quad (2.102)$$

$$p[\mathbf{K}_s^{-1}] = \omega \begin{bmatrix} -\sin \theta & \cos \theta & 0 \\ -\sin(\theta - 120^\circ) & \cos(\theta - 120^\circ) & 0 \\ -\sin(\theta + 120^\circ) & \cos(\theta + 120^\circ) & 0 \end{bmatrix} \quad (2.103)$$

where ω is the rotational speed of the reference frame. Using the trigonometric relationships given in Appendix A, the following equation can be derived

$$\mathbf{K}_s p[\mathbf{K}_s^{-1}] = \begin{bmatrix} 0 & 1 & 0 \\ -1 & 0 & 0 \\ 0 & 0 & 0 \end{bmatrix} \quad (2.104)$$

and the voltage equation for stator windings becomes

$$\mathbf{v}_{qd01} = \mathbf{r}_1 \mathbf{i}_{qd01} + \omega \boldsymbol{\lambda}_{dq1} + p \boldsymbol{\lambda}_{qd01} \quad (2.105)$$

where

$$(\boldsymbol{\lambda}_{dq1})^T = [\lambda_{d1} \quad -\lambda_{q1} \quad 0] \quad (2.106)$$

Similarly, the voltage equations of the rotor windings referred to the stator side can be obtained applying the transformation given in equation (2.87) to the rotor variables

$$\mathbf{v}'_{qd02} = \mathbf{r}'_2 \mathbf{i}'_{qd02} + (\omega - \omega_r) \boldsymbol{\lambda}'_{dq2} + p \boldsymbol{\lambda}'_{qd02} \quad (2.107)$$

$$\mathbf{v}'_{qd03} = \mathbf{r}'_3 \mathbf{i}'_{qd03} + (\omega - \omega_r) \boldsymbol{\lambda}'_{dq3} + p \boldsymbol{\lambda}'_{qd03} \quad (2.108)$$

where ω_r is the rotational speed of the rotor and

$$(\lambda'_{dq2})^T = [\lambda_{d2} \ -\lambda_{q2} \ 0] \quad (2.109)$$

$$(\lambda'_{dq3})^T = [\lambda_{d3} \ -\lambda_{q3} \ 0] \quad (2.110)$$

The voltage equations for stator windings in expanded form now can be written as

$$v_{q1} = r_1 i_{q1} + \omega \lambda_{d1} + p \lambda_{q1} \quad (2.111)$$

$$v_{d1} = r_1 i_{d1} - \omega \lambda_{q1} + p \lambda_{d1} \quad (2.112)$$

$$v_{01} = r_1 i_{01} + p \lambda_{01} \quad (2.113)$$

The voltage equations for rotor starting-cage windings in expanded form are

$$v'_{q2} = r'_2 i'_{q2} + (\omega - \omega_r) \lambda'_{d2} + p \lambda'_{q2} \quad (2.114)$$

$$v'_{d2} = r'_2 i'_{d2} - (\omega - \omega_r) \lambda'_{q2} + p \lambda'_{d2} \quad (2.115)$$

$$v'_{02} = r'_2 i'_{02} + p \lambda'_{02} \quad (2.116)$$

The voltage equations for rotor running-cage windings in expanded form are

$$v'_{q3} = r'_3 i'_{q3} + (\omega - \omega_r) \lambda'_{d3} + p \lambda'_{q3} \quad (2.117)$$

$$v'_{d3} = r'_3 i'_{d3} - (\omega - \omega_r) \lambda'_{q3} + p \lambda'_{d3} \quad (2.118)$$

$$v'_{03} = r'_3 i'_{03} + p \lambda'_{03} \quad (2.119)$$

The flux linkage equations for stator windings in expanded form are written as

$$\lambda_{q1} = (L_{l1} + M)i_{q1} + Mi'_{q2} + Mi'_{q3} \quad (2.120)$$

$$\lambda_{d1} = (L_{l1} + M)i_{d1} + Mi'_{d2} + Mi'_{d3} \quad (2.121)$$

$$\lambda_{01} = L_{l1}i_{01} \quad (2.122)$$

The flux linkage equations for rotor starting-cage windings in expanded form are

$$\lambda'_{q2} = Mi_{q1} + (L'_{l2} + M + L'_{23})i'_{q2} + (L'_{23} + M)i'_{q3} \quad (2.123)$$

$$\lambda'_{d2} = Mi_{d1} + (L'_{l2} + M + L'_{23})i'_{d2} + (L'_{23} + M)i'_{d3} \quad (2.124)$$

$$\lambda'_{02} = (L'_{l2} + L'_{23})i'_{02} + L'_{23}i'_{03} \quad (2.125)$$

Finally, the flux linkage equations for rotor running-cage windings in expanded form are

$$\lambda'_{q3} = Mi_{q1} + (L'_{l3} + M + L'_{23})i'_{q3} + (L'_{23} + M)i'_{q2} \quad (2.126)$$

$$\lambda'_{d3} = Mi_{d1} + (L'_{l3} + M + L'_{23})i'_{d3} + (L'_{23} + M)i'_{d2} \quad (2.127)$$

$$\lambda'_{03} = L'_{23}i'_{02} + (L'_{l3} + L'_{23})i'_{03} \quad (2.128)$$

Substituting equations (2.120)-(2.128) into equations (2.111)-(2.119), the voltage equations can be rewritten. The voltage equations for stator windings in expanded form are as follows

$$v_{q1} = r_1 i_{q1} + L_{11} p i_{q1} + M p i_{q2} + M p i_{q3} + \omega L_{11} i_{d1} + \omega M i_{d2} + \omega M i_{d3} \quad (2.129)$$

$$v_{d1} = r_1 i_{d1} + L_{11} p i_{d1} + M p i_{d2} + M p i_{d3} - \omega L_{11} i_{q1} - \omega M i_{q2} - \omega M i_{q3} \quad (2.130)$$

$$v_{01} = r_1 i_{01} + L_{11} p i_{01} \quad (2.131)$$

The voltage equations for rotor starting-cage windings in expanded form are

$$\begin{aligned} v_{q2} = & r_2 i_{q2} + (L_{22} + L_{23}) p i_{q2} + M p i_{q1} + (L_{23} + M) p i_{q3} \\ & + (\omega - \omega_r) M i_{d1} + (\omega - \omega_r)(L_{22} + L_{23}) i_{d2} + (\omega - \omega_r)(L_{23} + M) i_{d3} \end{aligned} \quad (2.132)$$

$$\begin{aligned} v_{d2} = & r_2 i_{d2} + (L_{22} + L_{23}) p i_{d2} + M p i_{d1} + (L_{23} + M) p i_{d3} \\ & - (\omega - \omega_r) M i_{q1} - (\omega - \omega_r)(L_{22} + L_{23}) i_{q2} - (\omega - \omega_r)(L_{23} + M) i_{q3} \end{aligned} \quad (2.133)$$

$$v_{02} = r_2 i_{02} + (L_{12} + L_{23}) p i_{02} + L_{23} p i_{03} \quad (2.134)$$

The voltage equations for rotor running-cage windings in expanded form are

$$\begin{aligned} v_{q3} = & r_3 i_{q3} + (L_{33} + L_{23}) p i_{q3} + M p i_{q1} + (L_{23} + M) p i_{q2} \\ & + (\omega - \omega_r) M i_{d1} + (\omega - \omega_r)(L_{33} + L_{23}) i_{d3} + (\omega - \omega_r)(L_{23} + M) i_{d2} \end{aligned} \quad (2.135)$$

$$\begin{aligned} v_{d3} = & r_3 i_{d3} + (L_{33} + L_{23}) p i_{d3} + M p i_{d1} + (L_{23} + M) p i_{d2} \\ & - (\omega - \omega_r) M i_{q1} - (\omega - \omega_r)(L_{33} + L_{23}) i_{q3} - (\omega - \omega_r)(L_{23} + M) i_{q2} \end{aligned} \quad (2.136)$$

$$v_{03} = r_3 i_{03} + (L_{13} + L_{23}) p i_{03} + L_{23} p i_{02} \quad (2.137)$$

where the self inductances are defined as

$$L_{11} = L_{11} + M \quad (2.138)$$

$$L'_{22} = L'_{l2} + M \quad (2.139)$$

$$L'_{33} = L'_{l3} + M \quad (2.140)$$

The voltage equations given in (2.129)-(2.137) are expressed in stationary reference frame by letting $\omega = 0$ and rearranged in compact form with zero sequence equations are omitted as follows

$$\begin{bmatrix} v_{q1} \\ v_{d1} \\ v_{q2} \\ v_{d2} \\ v_{q3} \\ v_{d3} \end{bmatrix} = \begin{bmatrix} r_1 + L_{11}p & 0 & Mp & 0 & Mp & 0 \\ 0 & r_1 + L_{11}p & 0 & Mp & 0 & Mp \\ Mp & -\omega_r M & r'_2 + (L'_{22} + L'_{23})p & -\omega_r (L'_{22} + L'_{23}) & (L'_{23} + M)p & -\omega_r (L'_{23} + M) \\ \omega_r M & Mp & \omega_r (L'_{22} + L'_{23}) & r'_2 + (L'_{22} + L'_{23})p & \omega_r (L'_{23} + M) & (L'_{23} + M)p \\ Mp & -\omega_r M & (L'_{23} + M)p & -\omega_r (L'_{23} + M) & r'_3 + (L'_{33} + L'_{23})p & -\omega_r (L'_{33} + L'_{23}) \\ \omega_r M & Mp & \omega_r (L'_{23} + M) & (L'_{23} + M)p & \omega_r (L'_{33} + L'_{23}) & r'_3 + (L'_{33} + L'_{23})p \end{bmatrix} \begin{bmatrix} i_{q1} \\ i_{d1} \\ i_{q2} \\ i_{d2} \\ i_{q3} \\ i_{d3} \end{bmatrix} \quad (2.141)$$

2.3 Voltage Equations in abc/qd Reference Frame

In order to express the double-cage induction machine in abc/dq reference frame, which retains the actual stator phase variables but transforms the rotor only to examine the transients of the machine, the \mathbf{K}_r transformation in equation (2.87) is applied to rotor variables. In this model, it is assumed that the q axis coincides with phase a of the stator. Substituting the equations (2.85) and (2.86) into (2.75), the flux linkage matrix can be written as follows

$$\begin{bmatrix} \lambda_{abc1} \\ \mathbf{K}_r^{-1} \lambda'_{qd02} \\ \mathbf{K}_r^{-1} \lambda'_{qd03} \end{bmatrix} = \begin{bmatrix} \mathbf{L}_{11} & \mathbf{L}'_{12} & \mathbf{L}'_{13} \\ (\mathbf{L}'_{12})^T & \mathbf{L}'_{22} & \mathbf{L}'_{23} \\ (\mathbf{L}'_{13})^T & (\mathbf{L}'_{23})^T & \mathbf{L}'_{33} \end{bmatrix} \begin{bmatrix} \mathbf{i}_{abc1} \\ \mathbf{K}_r^{-1} \mathbf{i}'_{qd02} \\ \mathbf{K}_r^{-1} \mathbf{i}'_{qd03} \end{bmatrix} \quad (2.142)$$

Rearranging this equation yields to

$$\begin{bmatrix} \lambda_{abc1} \\ \lambda'_{qd02} \\ \lambda'_{qd03} \end{bmatrix} = \begin{bmatrix} \mathbf{L}_{11} & \mathbf{L}'_{12}\mathbf{K}_r^{-1} & \mathbf{L}'_{13}\mathbf{K}_r^{-1} \\ \mathbf{K}_r(\mathbf{L}'_{12})^T & \mathbf{K}_r\mathbf{L}'_{22}\mathbf{K}_r^{-1} & \mathbf{K}_r\mathbf{L}'_{23}\mathbf{K}_r^{-1} \\ \mathbf{K}_r(\mathbf{L}'_{13})^T & \mathbf{K}_r(\mathbf{L}'_{23})^T\mathbf{K}_r^{-1} & \mathbf{K}_r\mathbf{L}'_{33}\mathbf{K}_r^{-1} \end{bmatrix} \begin{bmatrix} \mathbf{i}_{abc1} \\ \mathbf{i}'_{qd02} \\ \mathbf{i}'_{qd03} \end{bmatrix} \quad (2.143)$$

Using the trigonometric relations given in Appendix A, the elements of the impedance transformed matrix given in the above equation are obtained as follows

$$\begin{bmatrix} \lambda_{qd01} \\ \lambda'_{qd02} \\ \lambda'_{qd03} \end{bmatrix} = \begin{bmatrix} \mathbf{b}_{11} & \mathbf{b}_{12} & \mathbf{b}_{13} \\ \mathbf{b}_{21} & \mathbf{b}_{22} & \mathbf{b}_{23} \\ \mathbf{b}_{31} & \mathbf{b}_{32} & \mathbf{b}_{33} \end{bmatrix} \begin{bmatrix} \mathbf{i}_{qd01} \\ \mathbf{i}'_{qd02} \\ \mathbf{i}'_{qd03} \end{bmatrix} \quad (2.144)$$

$$\mathbf{b}_{11} = \mathbf{L}_{11} = \begin{bmatrix} L_{l1} + L_{m1} & -\frac{1}{2}L_{m1} & -\frac{1}{2}L_{m1} \\ -\frac{1}{2}L_{m1} & L_{l1} + L_{m1} & -\frac{1}{2}L_{m1} \\ -\frac{1}{2}L_{m1} & -\frac{1}{2}L_{m1} & L_{l1} + L_{m1} \end{bmatrix} \quad (2.145)$$

$$\mathbf{b}_{22} = \mathbf{K}_r\mathbf{L}'_{22}\mathbf{K}_r^{-1} = \begin{bmatrix} L_{l2} + M + L'_{23} & 0 & 0 \\ 0 & L_{l2} + M + L'_{23} & 0 \\ 0 & 0 & L_{l2} + L'_{23} \end{bmatrix} \quad (2.146)$$

$$\mathbf{b}_{33} = \mathbf{K}_r\mathbf{L}'_{33}\mathbf{K}_r^{-1} = \begin{bmatrix} L_{l3} + M + L'_{23} & 0 & 0 \\ 0 & L_{l3} + M + L'_{23} & 0 \\ 0 & 0 & L_{l3} + L'_{23} \end{bmatrix} \quad (2.147)$$

$$\mathbf{b}_{23} = \mathbf{b}_{32} = \mathbf{K}_r\mathbf{L}'_{23}\mathbf{K}_r^{-1} = \mathbf{K}_r(\mathbf{L}'_{23})^T\mathbf{K}_r^{-1} = \begin{bmatrix} L'_{23} + M & 0 & 0 \\ 0 & L'_{23} + M & 0 \\ 0 & 0 & L'_{23} \end{bmatrix} \quad (2.148)$$

which are previously derived in Section 2.1 and Section 2.2. The rest of the elements of the flux linkage matrix can be obtained as

$$\mathbf{b}_{12} = \mathbf{b}_{13} = \mathbf{L}'_{12} \mathbf{K}_r^{-1} = \mathbf{L}'_{13} \mathbf{K}_r^{-1} = \begin{bmatrix} M \cos \theta & M \sin \theta & 0 \\ M \cos(\theta - 120^\circ) & M \sin(\theta - 120^\circ) & 0 \\ M \cos(\theta + 120^\circ) & M \sin(\theta + 120^\circ) & 0 \end{bmatrix} \quad (2.149)$$

$$\begin{aligned} \mathbf{b}_{21} = \mathbf{b}_{31} &= \mathbf{K}_r (\mathbf{L}'_{12})^T = \mathbf{K}_r (\mathbf{L}'_{13})^T \\ &= \begin{bmatrix} L_m \cos \theta & L_m \cos(\theta - 120^\circ) & L_m \cos(\theta + 120^\circ) \\ L_m \sin \theta & L_m \sin(\theta - 120^\circ) & L_m \sin(\theta + 120^\circ) \\ 0 & 0 & 0 \end{bmatrix} \end{aligned} \quad (2.150)$$

The voltage equations of the stator windings in terms of abc variables are written as

$$\mathbf{v}_{abc1} = \mathbf{r}_1 \mathbf{i}_{abc1} + p \boldsymbol{\lambda}_{abc1} \quad (2.151)$$

and the voltage equations of the rotor windings referred to the stator side in terms of qd0 variables are

$$\mathbf{v}'_{qd02} = \mathbf{r}'_2 \mathbf{i}'_{qd02} + (\omega - \omega_r) \boldsymbol{\lambda}'_{dq2} + p \boldsymbol{\lambda}'_{qd02} \quad (2.152)$$

$$\mathbf{v}'_{qd03} = \mathbf{r}'_3 \mathbf{i}'_{qd03} + (\omega - \omega_r) \boldsymbol{\lambda}'_{dq3} + p \boldsymbol{\lambda}'_{qd03} \quad (2.153)$$

Substituting flux linkage matrix given in equation (2.144) into equations (2.151)-(2.153), the voltage equations can be written in expanded form as follows

$$\begin{aligned} v_{a1} &= r_1 i_{a1} + (L_{l1} + L_m) p i_{a1} - \frac{1}{2} L_m i_{b1} - \frac{1}{2} L_m i_{c1} \\ &\quad + p M \cos \theta i'_{q2} + p M \sin \theta i'_{d2} + p M \cos \theta i'_{q3} + p M \sin \theta i'_{d3} \end{aligned} \quad (2.154)$$

$$\begin{aligned} v_{b1} &= -\frac{1}{2} L_m i_{a1} + r_1 i_{b1} + (L_{l1} + L_m) p i_{b1} - \frac{1}{2} L_m i_{c1} \\ &\quad + p M \cos(\theta - 120^\circ) i'_{q2} + p M \sin(\theta + 120^\circ) i'_{d2} \\ &\quad + p M \cos(\theta - 120^\circ) i'_{q3} + p M \sin(\theta + 120^\circ) i'_{d3} \end{aligned} \quad (2.155)$$

$$\begin{aligned}
v_{c1} = & -\frac{1}{2}L_m i_{a1} - \frac{1}{2}L_m i_{b1} + r_1 i_{c1} + (L_{l1} + L_m) p i_{c1} \\
& + pM \cos(\theta + 120^\circ) i'_{q2} + pM \sin(\theta + 120^\circ) i'_{d2} \\
& + pM \cos(\theta + 120^\circ) i'_{q3} + pM \sin(\theta + 120^\circ) i'_{d3}
\end{aligned} \tag{2.156}$$

The voltage equations for rotor starting-cage windings in expanded form are

$$\begin{aligned}
v'_{q2} = & (\omega - \omega_r)(L_m \sin \theta i_{a1} + L_m \sin(\theta - 120^\circ) i_{b1} + L_m \sin(\theta + 120^\circ) i_{c1}) \\
& + r'_2 i'_{q2} + (L'_{22} + L'_{23}) p i'_{q2} + (\omega - \omega_r)(L'_{22} + L'_{23}) i'_{d2} \\
& + (L'_{23} + M) p i'_{q3} + (\omega - \omega_r)(L'_{23} + M) i'_{d3}
\end{aligned} \tag{2.157}$$

$$\begin{aligned}
v'_{d2} = & -(\omega - \omega_r)(L_m \cos \theta i_{a1} + L_m \cos(\theta - 120^\circ) i_{b1} + L_m \cos(\theta + 120^\circ) i_{c1}) \\
& - (\omega - \omega_r)(L'_{22} + L'_{23}) i'_{q2} + r'_2 i'_{d2} + (L'_{22} + L'_{23}) p i'_{d2} \\
& - (\omega - \omega_r)(L'_{23} + M) i'_{q3} + (L'_{23} + M) p i'_{d3}
\end{aligned} \tag{2.158}$$

$$v'_{02} = r'_2 i'_{02} + (L'_{l2} + L'_{23}) p i'_{02} + L'_{23} p i'_{03} \tag{2.159}$$

The voltage equations for rotor running-cage windings in expanded form are

$$\begin{aligned}
v'_{q3} = & (\omega - \omega_r)(L_m \sin \theta i_{a1} + L_m \sin(\theta - 120^\circ) i_{b1} + L_m \sin(\theta + 120^\circ) i_{c1}) \\
& + (L'_{23} + M) p i'_{q2} + (\omega - \omega_r)(L'_{23} + M) i'_{d2} \\
& + r'_3 i'_{q3} + (L'_{33} + L'_{23}) p i'_{q3} + (\omega - \omega_r)(L'_{33} + L'_{23}) i'_{d3}
\end{aligned} \tag{2.160}$$

$$\begin{aligned}
v'_{d3} = & -(\omega - \omega_r)(L_m \cos \theta i_{a1} + L_m \cos(\theta - 120^\circ) i_{b1} + L_m \cos(\theta + 120^\circ) i_{c1}) \\
& - (\omega - \omega_r)(L'_{23} + M) i'_{q2} + (L'_{23} + M) p i'_{d2} \\
& - (\omega - \omega_r)(L'_{33} + L'_{23}) i'_{q3} + r'_3 i'_{d3} + (L'_{33} + L'_{23}) p i'_{d3}
\end{aligned} \tag{2.161}$$

$$v'_{03} = r'_3 i'_{03} + (L'_{l3} + L'_{23}) p i'_{03} + L'_{23} p i'_{02} \tag{2.162}$$

In order to eliminate time varying inductances, the equations (2.154)-(2.162) are expressed in the stationary reference frame by letting $\omega = 0$. Assuming there is no

neutral line connected to the stator windings (i.e, the sum of line currents and their derivatives are equal to zero) the equation given in (2.163) is obtained for a double-cage induction motor at stationary reference frame with zero sequence equations omitted.

$$\begin{bmatrix} v_{a1} \\ v_{b1} \\ v_{c1} \\ v'_{q2} \\ v'_{d2} \\ v'_{q3} \\ v'_{d3} \end{bmatrix} = \begin{bmatrix} r_1 + L_{11}p & 0 & 0 & Mp & 0 & Mp & 0 \\ 0 & r_1 + L_{11}p & 0 & -\frac{1}{2}Mp & -\frac{\sqrt{3}}{2}Mp & -\frac{1}{2}Mp & -\frac{\sqrt{3}}{2}Mp \\ 0 & 0 & r_1 + L_{11}p & -\frac{1}{2}Mp & \frac{\sqrt{3}}{2}Mp & -\frac{1}{2}Mp & \frac{\sqrt{3}}{2}Mp \\ Mp & \omega_r \frac{\sqrt{3}}{2}L_m & -\omega_r \frac{\sqrt{3}}{2}L_m & r'_2 + (L'_{22} + L'_{23})p & -\omega_r(L'_{22} + L'_{23}) & (L'_{23} + M)p & -\omega_r(M + L'_{23}) \\ \omega_r M & -\frac{\sqrt{3}}{2}L_m p & \frac{\sqrt{3}}{2}L_m p & \omega_r(L'_{22} + L'_{23}) & r'_2 + (L'_{22} + L'_{23})p & \omega_r(M + L'_{23}) & (L'_{23} + M)p \\ Mp & \omega_r \frac{\sqrt{3}}{2}L_m & -\omega_r \frac{\sqrt{3}}{2}L_m & (L'_{23} + M)p & -\omega_r(M + L'_{23}) & r'_3 + (L'_{33} + L'_{23})p & -\omega_r(L'_{33} + L'_{23}) \\ \omega_r M & -\frac{\sqrt{3}}{2}L_m p & \frac{\sqrt{3}}{2}L_m p & \omega_r(M + L'_{23}) & (L'_{23} + M)p & \omega_r(L'_{33} + L'_{23}) & r'_3 + (L'_{33} + L'_{23})p \end{bmatrix} \begin{bmatrix} i_{a1} \\ i_{b1} \\ i_{c1} \\ i'_{q2} \\ i'_{d2} \\ i'_{q3} \\ i'_{d3} \end{bmatrix} \quad (2.163)$$

2.4 Voltage Equations in qd/abc Reference Frame

In order to express the double-cage induction machine in dq/abc reference frame, which retains the actual rotor phase variables but transforms the stator only to examine the transients of the machine, the K_s transformation in equation (2.82) is applied to stator variables. In this model, it is assumed that the q axis coincides with phase a of the rotor. Substituting the equation (2.81) into (2.75), the flux linkage matrix can be written as follows

$$\begin{bmatrix} K_s^{-1} \lambda_{qd01} \\ \lambda'_{abc2} \\ \lambda'_{abc3} \end{bmatrix} = \begin{bmatrix} L_{11} & L'_{12} & L'_{13} \\ (L'_{12})^T & L'_{22} & L'_{23} \\ (L'_{13})^T & (L'_{23})^T & L'_{33} \end{bmatrix} \begin{bmatrix} K_s^{-1} i_{qd01} \\ i'_{abc2} \\ i'_{abc3} \end{bmatrix} \quad (2.164)$$

Rearranging the above equation yields to

$$\begin{bmatrix} \lambda_{qd01} \\ \lambda'_{abc2} \\ \lambda'_{abc3} \end{bmatrix} = \begin{bmatrix} \mathbf{K}_s \mathbf{L}_{11} \mathbf{K}_s^{-1} & \mathbf{K}_s \mathbf{L}'_{12} & \mathbf{K}_s \mathbf{L}'_{13} \\ (\mathbf{L}'_{12})^T \mathbf{K}_s^{-1} & \mathbf{L}'_{22} & \mathbf{L}'_{23} \\ (\mathbf{L}'_{13})^T \mathbf{K}_s^{-1} & (\mathbf{L}'_{23})^T & \mathbf{L}'_{33} \end{bmatrix} \begin{bmatrix} \mathbf{i}_{qd01} \\ \mathbf{i}'_{abc2} \\ \mathbf{i}'_{abc3} \end{bmatrix} \quad (2.165)$$

The elements of the transformed impedance matrix given in the above equation are obtained using the trigonometric relations given in Appendix A similarly and expressed as follows

$$\begin{bmatrix} \lambda_{qd01} \\ \lambda'_{abc2} \\ \lambda'_{abc3} \end{bmatrix} = \begin{bmatrix} \mathbf{c}_{11} & \mathbf{c}_{12} & \mathbf{c}_{13} \\ \mathbf{c}_{21} & \mathbf{c}_{22} & \mathbf{c}_{23} \\ \mathbf{c}_{31} & \mathbf{c}_{32} & \mathbf{c}_{33} \end{bmatrix} \begin{bmatrix} \mathbf{i}_{qd01} \\ \mathbf{i}'_{abc2} \\ \mathbf{i}'_{abc3} \end{bmatrix} \quad (2.166)$$

$$\mathbf{c}_{11} = \mathbf{K}_s \mathbf{L}_{11} \mathbf{K}_s^{-1} = \begin{bmatrix} L_{l1} + M & 0 & 0 \\ 0 & L_{l1} + M & 0 \\ 0 & 0 & L_{l1} \end{bmatrix} \quad (2.167)$$

$$\mathbf{c}_{22} = \mathbf{L}'_{22} = \begin{bmatrix} L'_{l2} + L_{m1} + L'_{23} & -\frac{1}{2}L_{m1} & -\frac{1}{2}L_{m1} \\ -\frac{1}{2}L_{m1} & L'_{l2} + L_{m1} + L'_{23} & -\frac{1}{2}L_{m1} \\ -\frac{1}{2}L_{m1} & -\frac{1}{2}L_{m1} & L'_{l2} + L_{m1} + L'_{23} \end{bmatrix} \quad (2.168)$$

$$\mathbf{c}_{33} = \mathbf{L}'_{33} = \begin{bmatrix} L'_{l3} + L_{m1} + L'_{23} & -\frac{1}{2}L_{m1} & -\frac{1}{2}L_{m1} \\ -\frac{1}{2}L_{m1} & L'_{l3} + L_{m1} + L'_{23} & -\frac{1}{2}L_{m1} \\ -\frac{1}{2}L_{m1} & -\frac{1}{2}L_{m1} & L'_{l3} + L_{m1} + L'_{23} \end{bmatrix} \quad (2.169)$$

$$\mathbf{c}_{23} = \mathbf{L}'_{23} = \begin{bmatrix} L'_{23} + L_{m1} & -\frac{1}{2}L_{m1} & -\frac{1}{2}L_{m1} \\ -\frac{1}{2}L_{m1} & L'_{23} + L_{m1} & -\frac{1}{2}L_{m1} \\ -\frac{1}{2}L_{m1} & -\frac{1}{2}L_{m1} & L'_{23} + L_{m1} \end{bmatrix} \quad (2.170)$$

$$\mathbf{c}_{32} = (\mathbf{L}'_{23})^T = \begin{bmatrix} L'_{23} + L_{m1} & -\frac{1}{2}L_{m1} & -\frac{1}{2}L_{m1} \\ -\frac{1}{2}L_{m1} & L'_{23} + L_{m1} & -\frac{1}{2}L_{m1} \\ -\frac{1}{2}L_{m1} & -\frac{1}{2}L_{m1} & L'_{23} + L_{m1} \end{bmatrix} \quad (2.171)$$

which are previously derived in Section 2.1 and Section 2.2. The rest of the elements of the flux linkage matrix can be obtained as

$$\mathbf{c}_{12} = \mathbf{c}_{13} = \mathbf{K}_s \mathbf{L}'_{12} = \mathbf{K}_s \mathbf{L}'_{13} = \begin{bmatrix} L_m \cos \beta & L_m \cos(\beta - 120^\circ) & L_m \cos(\beta + 120^\circ) \\ L_m \sin \beta & L_m \sin(\beta - 120^\circ) & L_m \sin(\beta + 120^\circ) \\ 0 & 0 & 0 \end{bmatrix} \quad (2.172)$$

$$\mathbf{a}_{21} = \mathbf{a}_{31} = (\mathbf{L}'_{12})^T \mathbf{K}_s^{-1} = (\mathbf{L}'_{13})^T \mathbf{K}_s^{-1} = \begin{bmatrix} M \cos \beta & M \sin \beta & 0 \\ M \cos(\beta - 120^\circ) & M \sin(\beta - 120^\circ) & 0 \\ M \cos(\beta + 120^\circ) & M \sin(\beta + 120^\circ) & 0 \end{bmatrix} \quad (2.173)$$

The voltage equations of the stator windings in terms of $qd0$ variables are written as

$$\mathbf{v}_{qd01} = \mathbf{r}_1 \mathbf{i}_{qd01} + \omega \lambda_{dq1} + p \lambda_{qd01} \quad (2.174)$$

and the voltage equations of the rotor windings referred to the stator side in terms of abc variables

$$\mathbf{v}'_{abc2} = \mathbf{r}'_2 \mathbf{i}'_{abc2} + p \lambda'_{abc2} \quad (2.175)$$

$$\mathbf{v}'_{abc3} = \mathbf{r}'_3 \mathbf{i}'_{abc3} + p \lambda'_{abc3} \quad (2.176)$$

Substituting flux linkage matrix in equation (2.166) into equations (2.174)-(2.176), the voltage equations for stator windings can be written in expanded form as follows

$$\begin{aligned}
v_{q1} = & r_1 i_{q1} + (L_{l1} + M) p i_{q1} + \omega(L_{l1} + M) i_{d1} \\
& + \omega[L_m \sin \beta i_{a2}' + L_m \sin(\beta - 120^\circ) i_{b2}' + L_m \sin(\beta + 120^\circ) i_{c2}'] \\
& + \omega[L_m \sin \beta i_{a3}' + L_m \sin(\beta - 120^\circ) i_{b3}' + L_m \sin(\beta + 120^\circ) i_{c3}'] \\
& + p L_m \cos \beta i_{a2}' + p L_m \cos(\beta - 120^\circ) i_{b2}' + p L_m \cos(\beta + 120^\circ) i_{c2}' \\
& + p L_m \cos \beta i_{a3}' + p L_m \cos(\beta - 120^\circ) i_{b3}' + p L_m \cos(\beta + 120^\circ) i_{c3}'
\end{aligned} \tag{2.177}$$

$$\begin{aligned}
v_{d1} = & r_1 i_{d1} + (L_{l1} + M) p i_{d1} + \omega(L_{l1} + M) i_{q1} \\
& + \omega[L_m \cos \beta i_{a2}' + L_m \cos(\beta - 120^\circ) i_{b2}' + L_m \cos(\beta + 120^\circ) i_{c2}'] \\
& + \omega[L_m \cos \beta i_{a3}' + L_m \cos(\beta - 120^\circ) i_{b3}' + L_m \cos(\beta + 120^\circ) i_{c3}'] \\
& + p L_m \sin \beta i_{a2}' + p L_m \sin(\beta - 120^\circ) i_{b2}' + p L_m \sin(\beta + 120^\circ) i_{c2}' \\
& + p L_m \sin \beta i_{a3}' + p L_m \sin(\beta - 120^\circ) i_{b3}' + p L_m \sin(\beta + 120^\circ) i_{c3}'
\end{aligned} \tag{2.178}$$

$$v_{01} = r_1 i_{01} + L_{l1} p i_{01} \tag{2.179}$$

The voltage equations for rotor starting-cage windings in expanded form are

$$\begin{aligned}
v_{a2}' = & r_2' i_{a2}' + p M \cos \beta i_{q1}' + p M \sin \beta i_{d1}' \\
& + (L_{l2}' + L_m + L_{23}') p i_{a2}' - \frac{1}{2} L_m p i_{b2}' - \frac{1}{2} L_m p i_{c2}' \\
& + (L_{23}' + M) p i_{a3}' - \frac{1}{2} L_m p i_{b3}' - \frac{1}{2} L_m p i_{c3}'
\end{aligned} \tag{2.180}$$

$$\begin{aligned}
v_{b2}' = & r_2' i_{b2}' + p M \cos(\beta - 120^\circ) i_{q1}' + p M \sin(\beta - 120^\circ) i_{d1}' \\
& - \frac{1}{2} L_m p i_{a2}' + (L_{l2}' + L_m + L_{23}') p i_{b2}' - \frac{1}{2} L_m p i_{c2}' \\
& - \frac{1}{2} L_m p i_{a3}' + (L_{23}' + M) p i_{b3}' - \frac{1}{2} L_m p i_{c3}'
\end{aligned} \tag{2.181}$$

$$\begin{aligned}
v_{c2}' = & r_2' i_{c2}' + p M \cos(\beta + 120^\circ) i_{q1}' + p M \sin(\beta + 120^\circ) i_{d1}' \\
& - \frac{1}{2} L_m p i_{a2}' - \frac{1}{2} L_m p i_{b2}' + (L_{l2}' + L_m + L_{23}') p i_{c2}' \\
& - \frac{1}{2} L_m p i_{a3}' - \frac{1}{2} L_m p i_{b3}' + (L_{23}' + M) p i_{c3}'
\end{aligned} \tag{2.182}$$

Finally, the voltage equations for rotor running-cage windings in expanded form

$$\begin{aligned}
v_{a3}' &= r_3' i_{a3}' + pM \cos \beta i_{q1} + pM \sin \beta i_{d1} \\
&+ (L_{23}' + M) p i_{a2}' - \frac{1}{2} L_m p i_{b2}' - \frac{1}{2} L_m p i_{c2}' \\
&+ (L_{l3}' + L_m + L_{23}') p i_{a3}' - \frac{1}{2} L_m p i_{b3}' - \frac{1}{2} L_m p i_{c3}'
\end{aligned} \tag{2.183}$$

$$\begin{aligned}
v_{b3}' &= r_3' i_{b3}' + pM \cos(\beta - 120^\circ) i_{q1} + pM \sin(\beta - 120^\circ) i_{d1} \\
&- \frac{1}{2} L_m p i_{a2}' + (L_{23}' + M) p i_{b2}' - \frac{1}{2} L_m p i_{c2}' \\
&- \frac{1}{2} L_m p i_{a3}' + (L_{l3}' + L_m + L_{23}') p i_{b3}' - \frac{1}{2} L_m p i_{c3}'
\end{aligned} \tag{2.184}$$

$$\begin{aligned}
v_{c3}' &= r_3' i_{c3}' + pM \cos(\beta + 120^\circ) i_{q1} + pM \sin(\beta + 120^\circ) i_{d1} \\
&- \frac{1}{2} L_m p i_{a2}' - \frac{1}{2} L_m p i_{b2}' + (L_{23}' + M) p i_{c2}' \\
&- \frac{1}{2} L_m p i_{a3}' - \frac{1}{2} L_m p i_{b3}' + (L_{l3}' + L_m + L_{23}') p i_{c3}'
\end{aligned} \tag{2.185}$$

In order to eliminate time varying inductances, the equations (2.177)-(2.185) are expressed in the rotor reference frame by letting $\omega = \omega_r$. Assuming there is no neutral line connected to the rotor windings (i.e., the sum of line currents and their derivatives are equal to zero) the equation (2.186) is obtained for a double-cage induction motor at rotor reference frame with zero sequence equations omitted.

$$\begin{bmatrix} v_{q1} \\ v_{a1} \\ v_{a2} \\ v_{b2} \\ v_{c2} \\ v_{a3} \\ v_{b3} \\ v_{c3} \end{bmatrix} = \begin{bmatrix} r_1 + L_{11}p & \omega_r L_{11} & Mp & -\omega_r \frac{\sqrt{3}}{2} L_m & \omega_r \frac{\sqrt{3}}{2} L_m & Mp & -\omega_r \frac{\sqrt{3}}{2} L_m & \omega_r \frac{\sqrt{3}}{2} L_m \\ -\omega_r L_{11} & r_1 + L_{11}p & -\omega_r M & -\frac{\sqrt{3}}{2} L_m p & \frac{\sqrt{3}}{2} L_m p & -\omega_r M & -\frac{\sqrt{3}}{2} L_m p & \frac{\sqrt{3}}{2} L_m p \\ Mp & 0 & r_2' + (L_{22} + L_{23})p & 0 & 0 & (L_{23} + M)p & 0 & 0 \\ -\frac{1}{2}Mp & -\frac{\sqrt{3}}{2}Mp & 0 & r_2' + (L_{22} + L_{23})p & 0 & 0 & (L_{23} + M)p & 0 \\ -\frac{1}{2}Mp & \frac{\sqrt{3}}{2}Mp & 0 & 0 & r_2' + (L_{22} + L_{23})p & 0 & 0 & (L_{23} + M)p \\ Mp & 0 & (L_{23} + M)p & 0 & 0 & r_3' + (L_{33} + L_{23})p & 0 & 0 \\ -\frac{1}{2}Mp & -\frac{\sqrt{3}}{2}Mp & 0 & (L_{23} + M)p & 0 & 0 & r_3' + (L_{33} + L_{23})p & 0 \\ -\frac{1}{2}Mp & \frac{\sqrt{3}}{2}Mp & 0 & 0 & (L_{23} + M)p & 0 & 0 & r_3' + (L_{33} + L_{23})p \end{bmatrix} \begin{bmatrix} i_{q1} \\ i_{a1} \\ i_{a2} \\ i_{b2} \\ i_{c2} \\ i_{a3} \\ i_{b3} \\ i_{c3} \end{bmatrix}$$

(2.186)

2.5 Torque Expressions

The relation between the torque and rotor speed for the induction machine is given by the equation as follows

$$T_e = J \left(\frac{2}{P} \right) p \omega_r + T_L \quad (2.187)$$

Here, J is the inertia of the rotor, ω_r is the electrical rotor speed, P is the number of poles, T_L is the load torque on the shaft of the machine, and T_e is electromagnetic torque developed by the double-cage induction machine. The electromagnetic torque can be expressed in terms of machine variables as follows

$$T_e = \left(\frac{P}{2} \right) (\mathbf{i}_{abc1})^T \frac{\partial}{\partial \theta_r} [\mathbf{L}'_{12}] \mathbf{i}'_{abc2} + \left(\frac{P}{2} \right) (\mathbf{i}_{abc1})^T \frac{\partial}{\partial \theta_r} [\mathbf{L}'_{13}] \mathbf{i}'_{abc3} \quad (2.188)$$

Arranging the above equation using trigonometric relationships given in Appendix A, the expression of electromagnetic torque developed by the machine in terms of machine variables becomes

$$T_e = - \left(\frac{P}{2} \right) L_m \left\{ \begin{aligned} & [i_{a1}(\dot{i}'_{a2} - \frac{1}{2}\dot{i}'_{b2} - \frac{1}{2}\dot{i}'_{c2}) + i_{b1}(\dot{i}'_{b2} - \frac{1}{2}\dot{i}'_{a2} - \frac{1}{2}\dot{i}'_{c2}) + i_{c1}(\dot{i}'_{c2} - \frac{1}{2}\dot{i}'_{a2} - \frac{1}{2}\dot{i}'_{b2})] \sin \theta_r \\ & + \frac{\sqrt{3}}{2} [i_{a1}(\dot{i}'_{b2} - \dot{i}'_{c2}) + i_{b1}(\dot{i}'_{c2} - \dot{i}'_{a2}) + i_{c1}(\dot{i}'_{a2} - \dot{i}'_{b2})] \cos \theta_r \end{aligned} \right\} \\ - \left(\frac{P}{2} \right) L_m \left\{ \begin{aligned} & [i_{a1}(\dot{i}'_{a3} - \frac{1}{2}\dot{i}'_{b3} - \frac{1}{2}\dot{i}'_{c3}) + i_{b1}(\dot{i}'_{b3} - \frac{1}{2}\dot{i}'_{a3} - \frac{1}{2}\dot{i}'_{c3}) + i_{c1}(\dot{i}'_{c3} - \frac{1}{2}\dot{i}'_{a3} - \frac{1}{2}\dot{i}'_{b3})] \sin \theta_r \\ & + \frac{\sqrt{3}}{2} [i_{a1}(\dot{i}'_{b3} - \dot{i}'_{c3}) + i_{b1}(\dot{i}'_{c3} - \dot{i}'_{a3}) + i_{c1}(\dot{i}'_{a3} - \dot{i}'_{b3})] \cos \theta_r \end{aligned} \right\} \quad (2.189)$$

In order to express the electromagnetic torque in terms of qd/qd, abc/qd, and qd/abc variables, transformations given in equation (2.82) and (2.87) are applied to

the stator and rotor variables. The electromagnetic torque is expressed in terms of qd/qd variables as

$$T_e = \left(\frac{P}{2}\right) (\mathbf{K}_s^{-1} \mathbf{i}_{qd01})^T \frac{\partial}{\partial \theta_r} [\mathbf{L}'_{12}] \mathbf{K}_r^{-1} \mathbf{i}'_{qd02} + \left(\frac{P}{2}\right) (\mathbf{K}_s^{-1} \mathbf{i}_{qd01})^T \frac{\partial}{\partial \theta_r} [\mathbf{L}'_{13}] \mathbf{K}_r^{-1} \mathbf{i}'_{qd03} \quad (2.190)$$

Arranging the above equation using trigonometric relationships given in Appendix A, the expression of electromagnetic torque developed by the machine in terms of qd/qd variables becomes

$$T_e = \frac{3}{2} \left(\frac{P}{2}\right) M \{ (i_{q1} i'_{d2} - i_{d1} i'_{q2}) + (i_{q1} i'_{d3} - i_{d1} i'_{q3}) \} \quad (2.191)$$

The electromagnetic torque can be expressed in terms of abc/qd variables in a similar way as follows

$$T_e = \left(\frac{P}{2}\right) (\mathbf{i}_{abc1})^T \frac{\partial}{\partial \theta_r} [\mathbf{L}'_{12}] \mathbf{K}_r^{-1} \mathbf{i}'_{qd02} + \left(\frac{P}{2}\right) (\mathbf{i}_{abc1})^T \frac{\partial}{\partial \theta_r} [\mathbf{L}'_{13}] \mathbf{K}_r^{-1} \mathbf{i}'_{qd03} \quad (2.192)$$

which becomes

$$T_e = \left(\frac{P}{2}\right) M \left\{ \begin{aligned} & i'_{d2} (i_{a1} - \frac{1}{2} i_{b1} - \frac{1}{2} i_{c1}) + \frac{\sqrt{3}}{2} i'_{q2} (i_{b2} - i_{c2}) \\ & + i'_{d3} (i_{a1} - \frac{1}{2} i_{b1} - \frac{1}{2} i_{c1}) + \frac{\sqrt{3}}{2} i'_{q3} (i_{b2} - i_{c2}) \end{aligned} \right\} \quad (2.193)$$

Finally, the electromagnetic torque in terms of qd/abc variables is

$$T_e = \left(\frac{P}{2}\right) (\mathbf{K}_s^{-1} \mathbf{i}_{qd01})^T \frac{\partial}{\partial \theta_r} [\mathbf{L}'_{12}] \mathbf{i}'_{abc2} + \left(\frac{P}{2}\right) (\mathbf{K}_s^{-1} \mathbf{i}_{qd01})^T \frac{\partial}{\partial \theta_r} [\mathbf{L}'_{13}] \mathbf{i}'_{abc3} \quad (2.194)$$

which becomes

$$T_e = -\left(\frac{P}{2}\right)M \left\{ \begin{aligned} & i_{d1}(i'_{a2} - \frac{1}{2}i'_{b2} - \frac{1}{2}i'_{c2}) + \frac{\sqrt{3}}{2}i_{q1}(i'_{b2} - i'_{c2}) \\ & + i_{d1}(i'_{a3} - \frac{1}{2}i'_{b3} - \frac{1}{2}i'_{c3}) + \frac{\sqrt{3}}{2}i_{q1}(i'_{b3} - i'_{c3}) \end{aligned} \right\} \quad (2.195)$$

2.6 Steady-state Equivalent Circuit

The steady-state per phase equivalent circuit of a double-cage induction machine can be obtained from the voltage equations in arbitrary reference frame by letting

$$p = j(\omega_e - \omega) \quad (2.196)$$

where ω_e is the electrical supply frequency in radians per second. Substituting the above equation into stator and rotor q-axis voltages given in equations (2.111), (2.114), and (2.117) yields to

$$v_{q1} = r_1 i_{q1} + \omega \lambda_{d1} + j(\omega_e - \omega) \lambda_{q1} \quad (2.197)$$

$$v'_{q2} = r_2 i'_{q2} + (\omega - \omega_r) \lambda'_{d2} + j(\omega_e - \omega) \lambda'_{q2} \quad (2.198)$$

$$v'_{q3} = r_3 i'_{q3} + (\omega - \omega_r) \lambda'_{d3} + j(\omega_e - \omega) \lambda'_{q3} \quad (2.199)$$

It must be noted that the q-axis of stator coincides with phase a of the stator, so it can be written that

$$\tilde{F}_{q1} = \tilde{F}_{a1} \quad (2.200)$$

For steady-state conditions, the following expressions can be written

$$\tilde{F}_{d1} = j \tilde{F}_{q1} \quad (2.201)$$

$$\tilde{F}_{d2} = j \tilde{F}_{q2} \quad (2.202)$$

$$\tilde{F}_{d3} = j \tilde{F}_{q3} \quad (2.203)$$

Substituting equations (2.201)-(2.203) into (2.197)-(2.199) yields to

$$v_{q1} = r_1 i_{q1} + j \omega_e \lambda_{q1} \quad (2.204)$$

$$v_{q2} = r_2 i_{q2} + j(\omega_e - \omega_r) \lambda_{q2} \quad (2.205)$$

$$v_{q3} = r_3 i_{q3} + j(\omega_e - \omega_r) \lambda_{q3} \quad (2.206)$$

Rearranging the equations (2.204)-(2.206), the steady-state q-axis voltages can be obtained as follows

$$v_{q1} = r_1 i_{q1} + j \frac{\omega_e}{\omega_b} [(X_{l1} + X_M) i_{q1} + X_M i_{q2} + X_M i_{q3}] \quad (2.207)$$

$$v_{q2} = r_2 i_{q2} + j \left(\frac{\omega_e - \omega_r}{\omega_b} \right) [(X'_{l2} + X_M + X'_{23}) i_{q2} + (X_M + X'_{23}) i_{q3} + X_M i_{q1}] \quad (2.208)$$

$$v_{q3} = r_3 i_{q3} + j \left(\frac{\omega_e - \omega_r}{\omega_b} \right) [(X'_{l3} + X_M + X'_{23}) i_{q3} + (X_M + X'_{23}) i_{q2} + X_M i_{q1}] \quad (2.209)$$

where ω_b is the base frequency. Hence, the inductive reactances are calculated as

$$X_{l1} = \omega_b L_{l1} \quad (2.210)$$

$$X'_{l2} = \omega_b L'_{l2} \quad (2.211)$$

$$X'_{l3} = \omega_b L'_{l3} \quad (2.212)$$

$$X'_{23} = \omega_b L'_{23} \quad (2.213)$$

$$X_M = \omega_b M \quad (2.214)$$

Since the rotor terminals are short circuited, the rotor voltages are equal to zero. The q-axis voltage of stator is equal to the stator phase a voltage. So, the equivalent circuit satisfying the equations (2.207)-(2.209) is obtained and given in Figure 2.3

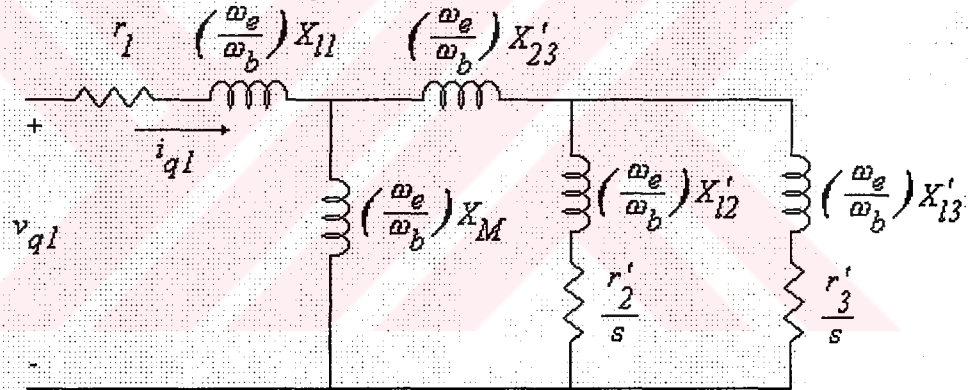


Figure 2.3 Equivalent circuit of double-cage induction machine

2.6.1 Analysis of the Equivalent Circuit

For the analysis of the steady-state per phase equivalent circuit of the DCIM given in Figure 2.3, the rotor circuit is considered to be consisting of one equivalent resistance and reactance such as in single-cage machine. The rotor equivalent resistance and reactance at any slip are obtained from the equivalent circuit and defined by the following equations (Waters & Willoughby, 1983)

$$r_e = \frac{r_2' r_3' (r_2' + r_3') + s^2 (r_2' x_3'^2 + r_3' x_2'^2)}{(r_2' + r_3')^2 + s^2 (x_2' + x_3')^2} \quad (2.215)$$

$$x_{run} = \frac{r_2'^2 x_3' + r_3'^2 x_2' + s^2 x_2' x_3' (x_2' + x_3')}{(r_2' + r_3')^2 + s^2 (x_2' + x_3')^2} + x_{23}' \quad (2.216)$$

Thevenin voltage, resistance and reactance of the stator side are obtained from the exact equivalent circuit and given below;

$$V_{th} = \frac{V_{q1} x_m}{\sqrt{r_1^2 + (x_1 + x_m)^2}} \quad (2.217)$$

$$r_{th} = \frac{x_m^2 r_1}{r_1^2 + (x_1 + x_m)^2} \quad (2.218)$$

$$x_{th} = \frac{x_m (r_1^2 + x_1^2) + x_1 x_m^2}{r_1^2 + (x_1 + x_m)^2} \quad (2.219)$$

where the reactances related to the inductances in the equivalent circuit are as follows

$$x_1 = \omega_e L_{l1} \quad (2.220)$$

$$x_2' = \omega_e L_{l2}' \quad (2.221)$$

$$x_3' = \omega_e L_{l3}' \quad (2.222)$$

$$x_{23}' = \omega_e L_{23}' \quad (2.223)$$

$$x_m = \omega_e M \quad (2.224)$$

The electromagnetic torque developed by the machine is calculated as

$$T = \frac{3}{\omega_s} \left(\frac{V_{th}^2}{(r_{th} + \frac{r_e}{s})^2 + (x_{th} + x_{run})^2} \frac{r_e}{s} \right) \quad (2.225)$$

where ω_s is the synchronous speed of the machine and expressed as

$$\omega_s = \frac{4\pi f}{P} \quad (2.226)$$

2.7 Determination of Machine Parameters

The parameter determination of a double-cage induction machine is quite a difficult task with respect to a single-cage machine. Because the additional rotor windings make the analysis of the equivalent circuit more complicated. Hence, optimization techniques are applied in the determination of the machine parameters. In the following, the genetic algorithm approach, which is an optimization technique, will be introduced.

2.7.1 Genetic Algorithm Approach

The Genetic Algorithm (GA) is an evolution program, which uses an iterative procedure to measure of its fitness function from the generated population of potential solutions. The members of the generated population are expressed in binary digits (or chromosomes) and the strength of each member is measured using the fitness function. At each iterative step, a new population is generated, by altering some members of the population using genetic operators, crossover and mutation, to fit more individuals to the solution. The generation of new populations continues until the best population is obtained to fit an optimum solution. The GA is applied to problems to find a global maximum/minimum of multivariable equations. The main advantage of GA is that it provides global optimum of the cost (fitness) function

without good estimation of initial values of the variables and the derivatives of the cost and constraints. During the application of the GA to an optimization problem, 6 stages given below should be completed.

- a) determination of the problem
- b) genetic representation
- c) creation of initial population
- d) An evaluation function
- e) genetic operators
- f) determination of parameters that GA uses

At the first step, the fitness function of a specific problem should be determined. Assume that the problem is to find a value of x which maximizes the value of a single variable function $F = f(x)$ within a given range, i.e., $f(x_0) \geq f(x)$ for all $x \in [x_{\min} \ x_{\max}]$.

At the second stage, the members of population (or variables) are expressed as binary vectors for their given ranges. For the problem given above, the range is $x_{\max} - x_{\min}$ and it should be divided into N equal size in order to meet the required precision. The number of bits (n) required to represent a binary vector (chromosome) is chosen considering the following criterion

$$2^n \geq N \quad (2.227)$$

Hence, a binary string $\{b_n b_{n-1} \dots b_0\}$ represents a real number x and can be converted from base 2 to base 10 as follows:

$$(\{b_n b_{n-1} \dots b_0\})_2 = \left(\sum_{i=0}^n b_i 2^i \right)_{10} = x \quad (2.228)$$

and the corresponding value of x is

$$x = x_{\min} + x \cdot \frac{x_{\max} - x_{\min}}{2^n - 1} \quad (2.229)$$

The chromosomes $\{00...0\}$ and $\{11...1\}$ represent the boundaries x_{\min} and x_{\max} , respectively.

At the third stage, an initial population of chromosomes is created. The size of population (P) is determined and the bits of the binary vectors are initialized randomly. Each individual member of population that is represented by a binary vector is considered to be a potential solution to the described problem.

At the fourth stage, the fitness of the each individual is evaluated using the evaluation function for binary vectors (v). This evaluation function is equivalent to fitness function such as $eval(v) = f(x)$.

The members of potential solutions are v_1, v_2, \dots, v_p and each correspond to the real values x_1, x_2, \dots, x_p . For a maximization problem, the member of the population that gives the highest value is chosen to be the best member.

At the fifth stage, the genetic operators, crossover and mutation, are used to alter the bits of each vector, thus creating the offspring of the generation. Mutation alters the bits of a binary vector and the probability of mutation (p_m) is determined by mutation rate. The selected bit of the binary vector for mutation is simply flipped. Crossover swaps the bits of two binary vectors and its probability (p_c) is determined by crossover rate. Hence, a new population is generated through the genetic operators that are supposed to give better potential solutions to the problem.

As a final stage, the size of population (P), the rate of mutation and crossover (p_m, p_c), and the number of generations should be determined before starting the procedure. After the each iteration, the GA creates a new population and the fitness

of the members in the generated population is evaluated until an optimum solution is obtained to the specified function (Michalewicz, 1992).

2.7.2. Motor Equations for Genetic Algorithm

The GA approach relies on the solution of the equations from the equivalent circuit of the DCIM. The nonlinear equations from the equivalent circuit of the machine are constructed such that they form a fitness function that the GA evaluates. A similar approach was proposed by (Nangsue et al, 1999) for a deep bar induction machine.

The steady-state per phase equivalent circuit of the DCIM was given in Figure 2.3. Two parallel rotor branches can be represented by an equivalent resistance and a series reactance as shown in Figure 2.4. The rotor equivalent resistance (r'_e) and reactance (x'_e) at any slip were given in section 2.6.1.

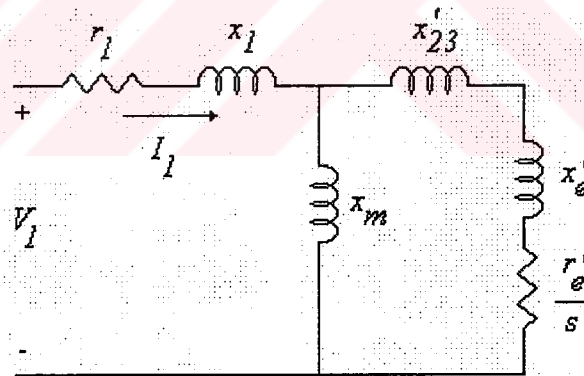


Figure 2.4 Equivalent single rotor circuit

The input power factor at full-load, electromagnetic torque developed by the machine at the full-load, break-down torque, starting torque and no-load impedance are used in fitness function of genetic algorithm. Hence, the following equations can be written as follows

$$F_1 = 100 \left(\frac{3V_{th}^2 r_{e0}}{T_{fl} w_s s_{fl} \left[\left(r_{th} + \frac{r_{e0}}{s} \right)^2 + (x_{th} + x_{run0})^2 \right]} - 1 \right) \quad (2.230)$$

$$F_2 = 100 \left(\frac{3V_{th}^2 r_{e2}}{T_{bd} w_s s_{bd} \left[\left(r_{th} + \frac{r_{e2}}{s} \right)^2 + (x_{th} + x_{run2})^2 \right]} - 1 \right) \quad (2.231)$$

$$F_3 = 100 \left(\frac{3V_{th}^2 r_{e1}}{T_{lr} w_s \left[\left(r_{th} + \frac{r_{e1}}{s} \right)^2 + (x_{th} + x_{run1})^2 \right]} - 1 \right) \quad (2.232)$$

r_{e0}, r_{e1}, r_{e2} are the full-load, locked-rotor, and breakdown resistances respectively. Similarly, $x_{run0}, x_{run1}, x_{run2}$ are the rotor reactances at full-load, locked-rotor, and breakdown, respectively. These values are calculated from (2.215) and (2.216) at the corresponding rotor speeds. Another equation for the full-load power factor equation is written as

$$F_4 = 100 \left(\frac{\cos \left(\tan^{-1} \left[\frac{x_{fl}}{r_{fl}} \right] \right)}{pf} - 1 \right) \quad (2.233)$$

where pf is the full-load power factor and

$$r_{fl} = r_1 + \frac{x_m^2 \left(\frac{r_{e0}}{s_{fl}} \right)}{\left(\frac{r_{e0}}{s_{fl}} \right)^2 + (x_m + x_{run0})^2} \quad (2.234)$$

$$x_{fl} = x_1 + \frac{x_m \left(\frac{r_{e0}}{s_{fl}} \right)^2 + x_m x_{run0}}{\left(\frac{r_{e0}}{s_{fl}} \right)^2 + (x_m + x_{run0})^2} \quad (2.235)$$

Finally, the equation for no-load impedance of the machine is written as

$$F_5 = 100 \left(\frac{\sqrt{r_1^2 + (x_1 + x_m)^2}}{Z_{nl}} - 1 \right) \quad (2.236)$$

where Z_{nl} is the no-load impedance. Hence, the fitness function for the genetic algorithm is constructed by combining the equations (2.230), (2.231), (2.232), (2.233), and (2.236) and defined as below

$$F = \frac{100}{100 + |F_1| + |F_2| + |F_3| + |F_4| + |F_5|} \quad (2.237)$$

The fitness function given in equation (2.237) is evaluated by GA iteratively and the optimum values of the equivalent circuit parameters can be obtained.

2.7.3. Machine Parameters

The test machine is a 3-phase, Y-connected, squirrel cage, 50 Hz, 4-pole, 380 V, 2.5 kW DCIM. The no-load, locked- rotor, break-down and full-load tests have been performed on the machine while it is Y connected. These test results are given in Table 2.1. Friction and windage losses of the machine have been measured to be 40W during the no-load test by gradually decreasing the stator voltage level. The inertia of the induction motor is $J=0.02002 \text{ kg.m}^2$ received from the manufacturer. The stator resistance per phase is measured as 3 ohms. The ratio of the resistance of the starting and running cage is also obtained to be $r_3'/r_2' = 0.75$ from the cross sectional areas of bottom and top slots of the rotor structure provided by the

manufacturer. This ratio reduces the number of unknown variables estimated in the genetic algorithm. The fitness function given in equation (2.237) is evaluated by a GA program, which is given in Appendix A. The GA parameters in this program are determined as follows

Population size=100

Generation number=10000

Crossover rate=0.8

Mutation rate=0.2

Table 2.1: Test on star-connected motor

Test	V	I	pf	T	rpm
No-load;	230V	1.30A	0.13	0Nm	1500rpm
Full-load;	230V	4.48A	0.87	16.8Nm	1430rpm
Break-down;	163V	8.04A	0.78	15.8Nm	1200rpm
Locked-rotor;	230V	22.5A	0.63	23.2Nm	0rpm

For the given number of iterations, the predicted machine parameters as a result of the GA are obtained and results are given in Table 2.2

Table 2.2: The DCIM parameters obtained from GA

r_1	r_2'	r_3'	x_1	x_2'	x_3'	x_{23}'	x_m'
3.0Ω	5.05Ω	3.77Ω	7.51Ω	0.22Ω	9.38Ω	1.39Ω	169.4Ω

2.8 Simulation and Experimental Results

The equivalent circuit parameters of the DCIM, which are obtained by GA, have been verified by computer simulations and experimental tests. Also, the validity of the mathematical models has been verified with these equivalent circuit parameters. The simulation study of the machine is carried out by using the qd/qd, abc/qd, and qd/abc models derived in previous sections. Numerical solutions of the equations that represent the behavior of the machine are obtained using fourth order Runge Kutta

integration method. The simulation results from all models are expected to be identical. Simulations are carried out using FORTRAN programming language. In order to investigate the validity of estimated machine parameters from GA, the free acceleration and load tests are carried out on the machine fed by the supply of 230 volts (line to neutral). During the tests, as shown in Figure 2.5, a separately excited dc generator is used as a load having the torque-speed characteristics given below

$$T_L = K\omega_r + T_{fw(g)} + T_{fw(m)} \quad (2.238)$$

where $T_{fw(g)} = 0.62 \text{ Nm}$ and $T_{fw(m)} = 0.26 \text{ Nm}$ are the friction and windage torque values of the generator and motor respectively. K is equal to 0.025 at light load and 0.074 at normal load, which are obtained from the dc generator parameters and the resistance connected to the terminals of the machine. The moment of inertia of the dc generator is 0.0223 kg.m^2 received from the manufacturer. This value is added to the moment of inertia of the motor ($J_r = 0.042 \text{ kg.m}^2$, which is the combined moment of inertia) during the simulation under load.

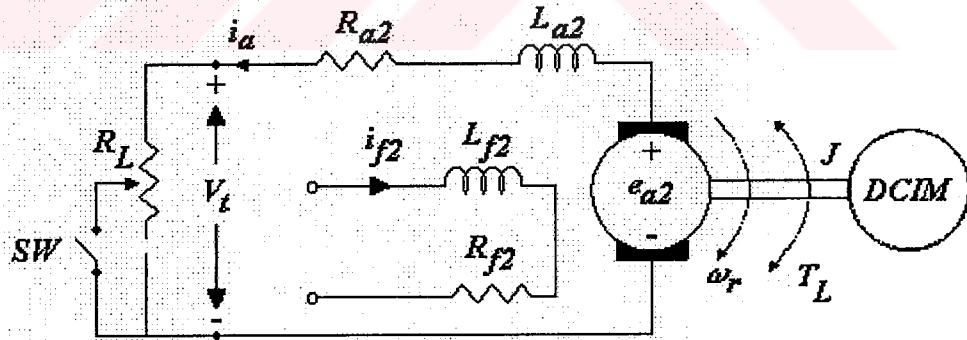


Figure 2.5 Circuit diagram for loading tests of DCIM

2.8.1 Load Test

The induction motor was initially loaded to a value of $K=0.025$ and the load was suddenly changed to a value of $K = 0.074$ by means of the external resistance switched on the terminals of dc generator. The simulation and experimental results of

rotor speed are given in Figure 2.6, for a time interval of 0.38 seconds. The ripples in the experimental speed waveform are due to the tachogenerator used for speed measurement. Transient response of the machine is mostly estimated via simulation with a speed error about %2.7.

In Figure 2.7, the simulation result for electromagnetic torque is shown. The electromagnetic torque is obtained from all models and all of the models give the same result. The shaft torque as a function of time is not recorded by the data acquisition system but its steady-state value is read. The rotor speed and shaft torque at light load are measured as 1478 rpm and 4.5 Nm, respectively while their values are 1448 rpm and 11.8 Nm under normal load when $K = 0.074$.

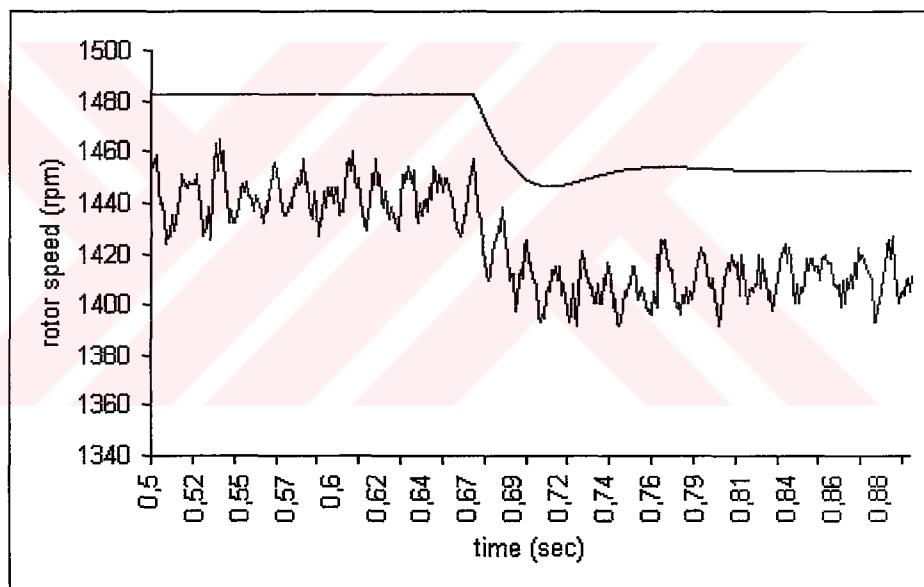


Figure 2.6 Speed response of the machine during transition from light load to normal load (upper trace-simulation, lower trace-experimental)

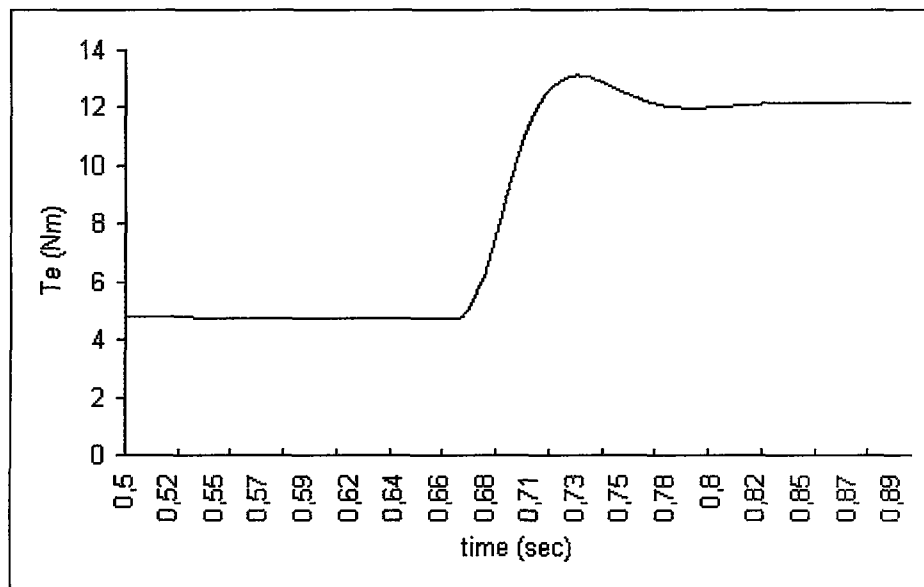


Figure 2.7 Torque response of the machine during transition from light load to normal load (simulation)

Figure 2.8 shows the experimental and simulation results of phase current during this test. The results show that measured and predicted values of stator current are close to each other.

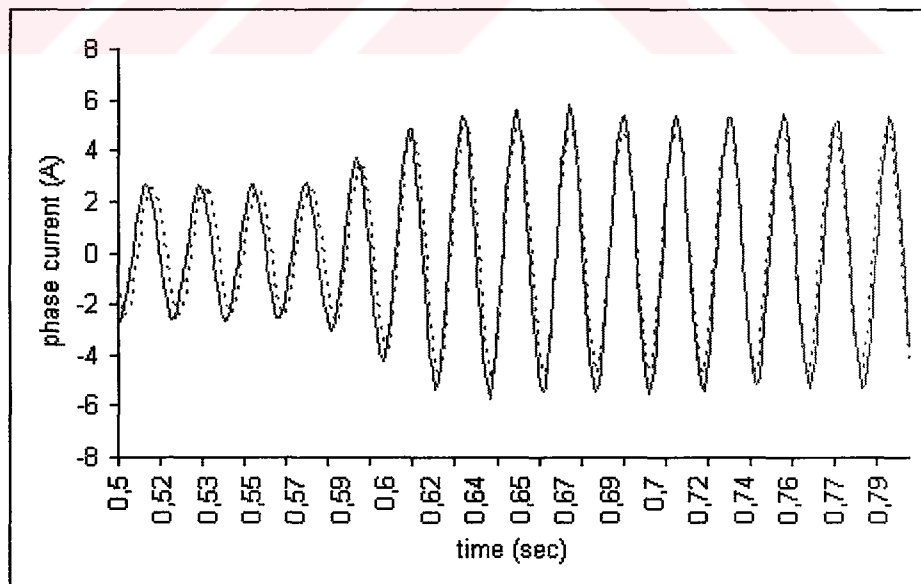


Figure 2.8 Phase current of the machine during transition from light load to normal load (dotted lines-simulation, continuous lines-experimental)

2.8.2 Free Acceleration Test

In this test, the shaft of the induction machine is uncoupled from the dc machine and it is started up under 230 volts (phase) directly switched on the stator terminals. The stator phase current is recorded by the data acquisition system. Figure 2.9 and Figure 2.10 show the rotor speed from simulation and experiment, respectively. The machine accelerates to no-load speed approximately in 0.2 seconds and this is predicted in simulations for all models. In Figure 2.11, the simulation result for electromagnetic torque is shown. This is also verified by all models of the machine.

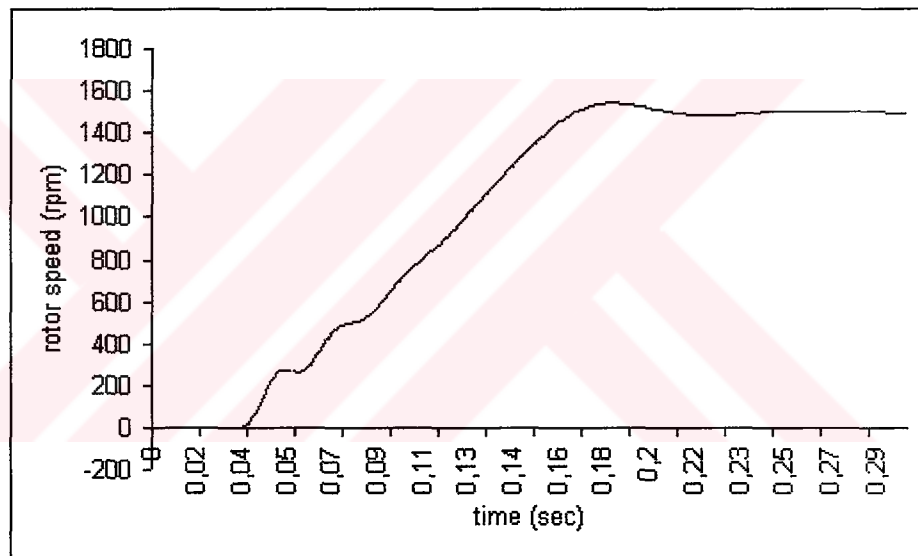


Figure 2.9 Rotor speed for free acceleration test (simulation)

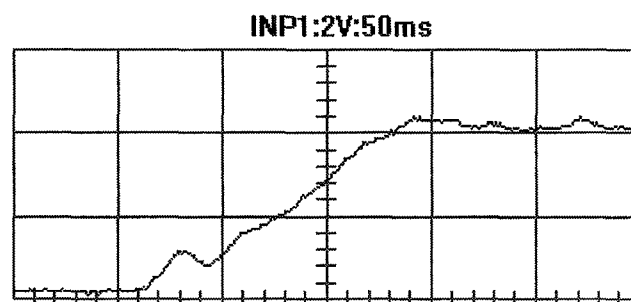


Figure 2.10 Rotor speed for free acceleration test (experiment, 750 rpm/div, time-base:0.05s/div)

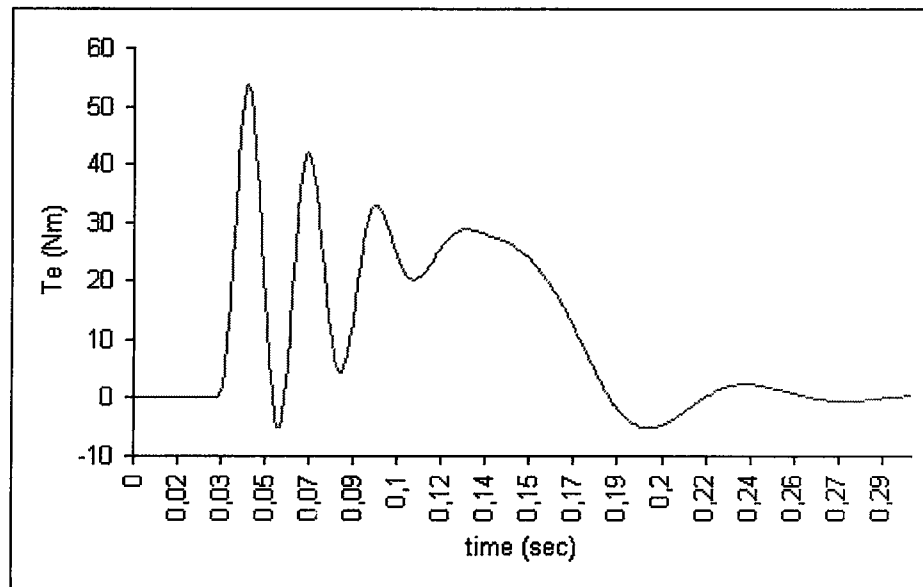


Figure 2.11 Electromagnetic torque for free acceleration test (simulation)

Figure 2.12 shows the digital simulation and experimental results of phase current for this test taking into account the synchronization between simulation and experimental work at starting instant. It is found that the peak value of starting current deviates from the simulation results and the results of analysis performed on exact equivalent circuit at the steady-state under locked rotor case. The reason is that the leakage reactances are affected from the saturation under heavy starting current. This is verified by applying different level of voltages to the stator as the rotor is blocked and the results are given in Table 2.3. The results show that the locked rotor impedance is changing according to the level of stator current while the magnetizing impedance is almost constant and not very much affected by the voltage level during this test.

Table 2.3: Locked rotor test under different supply voltages

Supply Voltage (V)	25	41	57	73	89	122	220
Line current (A)	1.48	2.88	4.22	5.54	7.02	10.1	19.8

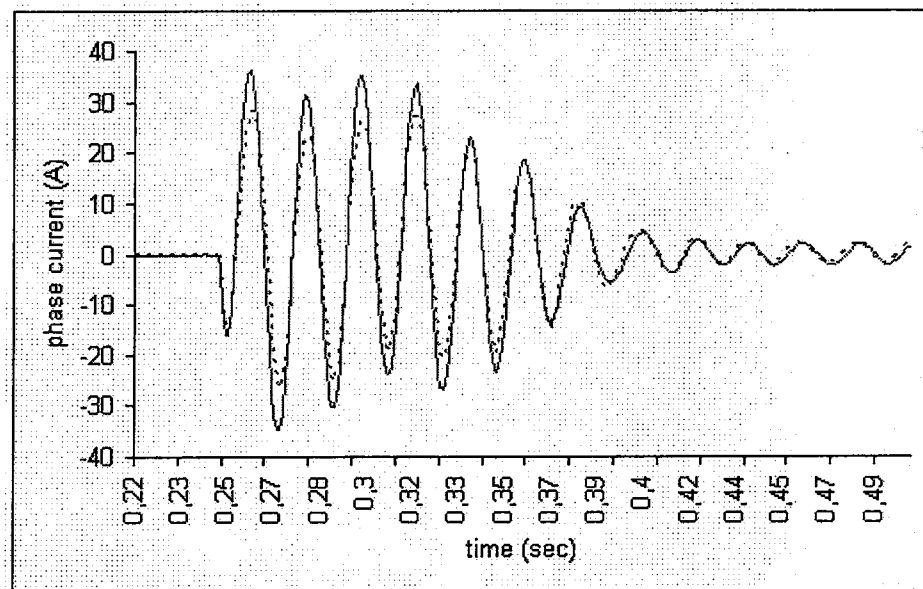


Figure 2.12 Phase current of the machine during free acceleration test (dotted lines-simulation, continuous lines-experiment)

2.8.3 Steady-state characteristics

The torque-slip characteristic of the machine that is obtained from the parameters above is given in Figure 2.13. When the torque-slip characteristic of the machine is compared with the experimental results given in Table 2.1, it shows that the genetic algorithm properly estimates the machine parameters. If the resistance ratio ($r'_3 / r'_2 = 0.75$) between the bottom and top slots is not used in the genetic algorithm, the GA still provides an estimation for the rotor resistances fitting the torque slip characteristics but the estimated rotor resistances deviate from this ratio and it affects the electrical transients as a result of rotor time constant.

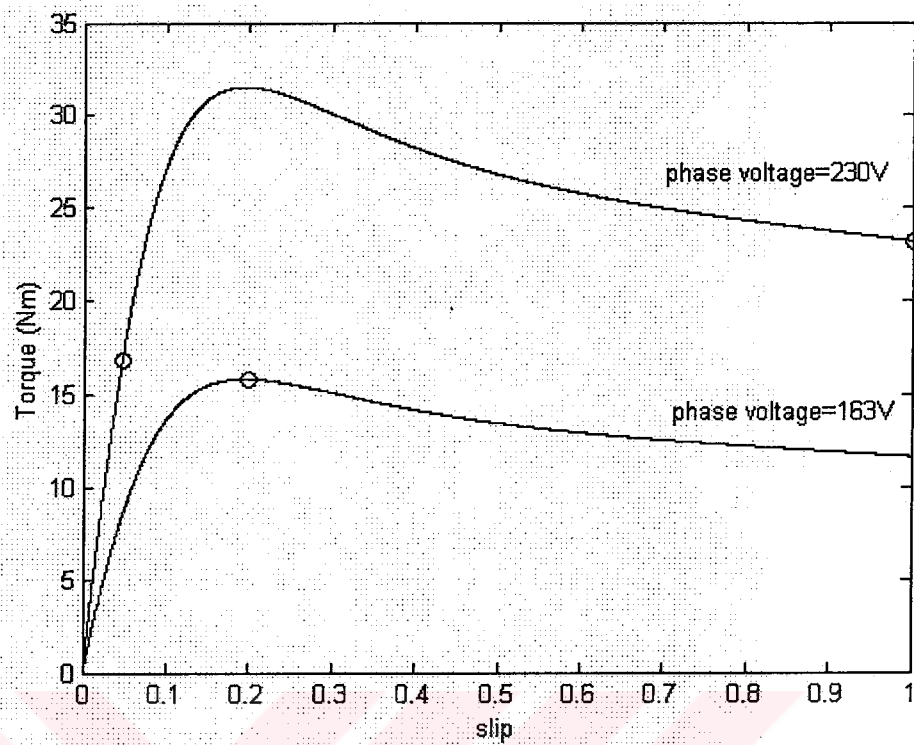


Figure 2.13 Steady-state torque-slip curves at rated and reduced armature terminal voltage. Continuous lines show the curve obtained from estimated parameters while the dots show measured values.

CHAPTER THREE

MODELING AND CONTROL OF THREE PHASE PWM AC-DC-AC VOLTAGE SOURCE CONVERTERS

3.1 Modeling of Line-Side PWM Voltage Source Converter

The circuit of the 3-phase PWM ac-dc-ac converter that is used to drive a double-cage induction machine (DCIM) is given in Figure 3.1. In this scheme, the line-side converter is supplied by balanced three-phase ac voltages and provides a constant dc voltage through the capacitor C. The value of the capacitor should be high enough to minimize the dc ripple voltage and provide energy storage. The converter stage consists of six switching devices each of which has an anti-parallel diode. The switching signals of upper side devices of each leg are shown by d_1, d_2, d_3 and those of lower side of each leg are simply their complements, which are shown by $\bar{d}_1, \bar{d}_2, \bar{d}_3$. This is because of that the switches of the same leg should not be turned on simultaneously to avoid the short circuit of the dc link. Also, a sufficient dead-time should be introduced between the turn on signals of the upper and lower side switches of the same leg. Series inductors L_s having an internal resistances R_s , are introduced at the ac lines of each phase for filtering of the currents. These inductances are also required for boost operation of the converter. The load connected across the dc link voltage terminals can be of linear or nonlinear type, such as a combination of passive elements or chopper and inverter fed drives.

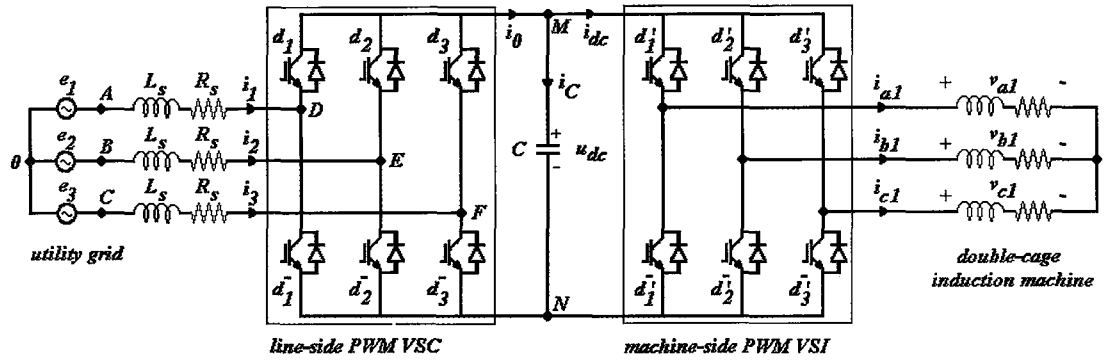


Figure 3.1 Electrical circuit of 3-phase PWM ac-dc-ac converter

A detailed analysis and modeling of the converter under RE load (a resistance connected in series with a back emf for modeling both rectifier and regenerative operation) was given by (Wu et al, 1990), (Wu et al, 1991a), and (Wu et al, 1991b). To obtain the mathematical model of the converter circuit, the following assumptions are made;

- the converter is fed from a balanced three-phase source, i.e. the sum of the instantaneous phase voltages is equal to zero,
- the three-phase system has no neutral line, i.e. the sum of the instantaneous phase currents and their derivatives is equal to zero,
- switching losses are neglected and each switching device is considered to be an ideal bilateral switch,
- the passive circuit components are assumed to be linear, i.e. the inductances are not affected by saturation,
- dead-time between the switches of the same leg is not taken into account.

The voltage equations of the line-side converter, which is shown in Figure 3.1, can be written for each phase as follows

$$L_s \frac{di_1}{dt} + R_s i_1 = V_{AD} = e_1 - V_{DO} = e_1 - (V_{DN} + V_{NO}) \quad (3.1)$$

$$L_s \frac{di_2}{dt} + R_s i_2 = V_{BE} = e_2 - V_{EO} = e_2 - (V_{EN} + V_{NO}) \quad (3.2)$$

$$L_s \frac{di_3}{dt} + R_s i_3 = V_{CF} = e_3 - V_{FO} = e_3 - (V_{FN} + V_{NO}) \quad (3.3)$$

The voltages at the converter input (points D, E, and F) with respect to neutral point (O) of the supply voltages are determined by the switching states of the converter. Since the upper and lower side switching signals are complemented, there are 8 different combinations of possible switching states. Hence, the above equations (3.1)-(3.3) can be expressed as

$$L_s \frac{di_1}{dt} + R_s i_1 = V_{AD} = e_1 - (d_1 u_{dc} + V_{NO}) \quad (3.4)$$

$$L_s \frac{di_2}{dt} + R_s i_2 = V_{BE} = e_2 - (d_2 u_{dc} + V_{NO}) \quad (3.5)$$

$$L_s \frac{di_3}{dt} + R_s i_3 = V_{CF} = e_3 - (d_3 u_{dc} + V_{NO}) \quad (3.6)$$

where d_1 , d_2 , and d_3 are the switching states of the upper side controlled solid-state devices.

For balanced three-phase supply voltages and there is no neutral line connected to the system, the sum of the line voltages and the sum of the line currents with their derivatives are equal to zero. Hence, the V_{NO} voltage can be obtained from the summation of equations (3.4)-(3.6) as follows

$$V_{NO} = -\frac{u_{dc}}{3} \sum_{k=1}^3 d_k \quad (3.7)$$

Substituting equation (3.7) into equations (3.4)-(3.6), the expression of the phase voltages can be obtained as

$$L_s \frac{di_1}{dt} = -R_s i_1 + e_1 - (d_1 u_{dc} - \frac{u_{dc}}{3} \sum_{k=1}^3 d_k) \quad (3.8)$$

$$L_s \frac{di_2}{dt} = -R_s i_2 + e_2 - (d_2 u_{dc} - \frac{u_{dc}}{3} \sum_{k=1}^3 d_k) \quad (3.9)$$

$$L_s \frac{di_3}{dt} = -R_s i_3 + e_3 - (d_3 u_{dc} - \frac{u_{dc}}{3} \sum_{k=1}^3 d_k) \quad (3.10)$$

Finally, the current equation at the dc link can be written as

$$C \frac{du_{dc}}{dt} = i_c = i_0 - i_{dc} = d_1 i_1 + d_2 i_2 + d_3 i_3 - i_{dc} \quad (3.11)$$

Assuming that the lossless converter is fed from a balanced three-phase system without a neutral connection, the mathematical model of the converter can be derived in convenient compact state-space form as follows (Blasko & Kaura, 1997)

$$L_s \frac{di_k}{dt} + R_s i_k = e_k - (u_{dc} d_k - \frac{u_{dc}}{3} \sum_{k=1}^3 d_k) \quad (3.12)$$

$$C \frac{du_{dc}}{dt} = \sum_{k=1}^3 d_k i_k - i_{dc} \quad (3.13)$$

where $k=1,2,3$, and R_s, L_s are the resistance and inductance of the inductor connected between converter and ac source. The switching losses of the converter are neglected. The balanced three-phase supply voltages (e_k), the upper side switching signals of each leg (d_k), and the load current (i_{dc}) are the inputs to the converter system, while the three-phase supply currents (i_k) and the dc link voltage (u_{dc}) are

the states. Using the equations (3.12) and (3.13), the block representation of the converter model can be given as shown in Figure 3.2.

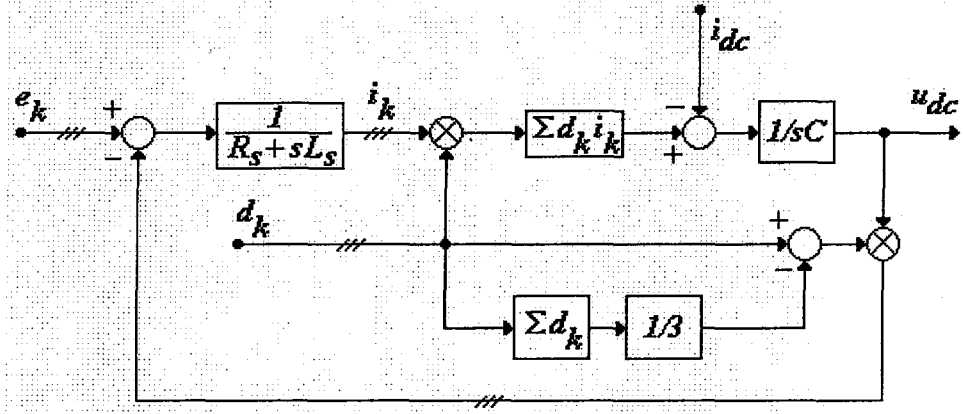


Figure 3.2 Block representation of line-side PWM voltage source converter model

The state-space equations given in (3.12) and (3.13) can also be written in explicit form as

$$Z\dot{x} = Ax + Bu \quad (3.14)$$

where

$$x = [i_1, i_2, i_3, u_{dc}]^T \quad (3.15)$$

$$u = [e_1, e_2, e_3, i_{dc}]^T \quad (3.16)$$

$$A = \begin{bmatrix} -R_s & 0 & 0 & -\left(d_1 - \frac{1}{3}\sum d_k\right) \\ 0 & -R_s & 0 & -\left(d_2 - \frac{1}{3}\sum d_k\right) \\ 0 & 0 & -R_s & -\left(d_3 - \frac{1}{3}\sum d_k\right) \\ d_1 & d_2 & d_3 & 0 \end{bmatrix} \quad (3.17)$$

$$Z = \begin{bmatrix} L_s & 0 & 0 & 0 \\ 0 & L_s & 0 & 0 \\ 0 & 0 & L_s & 0 \\ 0 & 0 & 0 & C \end{bmatrix} \quad (3.18)$$

$$B = \begin{bmatrix} 1 & 0 & 0 & 0 \\ 0 & 1 & 0 & 0 \\ 0 & 0 & 1 & 0 \\ 0 & 0 & 0 & 1 \end{bmatrix} \quad (3.19)$$

3.1.1 Current Control of Line-Side PWM Voltage Source Converter

In order to control ac line currents in PWM voltage source converters, an appropriate switching pattern for switching devices is required. There are various control methods that have been proposed, such as hysteresis current control (Ooi et al, 1987), predicted current control with fixed switching frequency (Wu et al, 1990), (Wu et al, 1991), and indirect current control (Dixon & Ooi, 1988). Hysteresis current control (HCC) is a simple and robust method that keeps the line current errors within a defined hysteresis band. The main disadvantage of HCC is the varying switching frequency depending on the load conditions. Predicted current control with a fixed switching frequency (PCFF) relies on the prediction of line currents from dc link voltage variations. In indirect current control (ICC), a standard sinusoidal PWM switching pattern is provided without needing current transducers. In PCFF and ICC, system parameters are required for obtaining sinusoidal PWM switching patterns and stability of the converter is dependent upon the parameter variations (Zargari & Joos, 1995).

When the current control of the line-side VSC is achieved by a hysteresis current controller, it first generates the command current waveforms and then forces the line currents (i_k) to trace command current waveforms (i_{ck}) within a limited hysteresis band. The appropriate switching waveforms of the switching devices in VSC are obtained from the tracking error of line currents to keep this error in the defined hysteresis band. Since the converter is desired to operate at a specified power factor,

the shapes of command currents are simply obtained from the supply voltages, which have the following form:

$$e_k = E_m \sin \left[\omega t - (k-1) \frac{2\pi}{3} \right] \quad (3.20)$$

Hence, the expression of generated command current waveforms is as follows

$$i_{ck} = I_{cm} \sin \left[\omega t - (k-1) \frac{2\pi}{3} + \theta_{vi} \right] \quad (3.21)$$

where I_{cm} is magnitude of command currents and θ_{vi} is the desired phase angle. Once the command current waveforms for the converter are obtained, the switching signals are generated according to the following logic:

$$i_{ck} - i_k > \varepsilon_h \Rightarrow d_k = 0, \bar{d}_k = 1 \quad (3.22)$$

$$i_{ck} - i_k < -\varepsilon_h \Rightarrow d_k = 1, \bar{d}_k = 0 \quad (3.23)$$

where $-\varepsilon_h$ and ε_h are the lower and upper limits of the hysteresis band, respectively. If the error in current tracking stays in the hysteresis band, the previous states of the switching signals are preserved.

3.1.2 Closed-loop voltage control

The generation of command current waveforms is achieved via a closed-loop control of the converter. Such a controller regulates the dc link voltage at the desired voltage level and adjusts the magnitude of command currents. Once the required magnitude of ac line currents is calculated, it is formed into command current waveforms of each phase. The hysteresis current controller then forces the ac line currents to track these command current waveforms as described in the previous

section. The block scheme of closed-loop hysteresis current controlled line-side voltage source converter is given in Figure 3.3. The design of closed-loop dc link voltage controller will be given in Section 3.5.

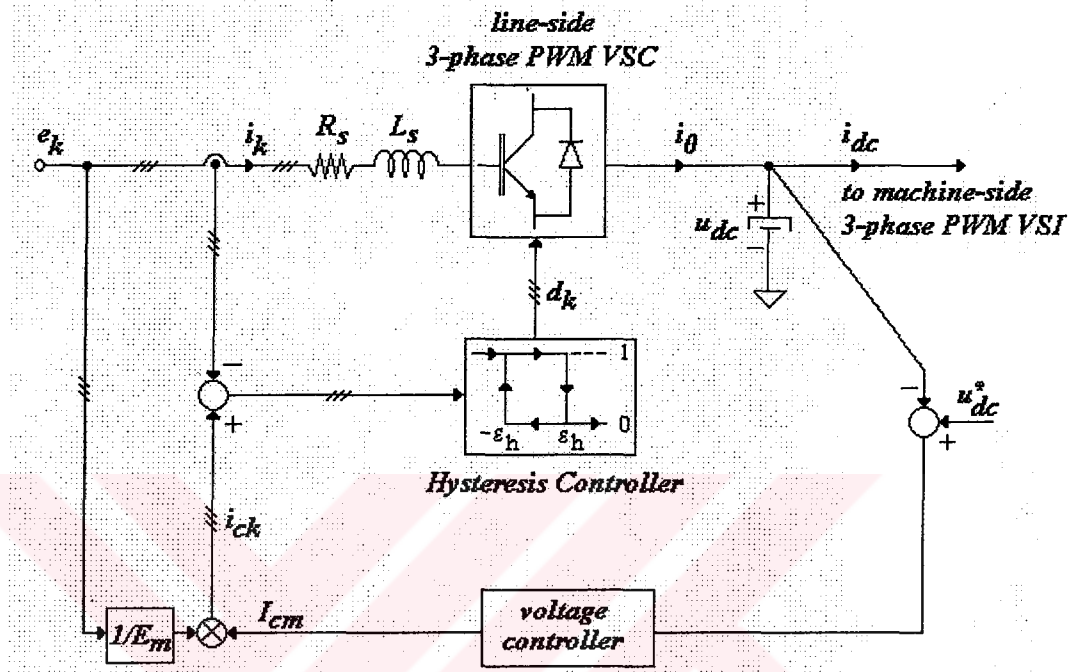


Figure 3.3 Closed-loop control scheme of 3-phase PWM ac-to-dc converter

3.1.3 Design Considerations of Line-Side PWM VSC

When the converter is fed from three-phase balanced supply voltages, which have the form given in equation (3.20), then the following condition should be satisfied for stable operation of this boost converter:

$$V_{dc} > \sqrt{3}E_m \quad (3.24)$$

This states that the dc link voltage should be greater than the peak of line-to-line voltage of the 3-phase voltage source. Usually the dc link voltage is chosen %5-10 above the peak of line-to-line input voltage of the rectifier. When the switching states of the converter is determined by PWM signals, the converter input voltage V is expressed as

$$V = KmV_{dc} \quad (3.25)$$

where $K = 1/2\sqrt{2}$ and m is the modulation index. The maximum value of the modulation index is $m = 1$ for sinusoidal PWM modulation and $m = 1.154$ for space-vector modulation.

The phasor diagrams depicting the unity power factor operation of the line-side converter in both rectifier and regenerative modes are shown in Figure 3.4. Neglecting the ac side resistance and converter losses, the following condition should be satisfied for unity power factor operation on the ac side of the converter:

$$V^2 = E^2 + (\omega L_s)^2 I^2 \quad (3.26)$$

where E and I are the rms supply phase voltage and current, respectively. Hence, the power rating of the converter can be derived as follows

$$P = 3E \frac{\sqrt{(m^2 V_{dc}^2 / 8 - E^2)}}{\omega L_s} \quad (3.27)$$

The power rating of the converter is directly proportional to the dc link voltage and inversely proportional to the line inductor value. As stated by equation (3.27), the appropriate values of circuit parameters can be chosen considering the power range of converter operation (Liserre, 2001).

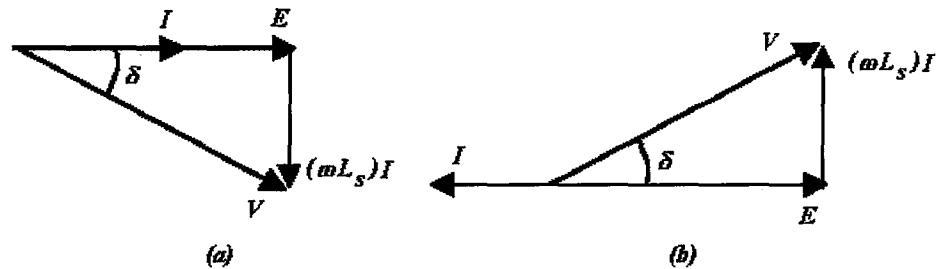


Figure 3.4 Unity power factor operation of the converter (a) rectifier (b) regenerative

3.1.4 Determination of DC Link Capacitor

Assuming that both converters are lossless, the average input power drawn from the grid will be equal to the average output power consumed by the DCIM. If the input and output ac currents are purely sinusoidal in a three-phase system, their instantaneous powers will be equal regardless of their fundamental operating frequency. However, the switching frequencies of the converters at the line-side and machine-side can be different. This means that the instantaneous powers at both sides are not the same due to harmonics generated by converters. So, an energy storage element is required for absorbing or delivering the difference between these instantaneous powers. For VSCs, the energy storage element is chosen to be a capacitor.

If both converter currents are equal on the dc side, the dc link voltage will remain constant as implied in equation (3.11). The charging and discharging current of the dc link capacitor is determined by the direction of the power flow. In rectification mode of the line-side converter, the time rate of change of the dc link voltage will be positive, if its dc side current (i_0) is greater than the load current (i_{dc}). Hence, a charging current flows into capacitor and increases the dc link voltage as a consequence. Conversely, if i_0 is lower than i_{dc} , a discharging current flows out of the dc link capacitor resulting in a decrease in the dc link voltage (Liserre, 2001).

The size of dc link capacitor depends on the amount of ac energy storage and voltage ripple. The integral of the difference between the instantaneous powers determines the energy absorbed or delivered by the dc link capacitor C. Hence, the peak to peak amplitude of energy ΔE can be expressed in terms of peak to peak ripple voltage ΔV_{dc} as follows (Kassakian et al, 1991):

$$\Delta E = \frac{C}{2} \left[\left(V_{dc} + \frac{\Delta V_{dc}}{2} \right)^2 - \left(V_{dc} - \frac{\Delta V_{dc}}{2} \right)^2 \right] \quad (3.28)$$

The peak to peak variation of ΔE is expressed as (Liao & Yeh, 2000)

$$\Delta E = \int_0^t [p_{out}(\tau) - p_{in}(\tau)] d\tau \quad (3.29)$$

where p_{out} and p_{in} are the instantaneous powers at the output and input, respectively. The required dc link capacitor can be calculated from equation (3.28) by determining the peak to peak variation of the difference between instantaneous powers.

In order that the converter can perform a fast transient response, the dc link capacitor value must be chosen low enough. On the contrary, its value must be chosen high enough for a better voltage filtering. These criteria should also be considered in the choice of the dc link capacitor value.

3.2 Modeling of Machine-Side PWM Voltage Source Inverter

The voltage source inverters supply variable voltage variable frequency waveforms to ac loads. The ac voltage waveforms are generated through sinusoidal PWM switching pattern, which is simply obtained from sine-triangular wave comparison. The machine-side VSI given in Figure 3.1 has the same electrical circuit that of line-side PWM VSC. The switching signals of upper side devices of each leg are shown by d'_1, d'_2, d'_3 and those of lower side of each leg are again their complements, which are shown by $\bar{d}_1, \bar{d}_2, \bar{d}_3$. The inverter is fed from dc link and supplies the stator windings of the DCIM on its ac side. For Y-connected DCIM stator windings, the voltage equations can be obtained in a similar way as described in Section 3.1. The phase voltages of DCIM stator windings are as follows:

$$v_{a1} = u_{dc} d'_1 - \frac{u_{dc}}{3} \sum_{k=1}^3 d'_k \quad (3.30)$$

$$v_{bs} = u_{dc}d'_2 - \frac{u_{dc}}{3} \sum_{k=1}^3 d'_k \quad (3.31)$$

$$v_{cs} = u_{dc}d'_3 - \frac{u_{dc}}{3} \sum_{k=1}^3 d'_k \quad (3.32)$$

The dc link current is expressed as

$$i_{dc} = i_{a1}d'_1 + i_{b1}d'_2 + i_{c1}d'_3 \quad (3.33)$$

The transformation given in equation (2.82) is applied to three-phase variables $(i_{abc1}, v_{abc1}, d'_k)$ in order to obtain two-phase stationary reference frame model $(\omega = 0)$ of the inverter as follows:

$$x_q = \frac{1}{3}(2x_a - x_b - x_c) \quad (3.34)$$

$$x_d = \frac{1}{\sqrt{3}}(-x_b + x_c) \quad (3.35)$$

where x_q, x_d represents transformed variables of three-phase quantities. Substituting equations (3.30)-(3.32) into (3.34) and (3.35) yields to

$$v_{q1} = u_{dc}d'_q \quad (3.36)$$

$$v_{d1} = u_{dc}d'_d \quad (3.37)$$

where d'_q, d'_d are the transformed inverter switching signals. The dc link voltage is now expressed in terms of transformed three-phase variables as follows

$$i_{dc} = \frac{3}{2}(i_{qs}d'_q + i_{ds}d'_d) \quad (3.38)$$

where i_{qs}, i_{ds} are the transformed machine currents.

The equations (3.36)-(3.38) represent the qd model of the inverter in stationary reference frame. Inverter output voltages v_{q1}, v_{d1} are the inputs to the qd model of the DCIM in stationary reference frame. The transformed inverter switching signals (d'_q, d'_d) , DCIM stator currents (i_{q1}, i_{d1}) , and dc link voltage (u_{dc}) are inputs to the inverter model. Finally, the dc link current of the inverter (i_{dc}) is the input to the line-side converter model. Using the equations (3.36)-(3.38), the block representation of the machine-side inverter model is obtained as shown in Figure 3.5.

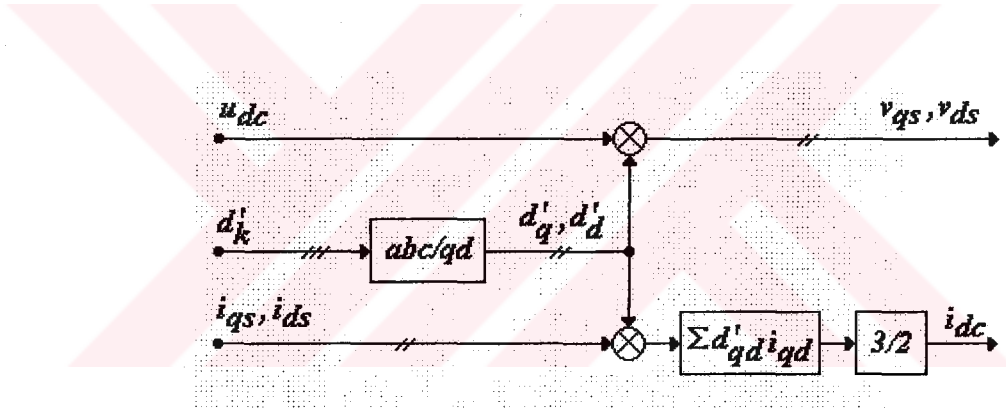


Figure 3.5 Block representation of machine-side PWM voltage source inverter model

3.2.1 Closed-loop speed control

The closed-loop speed control scheme of DCIM is given in Figure 3.6. The variable-speed control of DCIM is achieved by adjusting the slip factor by the speed controller. The output of the speed controller forms the desired slip for machine operation (ω_{slip}^*). Then the desired slip factor is added to the rotational speed of the DCIM (ω_r) and the command frequency (ω^*) signal for PWM VSI is formed. By keeping the V/f ratio constant within zero to rated frequency range, the command voltage signal (V^*) required magnitude for ac output voltage is calculated. Above the

rated frequency, the V/f ratio is reduced by limiting the voltage at rated level. This method relies on scalar control by V/f adjustment for induction machine stator voltages. In order to obtain speed feedback signal, a tacho-generator is needed. Since the slip limiter ensures that the machine operates within the defined slip limits, the current drawn by the DCIM is also indirectly limited. Hence, this method does not require an inner current-loop for limiting the machine currents (Dubey, 1989), (Trzynadlowski, 1994). The speed controller can be chosen as either digital PI or fuzzy PI controller and their performances obtained from computer simulation results will be given in Section 3.6.

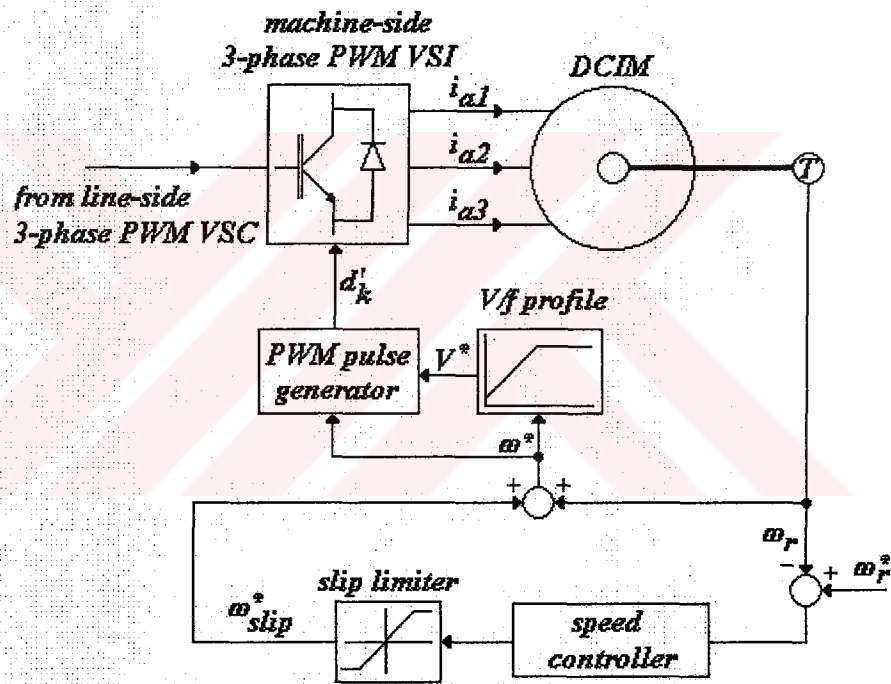


Figure 3.6 Closed-loop speed control scheme of the DCIM

3.3 Fuzzy Logic Control

The fuzzy set theory was first introduced by Zadeh in 1965. Since then, it has received attention by researchers in various areas and become a pioneering work for many scientific researches. In seventies, the term 'fuzzy control' was proposed based on fuzzy set theory. During last decades, fuzzy control has emerged in numerous applications of engineering (Ross, 1995).

Fuzzy logic control (FLC) relies on the use of linguistic approach in system control. Since the control rules and variables are expressed in linguistic terms, the logic is close to human thinking. Unlike classical control methods, precise mathematical models of systems are not required in FLC. It can provide the ability to control complex systems without needing accurate knowledge on those systems. With a prior knowledge or experience, the control of the systems can be achieved. In that way, FLC seems to offer an effective solution in the control of non-linear and time varying systems.

The use of FLC in power electronics is wide spread since power electronic systems are non-linear and time-varying in nature. The classical control techniques require exhaustive mathematical analysis on those systems. In addition, the robustness of controller to the variations of system parameters and disturbances are the major problems that have to be tackled. However, lack of a systematic design procedure and stability analysis is the drawback of FLC.

In this section, the closed-loop control of PWM VSCs will be introduced. The control design includes FLC and digital PI control techniques. DC link voltage control of line-side PWM VSC and speed control of DCIM via machine-side PWM VSC will be achieved using both control techniques. The simulation results both control methods will be compared.

3.3.1 Structure of Fuzzy Logic Control

The aim of fuzzy logic controller (FLC) is to provide a control output for the process. The structure of FLC is given in Figure 3.7. The input and output variables of FLC are crisp values and inside FLC these variables are processed through linguistic control rules. The FLC structure consists of the following modules:

Fuzzification Module: Converts the crisp values of input variables into fuzzy set, so the process variables are expressed in linguistic terms instead of quantitative terms.

A process variable is said to be a member of a fuzzy set by a degree defined by fuzzy membership functions.

Inference Module: Produces a fuzzy output depending on the fuzzified state variables and defined linguistic rules. The control action to be taken is obtained by inference mechanism.

Knowledge base: Consists of two modules called data base and rule base. The data base provides information for fuzzification and defuzzification procedures. The rule base provide information for control action.

Defuzzification Module: Converts the fuzzy set variables into crisp values.

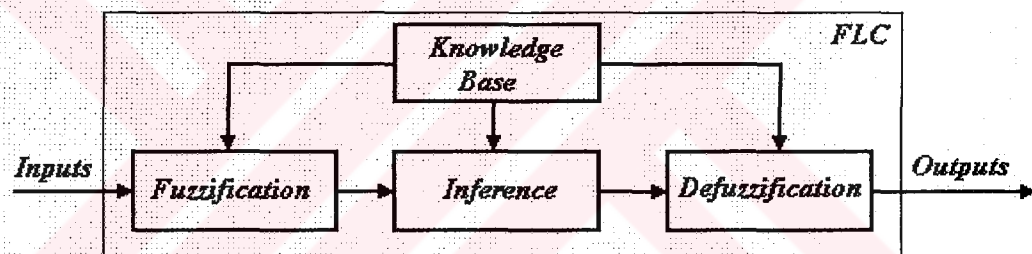


Figure 3.7 Structure of a fuzzy logic controller

3.3.2 Fuzzy Sets and Membership Functions

In classical sets, the membership of an element is well-defined and said to be 'crisp'. For a crisp set A defined in the universe of discourse U , any element u of U is either a member of A ($u \in A$) or not ($u \notin A$). However, in a universe containing fuzzy sets, the membership of any element is gradual. The element u may not only necessarily be a complete member of a fuzzy set, but also may be the member of other fuzzy sets defined on the same universe. The membership degree of an element in a fuzzy set is measured by a function that describes vagueness and ambiguity (Ross, 1995).

Let x be an element and A be a fuzzy set in the universe X . The membership of x in the fuzzy set A is characterized by a membership function μ_A such that

$$\mu_A(x) \in [0,1] \quad (3.39)$$

If the universe X is discrete and finite, the fuzzy A set can be expressed as

$$A = \left\{ \frac{\mu_A(x_1)}{x_1} + \frac{\mu_A(x_2)}{x_2} + \dots \right\} = \left\{ \sum_i \frac{\mu_A(x_i)}{x_i} \right\} \quad (3.40)$$

and if the universe X is continuous and infinite

$$A = \int \frac{\mu_A(x)}{x} \quad (3.41)$$

Fuzzy sets are described by their membership functions, each of which has its own shape. Through the membership functions, the elements of a fuzzy set are mapped to the unit interval $[0, 1]$, which is defined as membership degree. Commonly used membership functions in fuzzy logic control are given in Figure 3.8. These functions are normal fuzzy sets, i.e. at least one element x in the universe has unity membership value. Additionally, the membership functions that have smooth shapes, such as bell-shaped, sigmoid etc, can be used. However, their mathematical expression is rather complicated and increases the computational burden in implementation (Zakharov, 1996).

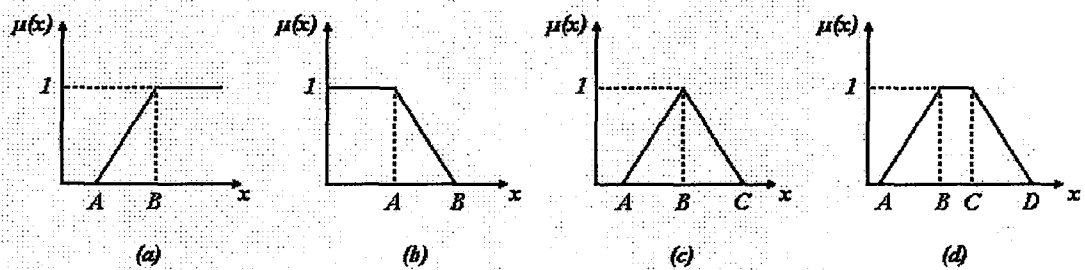


Figure 3.8 Commonly used membership functions

The Gamma-function given in Figure 3.8a is defined as follows:

$$\Gamma(x, A, B) = \begin{cases} 0 & x < A \\ \frac{(x-A)}{(B-A)} & A \leq x \leq B \\ 0 & x > B \end{cases} \quad (3.42)$$

The L-function given in Figure 3.8b is defined as follows:

$$L(x, A, B) = \begin{cases} 0 & x < A \\ \frac{(A-x)}{(B-A)} & A \leq x \leq B \\ 0 & x > B \end{cases} \quad (3.43)$$

The Lambda-function given in Figure 3.8c is defined as follows:

$$\Lambda(x, A, B, C) = \begin{cases} 0 & x < A \\ \frac{(A-x)}{(B-A)} & A \leq x \leq B \\ \frac{(B-x)}{(C-B)} & B \leq x \leq C \\ 0 & x > C \end{cases} \quad (3.44)$$

The Pi-function given in Figure 3.8d is defined as follows:

$$\Pi(x, A, B, C, D) = \begin{cases} 0 & x < A \\ \frac{(x-A)}{(B-A)} & A \leq x \leq B \\ 1 & B \leq x \leq C \\ \frac{(C-x)}{(D-C)} & C \leq x \leq D \\ 0 & x > D \end{cases} \quad (3.45)$$

3.3.2.1 Fuzzy Set Operations

The set operations used in fuzzy logic control are union, intersection, and complement, which are depicted in Figure 3.9. Let A and B be the fuzzy sets defined on the universe X. For any element x in the universe, the membership value of two fuzzy sets union is defined as

$$\forall x \in X : \mu_{A \cup B}(x) = \max \{ \mu_A(x), \mu_B(x) \} \quad (3.46)$$

The membership value of two fuzzy sets intersection is defined as

$$\forall x \in X : \mu_{A \cap B}(x) = \min \{ \mu_A(x), \mu_B(x) \} \quad (3.47)$$

and the complement of fuzzy set A is defined as

$$\forall x \in X : \mu_{\bar{A}}(x) = 1 - \mu_A(x) \quad (3.48)$$

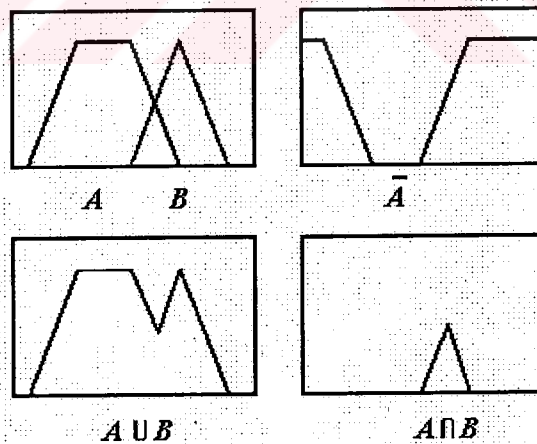


Figure 3.9 Fuzzy set operations

3.3.2.2 Fuzzy Relations

Fuzzy relations are used to map the elements of one universe to another universe through the Cartesian product of the two universes. A fuzzy relation can be

considered to be a mapping from a Cartesian product space to the unit interval $[0, 1]$ through the membership function of the relation $\mu_R(x, y)$, which is a set of ordered pairs from the two universes. Let A and B be the fuzzy sets defined on the universes X and Y, respectively. The Cartesian product between these fuzzy sets will result in a fuzzy relation $R = A \times B$ on the Cartesian product space $X \times Y$. The binary fuzzy relation R has the membership function defines as follows:

$$\mu_R(x, y) = \mu_{A \times B}(x, y) = \min\{\mu_A(x), \mu_B(y)\} \quad (3.49)$$

Let R and S be the fuzzy relations defined on Cartesian product space $X \times Y$. The union, intersection, and complement operations on fuzzy relations are defined as follow:

The union of the two fuzzy relations

$$\mu_{R \cup S}(x, y) = \max\{\mu_R(x, y), \mu_S(x, y)\} \quad (3.50)$$

The intersection of the two fuzzy relations

$$\mu_{R \cap S}(x, y) = \min\{\mu_R(x, y), \mu_S(x, y)\} \quad (3.51)$$

And, the complement of fuzzy relation R

$$\mu_{\bar{R}}(x, y) = 1 - \mu_R(x, y) \quad (3.52)$$

3.3.2.3 Linguistic variable

A linguistic variable can be defined as a variable whose value is a word or sentence in a natural or artificial language. In contrast to numerical variables, the values of a linguistic variable are not numbers. A linguistic variable can be expressed by a quintuple $(x, T(x), U, G, M)$. Here, x is symbolic name of the linguistic

variable. $T(x)$ is the term-set of x , which is a set of linguistic values that x can take over a defined physical domain U . G is a syntactic rule that generates the names of the values of x . M is a semantic function associated with the meaning of linguistic variable (Lee, 1990). For example, let *error* be a linguistic variable. The term-set of *error* can be

$$T(\text{error}) = \{NB, NM, NS, Z, PS, PM, PB\}$$

and each term of $T(\text{error})$ is defined by a fuzzy set over a normalized domain U , which is defined in the interval $[-1, 1]$. For example, the values of *error*, which are less than -0.5, can be interpreted as NB (negative big), the values greater than 0.5 as PB (positive big), and so on. The terms of $T(\text{error})$ can be represented by fuzzy sets as shown in Figure 3.10.

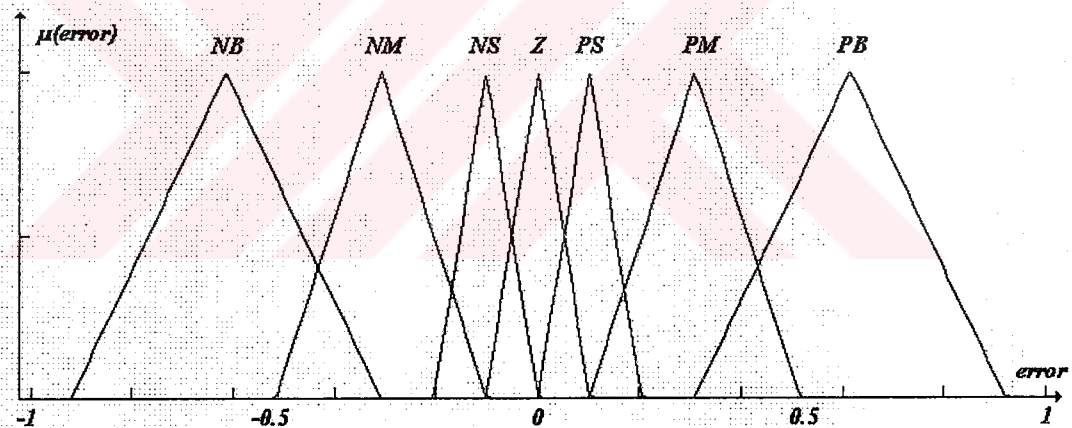


Figure 3.10 Representation of error as a linguistic variable

3.3.2.4 Fuzzy Rules

The behavior of fuzzy logic controller depends on the rules represented by expert knowledge about plant. The most common way to represent knowledge is to express it in IF-THEN rules such as

IF premise(antecedent) THEN conclusion(consequent)

This is a linguistic expression of a conditional statement in natural language. In fuzzy logic control, the antecedent is a condition in application and the consequent is the control action to be taken. For example,

IF (error is positive big) THEN (the output is positive big)

The statement implies that if the controlled variable of the fuzzy system is much far from the desired set point then a big increase in the controller output should be done.

Let A and B be fuzzy sets defined on X and Y , respectively. There many techniques for obtaining a fuzzy relation R based on the rule *IF A THEN B* or $R = A \rightarrow B$. These are known as fuzzy implications and mostly used in fuzzy control is Mamdani implication such that

$$R = A \rightarrow B \equiv A \cap B \quad (3.53)$$

and the membership function values of fuzzy relation R defined on the Cartesian product space $X \times Y$

$$\mu_R(x, y) = \min \{ \mu_A(x), \mu_B(y) \} \quad (3.54)$$

3.3.2.5 Aggregation of Rules

Fuzzy rule-based systems generally consist of more than one rule. In order to obtain an overall consequent from all individual consequents, two simple aggregation strategies are used:

1) *Conjunctive system of rules*: In this method the rules are connected by AND connectives. The aggregated output y can be obtained from r individual consequents and expressed as

$$y = y^1 \cap y^2 \cap \dots \cap y^r \quad (3.55)$$

which is defined by the membership function

$$\mu_y(y) = \min \{ \mu_y^1(y), \mu_y^2(y), \dots, \mu_y^r(y) \} \quad y \in Y \quad (3.56)$$

2) *Disjunctive system of rules*: In this method the rules are connected by OR connectives. The aggregated output y can be expressed as

$$y = y^1 \cup y^2 \cup \dots \cup y^r \quad (3.57)$$

which is defined by the membership function

$$\mu_y(y) = \max \{ \mu_y^1(y), \mu_y^2(y), \dots, \mu_y^r(y) \} \quad y \in Y \quad (3.58)$$

3.3.2.6 Inference Process

Let us consider a fuzzy system with two antecedents (x_1 and x_2) and one consequent (y). Let the fuzzy system be described by a collection of r linguistic IF-THEN rules such that

$$\text{IF } (x_1 \text{ is } A_1^k) \text{ AND } (x_2 \text{ is } A_2^k) \text{ THEN } (y^k \text{ is } B^k) \quad k = 1, 2, \dots, r \quad (3.59)$$

The aggregated output of r rules can be obtained based on the Mamdani implication method and for a set of disjunctive rules such that

$$\mu_{B^k}(y) = \max_k \left\{ \min \left[\mu_{A_1^k} \{x_1(i)\}, \mu_{A_2^k} \{x_2(j)\} \right] \right\} \quad k = 1, 2, \dots, r \quad (3.60)$$

In Figure 3.11, the graphical interpretation of the above equation is illustrated. The symbols A_{11} and A_{12} refer to first and second antecedents of the first rule,

respectively. Similarly, the symbols A_{21} and A_{22} refer to first and second antecedents of the second rule, respectively. The symbols B_1 and B_2 refer to consequents of the first and second rule, respectively. The aggregated membership function can be formed depending on the Mamdani implication method and disjunctive rules as shown. The crisp value for aggregated output y^* can be obtained by employing a defuzzification technique (Ross, 1995). Defuzzification techniques will be given in the following section.

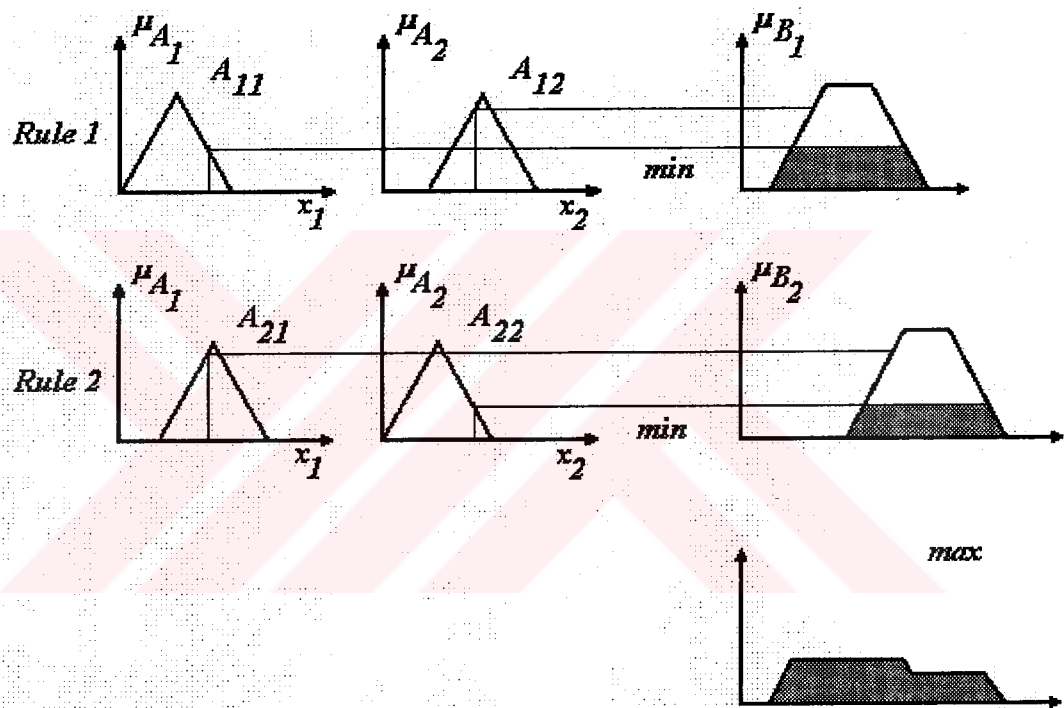


Figure 3.11 Graphical representation of inference

3.3.2.7 Defuzzification Methods

As mentioned before, defuzzification is the process of converting fuzzy quantities to precise quantities. A fuzzy output is obtained by combining all fuzzy output parts and the overall fuzzy output membership function can be expressed as

$$C = \bigcup_{i=1}^k C_i \quad (3.61)$$

The following methods are the most popular and commonly used ones for defuzzifying operation (Ross, 1995):

1) *Max-membership principle*: The graphical representation of this method is shown in Figure 3.12a. This method returns the value of element which has the maximum membership degree at the fuzzy output function such that

$$\mu_C(z^*) \geq \mu_C(z) \quad \forall z \in Z \quad (3.62)$$

2) *Centroid method*: The graphical representation of this method is shown in Figure 3.12b. This is also called center of gravity method and given by the algebraic expression as follows:

$$z^* = \frac{\int \mu_C(z).zdz}{\int \mu_C(z)} \quad (3.63)$$

3) *Weighted average method*: The graphical representation of this method is shown in Figure 3.12c. This method is valid for membership functions having symmetrical output and given by the algebraic expression as follows:

$$z^* = \frac{\sum \mu_C(z).z}{\sum \mu_C(z)} \quad (3.64)$$

4) *Mean-max membership*: This method is also called middle of maxima and given by the expression

$$z^* = \frac{a+b}{2} \quad (3.65)$$

where a and b are shown in Figure 3.12d.

5) *Center of sums*: This method involves the algebraic sum of the individual outputs instead of their union. The defuzzified output can be expressed as

$$z^* = \frac{\int z \sum_{k=1}^n \mu_{C_k}(z) dz}{\int \sum_{k=1}^n \mu_{C_k}(z) dz} \quad (3.66)$$

6) *Center of largest area*: In this method, the convex fuzzy sub region with the largest area is used to obtain the defuzzified value such that

$$z^* = \frac{\int \mu_{C_m}(z).z dz}{\int \mu_{C_m}(z)} \quad (3.67)$$

7) *First/Last of maxima*: This method uses the overall output of all individual fuzzy sets and determines the smallest value of the domain with maximized membership degree. The first of maxima is found such that

$$z^* = \inf \{z \in Z, \mu_{C_k}(z) = hgt(C_k)\} \quad (3.68)$$

And the last of maxima is found such that

$$z^* = \sup \{z \in Z, \mu_{C_k}(z) = hgt(C_k)\} \quad (3.69)$$

where *hgt* denotes the largest height in the union, supremum (sup) is least upper bound, and infimum (inf) is the greatest lower bound.

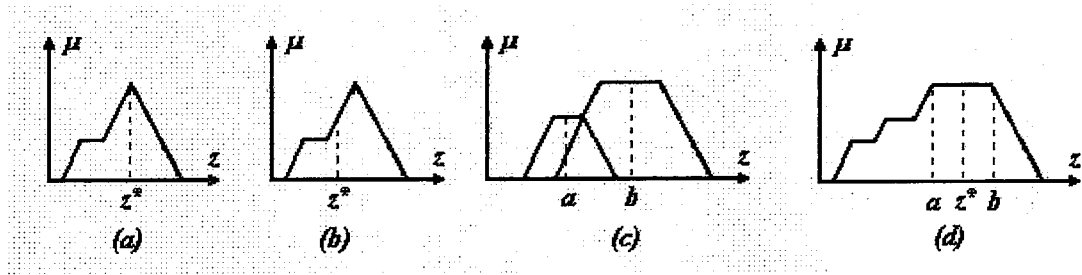


Figure 3.12 Graphical representations of defuzzification methods (a) Max-membership (b) centroid (c) weighted average (d) max-min membership

3.4 Digital Proportional-Integral Controller

In a closed-loop negative feedback system, the error is formed by the difference between the reference and actual values. The controller output for analog proportional-integral (PI) is expressed as

$$u(t) = K_p e(t) + K_i \int e(t) dt \quad (3.70)$$

where K_p and K_i are the proportional and integral error gain gains. Digital PI controller is the discrete form of the analog PI controller. The digital PI controller is incremental type and its output is expressed as a difference equation for a given sampling time (T_{smp}) as follows:

$$U(nT_{smp}) = U_p(nT_{smp}) + U_i(nT_{smp}) \quad (3.71)$$

where

$$U_p(nT_{smp}) = K_p E(nT_{smp}) \quad (3.72)$$

and

$$U_i(nT_{smp}) = U_i[(n-1)T_{smp}] + K_i T_{smp} E(nT_{smp}) \quad (3.73)$$

To calculate the controller output, the incremental form is used. In that way, the change of controller output (ΔU) is calculated from error (E) and change of error (ΔE) and the output (U) is calculated by adding the change of output (ΔU) to the sum of its previous values at each step. To calculate the change of output, its previous value is subtracted from its current value and

$$\begin{aligned}\Delta U(nT_{smp}) &= U(nT_{smp}) - U[(n-1)T_{smp}] \\ &= U_P(nT_{smp}) - U_P[(n-1)T_{smp}] + U_I(nT_{smp}) - U_I[(n-1)T_{smp}]\end{aligned}\quad (3.74)$$

which yields

$$\Delta U(nT_{smp}) = K_P \Delta E(nT_{smp}) + K_I T_{smp} E(nT_{smp}) \quad (3.75)$$

The parameters for the digital PI controller are now error gain (K_E) and change of error gain (K_{CE}), which can be expressed in terms of analog PI gains and sampling period as follow:

$$K_E = K_I T_{smp}, K_{CE} = K_P \quad (3.76)$$

3.5 DC link voltage control

Digital PI or fuzzy controllers can be used on the line-side PWM VSC in order to regulate the dc link voltage at a desired level u_{dc}^* . In the following, the design of digital PI and PI based fuzzy logic controllers is given.

3.5.1 DC link voltage control with PI Controller

The block scheme of PI controlled line-side PWM VSC is given in Figure 3.13. The dc link voltage u_{dc} is fed back to the control system and an error signal e is obtained. For digital implementation of the PI controller, an additional control signal

ce , change of error, is required and it is simply obtained from the difference between error and its previous value at k^{th} sampling instant such that

$$ce(k) = e(k) - e(k-1) \quad (3.77)$$

Since an incremental form is used in the design of digital PI controller, the output is also incremental. That means, the output determines the amount of change in command currents magnitude (ΔI_{cm}). Hence, the controller forms its output, the command currents magnitude, I_{cm} by adding the output generated by PI controller sequentially. The output of the closed-loop controller processed through the hysteresis current controller (HCC) in order to generate switching signals of line-side PWM VSC. Determination of controller gains will be discussed in Section 3.6.

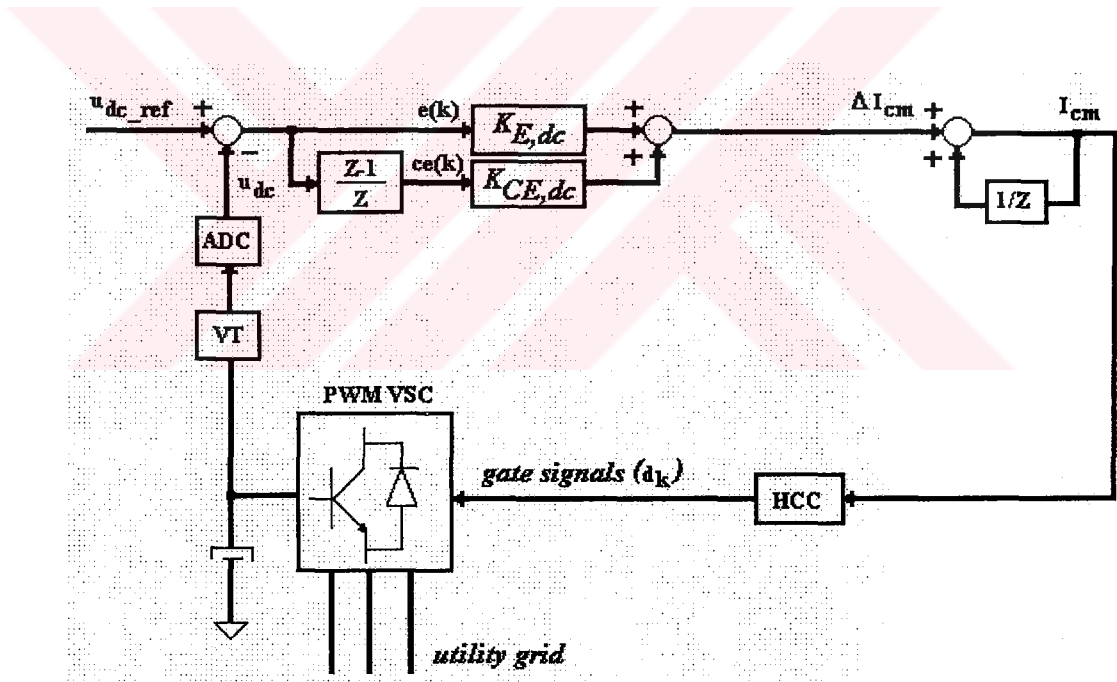


Figure 3.13 Block scheme of PI controlled line-side PWM VSC

3.5.2 DC link voltage control with FLC

The block scheme of fuzzy controlled line-side PWM VSC is given in Figure 3.14. Since the fuzzy controller is designed to be PI-like, the error and change of error signals are obtained and processed through the FLC.

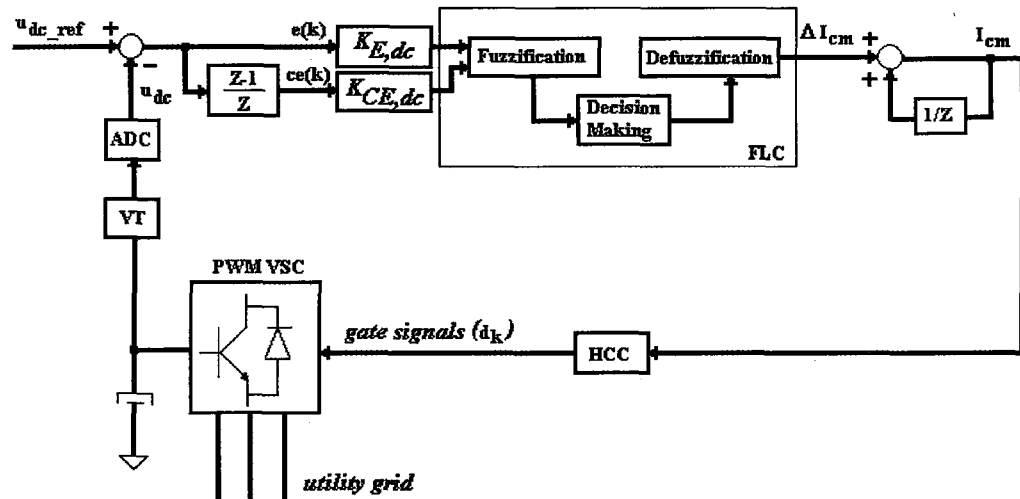


Figure 3.14 Block scheme of fuzzy controlled line-side PWM VSC

During fuzzification procedure, the membership functions given in Figure 3.15 are used. The crisp values of error and change of error are expressed in terms of 7 linguistic variables in the defined universe of discourse, which has the range between $[-512, +511]$. These are NB (negative big), NM (negative medium), NS (negative small), ZE (zero), PS (positive small), PM (positive medium), and PB (positive big). The membership functions have triangular waveform and membership degrees range in $[0, 1]$. The scaling of the range of universe is chosen such that it conforms the 10-bit A/D converter range considering the implementation procedure.

Error and change of error signals are expressed in 7 linguistic variables and total 49 rules can be constructed with two antecedents and one consequent. These rules are used for control action and shown in Table 3.1. The output of the fuzzy controller also expressed in terms of 7 linguistic variables. The membership functions used to describe the output of the controller is given in Figure 3.16. During inference process, Mamdani implication method is used for a disjunctive set of rules as described in Section 3.3.2.6.

Table 3.1: Rule matrix for PI based fuzzy controller

ce e	NB	NM	NS	Z	PS	PM	PB
NB	NB	NB	NB	NB	NM	NS	Z
NM	NB	NB	NB	NM	NS	Z	PS
NS	NB	NB	NM	NS	Z	PS	PM
Z	NB	NM	NS	Z	PS	PM	PB
PS	NM	NS	Z	PS	PM	PB	PB
PM	NS	Z	PS	PM	PB	PB	PB
PB	Z	PS	PM	PB	PB	PB	PB

For the design of fuzzy controller structure, MATLAB Fuzzy Logic Toolbox is used. The Fuzzy Logic Toolbox is a powerful program, which provides fuzzy inference system editor, ruler editor, membership function editor, fuzzy inference viewer, and output surface viewer. In this way, it is easier to create a fuzzy logic system. The computer simulation results of a closed-loop fuzzy controlled line-side PWM VSC will be given in Section 3.6

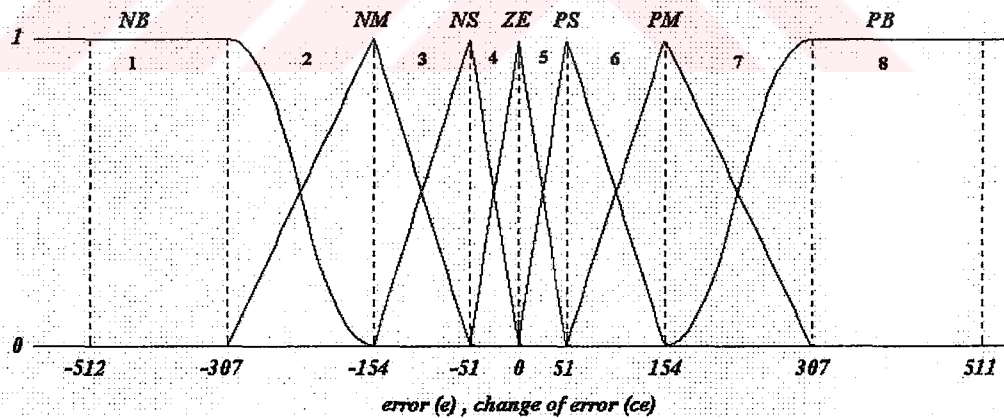


Figure 3.15 Membership functions for error and change of error

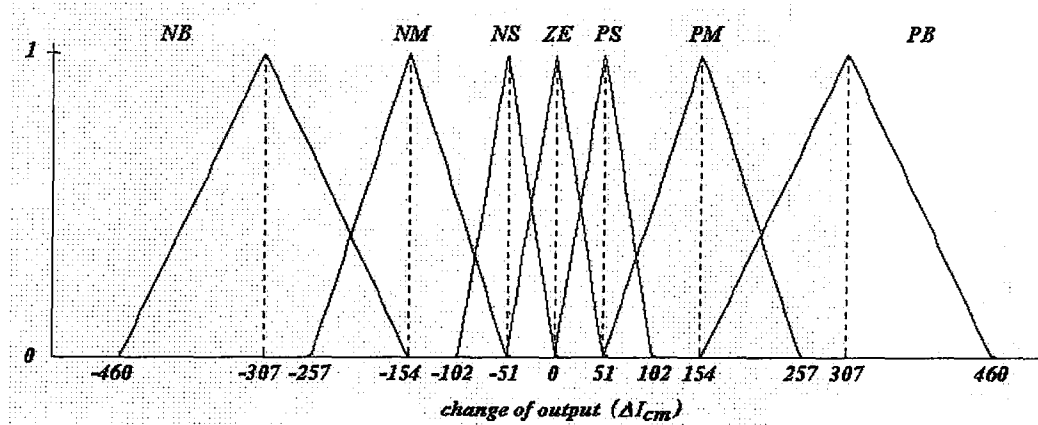


Figure 3.16 Membership functions for change of output

3.5.3 PI Speed Controller

In order to achieve speed control of DCIM, a digital PI controller is used as described in Section 3.4. The speed control of DCIM via slip regulation technique was described in Section 3.2.1 and closed-loop scheme with PI controller is shown in Figure 3.17.

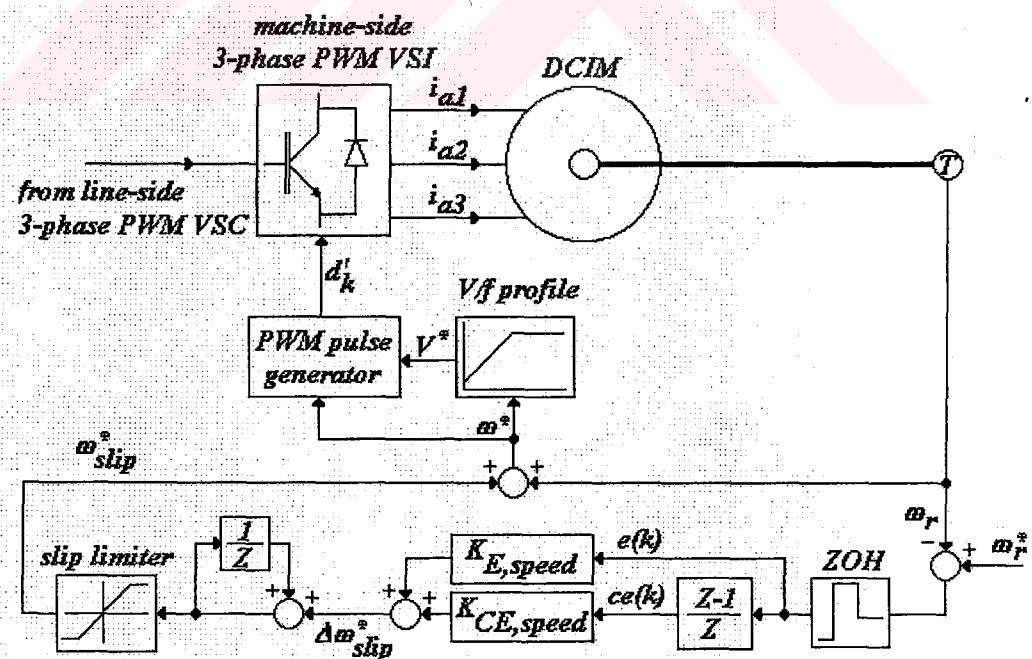


Figure 3.17 Closed-loop scheme of PI speed controller

3.6 System Parameters and Simulation Results

Computer simulations of the drive system are carried out in MATLAB Simulink environment. The mathematical models of the line-side PWM VSC, machine-side PWM VSC, and DCIM are constructed using Simulink blocks. Closed-loop controllers are introduced on the line-side converter with digital PI and fuzzy PI in order to make a comparison between the responses of both controllers. In speed control of DCIM, a digital PI controller is used. The complete Simulink model of each block will be given in Appendix B.

During simulations, the dc link reference voltage is set to 500V. The magnitude of the balanced ac supply voltages is set to 280V line-to-line. The circuit parameters for the line-side converter are chosen as

$$L_s = 50mH, R_s = 0.8ohms, C = 4.7mF$$

The hysteresis band limits for HCC used in the current controlled line-side PWM VSC is chosen to be 0.2A. The error and change of error gains are chosen to be the same for both digital PI and fuzzy PI controllers in order to investigate the performances of both controllers under the same conditions. The sampling rate of the digitized signals is chosen to be $T_{smp} = 0.25 ms$.

3.6.1. Instrumentation Gains for Simulation

The voltage and current feedback signals are obtained through sensors with different output signal levels and sampled by 10-bit A/D converter operating with signal levels of 0-5V, their gains are taken into account in the Simulink model. In the Simulink model, all waveforms (voltages, currents, and speed) that are sensed by A/D converter are multiplied by their determined gains, quantized and floored for integer operation.

The dc link voltage (u_{dc}) conversion range is (0-800V) to (0-5V) or (160:1) in the implemented system. Taking the A/D converter gain into account, the dc link voltage gain for Simulink model is obtained as follows:

$$K_{udc} = \frac{1}{160} \times \frac{1023}{5}$$

The supply voltages (e_{abc}) conversion range is from peak to peak values ($-E_m, E_m$) to (-2V, +2V) or normalized to 2 by their magnitudes. Supply voltage gain is calculated as

$$K_{eabc} = \frac{2}{E_m} \times \frac{1023}{5}$$

For the supply currents (i_{abc}) and dc link current (i_{dc}), the gain is calculated from the conversion range of (-10A, +10A) to (-2.5V, +2.5V) or (0.250V/A) as follows:

$$K_{iabc, idc} = 0.25 \times \frac{1023}{5}$$

For the dc link voltage control, the command currents magnitude (I_{cm}) is multiplied by the sampled supply voltage signals and then a gain factor of 1/32768 in order to obtain command current waveforms. The command currents magnitude is allowed to change between (-30720, +30720). Since the supply voltages are normalized to 2 instead of 2.5, this also produces a gain factor of 0.8 in the calculation of command currents magnitude. So, for a given range of command currents magnitude, it points out a supply current range of (-7.5A, +7.5A). Its maximum value can be found as follows:

$$I_{cm, \max} = \frac{30720}{32768} \times \frac{2}{2.5} \times 10 = 7.5A$$

Hence, for a stable operation of the converter, the peak value of the line currents should not exceed 7.5A

In DSP programming, inverter command frequency adjusted within the range of 0-2048, which corresponds to a frequency range of 0-62.5Hz for PWM waveform generation. Since the reference speed input is within the range of 0-5V, its value is multiplied by 2 in DSP program. The speed feedback signal obtained from the tachogenerator output has output range of 0-1875rpm to 0-5V and it is also multiplied by 2. Hence, in the Simulink model of the real system, the speed feedback is obtained from the electrical rotor speed of the DCIM and its gain in the model is calculated as follows:

$$K_{speed} = 2 \times \frac{2}{P} \times \frac{60}{2\pi} \times \frac{4}{1875} \times \frac{1023}{5}$$

3.6.2 Determination of Digital PI Parameters of Voltage Controller

In order to obtain suitable PI parameters of the voltage controller, the following procedure is applied: The converter is operated with a resistive load of 100ohms, error and change of error gains are set to 1, the command currents magnitude is adjusted in open-loop configuration so that the dc link voltage is built up at the reference value of 500V for the rectification mode of the converter slightly above its rated power, and the error and change of error signals are observed as shown in Figure 3.18. Since the error and change of error take values in the universe that has the range of [-512, +511], the maximum values of both signals, which are obtained from open-loop operation, are magnified with the appropriate gains so as not to extend these signals beyond the boundaries of the universe. In simulations, these gains are rounded to the nearest binary integer power considering the implementation on fixed point DSP. Hence, the arithmetic operation burden of the DSP is reduced to only bitwise shift operations instead floating point multiplication or division. Considering these criteria, the controller parameters for line-side converter are obtained as follows

$$K_{E,dc} = 1, K_{CE,dc} = 32$$

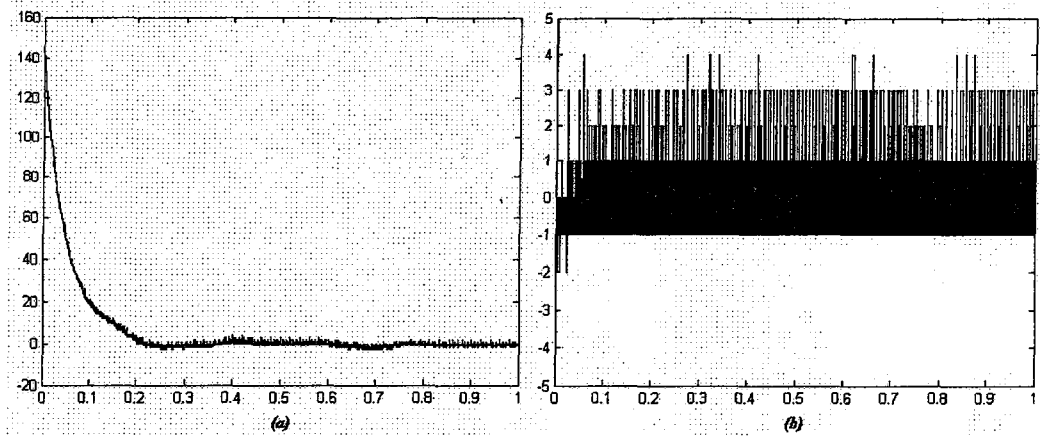


Figure 3.18 Open-loop responses for determination PI parameters on the line-side converter (a) error (b) change of error

3.6.3 Determination of Digital PI Parameters of Speed Controller

The PWM frequency of the machine-side PWM VSC is chosen to be 2kHz. The switching signals of this converter are obtained through sine-triangle comparison. The command frequency signal generated through speed controller is converted to sine wave through a reference generator taking the V/f profile of the DCIM into account. The parameters of the DCIM were given in Chapter 2. In the speed controller part, slip is limited to 15 percent of the rated frequency, i.e. 7.5Hz. The reference speed is set to 1350rpm. Finally, error and change of error gains are set to the values given below:

$$K_{E,speed} = \frac{1}{8}, K_{CE,speed} = \frac{1}{2}$$

3.6.4 Simulation Results

Computer simulation tests are performed for the motor and generator operation of the machine. The following value of the moment of inertia, which is the combination of DCIM and load, is used in the simulations:

$$J = 0.04 \text{ kg.m}^2$$

In both tests, the dc link voltage is stabilized at its reference value of 500V first. The initial value of dc link voltage is set to its peak line-to-line supply voltage value and then it is boosted up to 500V by the line-side converter. After the dc link voltage is stabilized, the switching signals of the machine-side PWM VSC are applied and the machine is accelerated to the reference speed of 1350rpm from standstill. The friction and windage torque is measured to be approximately 0.7Nm at the steady state value of this rotational speed. To take the effects of the friction and windage into account, a shaft torque proportional to square of the rotor speed is defined.

3.6.4.1 Motor Operation

In this test, the dc link voltage and rotor speed are stabilized at their reference values given above during 0-5s and 5-10s, respectively. While the DCIM is running at steady-state at no-load, a step shaft torque of 10Nm is applied to the machine for motoring operation during 10-15s. Then, the torque is removed and the machine is pulled back to no-load operation again during 15-20s.

In Figure 3.19, the dc link voltage and speed response of the DCIM with digital PI controller are given. The voltage oscillations during startup of the line-side converter are due to chosen PI parameters which makes the controller slower. Also, since the magnitude of the command currents are limited to 7.5A as described in Section 3.6.1, the response of the line-side converter is slower. The dc link voltage oscillations when the DCIM is under load are smaller than the oscillations when the machine is operating at no-load. The voltage and current waveforms on the ac line of the line-side converter are given in Figure 3.20 when the machine is operating as motor at steady-state. It can be seen that the converter operates as rectifier at unity power factor for motor operation of the DCIM. In Figure 3.21, the dc link voltage and speed responses of the DCIM are given, with a fuzzy PI controller employed on the line-side converter. The fuzzy controller gives a similar transient response to that of PI

controller, but its response is slightly faster and the magnitude of the voltage oscillations is considerably reduced. In Figure 3.22, the voltage and current waveforms on the ac line of the line-side converter are shown for rectifier operation at steady-state and when a fuzzy controller is employed on the line-side converter.

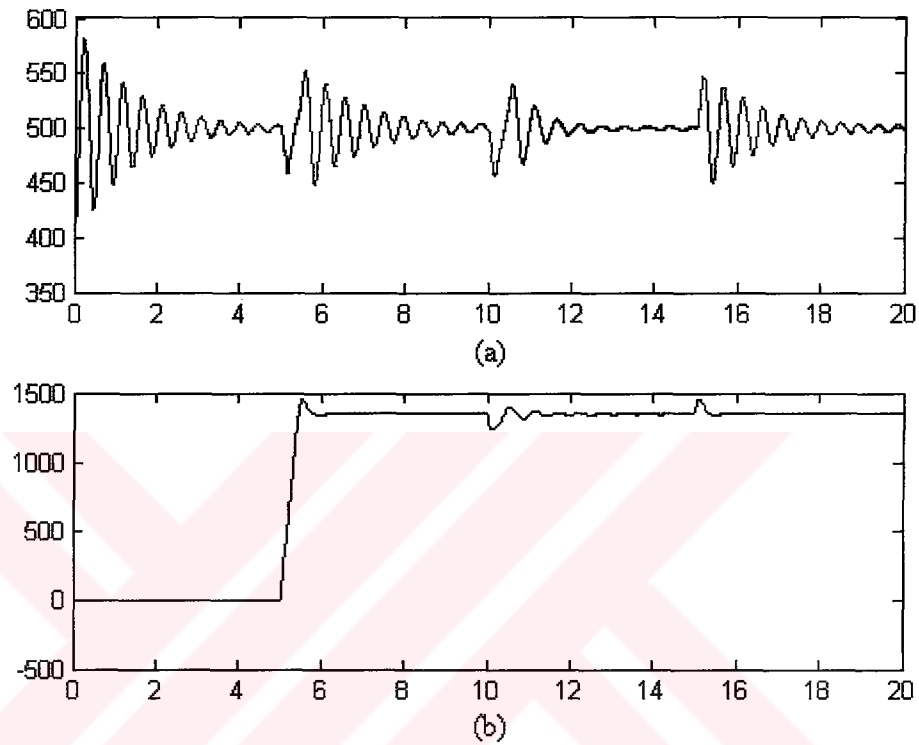


Figure 3.19 Simulation results for motor operation with digital PI controller on the line-side converter (a) dc link voltage (V) (b) rotor speed (rpm)

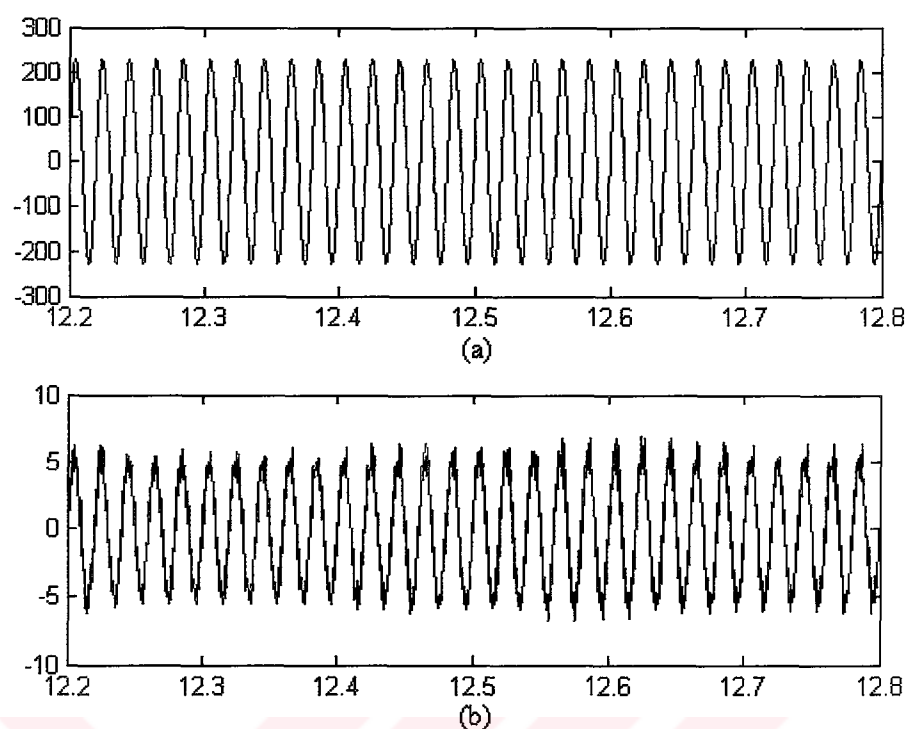


Figure 3.20 Simulation results for rectifier operation of the line-side converter at steady-state with digital PI controller (a) ac line voltage (V) (b) ac line current (A)

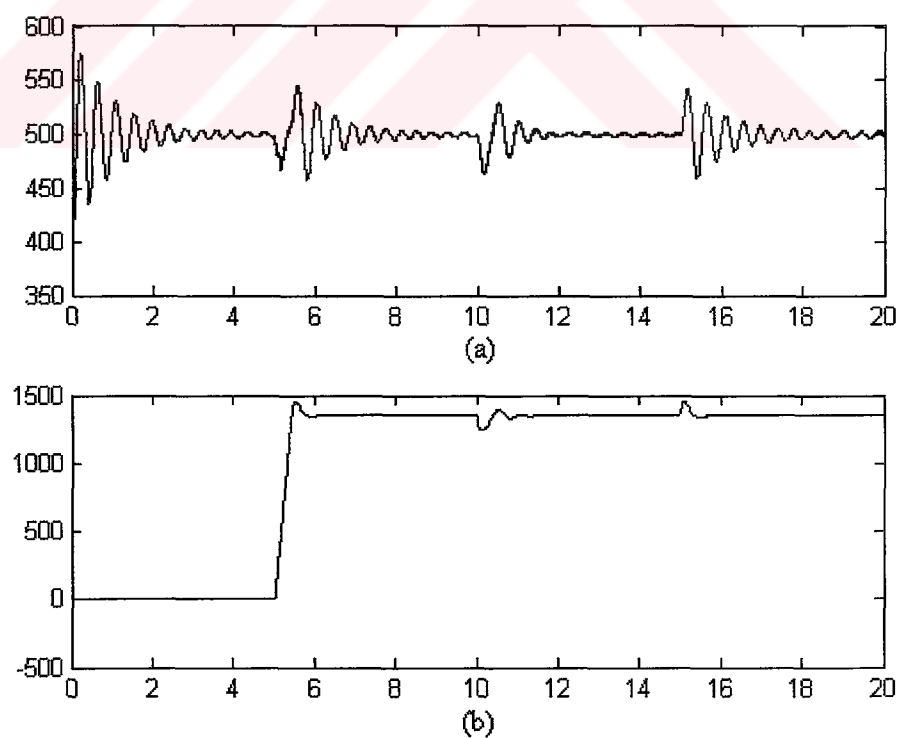


Figure 3.21 Simulation results for motor operation with fuzzy controller on the line-side converter (a) dc link voltage (V) (b) rotor speed (rpm)

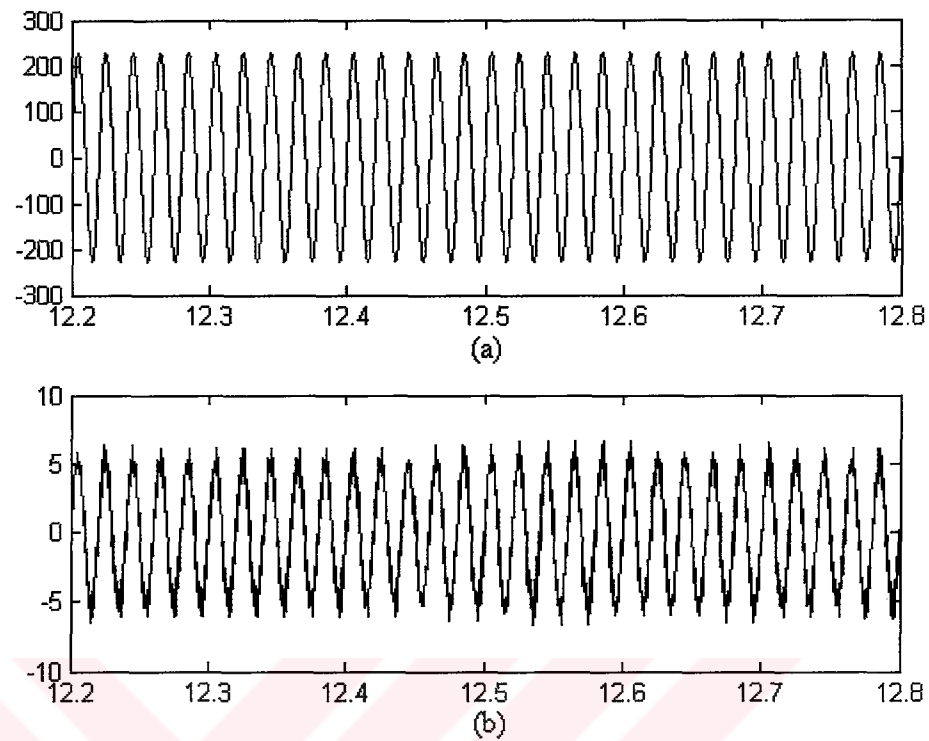


Figure 3.22 Simulation results for rectifier operation of the line-side converter at steady-state with fuzzy controller (a) ac line voltage (V) (b) ac line current (A)

3.6.4.2 Generator Operation

At the generator operation, a similar operating procedure is followed as described in the motoring case. A step shaft torque of -8Nm is applied to the DCIM during 10-15s and then the input torque is removed.

In Figure 3.23, the dc link voltage and speed response of the DCIM are shown with digital PI controller. The voltage and current waveforms on the ac line of the line-side converter are given in Figure 3.24 when the machine is operating as generator at steady-state. Figure 3.25 shows the dc link voltage and speed responses with fuzzy controller employed on the line-side converter, while Figure 3.26 shows the voltage and current waveforms on the ac line at steady-state.

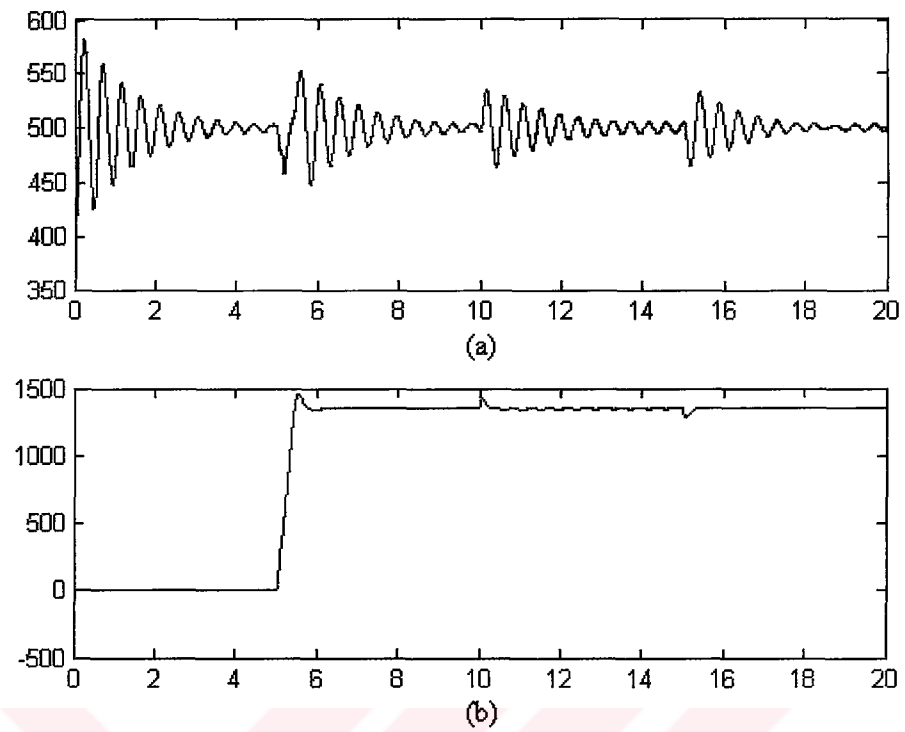


Figure 3.23 Simulation results for generator operation with digital PI controller on the line-side converter (a) dc link voltage (V) (b) rotor speed (rpm)

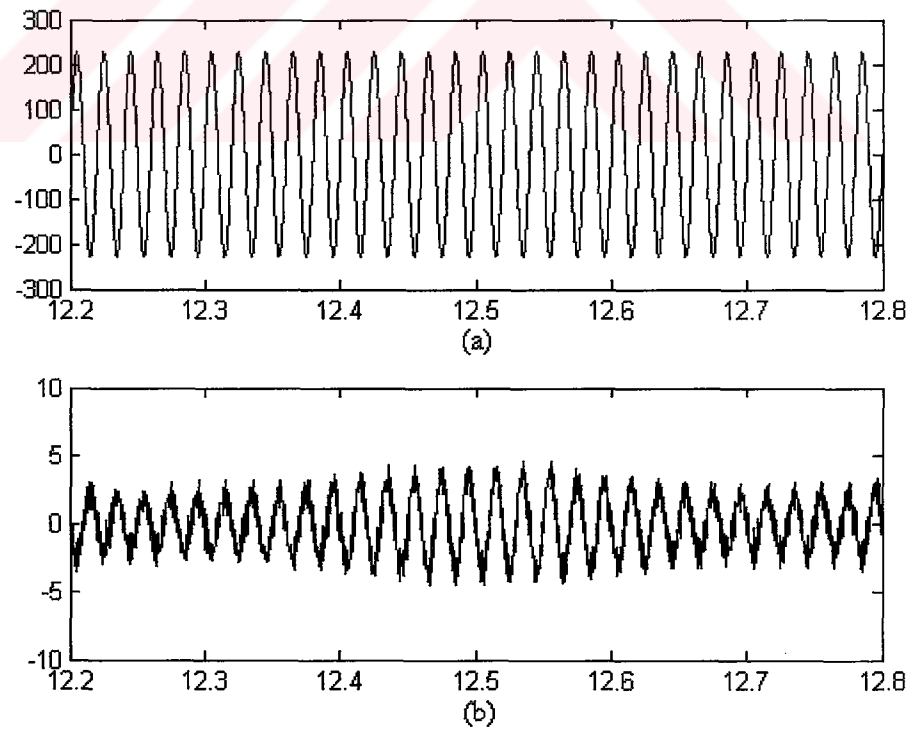


Figure 3.24 Simulation results for regenerative operation of the line-side converter at steady-state with digital PI controller (a) ac line voltage (V) (b) ac line current (A)

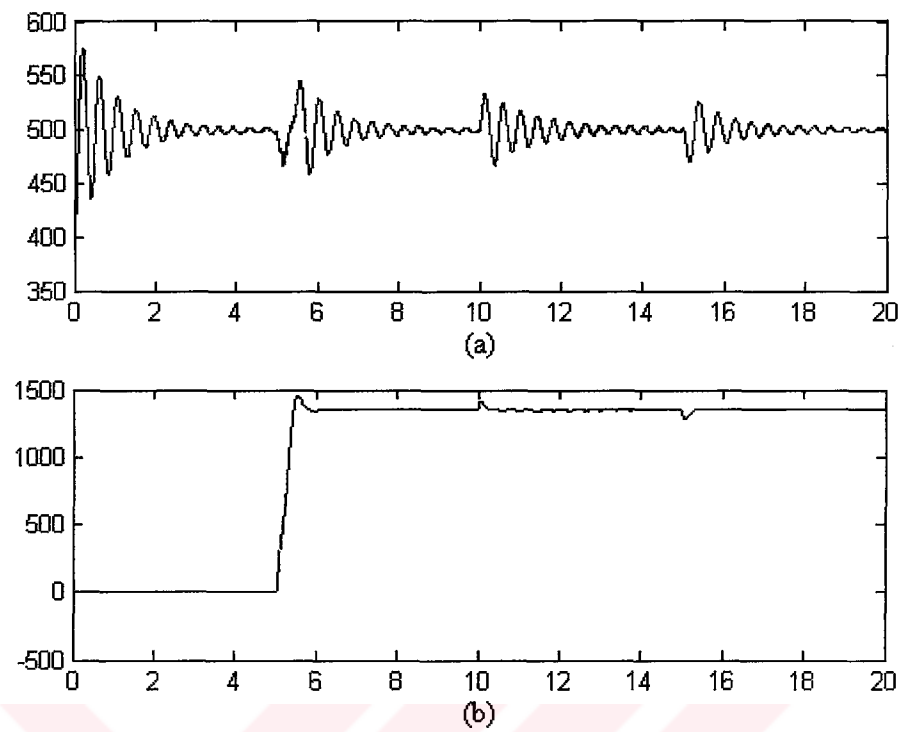


Figure 3.25 Simulation results for generator operation with fuzzy controller on the line-side converter (a) dc link voltage (V) (b) rotor speed (rpm)

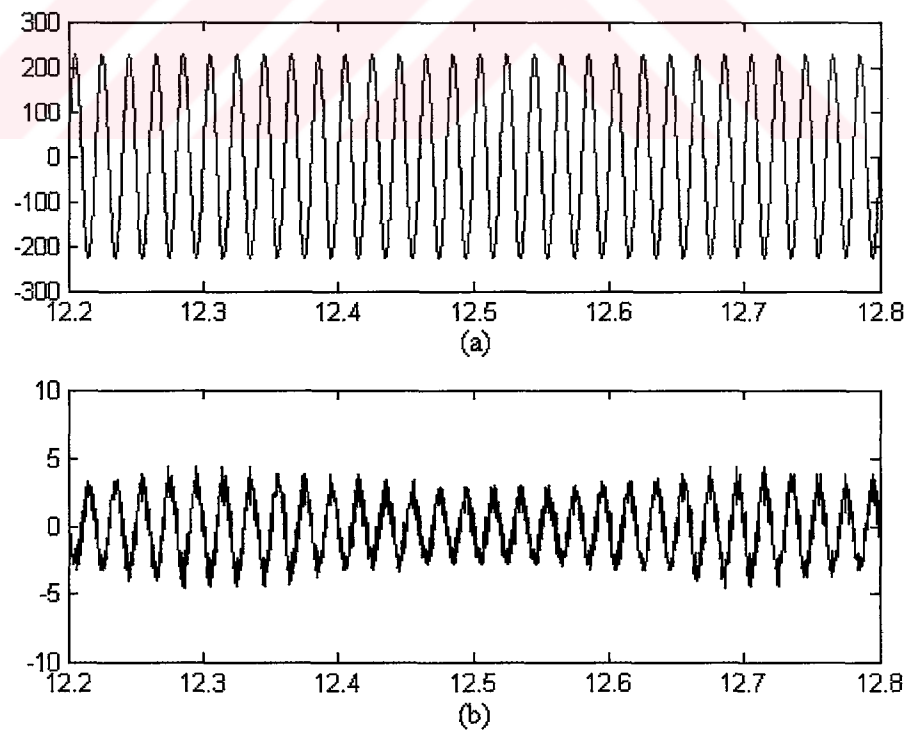


Figure 3.26 Simulation results for regenerative operation of the line-side converter at steady-state with fuzzy controller (a) ac line voltage (V) (b) ac line current (A)

CHAPTER FOUR

IMPLEMENTATION OF PWM CONVERTERS IN INDUCTION MACHINE DRIVE

The proposed drive system has been designed and implemented in laboratory in order to employ it in 2.5 kW wind energy conversion system. The complete block diagram of the designed drive system is given in Figure 4.1. The system consists of two back to back PWM converters that are connected between the stator of double-cage induction machine (DCIM) and the utility grid, TMS320F240 digital signal processor (DSP) that performs the control of the drive system, and other electronic circuitry. At the power converter stages, two 6MBP75RA120 FUJI insulated gate bipolar transistor (IGBT) intelligent power modules (IPMs) were used. Each IPM contains 6-pack IGBT, which are rated at 1200V, 75A and provided with internal gate drive and protection circuitry. Details of specifications on IPMs can be found in Appendix C.

Control of the complete system has been performed using a single TMS32F240 16-bit fixed-point digital signal processor (DSP) evaluation module board (EVM). The DSP has TMS320C2XX CPU core with 50ns instruction cycle time, 16K words on-chip flash memory, dual 10-bit on-chip analog to digital converter with multiplexed 16 channels and minimum conversion time of 6.6microseconds, PLL, Watchdog Timer, SCI, SPI, 28 multiplexed multi-functioning I/O ports, and Event Manager with 12 PWM/compare outputs and 3 general purpose timers having the feature of programmable PWM generation with adjustable dead-band, which is especially suitable for digital motor control applications. Also, it has the power drive protection circuitry, which allows the designer to introduce additional protection for

power converters in case any fault occurs. The software for controlling the complete system was developed using C compiler provided by Texas Instruments.

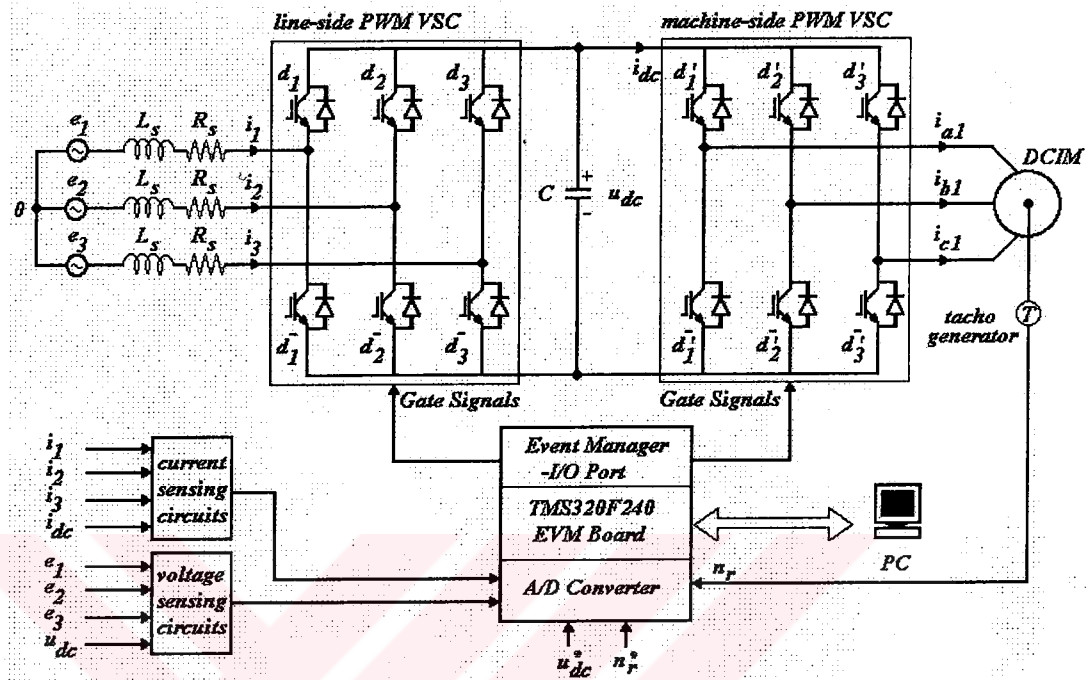


Figure 4.1 Block diagram of the implemented drive system

In the following, the rest of the electronic circuitry used in the drive system will be explained. These are gate drive interface, circuit for current and voltage sensing, speed feedback, and power supplies.

4.1 Gate Drive Interface

The gating signals of IGBTs are passed through the optocoupler drive interfaces. HCPL4504 high speed optocouplers have been employed for each IGBT of IPMs to isolate the control signals from the power stages. The circuit scheme of a single opto drive interface is shown in Figure 4.2. The gate signals are generated by TMS320F240 DSP EVM and passed through a buffer circuit using TL072 opamp in order to prevent overheating of DSP because of the currents drawn by the photo diodes (approximately 10mA for each).

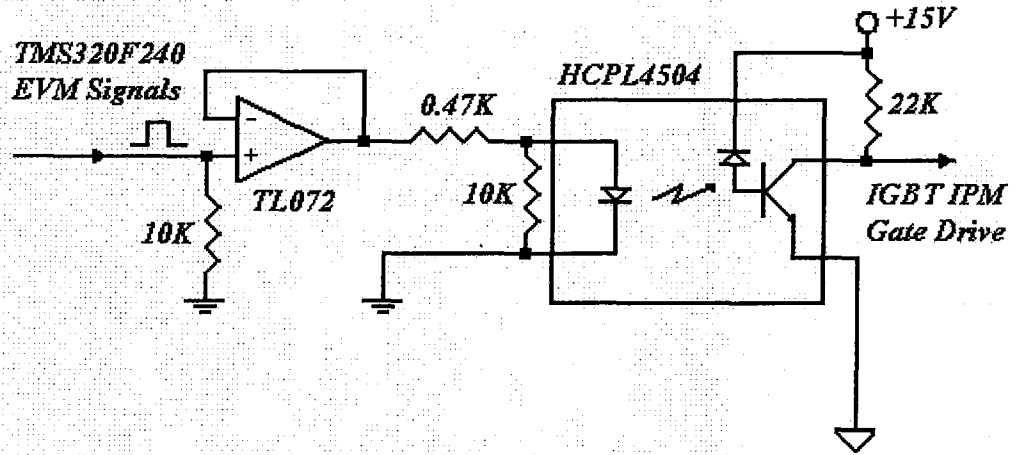


Figure 4.2 Optocoupler drive interface for gating signals of IGBTs

4.2 Voltage and Current Sensing Circuits

In order to obtain the feedback signals to the controller, hall-effect voltage and current sensors are used at ac line and dc link. Sensed signals are suited at 0-5V range for A/D converter inputs of the DSP. In Figure 4.3 and Figure 4.4, the circuits for voltage and current sensing are shown, respectively. The operation of the sensors relies on hall-effect principle (LEM, 1996). For the voltage measurement, the voltage sensor LV25-P requires a primary current (I_P) from the voltage terminals. Hence, a primary resistor with an appropriate watt (RP) should be introduced at the high voltage side of the sensor. The output of the voltage sensor should be terminated with a measurement resistor (R_M). The instantaneous voltage at the output of the sensor (V_M) is determined by the current transfer ratio (2500/1000 for LV25-P) and the measurement resistor as follows:

$$V_M = I_M R_M = \frac{2500}{1000} I_P R_M = \frac{2500}{1000} \frac{V_P}{R_P} R_M \quad (4.1)$$

Hence, the voltage turns ratio can be calculated from equation (4.1). With the gain of the additional amplifier circuit introduced, this ratio is adjusted to 160V:1V in the implemented system. For ac supply voltage measurement, a 2.5V offset is

introduced, but this offset is not necessary for the dc link voltage since it is unidirectional.

The hall-effect current sensors (LTA100P) have the instantaneous voltage output with the ratio of 100A/5V. This ratio is decreased in the physical system by introducing additional 10 turns around the measurement hole of the current sensor. Considering the gain of the amplifier circuit used in current sensing, the overall turns ratio is adjusted to 250mV/A. For both ac supply and dc link current measurements, a 2.5V offset is introduced in order to form the signals for A/D converter input of DSP.

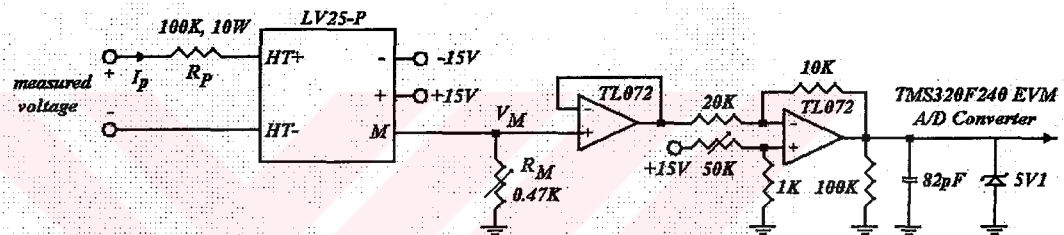


Figure 4.3 Voltage sensing circuit

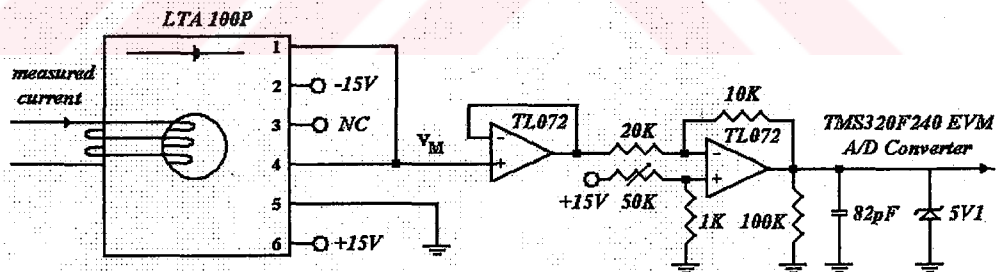


Figure 4.4 Current sensing circuit

4.3 Speed Feedback

A permanent magnet tachogenerator is used to provide the speed feedback. The output of the tachogenerator is passed through a first order low-pass passive filter in order to eliminate the measurement noise. The circuit for speed sensing is given in Figure 4.5. The ratio for speed measurement is adjusted to 1V/375rpm in the system.

Hence, the allowed speed range of the DCIM is chosen to be 0-1875rpm according the A/D signal level of DSP.

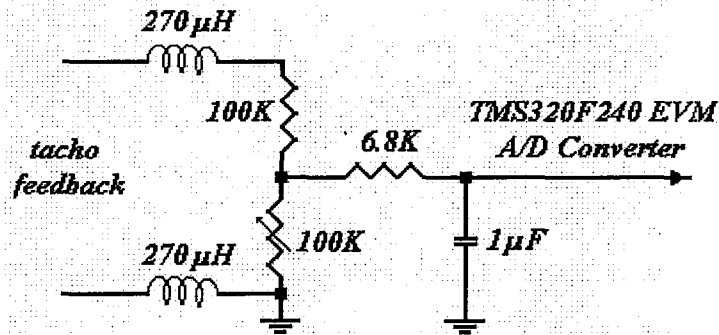


Figure 4.5 Filter circuit for tachometer feedback signal

4.4 Power Supply Circuits

Isolated power supplies are used in above electronic circuits. Transducers, optocoupler interface and gate drive circuits require $\pm 15V$ supplies. In these power supply circuits, 7815 and 7915 fixed voltage regulators are employed as shown in Figure 4.6.

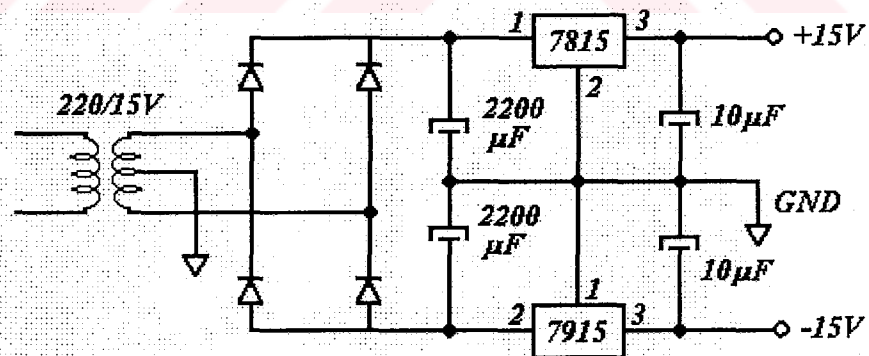


Figure 4.6 Power supply circuit

4.5 Experimental Setup

In experiments, a 3-phase, 380V, 50Hz, 4-pole double-cage induction machine, which is analyzed in details in Chapter 2, was used. In laboratory experiments, the

machine was controlled in motoring and generating mode of operation by a Ward-Leonard system, which consists of two back to back connected DC machines and is shown in Figure 4.7. The load torque on the shaft of the DCIM is adjusted via Ward-Leonard system. Hence, bidirectional power flow through the DCIM is achieved. The line-side converter was connected to the ac source at a voltage level of 280V (line to line) and the dc link voltage at the output of the converter was set to 500V.

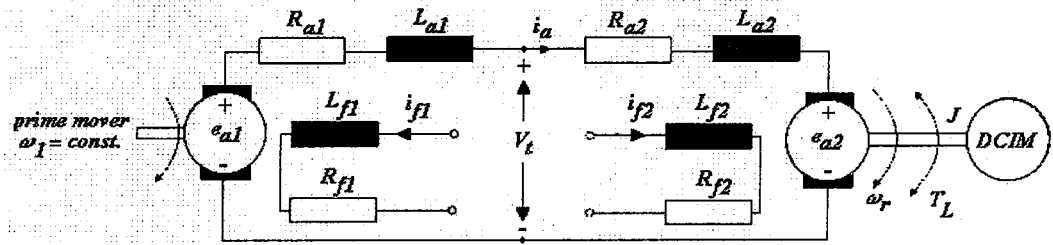


Figure 4.7 Ward-Leonard system

In the Ward-Leonard system, the armature emfs of the DC machines are (Ersak & Ermiş, 1997)

$$e_{a1} = K_1 \phi_1 \omega_1 = K'_1 i_{f1} \omega_1 \quad (4.2)$$

$$e_{a2} = K_2 \phi_2 \omega_r = K'_2 i_{f2} \omega_r \quad (4.3)$$

During steady-state condition, the difference between the armature emfs of the DC machines is equal to the total voltage drop on armature resistances as follows:

$$e_{a1} - e_{a2} = i_a (r_{a1} + r_{a2}) \quad (4.4)$$

The armature current is

$$i_a = \frac{K'_1 i_{f1} \omega_1 - K'_2 i_{f2} \omega_r}{r_{a1} + r_{a2}} \quad (4.5)$$

Hence, the load torque developed on the shaft coupled to the DCIM is expressed as

$$T_L = K_2' i_{f2} i_a = \frac{K_1' K_2' \omega_1 i_{f2}}{r_{a1} + r_{a2}} i_{f1} - \frac{K_2'^2 i_{f2}^2}{r_{a1} + r_{a2}} \omega_r \quad (4.6)$$

If i_{f2} is kept constant, then linearly varying load torque-speed characteristics are obtained as follows:

$$T_L = A i_{f1} - B \omega_r \quad (4.7)$$

4.6 Software Programming

The flowchart of the complete software program is given in Figure 4.8. The control software for TMS320F240 DSP was developed on Code Composer environment provided by Texas Instruments. Code Composer software is provided with C compiler, assembler, linker, and debugging tools, which are useful in developing programs for Texas DSPs. The project workspace includes 2 assembler source files (boot.asm and vectors.asm) for booting procedure and definition of interrupt vector locations, respectively. The run-time support object library (rts2xx.lib) contains the features of ANSI C, low-level support functions, intrinsic arithmetic routines, system startup routine etc. The header files (adc.h, c240app.h, pwm.h, and tst_main.h) contains the definitions and register addresses for A/D converter operation, PWM operation, peripheral register declarations, macro definitions, and other useful definitions. The linker command file (asd240.cmd) defines the memory mapping, which is necessary for vector, program memory, and data memory locations. The rest of the project is included with C source files developed for the control software. The project workspace on Code Composer environment is given in Appendix C.

At startup of the program, the variables needed for system control are initialized in a subroutine (initvars.c), such as sine table, initial values of control parameters for

the power circuitry, and essential definitions for PWM generation. Also, the wait-state generator, interrupts, and event manager setup are configured at startup.

The control logic of converter circuits and maximum power point tracking (MPPT) operation are depicted in subroutines in the flowchart. In the main program (asd240.c), the control, reference, and feedback signals are read through the A/D converter via a C subroutine (adc.c) and appropriate program subroutine for each power converter is called. The operation of line-side converter, machine-side converter, and MPPT are controlled via external switches, each determines the appropriate program routine to be executed. DC link and speed reference signal are generated externally and input to the A/D converter of DSP. In addition, the setting of DIP switches (DS1-8) on the EVM board determines whether the speed reference is controlled externally or it is determined internally for maximum power point operation.

In hysteresis current control subroutine (hcc.c), six I/O ports are used to generate gate signals of line-side converter according to the switching logic as mentioned in previous chapters. Sufficient dead-time between the two gate signals of each leg is introduced in order to prevent simultaneous conduction of IGBTs at the line-side converter. Also, the closed-loop control of dc link voltage is performed in this program routine.

4.6.1 Sinusoidal PWM Waveform Generation

Two synchronized timers are used in the C program (ev_pwm.c) to generate PWM signals for voltage source inverter, one is to provide the desired PWM frequency and the other is to generate an interrupt to update the PWM registers. The reason for using two timers is that the locations of power drive protection interrupt and Timer 1, which is used for PWM generation, are defined in the same global interrupt service routine. Hence, synchronizing Timer 2 with Timer 1 and enabling only Timer 2 interrupt, different interrupt service locations are used.

In order to generate a sine wave at desired frequency and amplitude for PWM switching, a lookup table is used, which is generated at startup. First, the command frequency of the inverter is calculated by the subroutine that performs closed-loop speed control operation. Here, it must be noted that the closed-loop speed control subroutine is called once after 128 cycles of program, so the sampling rate of the speed feedback is reduced, because one complete program cycle is too small (approximately 250 microseconds) with respect to mechanical time constant of the system. During the 128 cycle of the program, the average of speed of the machine is calculated and at the end of the cycle, the inverter command frequency is calculated through PI controller. The PWM registers are updated with sine values quickly after one PWM period ends. By the meantime, the incoming timer interrupt subroutine is called at the end of the PWM period and this subroutine provides the sine values for next PWM period. The step size to be taken on the sine table determines the frequency of the inverter. Two 16-bit registers are used to perform sine wave generation based on the method described in (DSP Solutions, 1999). One counter register accumulates the step-size (also the command frequency of the inverter) to determine the location of next sine value, the other register is the sine table pointer, which extracts the sine value from its location. The sine table has 1024 entries, so the upper 10 bits of the counter register determines the location of the next sine value. The upper 10 bits of counter register are loaded into table sine pointer, simply by bitwise shift operation, so the information in counter register is preserved. When the counter register overflows, one complete sine cycle is completed. In that way, the frequency of sine wave is determined by the following formula:

$$f = \frac{step}{T_{PWM} * 2^{16}} \quad (4.8)$$

For the PWM frequency of 2 kHz and step value (or the command frequency) ranging from 0 to 1638, the motor frequency is adjusted from 0 to 50Hz. Also, the modulation index is linearly changed from 0.128 to 0.96 within this range of frequency and kept constant at 0.96 above 50Hz.

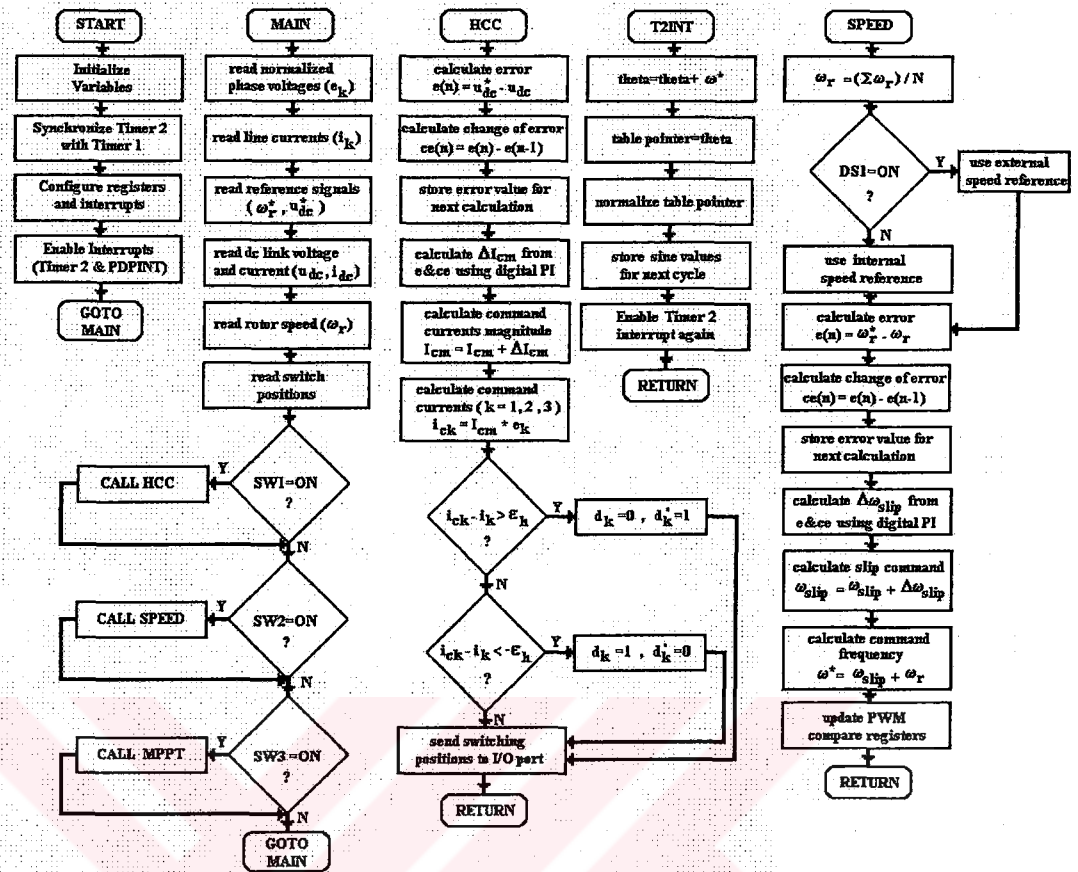


Figure 4.8 Flow-chart of the developed control software

4.6.2 Maximum Power Point Tracking Routine

In MPPT routine, the electrical power is measured via dc link voltage and current, and averaged over 4096 cycles of the program. The speed reference is increased or decreased after each 4096 cycles of the program by a small amount of change (18.75rpm) depending on the changes in electrical power and rotor speed (Altaş & Sharaf, 1996). The flowchart of MPPT routine is given in Figure 4.9.

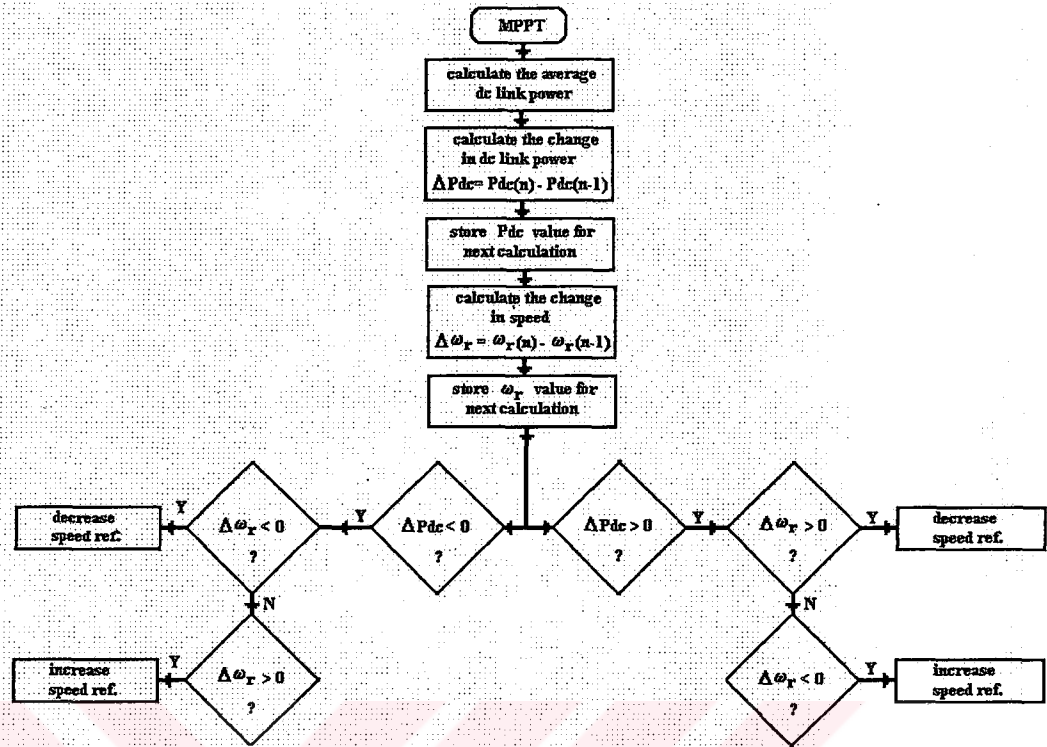


Figure 4.9 MPPT algorithm

4.7 Simulation and Experimental Results

Experiments are performed on DCIM and proposed drive system. Ward-Leonard system is used for adjusting the shaft torque of DCIM in both modes as mentioned before. When 280V line-to-line, 3-phase voltage is applied to the input of PWM line-side converter, the dc link capacitance is charged to peak value of line to line voltage through the anti-parallel diodes of IGBTs. In order to limit charging current of capacitor at startup, a resistance of 470 ohms is connected in series with the capacitor at the output of rectifier and after the capacitor is fully charged, the resistance is bypassed. The switching signals of the line-side converter are applied and the dc link voltage is boosted to its reference value of 500V. The circuit and control parameters of the line-side converter are given in Section 3.6 and Section 3.6.2

The drive system is tested for the motor and generator operations of the induction machine. The machine and speed control parameters are given in Section 2.7.3, Section 2.8, and Section 3.6.3. Experiments are performed at three stages.

- 1) No-load free acceleration test
- 2) Load test for motor and generator operation of the DCIM
- 3) Maximum power point tracking

In the following, the experimental results are given and compared to simulation results. The simulation study of the drive system is performed using MATLAB Simulink models, which are given in Appendix B. The instrumentation gains for system simulation were given in Section 3.6.1.

4.7.1 No-load operation as motor

After the dc link voltage is stabilized at 500 V, the inverter switching signals are applied and the rotor speed is accelerated to its reference value of 1350 rpm from standstill under no-load. Figure 4.10 shows the records of the experimental results of dc link voltage and rotor speed during free acceleration, while Figure 4.11 shows the simulation results of these variables. The voltage response of the line-side converter is slow, which causes a transient voltage oscillation after the overshoot of the speed.

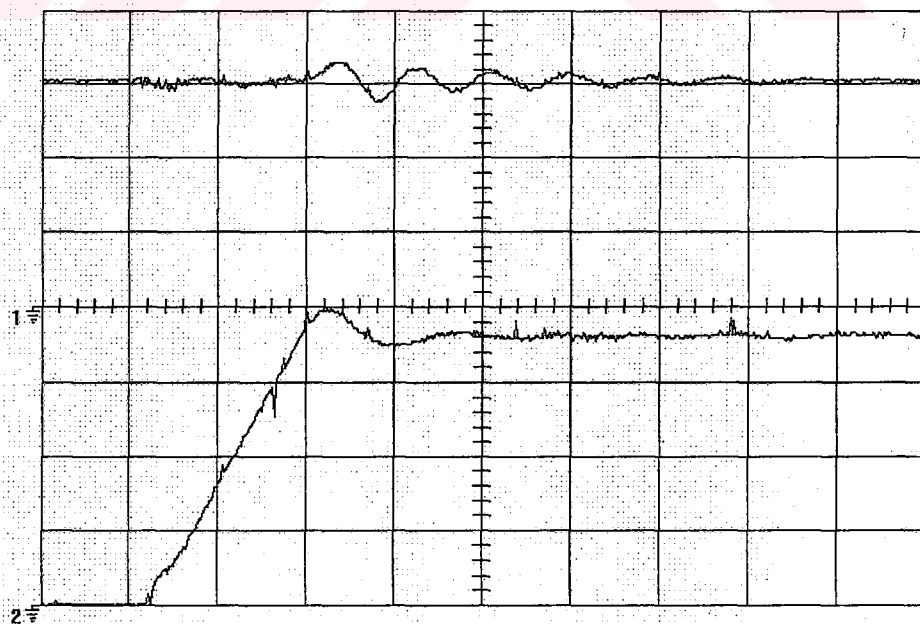


Figure 4.10 Experimental results during free acceleration of DCIM (upper trace: dc link voltage-160V/div, lower trace: rotor speed-375rpm/div, time/div: 0.5s)

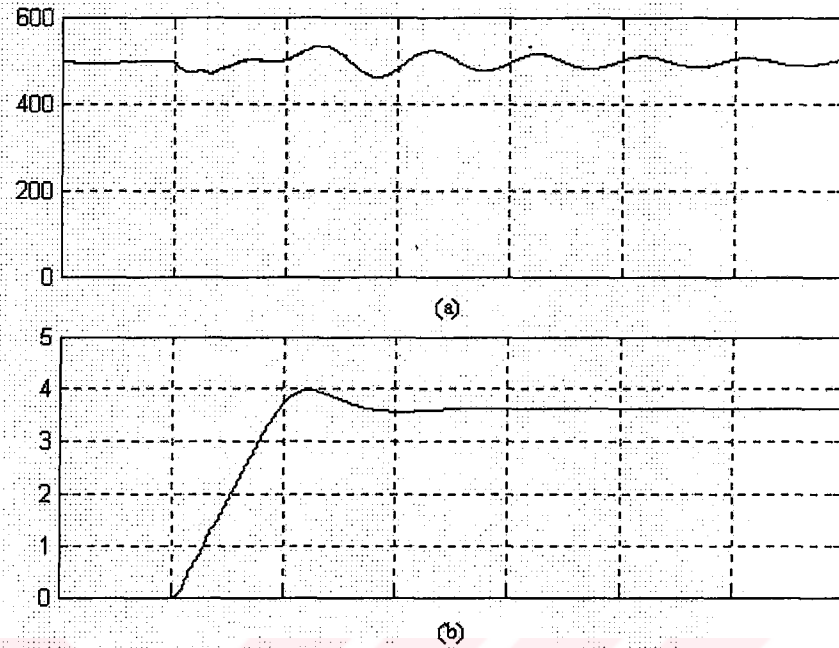


Figure 4.11 Simulation results during free acceleration of DCIM (a) dc link voltage, (b) rotor speed-375rpm/div, time/div: 0.5s

4.7.2 Load Tests

The stator terminals of the motor are energized via inverter after detecting rotor speed from the output of tacho-generator driven by the prime mover (Ward-Leonard system) and setting the reference frequency of the inverter to this rotor speed in electrical radian per second. Therefore, the induction motor is connected to the supply under zero torque developed at synchronous speed. It should be noted that this zero torque is expected to be obtained at steady-state, if the rotor rotates at synchronous speed. But during the closing time of three phase motor terminals to the 3-phase voltage source, the electromagnetic torque developed by the machine is not zero, and some amount of torque and current transients are expected. These records from the experiments and simulation results are given in Figure 4.12 and Figure 4.13. A significant negative deep of electromagnetic torque given in Figure 4.13 can be reduced by applying reduced terminal voltage to motor via inverter. In this study, the rotor speed is read from the output of tacho-generator as 1350 rpm just before feeding power to the machine through inverter. After energizing machine terminals

and getting steady-state operation, the shaft torque is changed by the prime mover. The experimental results will be given for motor and generator operation below.

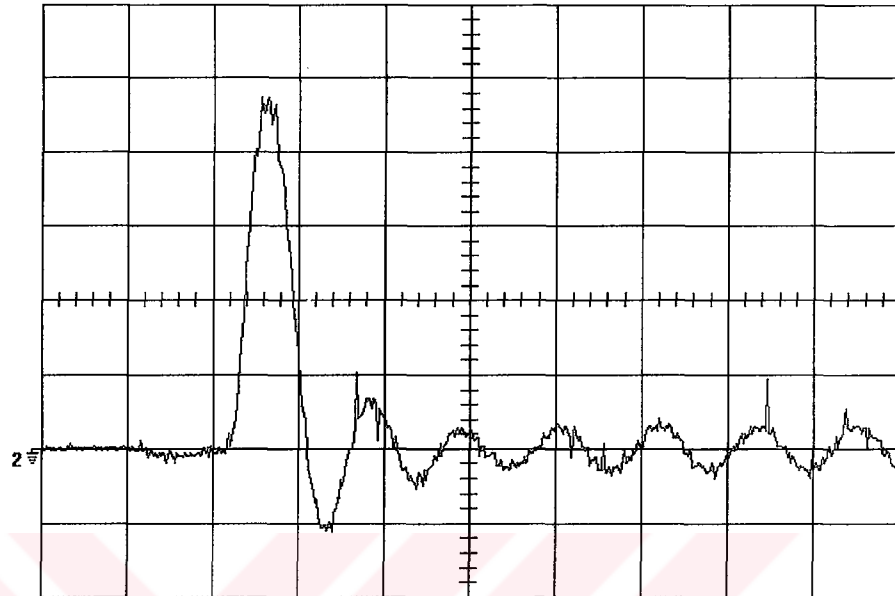


Figure 4.12 Machine phase current transient during closing at set rotor speed (trace- 5A/div, time/div: 20ms)

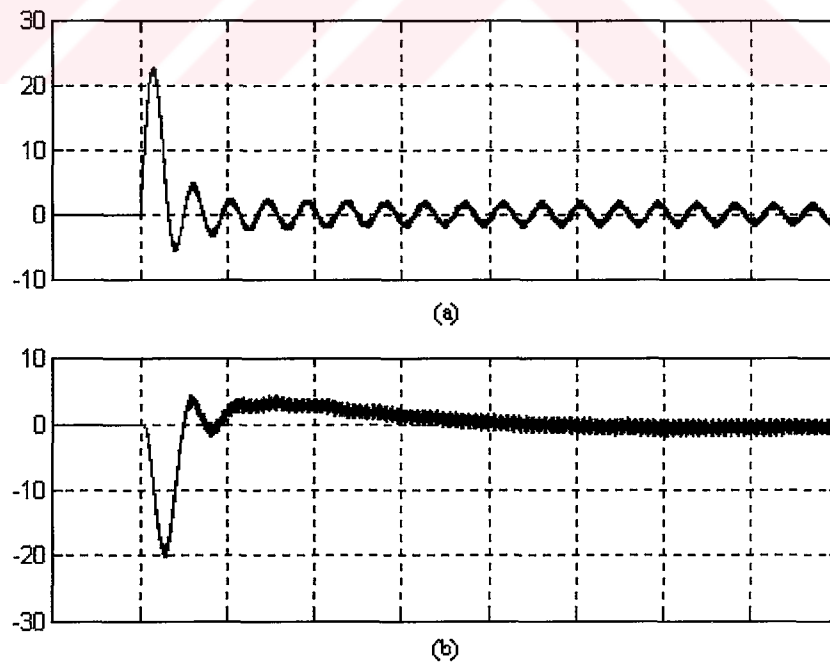


Figure 4.13 Simulation results of transient during closing at set rotor speed (a) machine phase current (A) (b) electromagnetic torque (Nm), time/div: 50ms

4.7.2.1 Motor Operation

Figure 4.14 shows the experimental results of motor line-to-line voltage and one phase current at steady-state. The measured value of the shaft torque was 10Nm and the rotor speed is set to 1350rpm. The stator phase current of the DCIM is approximately 6A under this loading condition at steady-state. The steady-state results obtained from computer simulation is given in Figure 4.15. The line-side converter input voltage and phase current are given in Figure 4.16. Three-phase, 280V line-to-line voltages have been applied to the converter by means of a variac. The peak value of the line currents is approximately 5A and the average electrical power drawn from the ac line was measured to be nearly 2kW. The simulation results for steady-state phase voltage and current are shown in Figure 4.17. In Figure 4.18 and Figure 4.19 simulation and experimental results of the dc link voltage and rotor speed under a step load change are shown, respectively. In experiments, while the machine is running as a motor, the shaft torque, 10Nm, was suddenly removed from the shaft, which is simulated as a step change of load torque in models.

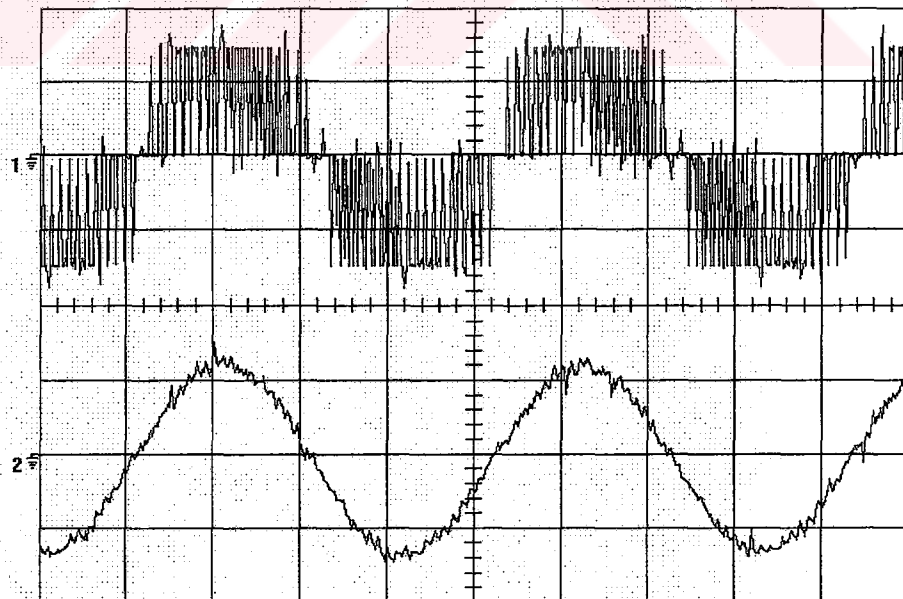


Figure 4.14 Motor operation at steady-state observed at motor load test (upper trace: line-to-line DCIM voltage-320V/div, lower trace: DCIM phase current: 5A/div, time/div: 5ms)

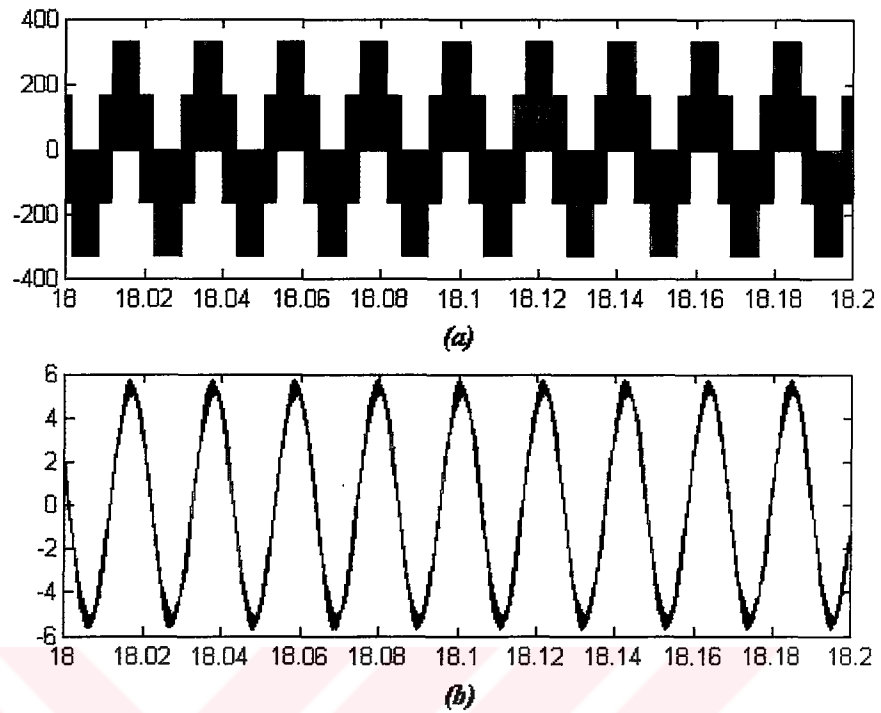


Figure 4.15 Simulation results for motor operation at steady-state (a) line-to-line voltage of DCIM (V), (b) DCIM phase current (A)

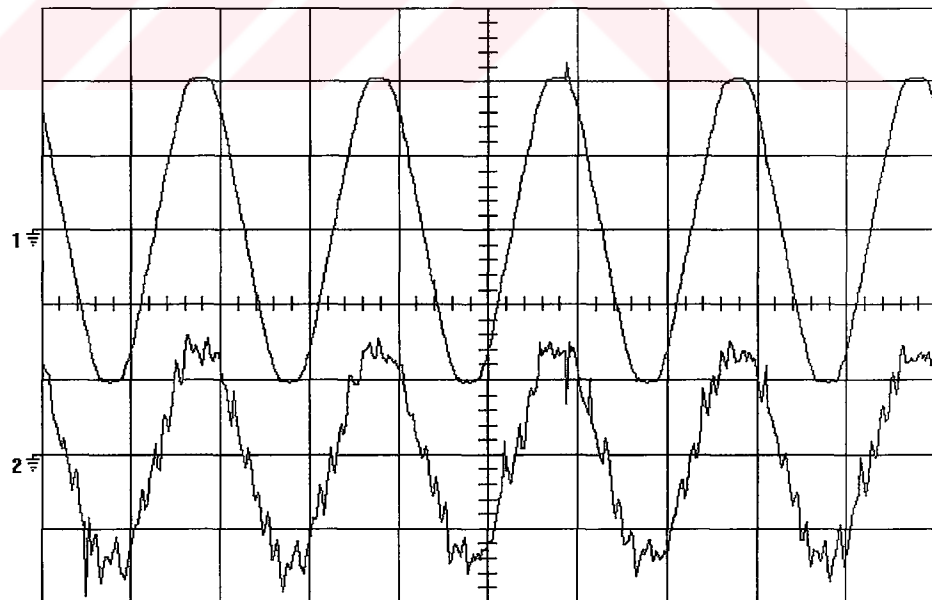


Figure 4.16 Rectifier operation of the line-side converter observed at motor load test (upper trace: phase voltage-110V/div, lower trace: phase current-4A/div, time/div: 10ms)

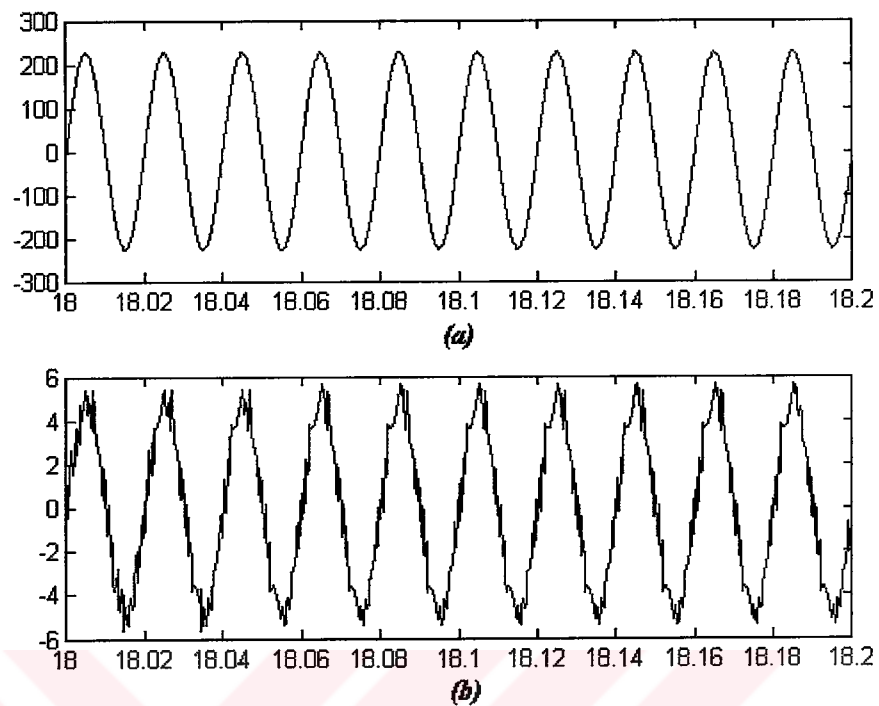


Figure 4.17 Simulation results for rectifier operation of the line-side converter (a) phase voltage (V) (b) phase current (A)

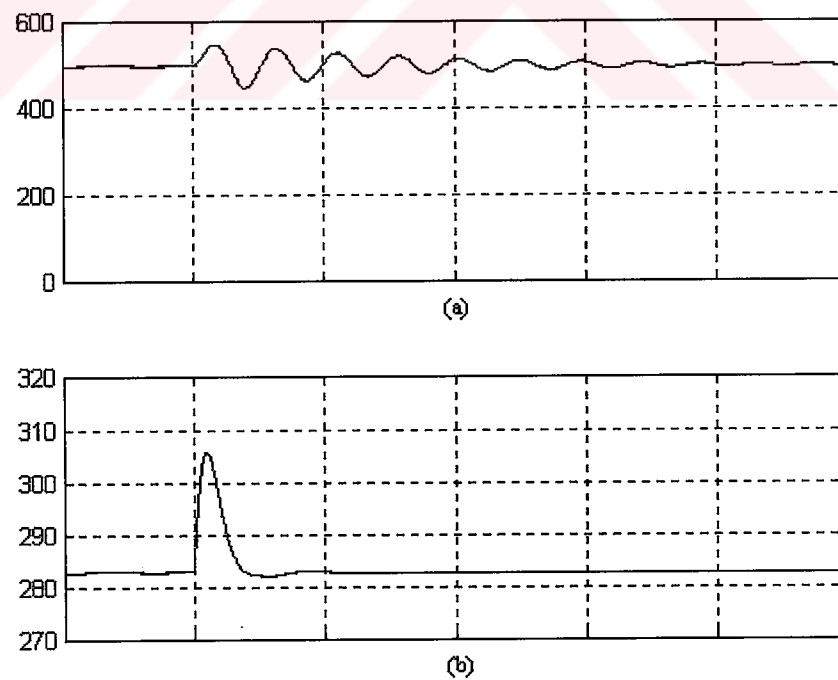


Figure 4.18 Simulation results for transient response under step load change for motoring operation (a) dc link voltage (V) (b) rotor speed (rpm), time/div: 1s

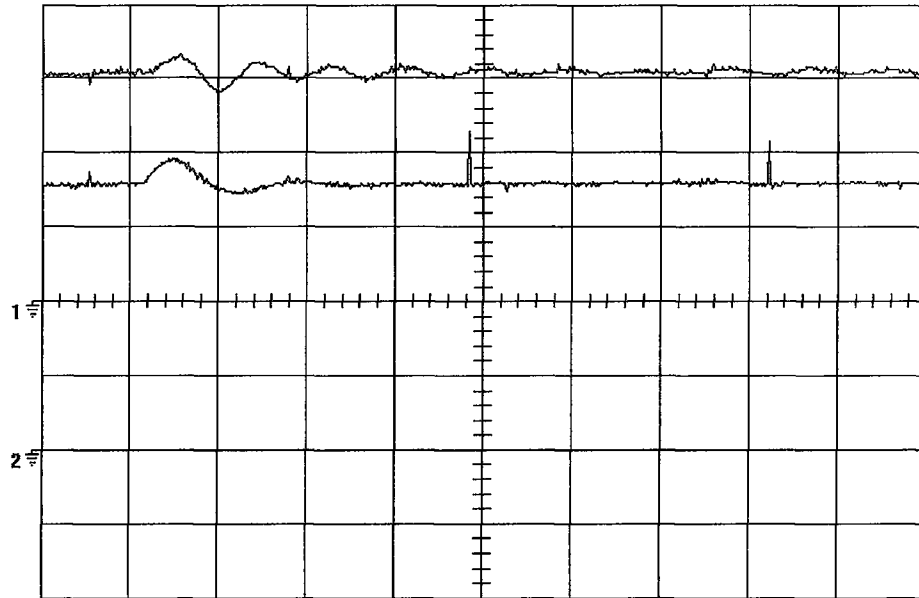


Figure 4.19 Experimental results under step load change for motoring operation (upper trace: dc link voltage-160V/div, lower trace: rotor speed-375rpm/div, time/div: 0.5s)

4.7.2.2 Generator operation

Figure 4.20 shows the line-to-line voltage and phase current of the DCIM at generator mode. The measured value of the shaft torque was -8Nm at 1350 rpm rotor speed, where minus sign indicates the reverse power flow. In Figure 4.21, computer simulation results are given for this operating condition of the drive system. In Figure 4.22, the phase voltage and current of the line-side converter are given for generator operation of the DCIM. The power delivered to the ac line was measured to be nearly 1kW. The simulation results of the line voltage and current are given in Figure 4.23. While the machine is running as a generator under the shaft torque of -8Nm, this load is removed. In Figure 4.24 and Figure 4.25 simulation and experimental results of the dc link voltage and rotor speed under a step input torque change in generator mode are shown, respectively.

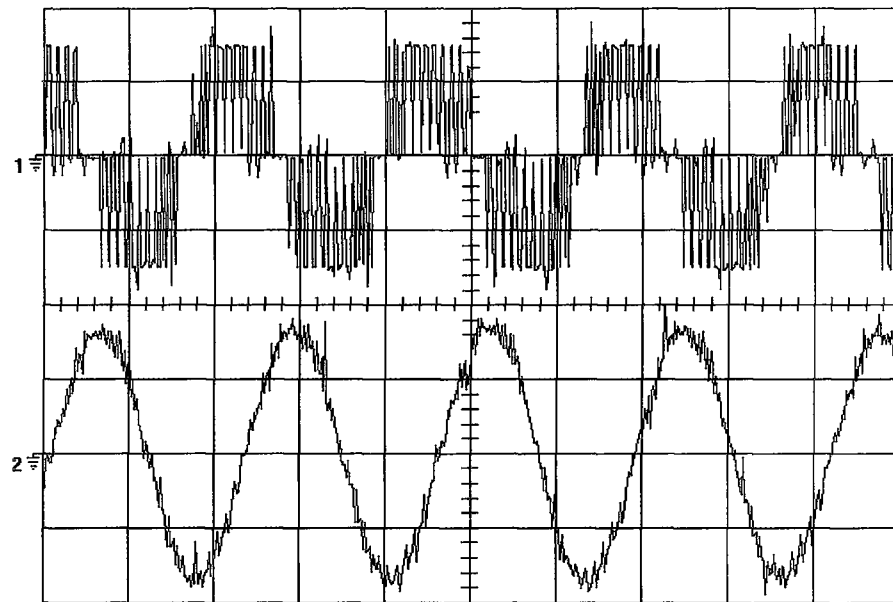


Figure 4.20 Generator operation at steady-state observed at generator load test (upper trace: DCIM line-to-line voltage-320V/div, lower trace DCIM phase current: 2A/div, time/div: 10ms)

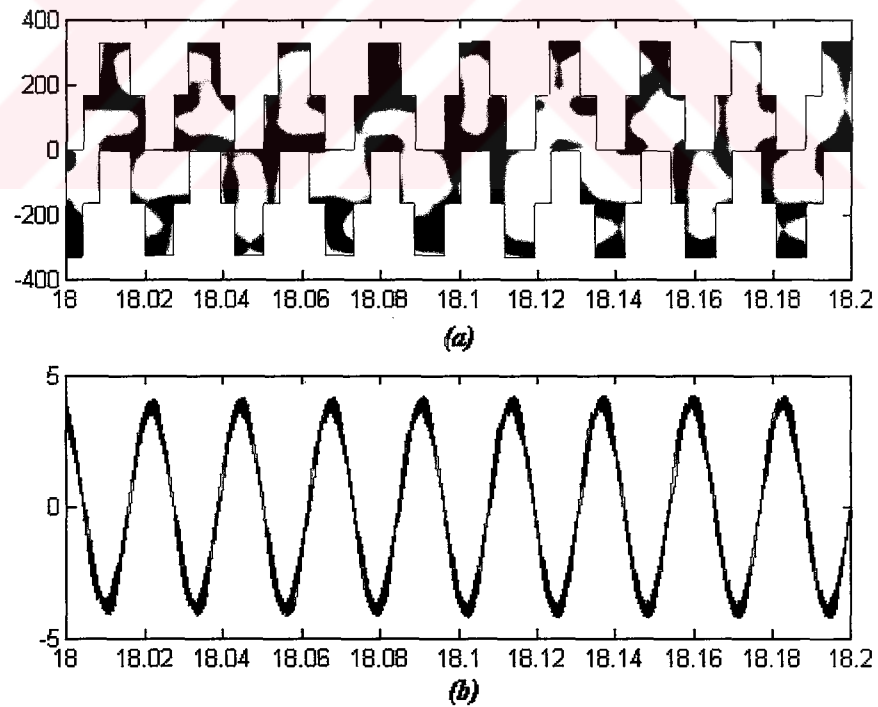


Figure 4.21 Simulation results for generator operation at steady-state (a) DCIM line-to-line voltage (V) (b) DCIM phase current (A)

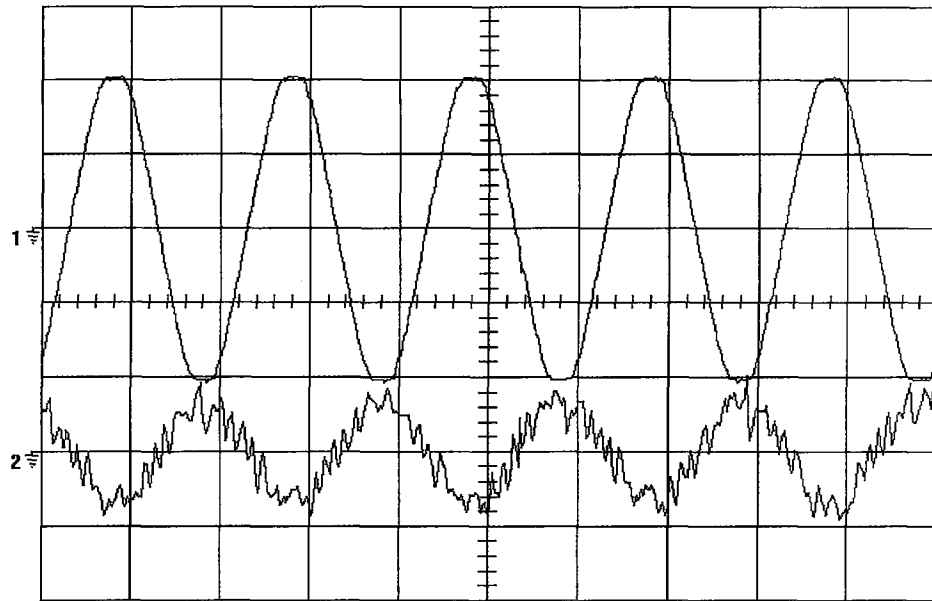


Figure 4.22 Regenerative operation of the line-side converter observed at generator load test (upper trace: phase voltage-110V/div, phase current-4A/div, time/div: 10ms)

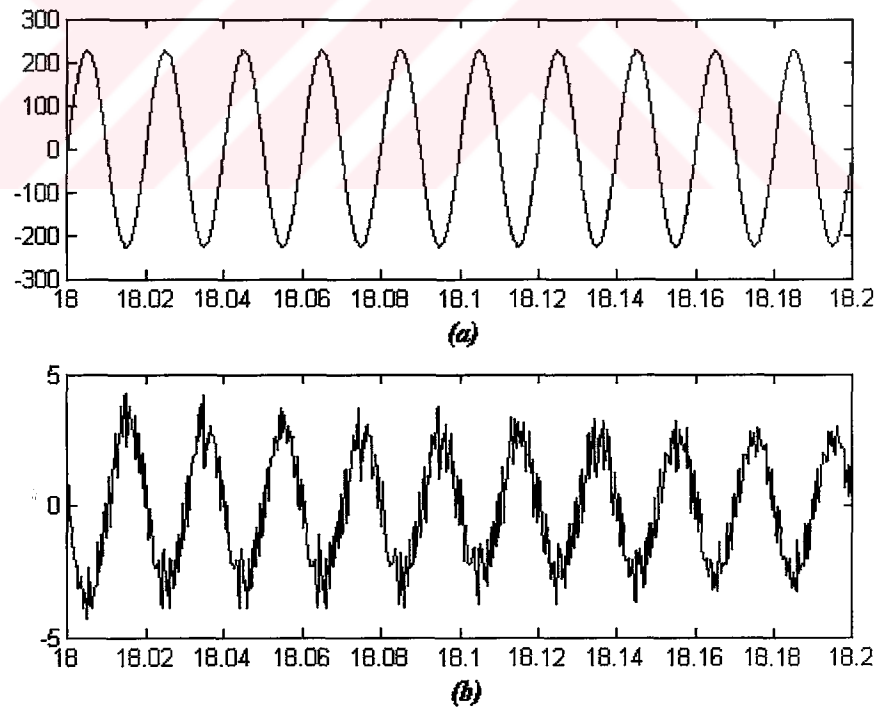


Figure 4.23 Simulation results for regenerative operation of the line-side converter
(a) DCIM phase voltage (V) (b) phase current (A)

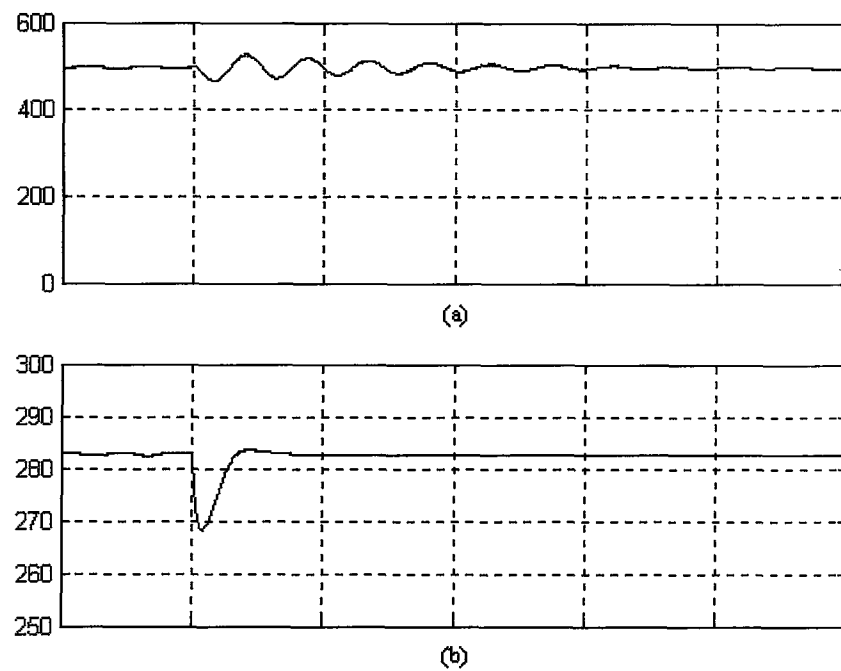


Figure 4.24 Simulation results for transient response under step load change for generator operation (a) dc link voltage (V) (b) rotor speed (rpm), time/div: 1s

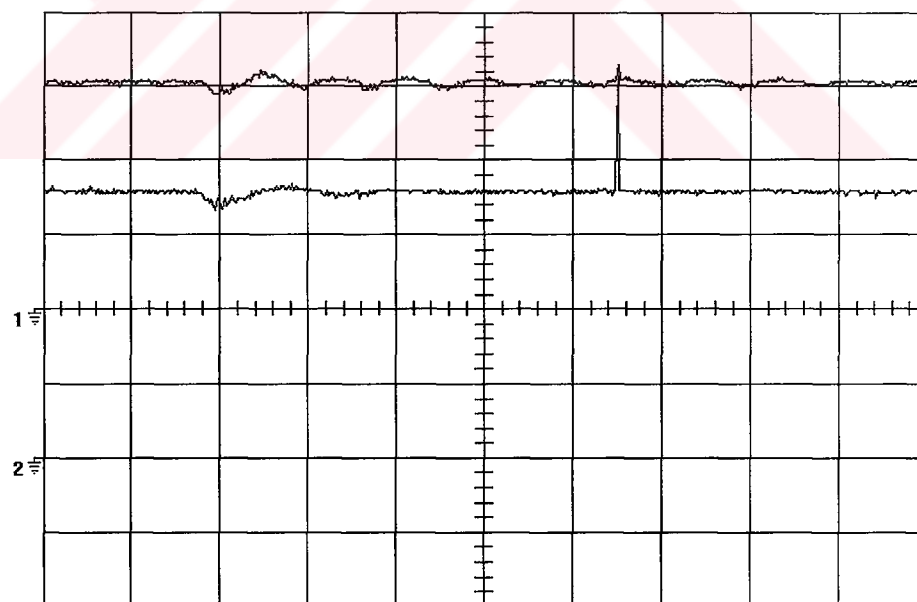


Figure 4.25 Experimental results under step load change for generator operation (upper trace: dc link voltage-160V/div, lower trace: rotor speed-375rpm/div, time/div: 0.5s)

4.7.3 Maximum Power Point Tracking Test

In order to extract maximum power from the wind turbine, a search algorithm was implemented in DSP. Before the algorithm starts, it is assumed the rotor of the DCIM is rotating at a speed (ω_r), determined by the speed reference (ω_r^*). To ensure that operation, first of all, the rotor of the DCIM is rotated by the prime mover. When the rotor speed reaches at a steady-state value, the four quadrant induction machine drive system is started in the procedure described in the previous section. The reference speed value is set to current value of rotational speed and the DCIM is energized via PWM inverter. At this point, the DCIM operates at no-load condition. When the maximum power tracking (MPPT) algorithm is started, the speed reference value is disturbed by a small amount of change ($\Delta\omega_r^*$). The electrical power is measured from the dc link, which is simply equal to

$$P_{dc} = \frac{1}{T} \int_0^T u_{dc} i_{dc} dt \quad (4.9)$$

The variation of the dc link power with respect to rotor speed is depicted in Figure 4.26. In this figure, the power-speed characteristic is obtained from a DC motor driven under constant field and armature voltage. The shaft of the DC motor is coupled to the DCIM in order to deliver power to the network via drive circuit. As it can be seen in the Figure 4.26, at speeds above maximum power point (1 and 2), the sign of the change of dc link power is the same as that of change of speed. Inversely, at speeds below maximum power point (3 and 4), the signs are opposite. In order to achieve the operation at maximum power point, the controller sets the change of speed reference ($\Delta\omega_r^*$) to a small negative value in cases 1 and 2; and to a small positive value in cases 3 and 4. Here, it must be noted that the average value of dc link power is negative for generator operation of the DCIM.

The experimental results of dc link voltage and rotor speed are given in Figure 4.27. Initially, the rotor is running at 820 rpm at no-load driven by the DC motor. When the DCIM is energized via four-quadrant drive, the rotor speed locked at this

value. After the MPPT algorithm is started, the drive system searches for the maximum power point. This is obtained at 477 rpm and the developed torque is measured to be 9 Nm. The variables measured are given in Table 4.1. Here, it is seen that increasing armature current reduces the applied terminal voltage to the DC motor. This causes the maximum power delivered by the DCIM reduce.

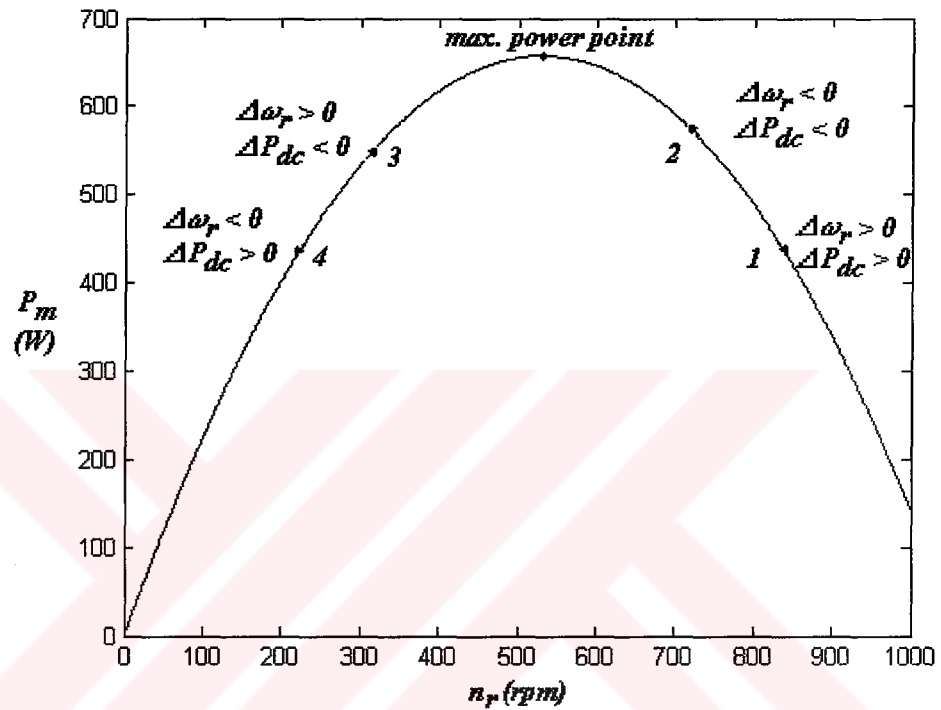


Figure 4.26 Variation of dc link power with respect to rotor speed

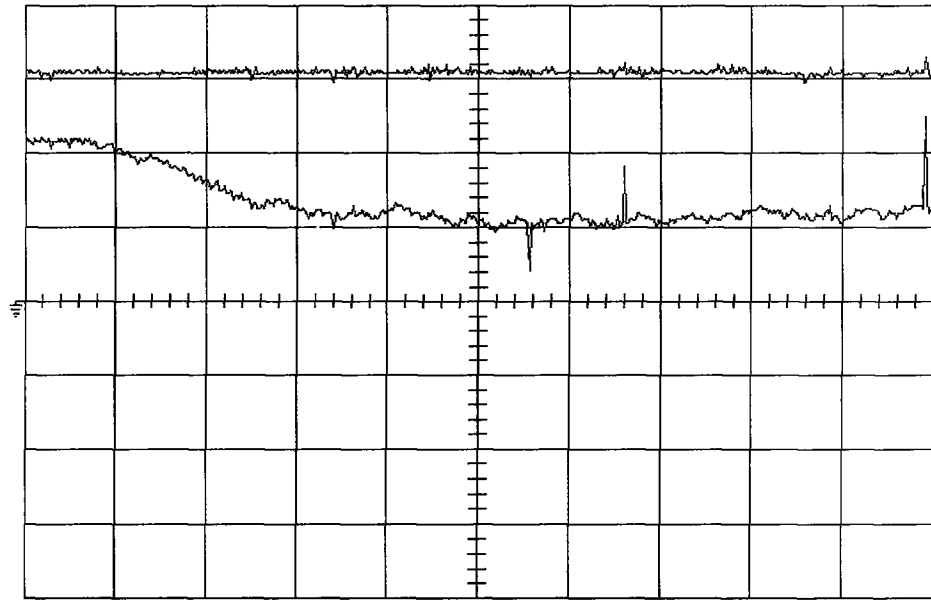


Figure 4.27 Experimental results during maximum power point tracking operation
(upper trace: dc link voltage-160V/div, lower trace: rotor speed-375rpm/div,
time/div-10s)

4.7.3.1 Analysis of DC Motor for Maximum Power Point Operation

The wind turbine is emulated by a DC motor because the shaft power-rotor speed characteristic of a DC motor has similar waveshape to power-speed characteristic of a wind turbine at constant wind speed.

The back emf that the motor produces at a constant rotor speed is

$$e_{a2} = K' i_{f2} \omega_r \quad (4.10)$$

and the torque produced by the motor is

$$T_L = \frac{V_i K' i_{f2}}{R_{a2}} - \frac{(K' i_{f2})^2}{R_{a2}} \omega_r \quad (4.11)$$

The electromechanical power developed by the motor is

$$P = T_L \omega_r = \frac{V_t K' i_{f2}}{R_{a2}} \omega_r - \frac{(K' i_{f2})^2}{R_{a2}} \omega_r^2 \quad (4.12)$$

The rotor speed where maximum power is developed by the motor ($\omega_{r, \max P}$) is obtained from $\frac{dP}{d\omega_r} = 0$ and

$$\omega_{r, \max P} = \frac{1}{2} \frac{V_t}{(K' i_{f2})} \quad (4.13)$$

which yields

$$P_{\max} = \frac{1}{4} \frac{V_t^2}{R_{a2}} \quad (4.14)$$

It is easily seen that the maximum power developed by the motor solely depends on the applied armature terminal voltage. For an armature resistance of $R_{a2} = 3.8 \text{ ohms}$ of the DC machine and the operating conditions given in Table 4.1, the maximum power delivered by this machine is $P_{\max} = 532 \text{ W}$ at the rotational speed $\omega_{r, \max P} = 43 \text{ rad/s}$.

Table 4.1: Measured quantities during MPPT

DC motor terminal voltage (V)	DC motor armature current (A)	DC motor field current (A)	Rotor speed (rpm)	Torque (Nm)	
100	0.9	0.35	820	0	No-load
90	9.5	0.35	477	9	Max. power

CHAPTER FIVE

WIND ENERGY CONVERSION SYSTEMS

5.1 Torque and Power Characteristics of a Wind Turbine

The mechanical characteristics of a wind turbine are formulated by power and torque equations. The mechanical power and torque developed by a wind turbine are given by the following formulas (Buehring & Freris, 1981):

$$P_t = 0.5 C_p(\beta, \lambda) \rho \pi R^2 v^3 \text{ (Watts)} \quad (5.1)$$

$$T_t = 0.5 \frac{C_p(\beta, \lambda)}{\lambda} \rho \pi R^3 v^2 \text{ (Nm)} \quad (5.2)$$

Here, ρ is the air density (kg/m^3), R is the turbine radius (m), v is the wind velocity (m/s), β is the blade pitch angle (degree), and λ is the tip-speed ratio which is defined as

$$\lambda = \frac{\omega_t R}{v} \quad (5.3)$$

where ω_t is the rotational speed of the turbine in rad/s. In equation (5.1) and (5.2), the term $C_p(\beta, \lambda)$ is the power coefficient of the turbine, which is dependent on the pitch blade angle and tip-speed ratio and determines the characteristics of power versus rotational speed. The ratio of the power coefficient to tip-speed ratio is the torque coefficient $C_T(\beta, \lambda)$ of the turbine and given by

$$C_T(\beta, \lambda) = \frac{C_p(\beta, \lambda)}{\lambda} \quad (5.4)$$

In Figure 5.1 and Figure 5.2 typical power and torque coefficient characteristics of a wind turbine are shown, respectively. A wind turbine can operate at its maximum power point for a given optimum tip-speed ratio as shown in Figure 5.1. Hence, it can be seen that the maximum power locus of the wind turbine varies with the cube of the wind speed or rotor speed as equation (5.1) implies. Similarly, from equation (5.2), the torque values corresponding to maximum power points vary with square of the wind speed or rotor speed. So, this requires speed control on the shaft of the generator coupled to the turbine (Buehring & Freris, 1981). Wind turbines that are used for electricity generation are typically horizontal axis and two or three-bladed. These types of wind turbines are designed to operate at higher tip-speed ratios. So, their starting torque is low and in some cases they need to be started (Ackermann & Söder, 2000). However, by employing blade pitch angle control, it is possible to obtain larger starting torque from the turbine as shown in Figure 5.2.

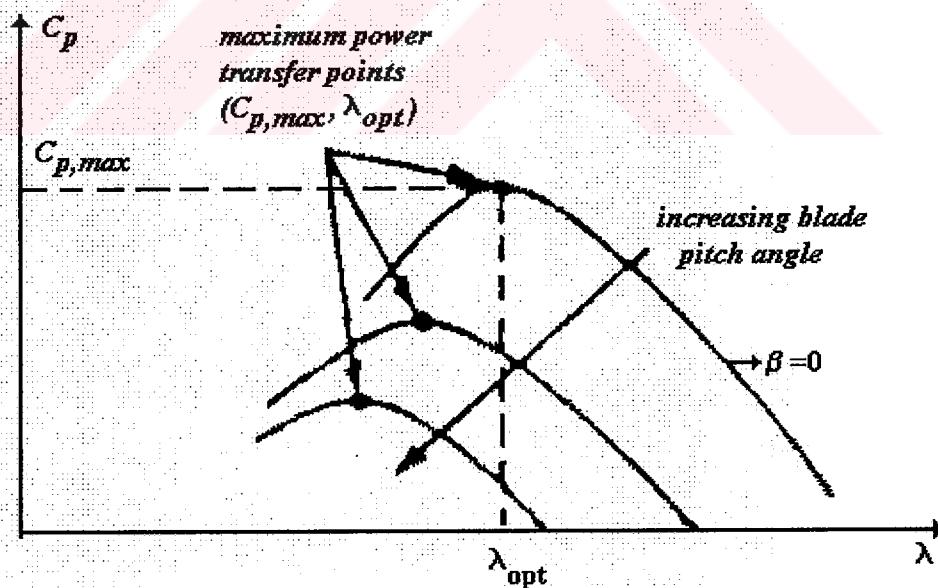


Figure 5.1 Power coefficient characteristics

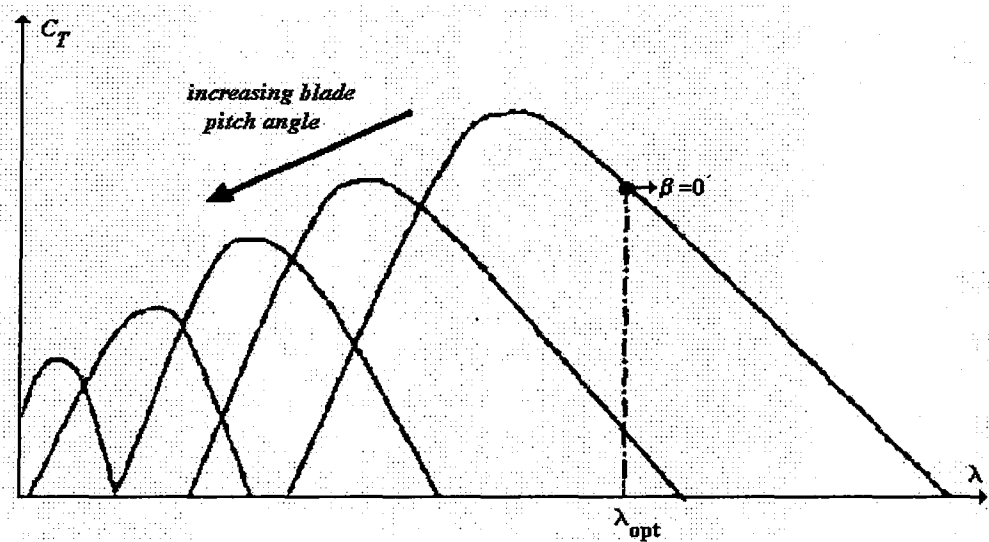


Figure 5.2 Torque coefficient characteristics

5.2 Classification of Wind Energy Conversion Systems

Types of wind energy conversion systems (WECS) are determined by their operation which depends on the turbine speed and generator output frequency. They can be classified into 3 groups as follow:

- a) Constant-speed constant-frequency (CSCF) systems
- b) Variable-speed constant-frequency (VSCF) systems
- c) Variable-speed variable-frequency (VSVF) systems

In the following, an overview of WECS types is given. The torque and power characteristics of wind turbine are required for dynamic simulations of the systems; hence, they will be given in the following section.

5.2.1 Constant-speed constant-frequency (CSCF) systems

The terminals of the ac generator of which shaft is driven by the wind turbine are directly connected to the utility grid in such systems. A three-phase synchronous or induction machine can be used as a generator. When a synchronous generator is used, the rotational speed is strictly fixed and determined by the grid frequency.

However, the rotational speed slightly changes when an induction generator is used. This speed change is over the stable operation region of the induction generator and very small. The shaft speed is also required to be above synchronous speed to maintain generator operation.

The rotational speed of wind turbine is considerably low in comparison with that of the conventional electrical machines. So, in the CSCF systems, a gearbox mechanism is needed in order to increase the turbine shaft speed to synchronous speed of the generator. It is also possible to use a generator with large number of poles so that the gearbox can be omitted, and direct coupling between generator and turbine may be achieved.

In Figure 5.3, a low and medium power WECS application is shown where a synchronous generator is used with diesel generators in a local grid system (Khater, 1996). Voltage regulation and power factor adjustment is achieved via controlling the excitation current of the synchronous generator. In large scale grid connected wind power applications, synchronous generator outputs are directly connected to utility grid and control technique is the same as given in this application. The connection scheme is the same when an induction generator is used. However, power factor cannot be controlled in this case and the reactive power is supplied to the induction machine from the utility grid for generator operation. Additional capacitors should be inserted at the induction generator terminals for power factor correction.

Because the maximum power developed by the wind turbine varies over a wide range of rotational speed, the CSCF systems are not efficient. They can not extract the whole energy that is produced by the wind turbine at all wind speeds. However, complexity and the initial cost of these systems are considerably low.

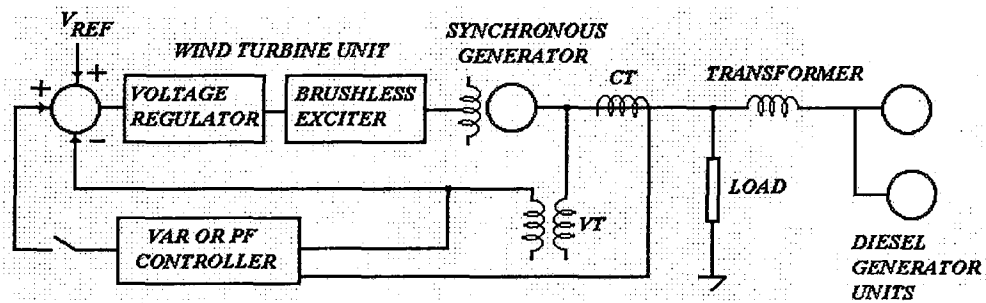


Figure 5.3 CSCF system with field excited synchronous generator.

5.2.2 Variable-speed constant-frequency (VSCF) systems

Variable speed wind energy systems are more efficient but more complex compared to constant speed systems. The maximum power developed by the wind turbine can be extracted by means of a maximum power point tracker control. Variable speed operation can be maintained in various ways and numerous papers can be found in literature with different type of proposed systems. In such systems, the generator output can not be directly connected to utility grid since the generator output voltage and frequency are variable in nature. In order to make synchronization with utility grid, the voltage and frequency converters can be employed between the wind turbine generator and power system.

In Figure 5.4, a VSCF application is shown. The variable speed operation is achieved by the control of power electronic converters. Also, the proposed system contains blade pitch angle control for starting and power regulation above maximum speed. At low wind speeds, pitch angle control improves torque coefficient ($C_T(\beta, \lambda)$) of the turbine providing higher starting torque. At high wind speeds, the power produced by the turbine is limited by pitch angle control as well (Lima et al, 1999).

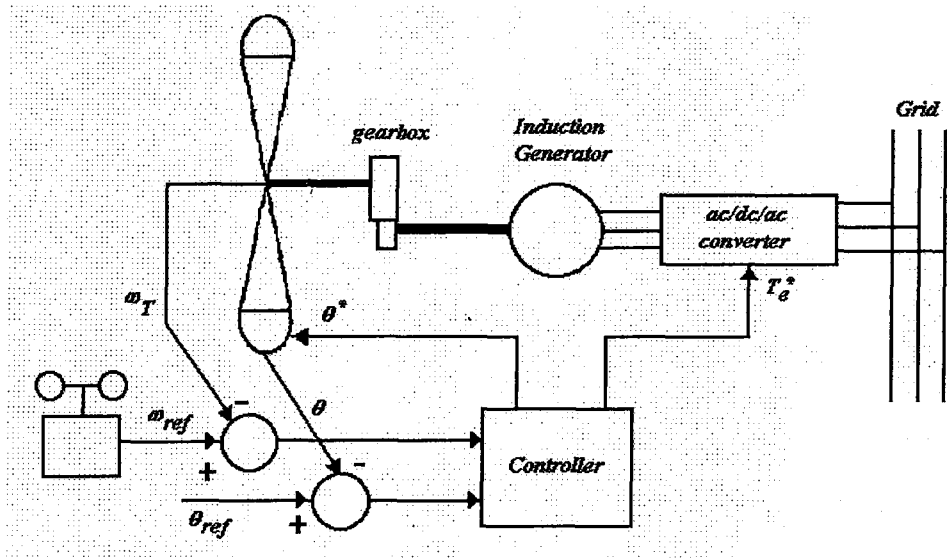


Figure 5.4 VSCF system with pitch blade angle control

The system given in Figure 5.5 employs a slip-ring induction machine, which is used as generator. In this system the generator output is directly connected to the utility grid and variable speed operation is achieved by external rotor resistance control of the machine via a solid-state controller (Velayudhan et al, 1984). The method relies on the dynamics of the systems such that

$$T_a = J \frac{d\omega}{dt} = T_w - T_d \quad (5.5)$$

where

T_a is the accelerating torque (Nm),

T_w is the torque available from the wind turbine (Nm),

T_d is the torque developed by the induction generator (Nm),

J is the combined moment of inertia of the rotating system (kg.m^2),

ω is the angular velocity (rad/s).

T_w depends on wind velocity and rotational speed while. T_d depends on rotor resistance and rotational speed. The torque developed by the induction generator decreases as the rotor resistance increases and vice versa (ensuring that the rotor

speed is maintained constant). Under varying wind conditions, the turbine will be accelerating ($T_a > 0$) or decelerating ($T_a < 0$). The adjustment criteria is to minimize T_a such that the rotor resistance is decreased while the turbine is accelerating ($\frac{d\omega}{dt} > 0$) and the rotor resistance is increased while the turbine is decelerating ($\frac{d\omega}{dt} < 0$). The advantage of this system used here is to employ a low power rated converters on the rotor part of the generator.

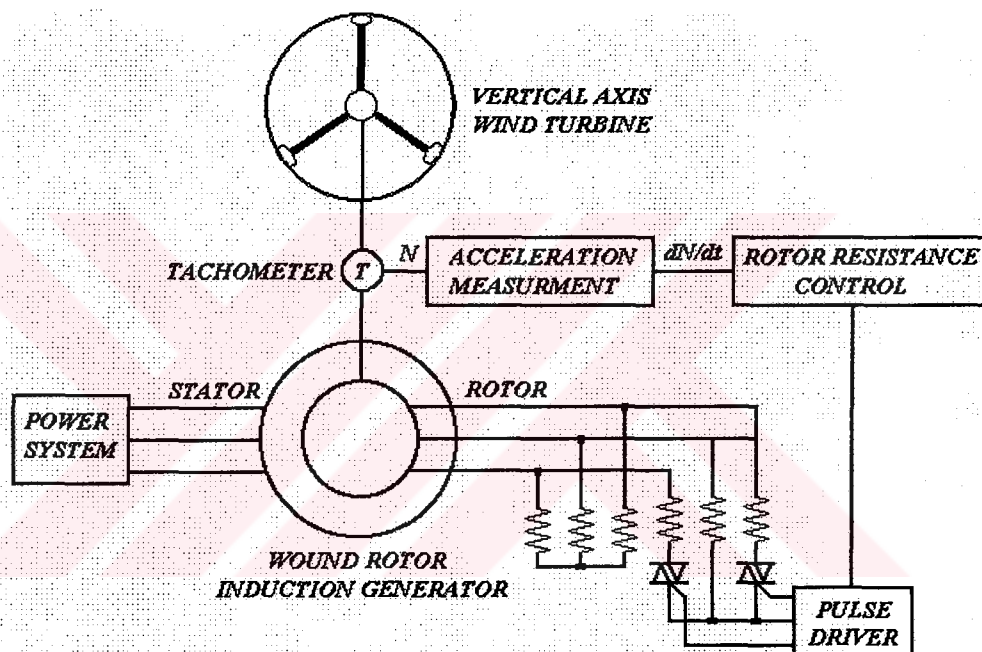


Figure 5.5 VSCF system with a slip ring induction machine

Another VSCF system is shown in Figure 5.6. Here, variable speed operation is achieved by fuzzy controlled PWM converters. The reactive power of the induction generator required is supplied by PWM converter at the machine side and the power factor is unity at the line side. Three fuzzy logic controllers (FLC) performs the following operations: generator speed tracking control (FLC1) for maximum power point tracking from the wind turbine; generator flux programming control (FLC2) for efficiency control of the generator; closed-loop generator speed control (FLC3) for ensuring the operation of the machine at the desired speed. The main advantage of the proposed system is that the current control at the line-side with minimized

harmonic content and unity power factor (Simoes et al, 1997). The main disadvantage of the system here is to employ the converters at full power rating of the WECS.

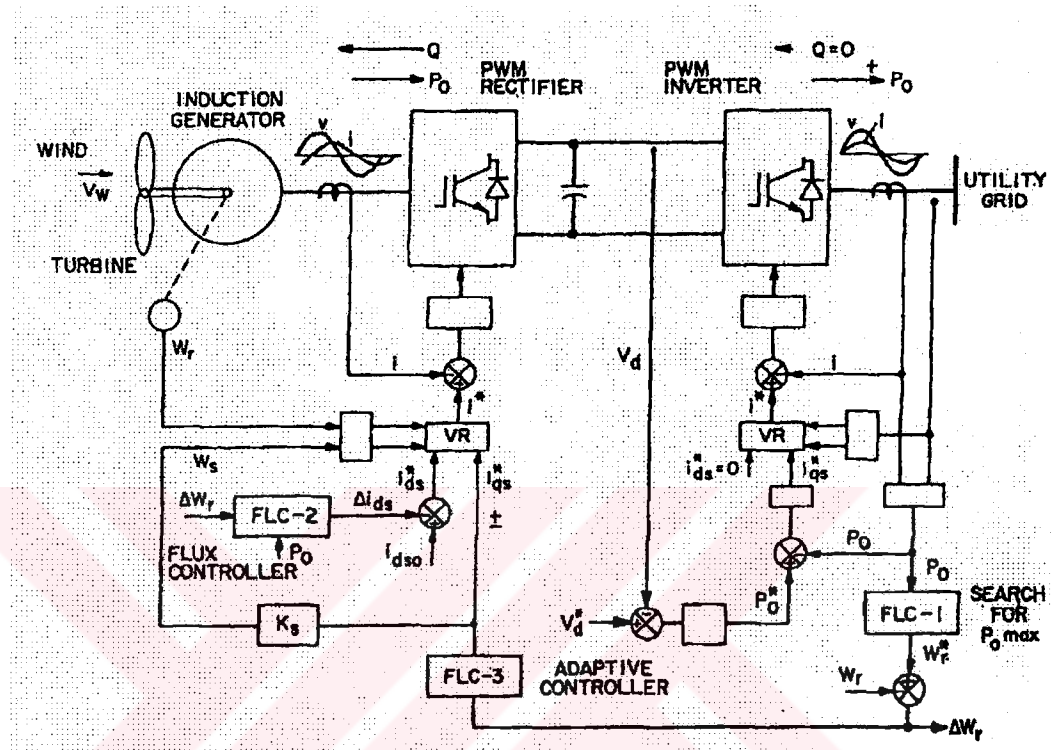


Figure 5.6 VSCF system with fuzzy controlled PWM converters

In the proposed system given in Figure 5.7, a brushless doubly-fed induction machine (BDFM) is used as generator. Such a machine has two separate windings and by adjusting the frequency of the control windings, the rotor speed can be controlled. BDFM has two separate winding with different pole number. The relationship between rotor shaft speed and stator frequencies of power and control stator windings is given as follows:

$$f_c = f_r(P_p + P_c) - f_p \quad (5.6)$$

where

P_p and P_c are the pole pair numbers of the stator power and control windings respectively.

f_p is the utility grid frequency

f_r is the shaft speed dictated by the variable-speed generation algorithm

f_c is the required converter output frequency of the control windings.

Hence, the variable-speed operation of the system is achieved via the excitation of the control windings. In this system, since the converters are employed at the stator control windings, the power ratings of the converters are quite low, which is approximately 25 percent of the system kVA rating and brushes are not needed (Brune et al, 1994).

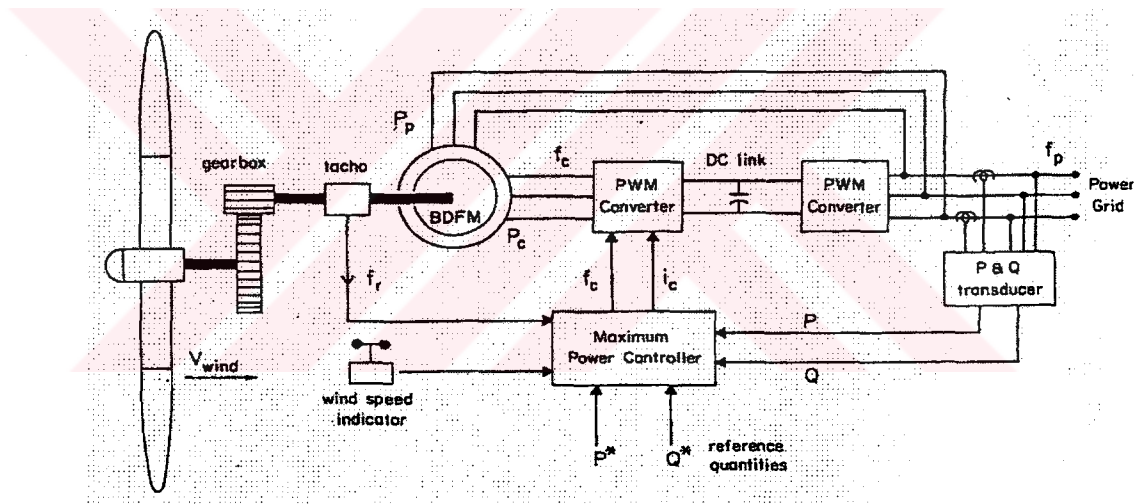


Figure 5.7 VSCF system with brushless doubly-fed induction generator

The system given in Figure 5.8 is a wind-driven slip energy recovery system and is used to recover the energy that would be dissipated in the rotor windings (Akpınar & Pillay, 1990). In this system, the grid-connected wound rotor induction generator is driven by a vertical axis wind turbine. The generator is also connected to grid by its rotor through six-pulse fully controlled converters. The system delivers power to grid in both sub-synchronous and super-synchronous modes of operation depending on the wind conditions. By appropriately adjusting the firing angles of the converters

(α_1, α_2) specific operation mode of the induction generator is determined as follows (Üçtuğ et al, 1994), (Çadırcı & Ermiş, 1992):

Supersynchronous mode	Subsynchronous mode
$-1 \leq s \leq 0$	$0 \leq s \leq 1$
$0^\circ \leq \alpha_1 \leq 90^\circ$	$90^\circ \leq \alpha_1 \leq 180^\circ$
$90^\circ \leq \alpha_2 \leq 180^\circ$	$0^\circ \leq \alpha_2 \leq 90^\circ$

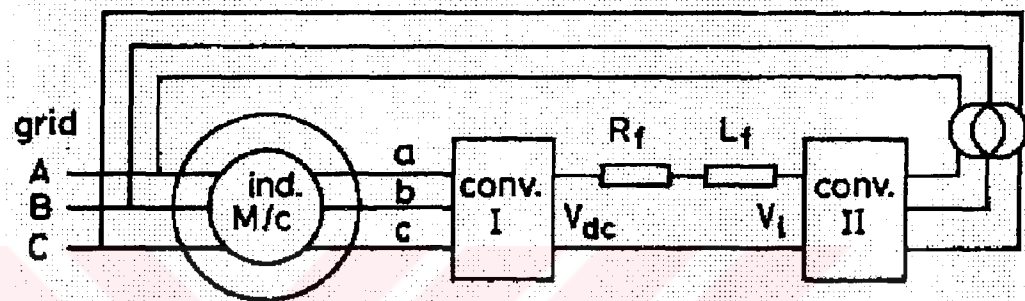


Figure 5.8 VSCF system with slip-energy recovery drive

5.2.3 Variable-speed variable-frequency (VSVF) systems

VSVF systems are generally autonomous systems that are used for charging batteries or heating loads. Permanent magnet generators, synchronous generators, or capacitor self-excited induction generators can be used in such systems. The output of the generator may be converted to dc at desired voltage level. A system that is used for feeding an autonomous load is given in Figure 5.9. The control of the armature terminals voltages is achieved via field current control of the synchronous generator and the terminals are connected to a 3-phase uncontrolled rectifier for supplying the battery and load. (Ermiş et al, 1992). A chopper circuit between the rectifier and battery is used to control the maximum power flow and voltage level across the battery terminals.

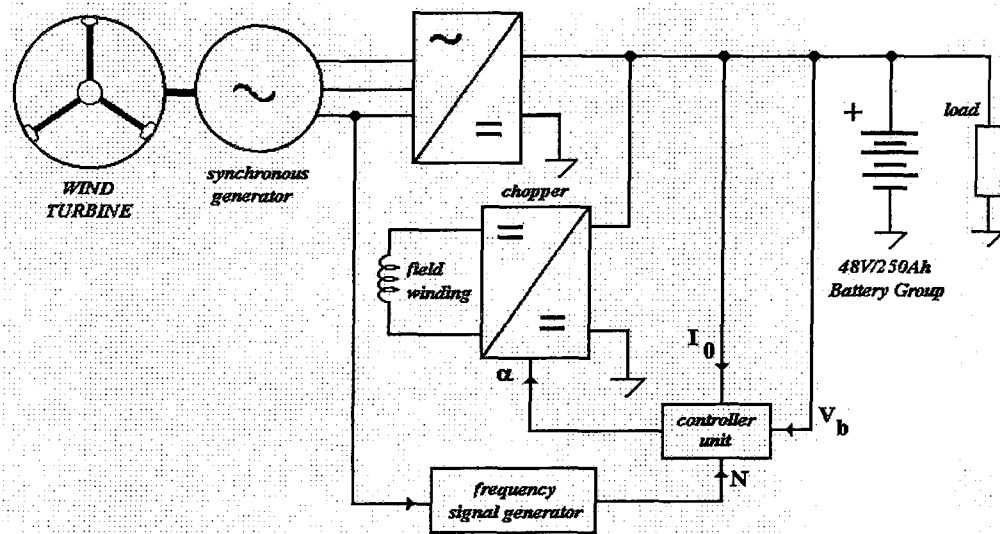


Figure 5.9 VSVF system with a field excited synchronous generator

In Figure 5.10, a VSVF system with a capacitor excited induction generator is shown. Here, the required reactive power for induction generator is controlled by a fixed capacitor and thyristor controlled inductor. The variable-voltage variable frequency output of the induction generator can be converted to other forms via solid-state converters for autonomous loads (Khater, 1996).

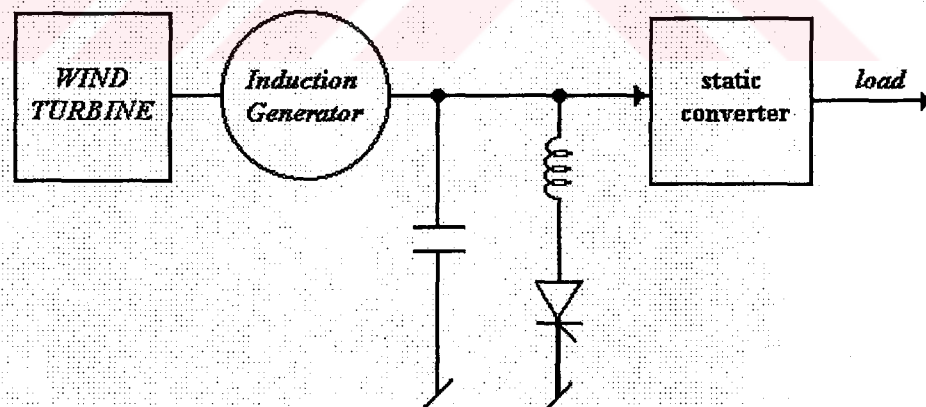


Figure 5.10 VSVF system with a capacitor excited induction generator

5.3 Wind Turbine Modeling

The mechanical power and torque developed by the wind turbines are given by the equations (5.1) and (5.2). In the modeling of the wind turbines, power or torque

coefficient of the wind turbine must be known. The characteristics of the wind turbine have a nonlinear relationship with the tip-speed ratio, which is determined by the equation (5.3), and were given in Figure 5.2 and Figure 5.3. These nonlinear functions can be either approximated to a polynomial function with curve fitting (Simoes et al, 1997) or a lookup table can be employed.

For a wind turbine with fixed-pitch-blade angle and blade length of 2.75m, the SIMULINK model of the wind turbine is constructed. In this model, the turbine power coefficient is determined referring to the equation (5.1) for a given wind velocity, turbine rotational speed, and the constants rotor radius and air density. Once the power coefficient is determined, the torque coefficient of the machine is calculated from equation (5.4) and stored in a lookup table. For the value of the tip-speed ratio at stand still, the torque coefficient is set to zero in the lookup table, so the starting torque of the turbine is zero. In simulations, turbine is started by the induction machine in motor mode, which is the starting procedure in implementation.

The approximate $C_p - \lambda$ characteristic of the turbine is obtained by using the formula as follows

$$C_p = Ae^{-B(\lambda-C)^2} \quad (5.7)$$

In this formula, the constant A determines the maximum power coefficient ($C_{p,max}$), B determines the shape of the curve, and C determines the optimum value of the tip-speed ratio (λ_{opt}), which corresponds to the maximum power point of the turbine. Also, if the data of the $C_p - \lambda$ curve exists, the parameters in equation (5.7) can be estimated using curve fitting methods, such as least-square method.

In the study of simulation, the constants of $C_p - \lambda$ curve are chosen as A=0.4, B=0.2, C=4.3 and the power and torque coefficients as a function of tip-speed ratio are obtained as shown in Figure 5.11 and Figure 5.12, respectively. The parameters

are chosen such that the turbine produces approximately 3 kW of maximum mechanical power at 8 m/s wind velocity and an optimum tip-speed ratio of 4.3.

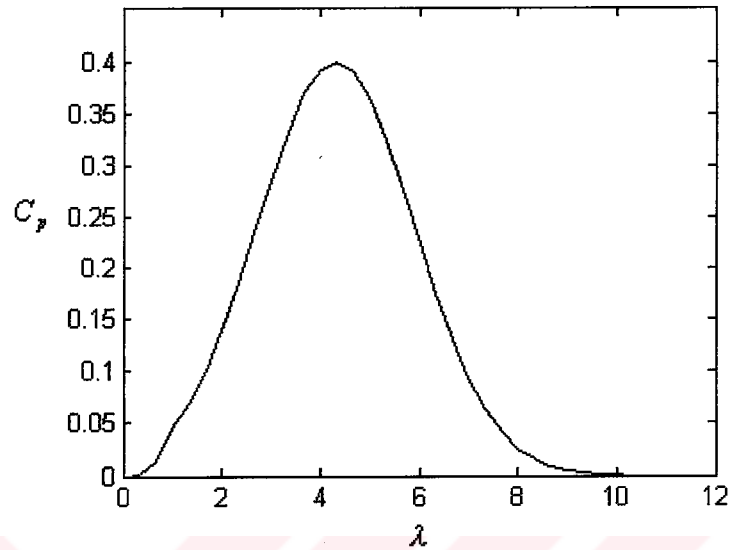


Figure 5.11 Power coefficient of the wind turbine versus tip-speed ratio

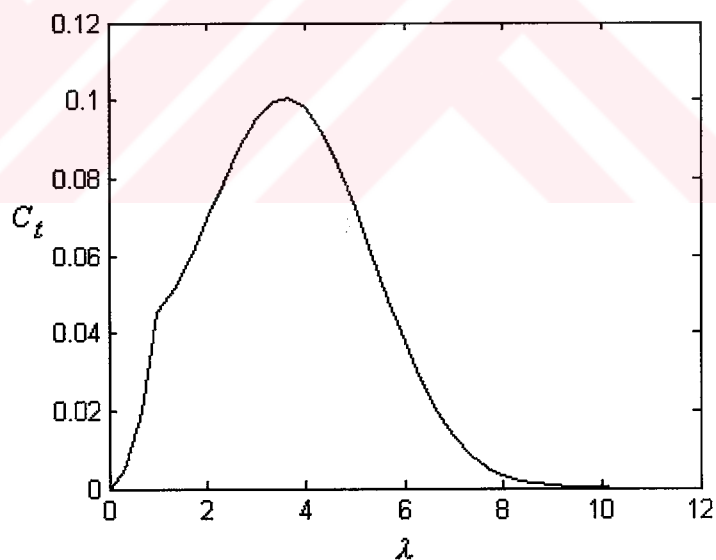


Figure 5.12 Torque coefficient of the wind turbine versus tip-speed ratio

5.3.1 Efficiency Analysis of Double-Cage Induction Machine

The steady-state equivalent circuit of a double-cage induction machine (DCIM) at a supply voltage frequency of ω_e is given in Figure 5.13. Here ω_e and ω_b are the

electrical supply frequencies at the given and the rated values, respectively. The machine parameters have their values at rated frequency. Core loss resistance is not shown in the equivalent circuit. The reactance values in the equivalent circuit are calculated as follows:

$$x = \left(\frac{\omega_e}{\omega_b} \right) X \quad (5.8)$$

where x and X are the reactance values at the given supply electrical frequency and rated supply frequency, respectively. From the analysis of the equivalent circuit, the efficiency can be calculated as follows

The input impedance seen by the source is

$$Z_{in} = (r_1 + jx_1) + (jx_m) // [jx'_{23} + (\frac{r'_2}{s} + jx'_2) // (\frac{r'_3}{s} + jx'_3)] = |Z_{in}| \angle \phi \quad (5.9)$$

The stator current is

$$I_1 = \frac{V_1}{Z_{in}} \quad (5.10)$$

where V_1 is the per phase supply voltage. The electrical power is

$$P_{elect} = 3V_1 I_1 \cos \phi \quad (5.11)$$

The rotor current is

$$I'_2 = \frac{E_g}{[jx'_{23} + (\frac{r'_2}{s} + jx'_2) // (\frac{r'_3}{s} + jx'_3)]} = \frac{V_1 - I_1(r_1 + jx_1)}{[jx'_{23} + (\frac{r'_2}{s} + jx'_2) // (\frac{r'_3}{s} + jx'_3)]} \quad (5.12)$$

The electromagnetic torque is

$$T_e = \frac{3}{\omega_s} |I_2'|^2 r_{eq}' \quad (5.13)$$

where r_{eq}' is the equivalent rotor resistance at the specific operating condition (i.e. at a given slip, so in the above formula it is not divided by slip), $\omega_s = \frac{2}{P} \omega_e$ is the synchronous speed, and $s = \frac{\omega_s - \omega_r}{\omega_s}$ is the slip factor. Equivalent rotor resistance (r_{eq}') and the reactance (x_{eq}') referred to the stator side were given in equations (2.215) and (2.216). The mechanical power is

$$P_{mech} = \omega_r T_e \quad (5.16)$$

where

$$\omega_r = (1 - s) \omega_s \quad (5.17)$$

Hence, the efficiency is calculated for the motor operation as follows:

$$\eta = \frac{P_{mech}}{P_{elect}} \quad (5.18)$$

and the efficiency for the generator operation is as follows:

$$\eta = \frac{P_{elect}}{P_{mech}} \quad (5.19)$$

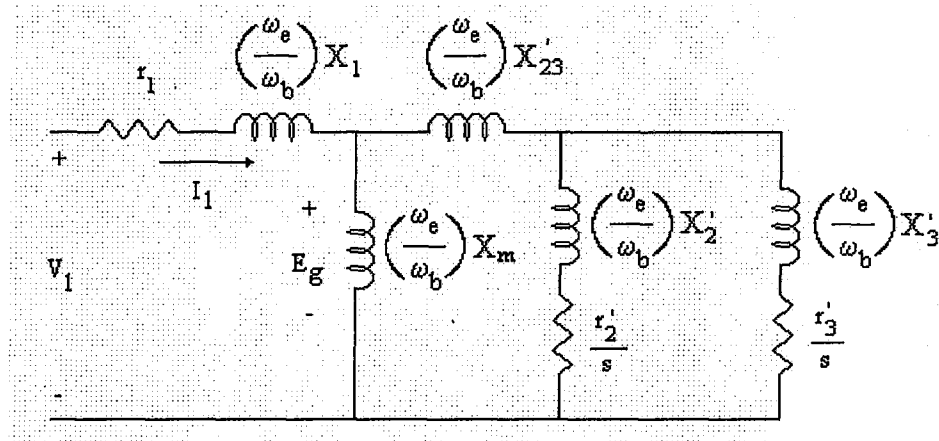


Figure 5.13 Equivalent circuit of double-cage induction machine

5.3.2 Effect of Gearbox on the Machine Efficiency

Here, the aim is to investigate the effect of the gearbox ratio on the overall efficiency of the system. The system that is simulated in this part for the efficiency prediction of machine is a type of constant-speed constant-frequency. The stator terminals of the double-cage induction machine (DCIM) are connected to the grid as it is shown in Figure 5.14. While the turbine speed is transmitted to the DCIM shaft by a speed-up gearbox with a ratio of n_{gear} , the turbine torque is transmitted to the DCIM shaft by the inverse of gear ratio.

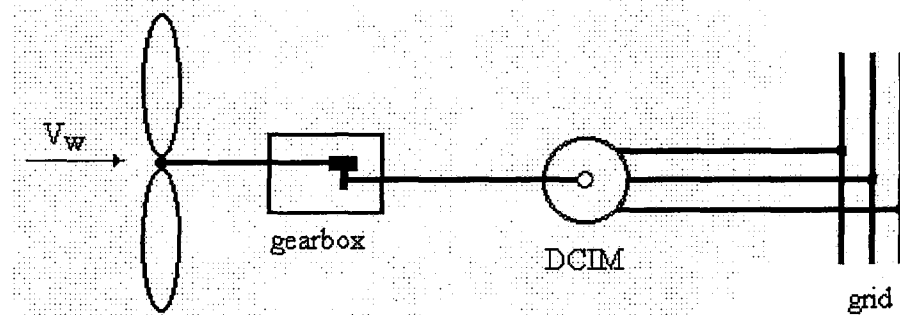


Figure 5.14 Direct grid connection scheme

In the SIMULINK modeling of this direct grid connected system, the mathematical models of the turbine and DCIM are used. The SIMULINK model of CSCF system is given in Appendix B. In the model of the system, the mechanical

speed output of the DCIM is reduced by the gear ratio (n_{gear}) and formed an input to the wind turbine model. Similarly, the turbine torque output appears as a negative load torque in the DCIM model after being reduced by the same gear ratio. The electrical terminals of the DCIM are connected to the 230V, 50Hz utility grid. The wind velocity is a constant input in the wind turbine model. The following results, which are given in Table 5.1, are obtained from the simulation of the system during steady-state for different wind conditions and gear ratios. The core loss of the machine is calculated by taking the core loss resistance into account for each operating condition and subtracted from the electrical power obtained from simulation in order to calculate overall efficiency. The per phase core loss resistance is measured as $R_c = 1350\Omega$.

From the results, it can be seen that at low wind velocities, the gear ratio should be reduced in order to keep the operation of the system near to the maximum power point. This ratio is fixed unless a control mechanism exists to control this gear ratio and should be selected to extend the operation over a wide range of wind velocities. When considering a constant speed wind energy conversion system, the total energy development is highly dependent upon the gear ration chosen (Zinger & Muljadi). Hence, the selection of the gearbox ratio depends on the wind conditions where the turbine will be installed in.

5.4 Speed Control of DCIM driven by the Wind Turbine

The block scheme of the implemented variable speed wind energy conversion system was given in Figure 1.1. The system consists of a current controlled PWM voltage source converter (VSC) on the line-side, a PWM voltage source inverter (VSI) on the machine-side, and a double-cage induction machine (DCIM) driven by a wind turbine. The wind turbine is coupled to the DCIM through a speed-up gearbox. There are two closed-loop controllers in the system. The PI controller on the line-side converter regulates the dc link voltage at the desired level and the PI controller on the machine-side inverter adjusts the rotor speed at the given reference value.

Table 5.1: CSCF operation under varying gear ratios ($R = 2.75m$, $\lambda_{opt} = 4.3$)

v (m/s)	P_{t_max} (W)	n_{gear}	ω_r (rd/s)	P_e (W)	P_m (W)	η	T_t (Nm)	T_e (Nm)
10	5810	1/9	167.9	-4176	-5060	0.825	271.5	-30.1
		1/10	169.3	-4572	-5660	0.808	334.6	-33.5
		1/11	169.6	-4667	-5805	0.804	376.5	-34.2
		1/12	169.1	-4540	-5600	0.811	397.5	-33.1
8	2975	1/10	161.7	-1905	-2165	0.880	133.9	-13.4
		1/11	162.7	-2300	-2628	0.875	177.8	-16.1
		1/12	163.2	-2517	-2890	0.871	212.5	-17.7
		1/13	163.4	-2587	-2974	0.870	236.7	-18.2
		1/14	163.3	-2547	-2920	0.872	250.7	-17.9
6	1255	1/14	159.4	-905	-1060	0.854	93.1	-6.6
		1/15	159.6	-1007	-1173	0.859	110.2	-7.3
		1/16	159.8	-1065	-1235	0.862	123.8	-7.7
		1/17	159.8	-1084	-1255	0.864	133.5	-7.8
		1/18	159.8	-1070	-1240	0.863	139.8	-7.7
4	372	1/21	157.8	-195	-320	0.609	36.7	-2.05
		1/22	157.8	-215	-340	0.633	47.8	-2.2
		1/23	157.9	-235	-360	0.653	52.3	-2.3
		1/24	157.9	-244	-370	0.659	56.1	-2.35
		1/25	157.9	-245	-372	0.659	58.9	-2.4

5.4.1 Simulations Results of Variable-Speed Drive with Wind Turbine

The system is simulated under certain wind conditions and its performance is investigated. The computer simulations are carried out using MATLAB Simulink models of the DCIM, PWM converters, wind turbine, and closed-loop controllers, which are given in Appendix B. The wind turbine used in the implemented system is a fixed pitch, three-bladed and horizontal axis type. In the modeling of the wind turbine, a lookup table is used which determines the turbine torque coefficient versus

tip-speed ratio. Since the starting torque of the turbine is very low, the starting of the turbine rotation is achieved by the motor operation of the DCIM. Also, a starting process under supervisory controller is required in order to prevent the over-speeding of the turbine, especially in high wind speed conditions. The combined moment of inertia of the overall system was approximated to be equal to the turbine moment of inertia plus the moment of inertia values of the generator and the drive train, which is assumed to be 10 percent of the turbine moment of inertia. Assuming each turbine blade as a uniform rod with a blade length of R and the weight of m , the total moment of inertia of the three-bladed turbine is calculated approximately as follows

$$J_t = mR^2 \quad (5.20)$$

Including the drive train and generator moment of inertia to that of the turbine, the total moment of inertia value of the mechanical system is referred to the shaft of the DCIM with the speed-up gear ratio as follows

$$J_{eq} = 1.1 \frac{J_t}{n_{gear}^2} \quad (5.21)$$

In computer simulations, the parameters of the implemented wind turbine are used and their values are given in Table 5.2. The digital PI parameters and feedback gains are modified such that the system gives a better response with higher moment of inertia and the characteristics of the wind turbine. The parameters of the electric circuit and controllers are given in Table 5.3.

Table 5.2: Wind turbine parameters

$n_{gear} = 10$	speed-up gear ratio
$m = 20kg$	weight of each turbine blade
$R = 2.75m$	blade length
$J_t = 151kg.m^2$	turbine moment of inertia
$J_{eq} = 1.66kg.m^2$	total moment of inertia value referred to DCIM shaft

Table 5.3: Electrical circuit and control parameters

$E_m = 170\sqrt{2}$	magnitude of the ac supply voltages
$\omega_s = 2\pi.50\text{rad/s}$	electrical supply frequency
$L_s = 50\text{mH}$	ac line filter inductance
$R_s = 0.8\text{ohms}$	resistance of filter inductance
$C = 1200\mu\text{F}$	dc link capacitor
$T_{\text{cmp}} = 250\mu\text{s}$	sampling rate
$u_{dc}^* = 500\text{V}$	dc link voltage reference value
$K_{E,dc} = 4, K_{CE,dc} = 64K_{E,dc}$	PI voltage controller gains
$K_{udc} = \frac{1}{160} \times \frac{1023}{5}$	dc link voltage feedback gain
$K_{eabc} = \frac{2}{E_m} \times \frac{1023}{5}$	measurement gain of supply voltages
$K_{iabc} = 0.125 \times \frac{1023}{5}$	feedback gain of line currents
$HBW = 10$	hysteresis bandwidth, corresponds to 0.4A
$K_{E,speed} = \frac{1}{8}, K_{CE,speed} = 4K_{E,speed}$	PI speed controller gains
$N = 128T_{\text{cmp}}$	speed sampling rate

In simulations, first the DC link voltage is stabilized at its reference value of 500V between 0-2s and then the reference speed is increased as a step function (375 rpm) at $t=2\text{s}$. The system is started up under wind speed zero in order to simulate the condition when the tail vane is locked and the turbine is directed out of wind. The friction losses of the mechanical system are measured to be 500W at 1500 rpm and taken into account in simulations. They are assumed to be proportional to the rotor speed and modeled as positive input torque to the shaft of the DCIM. In Figure 5.15, the free acceleration of the rotor from standstill to 375 rpm and the developed

electromagnetic torque of the DCIM when the turbine is directed out of wind are shown.

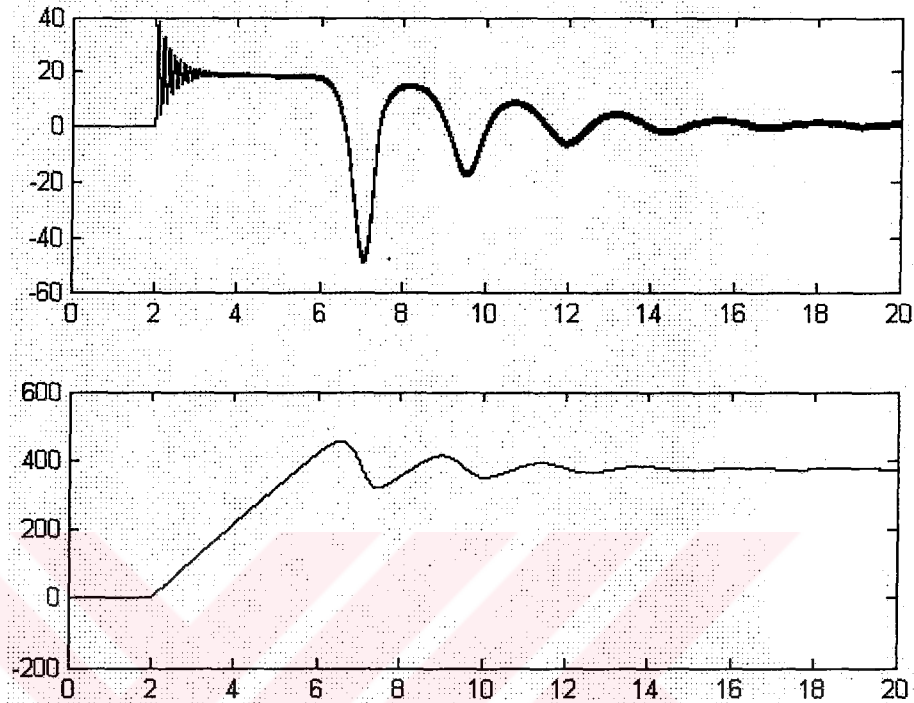


Figure 5.15 Free acceleration of the DCIM to 375 rpm when the turbine is directed out of wind (top: electromagnetic torque of DCIM, bottom: DCIM rotor speed)

At the second stage, the rotational speed is increased to 1500 rpm when the tail vane is closed and the turbine is directed out of wind again. The free acceleration of the DCIM from standstill to 1500 rpm is shown in Figure 5.16. In Figure 5.17, steady-state waveforms of the ac line supply voltage and current are shown when the DCIM is operating as motor at a rotor speed of 1500 rpm. In Figure 5.18, DCIM phase voltage and current are shown at steady-state for the same operating conditions. In this condition, since the DCIM operates as motor, the line-side converter operates as rectifier and draws approximately 500W from the ac line to compensate the frictional losses.

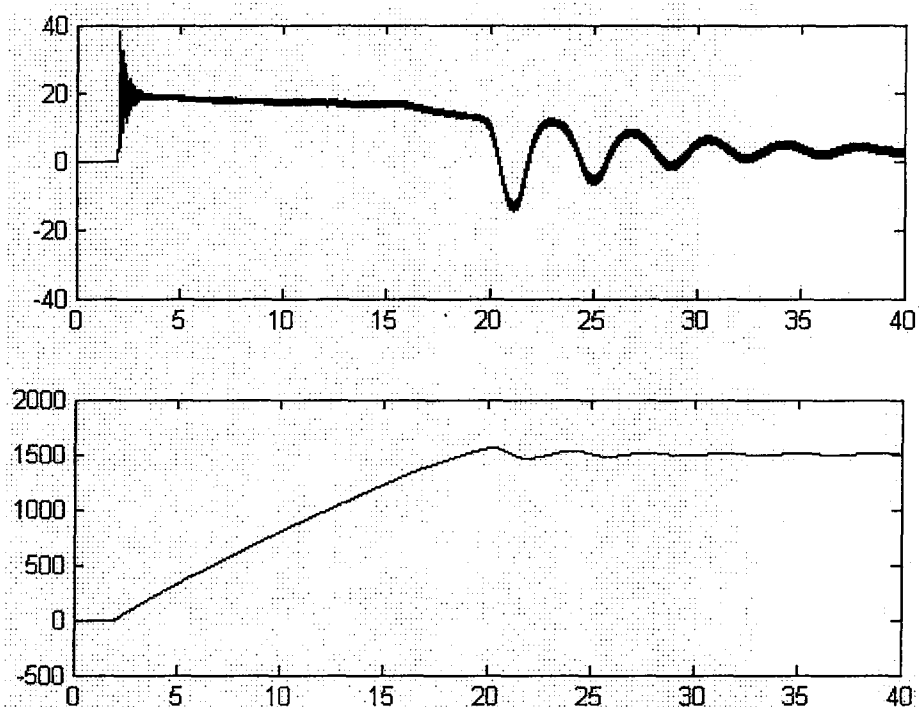


Figure 5.16 Free acceleration of the DCIM to 1500 rpm when the turbine is directed out of wind (top: electromagnetic torque of DCIM, bottom: DCIM rotor speed)

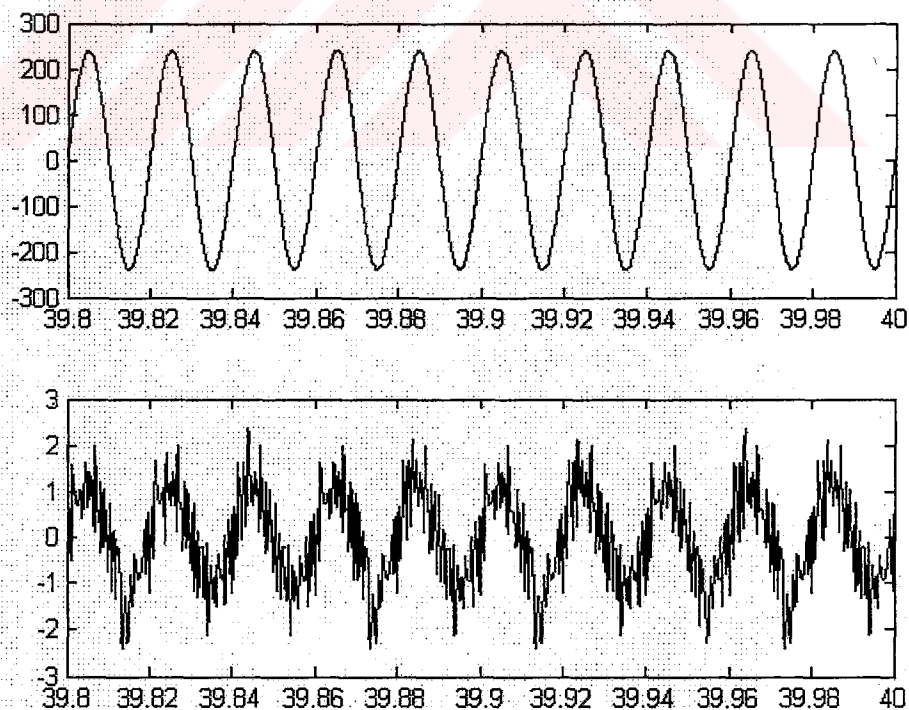


Figure 5.17 Supply voltage and current at the line-side converter at the rotational speed of 1500 rpm when the turbine is directed out of wind

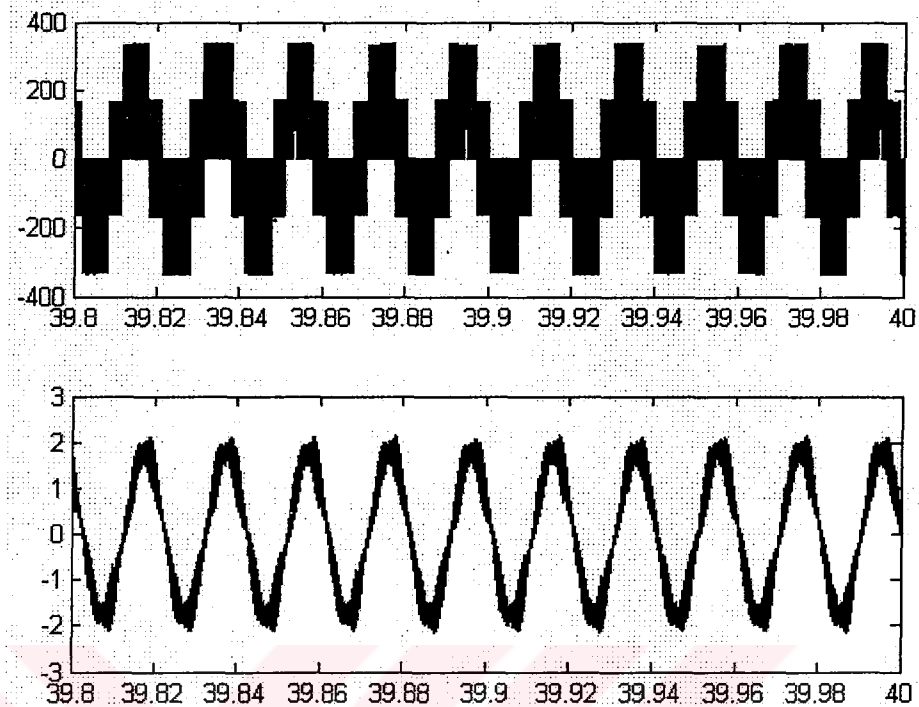


Figure 5.18 DCIM phase voltage and current at the rotational speed of 1500 rpm when the turbine is directed out of wind

At the third stage, the wind speed is set to 8m/s when the rotational speed is 1500 rpm. The steady-state waveforms of the ac line voltage and current are shown in Figure 5.19. In Figure 5.20, the DCIM phase voltage and current are given for this operating condition. The wind turbine operates at a tip-speed ratio of 5.4 for this operating condition and the corresponding power coefficient is approximately 0.3. The turbine develops a mechanical power of 2.3kW at this operating point. The net electrical power delivered to the grid is approximately 1.5kW.

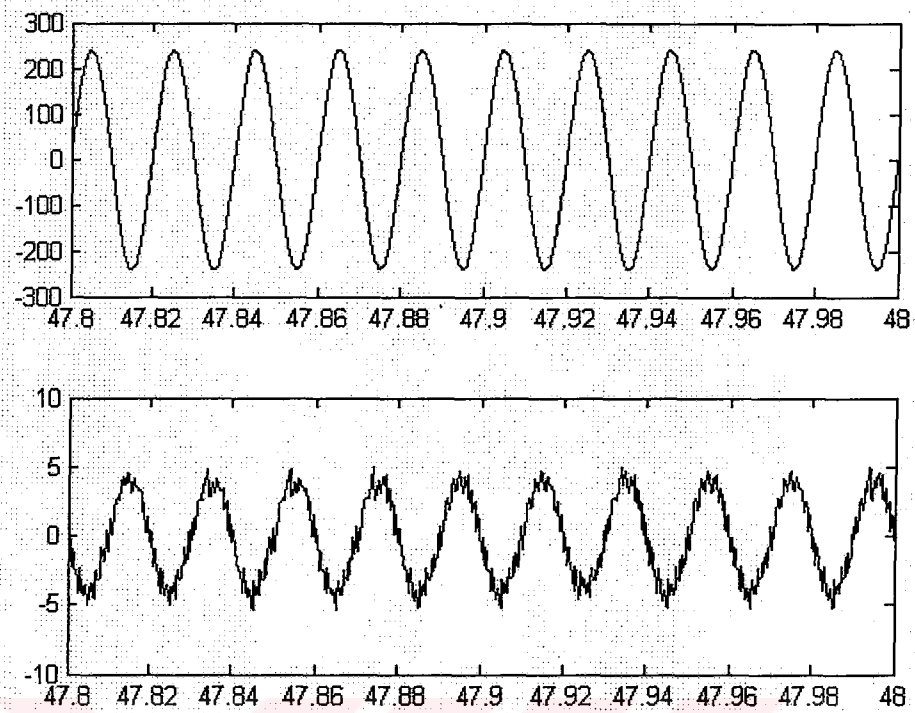


Figure 5.19 Supply voltage and current at the line-side converter at the wind speed of 8m/s and the rotational speed of 1500 rpm.

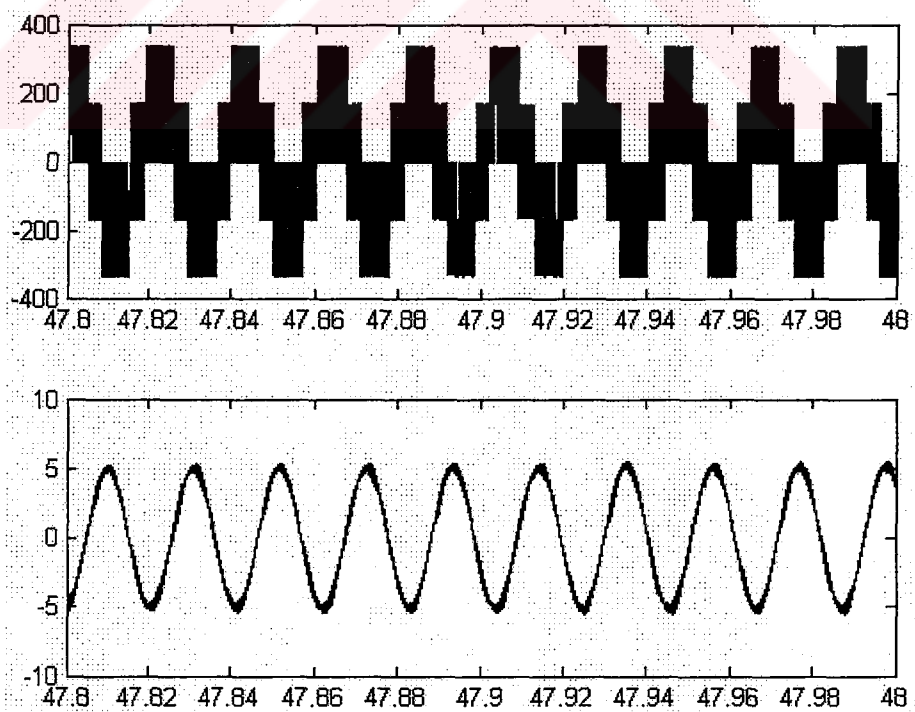


Figure 5.20 DCIM phase voltage and current at the wind speed of 8m/s and the rotational speed of 1500 rpm.

5.5 Experimental Results

Experimental works are carried out on the wind turbine designed and implemented. The wind turbine used in the system is a horizontal axis, three-bladed, fixed pitch angle turbine with a blade length of 2.75m. A free yaw mechanism that consists of a tail vane is used to turn the nacelle to the wind direction such that it is perpendicular to the swept rotor area. The turbine drives the DCIM on the shaft through a gearbox of which speed-up ratio is chosen to be 10. The DCIM is controlled via PWM VSCs to achieve variable-speed operation of the generator.

In experiments, the reference rotor speed of the DCIM is set to a fixed value. For this operating condition of the system, the wind speed, the rms ac line current, the dc link current, and the rotor speed of the DCIM are recorded over a long time range. In Figure 5.21 and Figure 5.22, the recorded rms values of ac line current and the rotor speed of the DCIM over a time range of 545 seconds are shown, respectively. During this measurement, rotor reference speed is fixed to 940 rpm and the PI speed controller keeps the actual rotational speed almost stable at the reference value. In normal operating conditions, some small excursions of the actual rotor speed occur due to turbulent wind conditions. Also, a large excursion has been observed during 404-423s due to wind gusts. The line current changes between 2.5A and 0.8A because of shaft power fluctuation. Figure 5.23 shows the recorded dc link current during measurement. The sign of the dc link current indicates the direction of power flow. The negative value of the dc link current indicates that the power flow is from generator to the grid and inversely from grid to generator for positive values of the dc link current. Especially, during 97-129s, wind condition is quite stable and approximately 1kW power is delivered to the grid. This corresponds to time interval when the wind speed reaches its highest value. The recorded wind speed during this measurement is shown in Figure 5.24. The system generates constant real power as the wind flows regularly in one direction. Under this condition, the fluctuations in the wind speed are mostly absorbed by the wind turbine due to its high moment of inertia. However, the oscillations in the dc link current, and as a consequence the

instantaneous electrical power, can be observed in these long term recordings due to rapidly changing wind direction. The responses of the converters to these rapid changes are satisfactory. The line-side converter quickly responds to the load changes and regulates the dc link voltage at its given reference value. The speed controller also shows a good performance and recovers the rotational speed from the disturbing effects of the wind gusts. In Figure 5.25 and Figure 5.26, the recorded values of dc link current and the wind speed of the DCIM over a time range of 289 seconds are shown, respectively. These quantities are recorded when the rotor speed of the DCIM is set to 865 rpm.

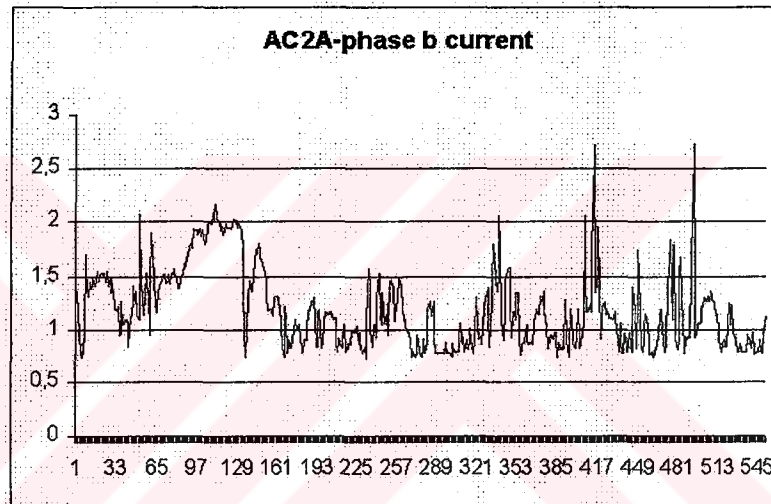


Figure 5.21 Recorded rms values of the ac line current at a rotor speed of 940 rpm.

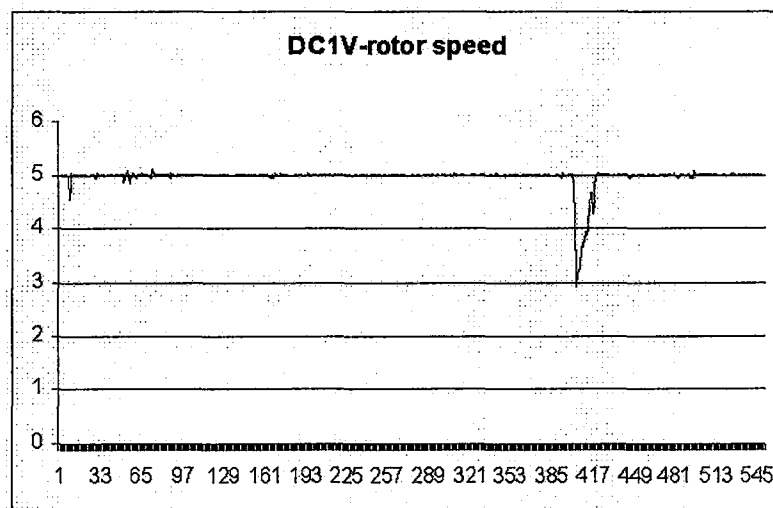


Figure 5.22 Recorded rotor speed of the DCIM (188 rpm/div)

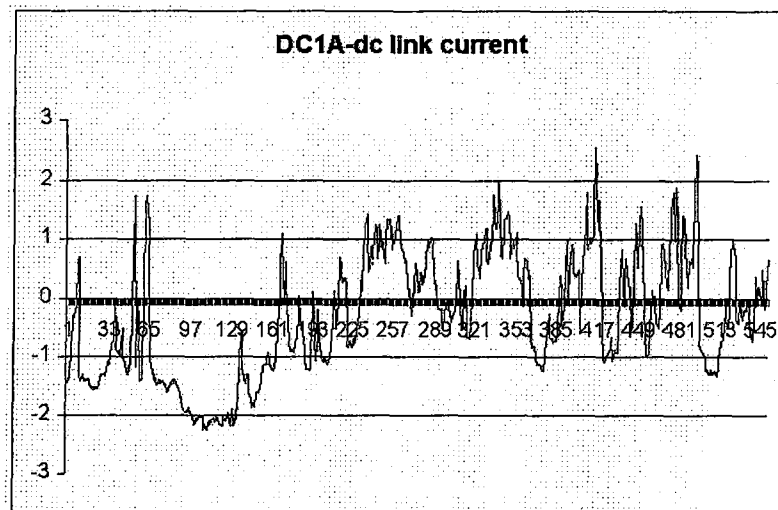


Figure 5.23 Recorded dc link current at a rotor speed of 940 rpm

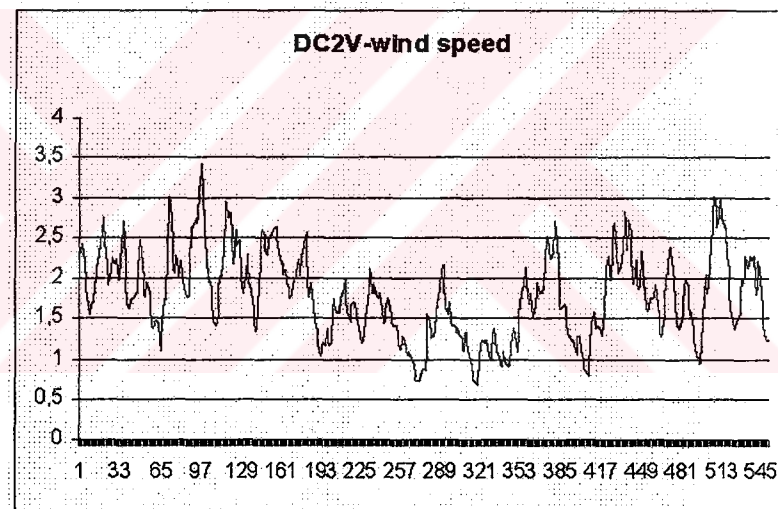


Figure 5.24 Recorded wind speed at a rotor speed of 940 rpm (3.2m/s/div)

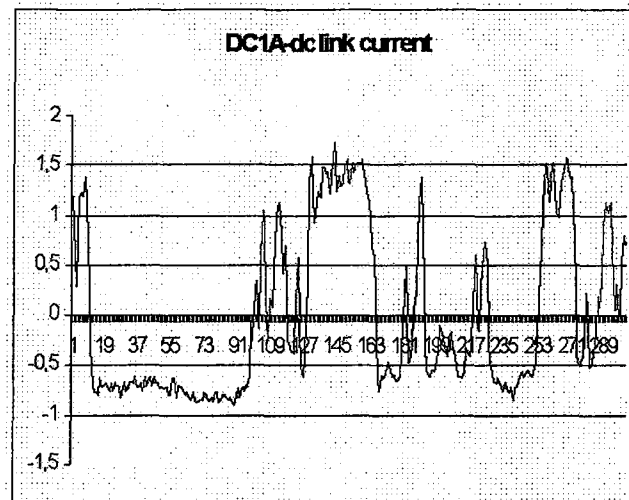


Figure 5.25 Recorded dc link current at a rotor speed of 865 rpm

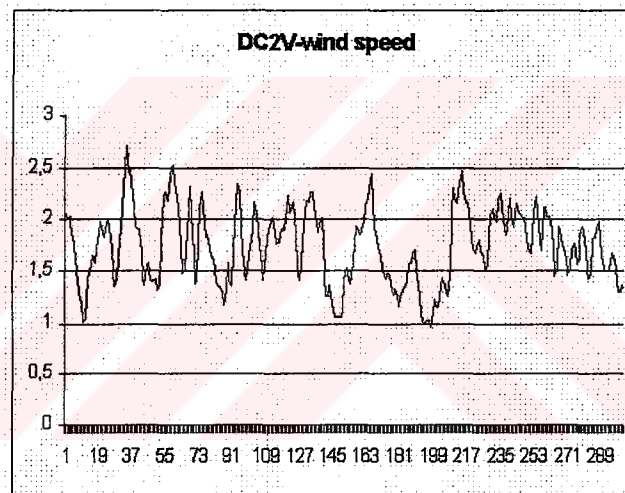


Figure 5.26 Recorded wind speed at a rotor speed of 865 rpm (3.2m/s/div)

In Figure 5.27, the recorded waveforms of voltage and current on the grid are shown, when the rotor speed of the DCIM is fixed at 940 rpm. The line to neutral supply voltage is fixed at 180V rms and the rms ac line current is measured approximately 2A. These waveforms are recorded when the power delivered to the grid is measured to be approximately 1kW. The measured quantities are also recorded at another rotor speed of the DCIM. In Figure 5.28, the recorded waveforms of voltage and current on the grid are shown, when the rotor speed of the DCIM is fixed at 865 rpm. The measured value of the rms ac line current is approximately 1.2A. These waveforms are recorded when the power delivered to the grid is

measured to be approximately 600W. As shown from these figures, the line-side converter keeps the operation at unity power factor and line currents approximately sinusoidal except switching transients in hysteresis band. The ac line current waveforms shown in these figures contain an acceptable level of distortion. The line currents are forced to stay in a fixed hysteresis bandwidth of 0.4A and the increase in execution time of the DSP reduces the maximum switching frequency of the hysteresis current controller. This causes some amount of error in tracking of actual ac line currents, which in effect violates the defined hysteresis band. As a result, the total harmonic distortion is at higher levels when the peak current is lower but it is reduced as the magnitude of the ac line currents increase. The instantaneous wind speed and DCIM phase current waveforms obtained at 940 rpm and 865 rpm are shown in Figure 5.29 and Figure 5.30, respectively. The switching frequency of the PWM converter connected to the DCIM terminals is 2 kHz. Therefore, the effect of this switching is clearly observed on DCIM current waveform. The audible noise is not taken into consideration. In order to reduce the switching losses in the converter, the switching frequency is kept lower at the value of 2 kHz.

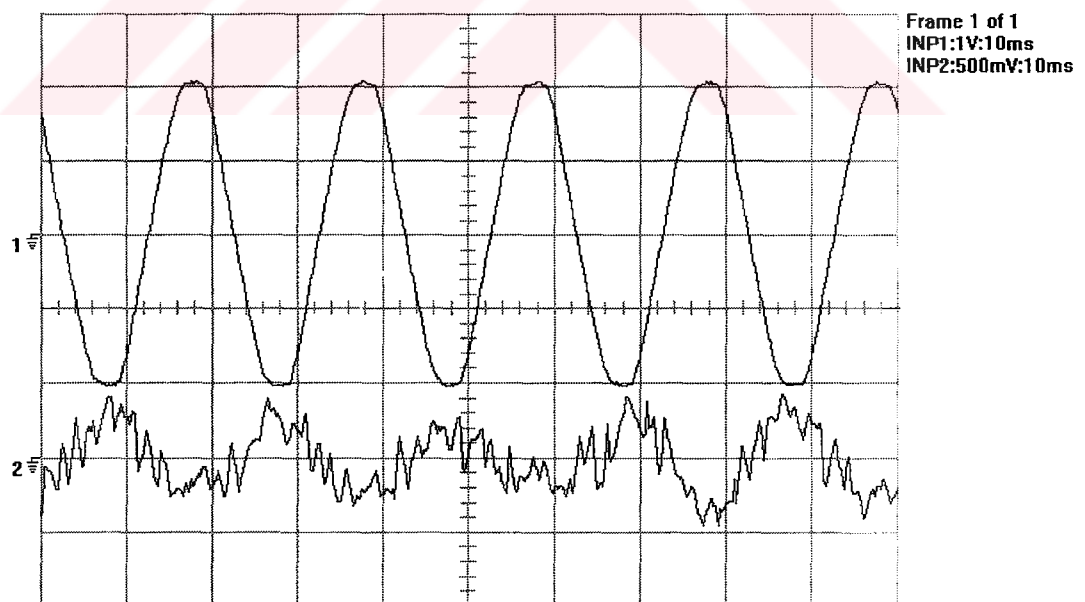


Figure 5.27 Grid voltage and current on the line side when the rotor speed is fixed at 940 rpm (upper trace: grid voltage-125V/div, lower trace: grid current-4A/div)

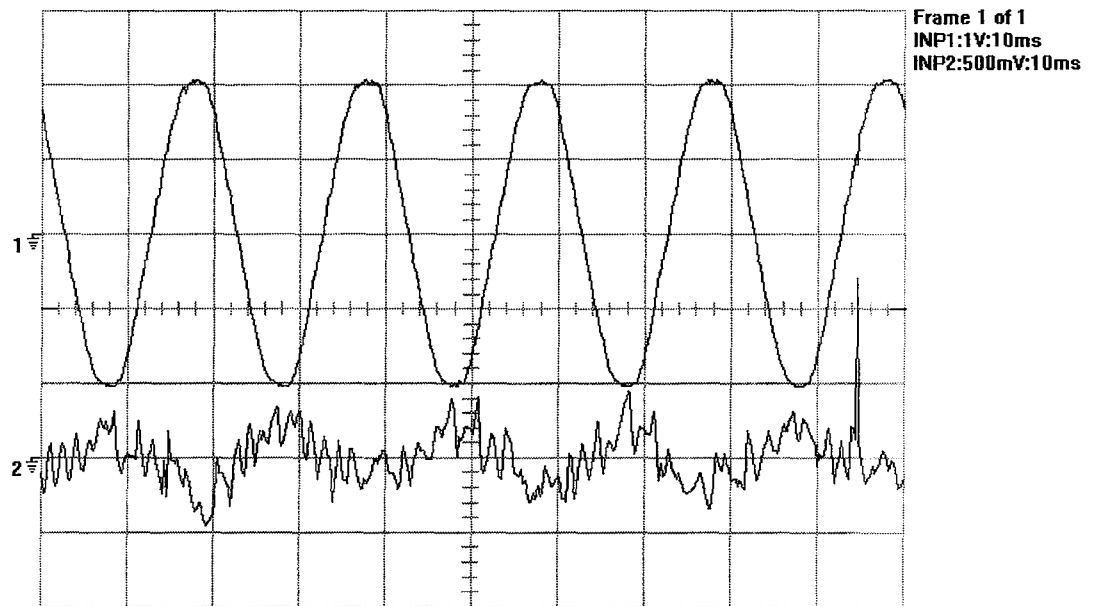


Figure 5.28 Grid voltage and current on the line side when the rotor speed is fixed at 865 rpm (upper trace: grid voltage-125V/div, lower trace: grid current-4A/div)

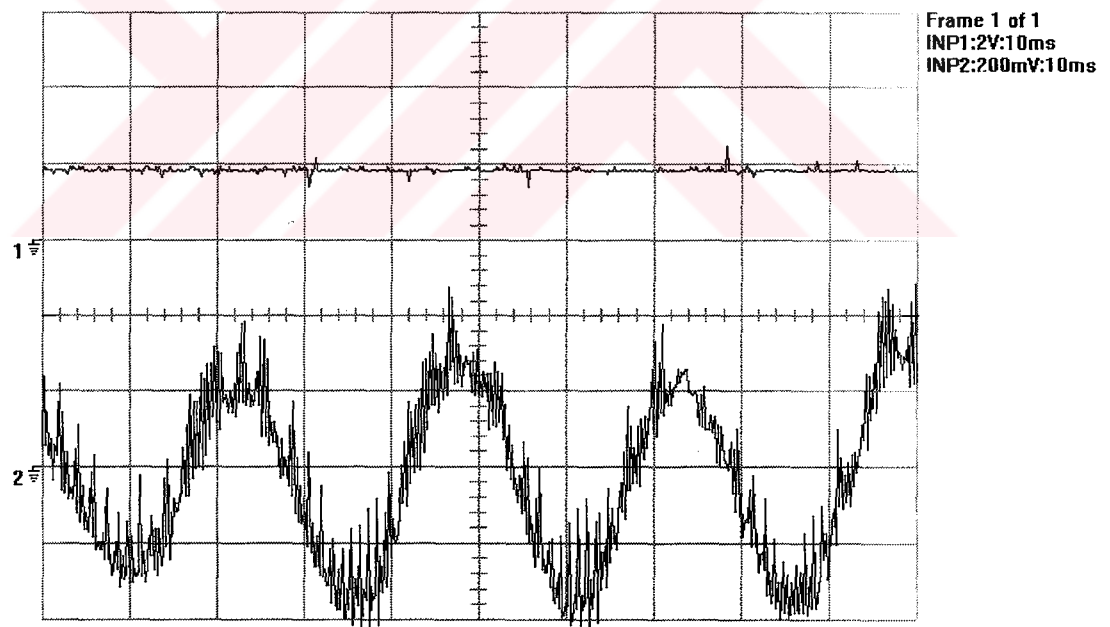


Figure 5.29 DCIM phase current and wind speed when the rotor speed is fixed at 940 rpm (upper trace: wind speed-3.2 m/s/div, lower trace: DCIM phase current-2A/div)

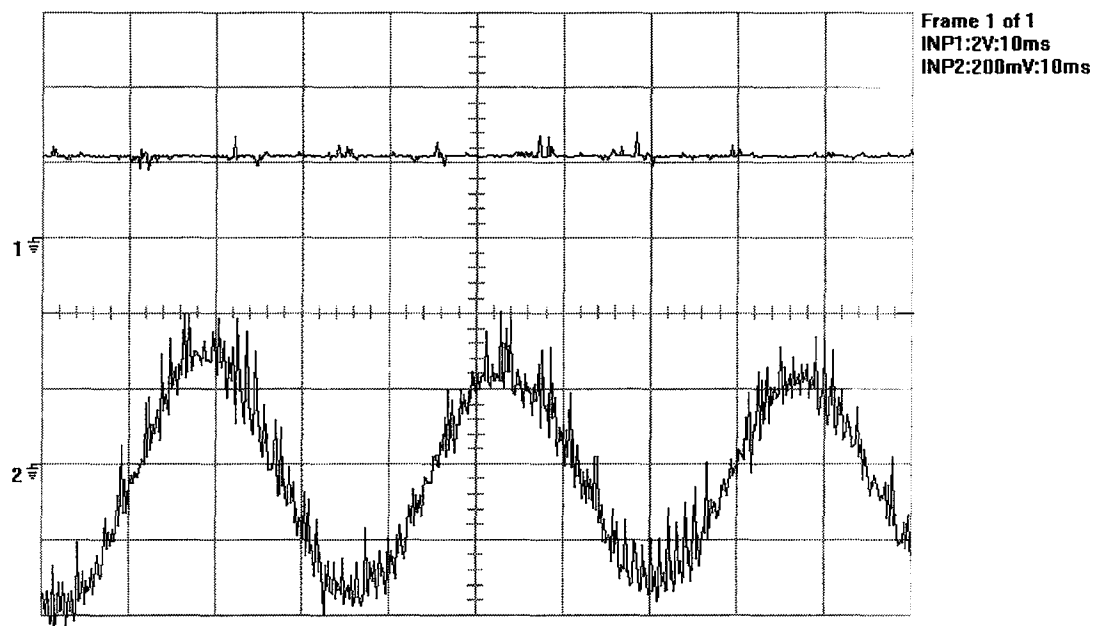


Figure 5.30 DCIM phase current and wind speed when the rotor speed is fixed at 865 rpm (upper trace: wind speed-3.2 m/s/div, lower trace: DCIM phase current-2A/div)

CHAPTER SIX

CONCLUSIONS

The abc/qd and qd/abc models have been obtained for a double-cage induction machine by using the transformations applied for the standard qd/qd model of the machine in reference frame theory. The simulation results during the transient and steady-state operations have been obtained from the models and compared with the test results. The genetic algorithm has been employed for the off-line determination of the motor parameters. This algorithm is sufficiently good for the estimation of these parameters, if the exact equivalent circuit equations in the cost function are properly defined. It is observed that the GA may not converge to a feasible solution if some of those equations are written from exact equivalent circuit and some of them are written from approximate equivalent circuit. Also, the mutual inductance between top and bottom part of the rotor slots, which does not exist in the double-cage induction machine models obtained from universal machine model, is considered in the formulation for the GA. With the equivalent circuit parameters obtained from GA and the derived models of the DCIM, the simulation results depicting the behavior of the machine closely matches to experimental results. However, the measured value of the peak starting current under no-load deviates from the simulation results. The reason for that is the effect of saturation on leakage reactances due to the high starting current, which is not included into the dynamic model of the machine. Also, the breakdown torque used in the GA is measured at the reduced voltage level because the dc machine ratings are not enough to load the induction motor up to breakdown torque under rated voltage. However, the peak of the torque at the rated voltage may not proportionally increase with the square of the voltage due to the saturation in the magnetic circuit.

The mathematical models of the PWM ac-dc-ac converters have been derived and combined with the DCIM model for computer simulations. The modeling of digital PI and fuzzy logic controllers are also included into these models. The system is simulated for motor and generator operation of the DCIM with these two types of controllers. The performance of the fuzzy logic controller due to the variation of the dc link voltage and rotor speed is found to be slightly better than PI controller with the same controller gains and operating conditions of the system.

The results obtained from simulations are verified by experimental ones carried out on the implemented system in the laboratory. Two back to back DSP based PWM converters are designed to control the power flow in the WECS. The control of the complete system was achieved by one fixed-point DSP. Total execution time of the DSP in one cycle of the program was approximately 250 microseconds, which is enough to control the system. In the implementation of the closed-loop controllers, the PI type is chosen because the execution time of the DSP increases with the application of the FLC due to increasing computational burden. One FLC routine brings an extra computational delay of approximately 200 microseconds and the total execution time of the DSP is almost doubled when a FLC are employed for speed or voltage control instead of PI. As a result, the maximum switching frequency of the line-side converter is reduced since the HCC updates the switching positions over a program cycle. Hence, the current tracking error on the line-side converter increases and this results in poor line current waveforms.

The experimental and simulation result show that even if the inverter output voltage is applied to the motor terminals at the frequency, which is equal to electrical rotor speed, the electromagnetic torque developed by the machine has a deep negative value. In order to eliminate this instant negative torque, which may cause damage on the coupling system, the effective value of voltage should be increased slowly with a ramp function. Laboratory tests are carried out for emulating the WECS and to investigate the performance of the implemented drive system. Since the power-speed characteristic of a dc machine is similar to that of wind turbine, the maximum power point tracking routine is also tested on the system in laboratory.

This simple search algorithm works well under stable loading conditions and lower moment of inertia of the system.

The performance of the system with a wind turbine is investigated by simulations including the turbine model to the derived converter and machine models. Hence, a complete model of the system is obtained. The implemented drive system is tested with a wind turbine and the electrical quantities are recorded during the operation of the system. Power fluctuations shown in the experimental records are due to turbulent wind conditions. The stability of the converters in the system is satisfactory under randomly varying wind conditions.



REFERENCES

Ackermann, T., & Söder, L. (2000). Wind Energy Technology and Current Status: a review. Renewable and Sustainable Energy Reviews. 4, 315-374.

Adkins, B., & Harley, R. (1975). The General Theory of Alternating Current Machines: Application to Practical Problems. London: Chapman and Hall.

Akagi, H., Tsukamoto, & Y., Nabae, A. (1990). Analysis and design of an active power filter using quad-series voltage source PWM converter. IEEE Transactions on Industry Applications. 26, no.1, 93-98.

Alger, P.L. (1965). The Nature of Induction Machines. London: Gordon and Breach.

Altas, I.H., & Sharaf, A.M. (1996). A novel on-line MPP search algorithm for PV arrays. IEEE Transactions on Energy Conversion. 11, no.4, 748-754.

Akpınar, E., & Pillay, P. (1990). Modeling and Performance of Slip Energy Recovery Induction Motor Drives. IEEE Transactions on Energy Conversion. 5, no. 1, 203-210.

Akpınar E., & Ungan, E. (1999). ABCdq Model of a 3-phase Induction Motor for Bus Transfer and Drives. Proceedings of International Conference on Power System Transients, June 20-24, Budapest, Hungary, 265-270.

Bansal, R.C., Bhatti, T.S., & Kothari, D.P. (2003). Bibliography on the Application of Induction Generators in Nonconventional Energy Systems. IEEE Transactions on Energy Conversion. 18, no.3 433-439.

- Blasko, V., & Kaura, V. (1997). A New Mathematical Model and Control of a Three-Phase AC-DC Voltage Source Converter. IEEE Transactions on Power Electronics. 12, no.1, 116-123.
- Brune, C.S., Spee, R., & Wallace, A.K. (1994). Experimental evaluation of a variable-speed doubly-fed wind power generation system. IEEE Transactions on Industry Applications. 30, no. 3, 648-655.
- Buehring, I.K., & Freris, L.L. (1981). Control policies for wind-energy conversion systems. IEE Proceedings. 128, pt. C, no.5, 253-261
- Chalmers, B.J., & Mulki, A.S. (1970). Design Synthesis of Double Cage Induction Motors. Proceedings of IEE. 117, no. 7, 1257-1263.
- Chapman, S.J. (2002). Electric Machinery Fundamentals (3rd ed.). New York: McGraw-Hill.
- Çadırcı, I., & Ermiş, M. (1992). Double-output induction generator operating at subsynchronous and supersynchronous speeds: steady-state performance optimization and wind-energy recovery. IEE Proceedings-B. 139, no.5, 429-442.
- Çadırcı, I., Ermiş, M., Nalçacı, E., Ertan, B., & Rahman M. (1999). A Solid State Direct On Line Starter for Medium Voltage Induction Motors with Minimized Current and Torque Pulsations. IEEE Transactions on Energy Conversion. 14, no. 3, 402-412.
- Dixon, J.W., & Ooi, B.T. (1988). Indirect current control of a unity power factor sinusoidal current boost type three-phase rectifier. IEEE Transactions on Industrial Electronics. 35, no.4, 508-515.
- DSP Solutions (1999). Creating a Sine Modulated PWM Signal Using the TMS320F240 EVM. Application Report: SPRA411. USA: Texas Instruments Inc.

Dubey, G.K. (1989). Power Semiconductor Controlled Drives.
New York: Prentice-Hall.

Ermış, M., Ertan, H.B., Akpınar, E., & Ülgüt, F. (1992). Autonomous wind-energy conversion system for maximum power transfer with a simple controller.
IEE Proceedings-B. 139, no. 5, 421-428.

Ersak, A., & Ermış, M. (1997). Principles of Electromechanical Energy Conversion.
Ankara: METU Press.

Fitzgerald, A.E., Kingsley, C. Jr., & Umans, D. (2003). Electric Machinery (6th ed.).
New York: McGraw-Hill.

Hansen, N.H., Helle, L., Blaabjerg, F., Ritchie, E., Munk-Nielsen, S., Bindner, H., Sorensen, P., & Bak-Jensen, B. (2001). Conceptual Survey of Generators and Power Electronics for Wind Turbines. Denmark: Ris National Laboratory Report.

IEEE Standard no.112-1996 (1997). Test Procedure for Polyphase Induction Motors and Generators. New York: IEEE Press.

Kassakian, J.G., Schlecht, M.F., & Verghese, G.C. (1991). Principles of Power Electronics. New York: Addison Wesley Publications.

Khalil, N.A., Tan, O.T., & Baran, I.U. (1982). Reduced Order Models for Double Cage Induction Motors. IEEE Transactions on Power Apparatus and Systems. PAS-101, no. 9, 3135-3140.

Khater, F.M.H. (1996). Power electronics in wind energy conversion systems. Proceedings of Energy Conversion Engineering Conference. 3, 1773-1776.

Kostenko, M., & Piotrovsky, L. (1977). Electrical Machines vol.2 Alternating Current Machines. Moscow: MIR Publishers.

Krause, P.C., Wasynczuk, O., & Sudhoff, S.D. (1994). Analysis of Electric Machinery. New York: IEEE Press.

Lee, C.C. (1990). Fuzzy Logic in Control Systems: Fuzzy Logic Controller-Part I. IEEE Transactions on Systems, Man, and Cybernetics. 20, no.2, 404-418.

Lee, C.C. (1990). Fuzzy Logic in Control Systems: Fuzzy Logic Controller, Part II. IEEE Transactions on Systems, Man, and Cybernetics. 20, no.2, 419-435.

LEM (1996). Isolated Current and Voltage Transducers: Characteristics–Applications–Calculations. Switzerland: LEM Corporate Communications.

Liao, J.C., & Yeh, S.N. (2000). A Novel Instantaneous Power Control Strategy and Analytic Model for Integrated Rectifier/Inverter Systems. IEEE Transactions on Power Electronics. 15, no.6, 996-1006

Lima, M.L., Silvino, J.L., & Resende, P. (1999). H_{∞} controller for a variable-speed adjustable-pitch wind energy conversion system. Proceedings of IEEE International Symposium on Industrial Electronics. Slovenia, 2, 556-561.

Liserre, M. (2001). Innovative control techniques of power converters for industrial automation. Politecnico di Bari, Italy Ph.D. Thesis.

Michalewicz, Z. (1992). Genetic Algorithms + Data Structures = Evolution Programs. New York: Springer.

Nabeta, S.I., Chabu, I.E., Cardoso, J.R., & Foggia, A. (1997). Double Cage Induction Motor Modelling Using Finite Elements. Electric Machines and Drives Conference Record. 18-21 May, WA2/5.1-WA2/5.3.

Nangsue, P., Pillay, P., & Conry, S.E. (1999). Evolutionary Algorithms for Induction Motor Parameter Determination. IEEE Transactions on Energy Conversion.

14, no. 3, 447-453.

Ooi, B.T., Salmon, J.C., & Dixon, J.W. (1987). A three-phase controlled current PWM converter with leading power factor. IEEE Transactions on Industry Applications. IA-23, no.1, 78-84.

Ong, C.M. (1998). Dynamic Simulation of Electric Machinery Using Matlab/Simulink. New Jersey: Prentice Hall.

Pena, R., Cardenas, R., Blasco, R., Asher, G., & Clare, J. (2001). A cage induction generator using back to back PWM converters for variable speed grid connected wind energy system. Proceedings of IECON 2001. Denver, USA, 2, 1376-1381.

Raviraj, V.S.C., & Sen, P.C. (1997). Comparative Study of Proportional-Integral, Sliding Mode, and Fuzzy Logic Controllers for Power Converters. IEEE Transactions on Industry Applications. 33, no.2, 518-524.

Richards, G. (1988). Reduced Order Model for Single and Double Cage Induction Motors During Startup. IEEE Transactions on Energy Conversion. 3, no. 2, 335-341.

Richards, G., & Sarma, P.R.R. (1994). Reduced Order Models for Induction Motors with Two Rotor Circuits. IEEE Transactions on Energy Conversion. 9, no. 4, 673-678.

Ross, T.J. (1995). Fuzzy Logic with Engineering Applications. New York: McGraw-Hill.

Shahalami, S.H., & Saadate, S. (1998). Genetic Algorithm Approaches in the Identification of Squirrel Cage Induction Motor's Parameters. Proceedings of International Conference on Electrical Machines. Istanbul, 908-913.

Simoes, M.G., Bose, B.K., & Spiegel, R.J. (1997a). Design and Performance Evaluation of a Fuzzy-Logic Based Variable Speed Wind Generation System. IEEE Transactions on Industry Applications. 33, no. 4, 956-965.

Simoes, M.G., Bose, B.K., and Spiegel, R.J. (1997b). Fuzzy logic based intelligent control of a variable speed cage machine wind generation system. IEEE Transactions on Power Electronics. 12, no. 1, 87-95.

Singh, B.N., Singh, B., & Singh, B.P. (1999). Fuzzy Control of Integrated Current-Controlled Converter-Inverter –Fed Cage Induction Motor Drive. IEEE Transactions on Industry Applications. 35, no.2, 405-412.

Skvarenina, T.L. (2002). Power Electronics Handbook. New York: CRC Press.

Sürgevil, T., & Akpınar, E. (2003). abc/qd, qd/abc Model of a Double-Cage Induction Machine and Determination of Parameters Using Genetic Algorithm. Journal of Electric Power Components and Systems. 31, no:12, pp: 1115-1131.

Trzynadlowski, A.M. (1994). The Field Orientation Principle in Control of Induction Motors. Boston: Kluwer Academic Publishers.

Üçtuğ, M.Y., Eskandarzadeh, I., & İnce, H. (1994). Modelling and output power optimization of a wind turbine driven double output induction generator. IEE Proceedings of Electric Power Applications. 141, no. 2, 33-38.

Velayudhan, C., Bundell, J.H., & Leary, B.G. (1984). A solid-state controller for a wind driven slip-ring induction generator. Proceedings of IEEE. 72, no. 8, 1097-1099.

Walker, J.F., & Jenkins, N. (1997). Wind Energy Technology. Chichester: John Wiley & Sons

Waters, S.S., & Willoughby, R.D. (1983). Modeling Induction Motors for System Studies. IEEE Transactions on Industry Applications. IA-19, no. 5, 875-878.

WEB_1 (2003). American Wind Energy Association Web Site. Complimentary Resource Library, Wind Power Outlook.
<http://www.awea.org/pubs/complimentary.html>. 15/12/2003.

WEB_2 (2003). Bradley University Web Site. DSP Controllers-An Emerging Tool for Electric Motor Drives, by Andrzej M. Trzynadlowski.
http://sant.bradley.edu/ienews/98_3/trzynad.htm. 15/12/2003.

Wu, R., Dewan, S.B., & Slemon, G.R. (1990). A PWM ac-to-dc converter with fixed switching frequency. IEEE Transactions on Industry Applications. 26, no.5, 880-885

Wu, R., Dewan, S.B., & Slemon, G.R. (1991a). Analysis of an ac-to-dc voltage source converter using PWM with phase amplitude control. IEEE Transactions on Industry Applications. 27, no.2, 355-364.

Wu, R., Dewan, S.B., & Slemon, G.R. (1991b). Analysis of a PWM ac to dc voltage source converter under the predicted current control with a fixed switching frequency. IEEE Transactions on Industry Applications. 27, no.4, 756-764.

Zakharov, A. (1996). Investigation of DC Servo Drive with Fuzzy Logic Control. Technical University of Budapest M.Sc. Thesis.

Zargari, N.R., & Joos, G. (1995). Performance investigation of current-controlled voltage-regulated PWM rectifier in rotating and stationary frames. IEEE Transactions on Industrial Electronics. 42, no.4, 396-401.

Zinger, D.S., Muljadi, E. (1997). Annualized Wind Energy Improvement Using Variable-Speeds. IEEE Transactions on Industry Applications. 33, no.6 1444-1447.

FURTHERWORK

The simulations have not been performed yet for the recorded wind speed, since the complete data for the turbine modeling are not provided by the manufacturer and the wind direction is not recorded in experiments. The modeling of the turbine can be obtained from long term measurements including the wind direction. By adjusting the rotational speed over a wide range of operation and recording the measurements over a long time range, the power-speed characteristic of the turbine can be obtained. Hence, the turbine model used in simulations can be replaced by a new one with only a few modifications. By including the wind direction into turbine model, it is possible to predict the dynamic behavior of the implemented system under varying wind conditions.

APPENDIX A

Trigonometric Relations

$$\cos x + \cos(x - 120^\circ) + \cos(x + 120^\circ) = 0$$

$$\sin x + \sin(x - 120^\circ) + \sin(x + 120^\circ) = 0$$

$$\sin x \cos x + \sin(x - 120^\circ) \cos(x - 120^\circ) + \sin(x + 120^\circ) \cos(x + 120^\circ) = 0$$

$$\cos^2 x + \cos^2(x - 120^\circ) + \cos^2(x + 120^\circ) = \frac{3}{2}$$

$$\sin^2 x + \sin^2(x - 120^\circ) + \sin^2(x + 120^\circ) = \frac{3}{2}$$

$$\sin x \cos y + \sin(x - 120^\circ) \cos(y - 120^\circ) + \sin(x + 120^\circ) \cos(y + 120^\circ) = \frac{3}{2} \sin(x - y)$$

$$\sin x \sin y + \sin(x - 120^\circ) \sin(y - 120^\circ) + \sin(x + 120^\circ) \sin(y + 120^\circ) = \frac{3}{2} \cos(x - y)$$

$$\cos x \sin y + \cos(x - 120^\circ) \sin(y - 120^\circ) + \cos(x + 120^\circ) \sin(y + 120^\circ) = -\frac{3}{2} \sin(x - y)$$

$$\cos x \cos y + \cos(x - 120^\circ) \cos(y - 120^\circ) + \cos(x + 120^\circ) \cos(y + 120^\circ) = \frac{3}{2} \cos(x - y)$$

$$\sin x \cos y + \sin(x + 120^\circ) \cos(y - 120^\circ) + \sin(x - 120^\circ) \cos(y + 120^\circ) = \frac{3}{2} \sin(x + y)$$

$$\sin x \sin y + \sin(x + 120^\circ) \sin(y - 120^\circ) + \sin(x - 120^\circ) \sin(y + 120^\circ) = -\frac{3}{2} \cos(x + y)$$

$$\cos x \sin y + \cos(x + 120^\circ) \sin(y - 120^\circ) + \cos(x - 120^\circ) \sin(y + 120^\circ) = \frac{3}{2} \sin(x + y)$$

$$\cos x \cos y + \cos(x + 120^\circ) \cos(y - 120^\circ) + \cos(x - 120^\circ) \cos(y + 120^\circ) = \frac{3}{2} \cos(x + y)$$

Basic Genetic Algorithm C Source Code, Applied for the Parameter Determination of Double-Cage Induction Machine

```
//-----  
#include <vc1\condefs.h>  
#include <stdio.h>  
#include <stdlib.h>  
#include <string.h>  
  
#pragma hdrstop  
//-----  
#include <stdio.h>  
#include <stdlib.h>  
#include <math.h>  
  
#define NVAR 8  
  
double Vs,Vsbd,Tfl,Tbd,Tlr,Ws,pf;  
double sfl,slr,sbd,Znl;  
double Re0,Xrun0,Re1,Xrun1,Re2,Xrun2;  
double Vth,Rth,Xth,Rfl,Xfl,Rlr,Xlr,Rbd,Xbd;  
double x[NVAR+1];  
  
//x[1]=R1  
//x[2]=X1  
//x[3]=XM  
//x[4]=R2  
//x[5]=R3  
//x[6]=X2  
//x[7]=X3  
//x[8]=X23  
  
#define Re0  
((x[4]*x[5]*(x[4]+x[5])+sfl*sfl*(x[4]*x[7]*x[7]+x[5]*x[6]*x[6]))/((x[4]+x[5])*(x[4]+x[5])+sfl*sfl*(x[6]+x[7])*(x[6]+x[7])))  
#define Xrun0  
((x[4]*x[4]*x[7]+x[5]*x[5]*x[6]+sfl*sfl*x[6]*x[7]*(x[6]+x[7]))/((x[4]+x[5])*(x[4]+x[5])+sfl*sfl*(x[6]+x[7])*(x[6]+x[7]))+(x[8]))  
#define Re1  
((x[4]*x[5]*(x[4]+x[5])+slr*slr*(x[4]*x[7]*x[7]+x[5]*x[6]*x[6]))/((x[4]+x[5])*(x[4]+x[5])+slr*slr*(x[6]+x[7])*(x[6]+x[7])))  
#define Xrun1  
((x[4]*x[4]*x[7]+x[5]*x[5]*x[6]+slr*slr*x[6]*x[7]*(x[6]+x[7]))/((x[4]+x[5])*(x[4]+x[5])+slr*slr*(x[6]+x[7])*(x[6]+x[7]))+(x[8]))  
#define Re2  
((x[4]*x[5]*(x[4]+x[5])+sbd*sbd*(x[4]*x[7]*x[7]+x[5]*x[6]*x[6]))/((x[4]+x[5])*(x[4]+x[5])+sbd*sbd*(x[6]+x[7])*(x[6]+x[7])))  
#define Xrun2  
((x[4]*x[4]*x[7]+x[5]*x[5]*x[6]+sbd*sbd*x[6]*x[7]*(x[6]+x[7]))/((x[4]+x[5])*(x[4]+x[5])+sbd*sbd*(x[6]+x[7])*(x[6]+x[7]))+(x[8]))  
  
#define Vth Vs*x[3]/sqrt(x[1]*x[1]+(x[2]+x[3])*(x[2]+x[3]))  
#define Rth (x[3]*x[3]*x[1])/(x[1]*x[1]+(x[2]+x[3])*(x[2]+x[3]))
```

```

#define Xth
(x[3]*(x[1]*x[1]+x[2]*x[2])+x[3]*x[3]*x[2])/(x[1]*x[1]+(x[2]+x[3])*(
x[2]+x[3]))

#define FUNCTION1
100*100*pow((3*Vth*Vth*Re0/(Tfl*Ws*sfl*(pow((Rth+Re0/sfl),2)+pow((Xt
h+Xrun0),2)))-1),2) /*Tfl*/
#define FUNCTION2
100*100*pow((3*Vth*Vth*Re2/(Tbd*Ws*sbd*(pow((Rth+Re2/sbd),2)+pow((Xt
h+Xrun2),2)))-1),2) /*Tbd*/
#define FUNCTION3
100*100*pow((3*Vth*Vth*Re1/(Tlr*Ws*(pow((Rth+Re1),2)+pow((Xth+Xrun1
),2)))-1),2) /*Tlr*/

#define Rfl
x[1]+(x[3]*x[3]*Re0/sfl)/((Re0/sfl)*(Re0/sfl)+(x[3]+Xrun0)*(x[3]+Xru
n0))
#define Xfl
x[2]+(x[3]*((Re0/sfl)*(Re0/sfl)+Xrun0*Xrun0)+x[3]*x[3]*Xrun0)/((Re0/
sfl)*(Re0/sfl)+(x[3]+Xrun0)*(x[3]+Xrun0))
#define FUNCTION4 100*100*pow((cos(atan((Xfl)/(Rfl)))/pf-1),2)
/*pf*/

#define FUNCTION5
100*100*pow((sqrt(x[1]*x[1]+(x[2]+x[3])*(x[2]+x[3]))/Znl-1),2)
/*Znl*/
#define FUNCTION6 100*100*pow((x[4]-(0.75*x[5])),2)

#define FUNCTION
100/(100+(sqrt(FUNCTION1)+sqrt(FUNCTION2)+sqrt(FUNCTION3)+sqrt(FUNCT
ION4)+sqrt(FUNCTION5)+sqrt(FUNCTION6)))
//#define FUNCTION
100/(100+(sqrt(FUNCTION1)+sqrt(FUNCTION2)+sqrt(FUNCTION3)+sqrt(FUNCT
ION4)+sqrt(FUNCTION5)))

#define MAXPOPSIZE 100
#define TRUE 1
#define FALSE 0

void main();

int MINMAX; /* maximize or minimize */
int POPSIZE; /* population size */
int MAXGENS; /* max number of generations */
float PXOVER; /* crossover rate */
float PMUTATION; /* mutation rate */
int generation; /* current generation no. */
int cur_best; /* best individual */
FILE *galog; /* an output file */

struct genotype /* genotype (GT), a member of population */
{
    double gene[NVARS]; /* a string of variables */
    double fitness; /* GT's fitness */
    double upper[NVARS]; /* GT's variables upper bound */
    double lower[NVARS]; /* GT's variables lower bound */
    double rfitness; /* relative fitness */
    double cfitness; /* cumulative fitness */
};

```



```

struct genotype population[MAXPOPSIZE+1];    /* population */
struct genotype newpopulation[MAXPOPSIZE+1]; /* new population; */
/* replaces the */
/* old generation */

/* Declaration of procedures used by this genetic algorithm */

void initialize(void);
double randval(double, double);
void evaluate(void);
void keep_the_best(void);
void elitist(void);
void select(void);
void crossover(void);
void Xover(int,int);
void swap(double *, double *);
void mutate(void);
void report(void);
/*****
/* Initialization function: Initializes the values of genes */
/* within the variables bounds. It also initializes (to zero) */
/* all fitness values for each member of the population. It */
/* takes upper and lower bounds of each variable. It randomly */
/* generates values between these bounds for each gene of each*/
/* genotype in the */
*****/

void initialize(void)
{
    int i, j;
    double lbound, ubound;

    /* initialize variables within the bounds */

    for (i = 0; i < NVARS; i++)
    {
        printf("enter lowerbound and upperbound of variable %i>",i);
        scanf("%lf",&lbound);
        scanf("%lf",&ubound);

        for (j = 0; j < POPSIZE; j++)
        {
            population[j].fitness = 0;
            population[j].rfitness = 0;
            population[j].cfitness = 0;
            population[j].lower[i] = lbound;
            population[j].upper[i] = ubound;
            population[j].gene[i] = randval(population[j].lower[i],
                population[j].upper[i]);
        }
    }
}

/*****
/* Random value generator: Generates a value within bounds */
*****/

```

```

double randval(double low, double high)
{
double val;
val = ((double) (rand()%1000)/1000.0)*(high - low) + low;
return(val);
}

/*****
/* Evaluation function: This takes a user defined function.  */
/* Each time this is changed, the code has to be recompiled.  */
*****/

void evaluate(void)
{
int mem;
int i;

for (mem = 0; mem < POPSIZE; mem++)
{
for (i = 0; i < NVAR; i++)
x[i+1] = population[mem].gene[i];
if (MINMAX==1)
{
population[mem].fitness = FUNCTION;
}
else
{
population[mem].fitness = -(FUNCTION);
}
}
}

/*****
/* Keep_the_best function: This function keeps track of the  */
/* best member of the population. Note that the last entry in */
/* the array Population holds a copy of the best individual  */
*****/

void keep_the_best()
{
int mem;
int i;
cur_best = 0; /* stores the index of the best individual */
for (mem = 0; mem < POPSIZE; mem++)
{
if (population[mem].fitness > population[POPSIZE].fitness)
{
cur_best = mem;
population[POPSIZE].fitness = population[mem].fitness;
}
}
/* once the best number in the population is found, copy the genes
*/
for (i = 0; i < NVAR; i++)
population[POPSIZE].gene[i] = population[cur_best].gene[i];
}

```

```

/*****
/* Elitist function: The best member of the previous generation */
/* is stored as the last in the array. If the best member of
/* the current generation is worse then the best member of the
/* previous generation, the latter one would replace the worst
/* member of the current population
*****/

void elitist()
{
int i;
double best, worst;          /* best and worst fitness values */

int best_mem, worst_mem; /* indexes of the best and worst member */

best = population[0].fitness;
worst = population[0].fitness;
for (i = 0; i < POPSIZE - 1; ++i)
{
    if(population[i].fitness > population[i+1].fitness)
    {
        if (population[i].fitness >= best)
        {
            best = population[i].fitness;
            best_mem = i;
        }
        if (population[i+1].fitness <= worst)
        {
            worst = population[i+1].fitness;
            worst_mem = i+1;
        }
    }
    else
    {
        if (population[i].fitness <= worst)
        {
            worst = population[i].fitness;
            worst_mem = i;
        }
        if (population[i+1].fitness >= best)
        {
            best = population[i+1].fitness;
            best_mem = i+1;
        }
    }
}

/* if best individual from the new population is better than */
/* the best individual from the previous population, then    */
/* copy the best from the new population; else replace the   */
/* worst individual from the current population with the     */
/* best one from the previous generation                      */

if (best >= population[POPSIZE].fitness)
{
    for (i = 0; i < NVAR; i++)
        population[POPSIZE].gene[i] = population[best_mem].gene[i];
    population[POPSIZE].fitness = population[best_mem].fitness;
}
else

```

```

    {
        for (i = 0; i < NVAR; i++)
            population[worst_mem].gene[i] = population[POPSIZE].gene[i];
        population[worst_mem].fitness = population[POPSIZE].fitness;
    }
}
/*****
/* Selection function: Standard proportional selection for
/* maximization problems incorporating elitist model - makes
/* sure that the best member survives
*****/

void select(void)
{
    int mem, i, j, k;
    double sum = 0;
    double p;
    /* find total fitness of the population */
    for (mem = 0; mem < POPSIZE; mem++)
    {
        sum += population[mem].fitness;
    }
    /* calculate relative fitness */
    for (mem = 0; mem < POPSIZE; mem++)
    {
        population[mem].rfitness = population[mem].fitness/sum;
    }
    population[0].cfitness = population[0].rfitness;

    /* calculate cumulative fitness */
    for (mem = 1; mem < POPSIZE; mem++)
    {
        population[mem].cfitness = population[mem-1].cfitness +
            population[mem].rfitness;
    }
    /* finally select survivors using cumulative fitness. */

    for (i = 0; i < POPSIZE; i++)
    {
        p = rand()%1000/1000.0;
        if (p < population[0].cfitness)
            newpopulation[i] = population[0];
        else
        {
            for (j = 0; j < POPSIZE; j++)
                if (p >= population[j].cfitness &&
                    p < population[j+1].cfitness)
                    newpopulation[i] = population[j+1];
        }
    }
    /* once a new population is created, copy it back */

    for (i = 0; i < POPSIZE; i++)
        population[i] = newpopulation[i];
}

/*****
/* Crossover selection: selects two parents that take part in
/* the crossover. Implements a single point crossover
*****/

```

```

/*****/

void crossover(void)
{
    int i, mem, one;
    int first = 0; /* count of the number of members chosen */
    double x;

    for (mem = 0; mem < POPSIZE; ++mem)
    {
        x = rand()%1000/1000.0;
        if (x < PXOVER)
        {
            ++first;
            if (first % 2 == 0)
                Xover(one, mem);
            else
                one = mem;
        }
    }
}
/*****/
/* Crossover: performs crossover of the two selected parents. */
/*****/

void Xover(int one, int two)
{
    int i;
    int point; /* crossover point */

    /* select crossover point */
    if(NVARS > 1)
    {
        if(NVARS == 2)
            point = 1;
        else
            point = (rand() % (NVARS -1)) + 1;

        for (i = 0; i < point; i++)
            swap(&population[one].gene[i], &population[two].gene[i]);
    }
}
/*****/
/* Swap: A swap procedure that helps in swapping 2 variables */
/*****/

void swap(double *x, double *y)
{
    double temp;

    temp = *x;
    *x = *y;
    *y = temp;
}

/*****/
/* Mutation: Random uniform mutation. A variable selected for */
/* mutation is replaced by a random value between lower and */
/* upper bounds of this variable */
/*****/

```

```

/*****/

void mutate(void)
{
    int i, j;
    double lbound, hbound;
    double x;

    for (i = 0; i < POPSIZE; i++)
        for (j = 0; j < NVAR; j++)
        {
            x = rand()%1000/1000.0;
            if (x < PMUTATION)
            {
                /* find the bounds on the variable to be mutated */
                lbound = population[i].lower[j];
                hbound = population[i].upper[j];
                population[i].gene[j] = randval(lbound, hbound);
            }
        }
}

/*****/
/* Report function: Reports progress of the simulation. Data */
/* dumped into the output file are separated by commas */
/*****/

void report(void)
{
    int i;
    double best_val; /* best population fitness */
    double avg; /* avg population fitness */
    double stddev; /* std. deviation of population fitness */
    double sum_square; /* sum of square for std. calc */
    double square_sum; /* square of sum for std. calc */
    double sum; /* total population fitness */

    sum = 0.0;
    sum_square = 0.0;

    for (i = 0; i < POPSIZE; i++)
    {
        sum += population[i].fitness;
        sum_square += population[i].fitness * population[i].fitness;
    }
    if (MINMAX==1)
    {
        avg = sum/(double)POPSIZE;
        best_val = population[POPSIZE-1].fitness;
    }
    else
    {
        avg = -sum/(double)POPSIZE;
        best_val = -(population[POPSIZE-1].fitness);
    }
    square_sum = avg * avg * (double)POPSIZE;
    stddev = sqrt((sum_square - square_sum)/(POPSIZE - 1));

    fprintf(galog, "\n%5d, %6.3f,%6.3f,%6.3f \n\n", generation,
        best_val, avg, stddev);
}

```

```

}
/*****
/* Main function: Each generation involves selecting the best */
/* members, performing crossover & mutation and then          */
/* evaluating the resulting population, until the terminating */
/* condition is satisfied                                     */
*****/

void main(void)
{
    int i;
    printf("maximize(1) or minimize(0) the function>");
    scanf("%d",&MINMAX);
    printf("enter population size (max 100)>");
    scanf("%d",&POPSIZE);
    printf("enter generation number (greater than 500)>");
    scanf("%d",&MAXGENS);
    printf("enter crossover rate (about 0.8)>");
    scanf("%f",&PXOVER);
    printf("enter mutation rate (about 0.2)>");
    scanf("%f",&PMUTATION);

    Vs=230;
    Vsbd=163;
    Tfl=16.8;
    Tlr=23.2;
    Tbd=31.5;
    sfl=0.0467;
    slr=1.0000;
    sbd=0.2000;
    Znl=176.9;
    pf=0.8700;
    Ws=157.1;

    //sfl=0.047;
    //sbd=0.267;
    //printf("full-load rotor resistance (Re_fl)=");
    //scanf("%lf",&Re_fl);
    //printf("full-load rotor reactance (Xrun_fl)=");
    //scanf("%lf",&Xrun_fl);
    //printf("locked-rotor resistance (Re_lr)=");
    //scanf("%lf",&Re_lr);
    //printf("locked-rotor reactance (Xrun_lr)=");
    //scanf("%lf",&Xrun_lr);
    //printf("breakdown rotor reactance (Xrun_bd)=");
    //scanf("%lf",&Xrun_bd);
    //printf("full-load slip (sfl)=");
    //scanf("%lf",&sfl);
    //printf("breakdown slip (sbd)=");
    //scanf("%lf",&sbd);

    if ((galog = fopen("galog.txt","w"))==NULL)
    {
        exit(1);
    }
    generation = 0;

    fprintf(galog, "\n generation best    average standart \n");
    fprintf(galog, " number        value  fitness deviation \n");

```

```

initialize();
evaluate();
keep_the_best();
while(generation<MAXGENS)
{
    generation++;
    select();
    crossover();
    mutate();
    report();
    evaluate();
    elitist();
}
fprintf(galog,"\n\n Simulation completed!!!\n");
fprintf(galog,"\n Best member: \n");

for (i = 0; i < NVARs; i++)
{
    fprintf (galog,"\n var(%d) =
%3.3f",i,population[POPSIZE].gene[i]);
}
if (MINMAX==1)
{
    fprintf(galog,"\n\n Best fitness =
%3.3f",population[POPSIZE].fitness);
}
else
{
    fprintf(galog,"\n\n Best fitness = %3.3f",-
(population[POPSIZE].fitness));
}
fclose(galog);

printf("\n\n Simulation completed!!!\n");
printf("\n Best member: \n");

for (i = 0; i < NVARs; i++)
{
    printf ("\n var(%d) = %3.3f",i,population[POPSIZE].gene[i]);
}
if (MINMAX==1)
{
    printf("\n\n Best fitness =
%3.3f\n",population[POPSIZE].fitness);
}
else
{
    printf("\n\n Best fitness = %3.3f\n",-
(population[POPSIZE].fitness));
}
printf(" Intermediate steps are in GALOG.TXT\n");
}

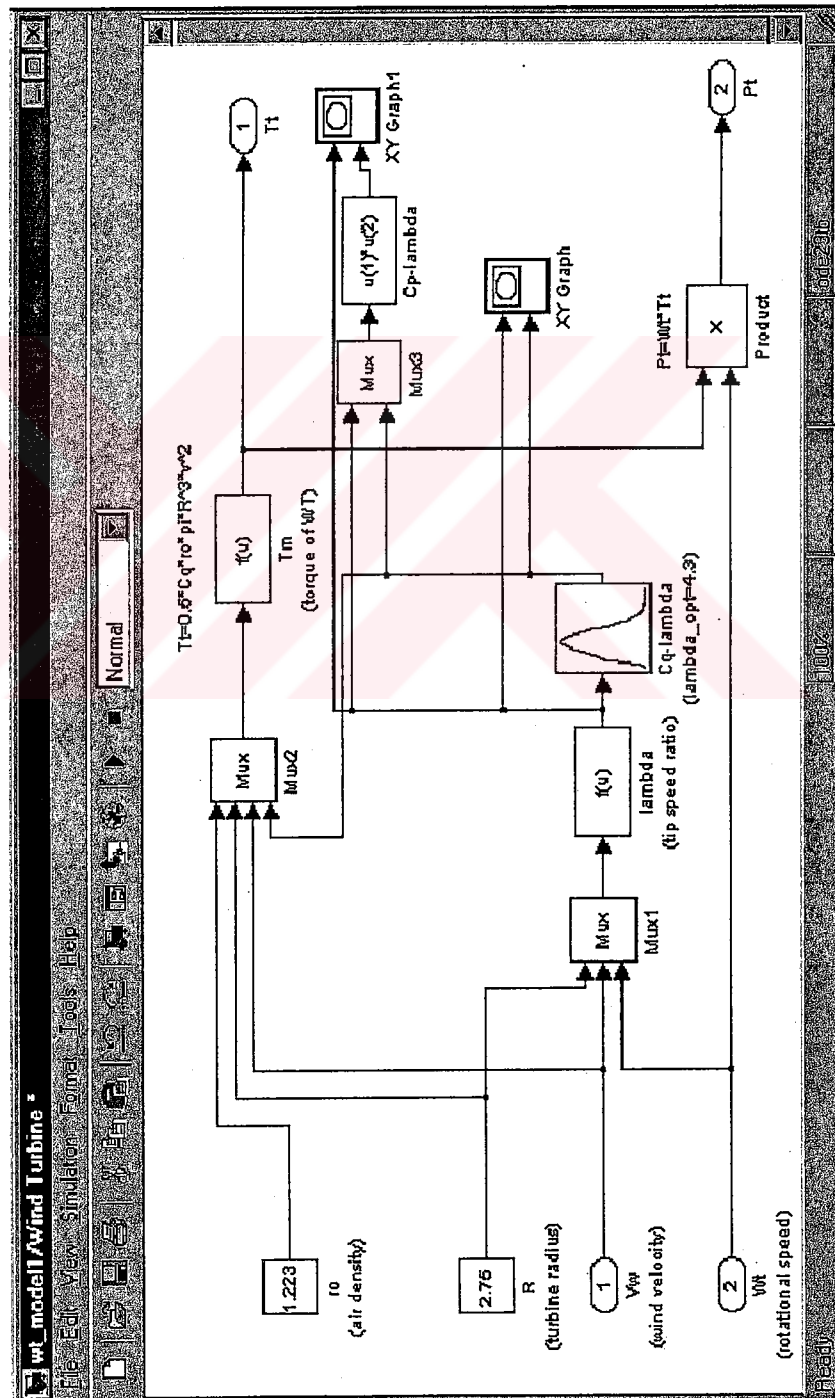
/*****END*****/
*****/

//-----

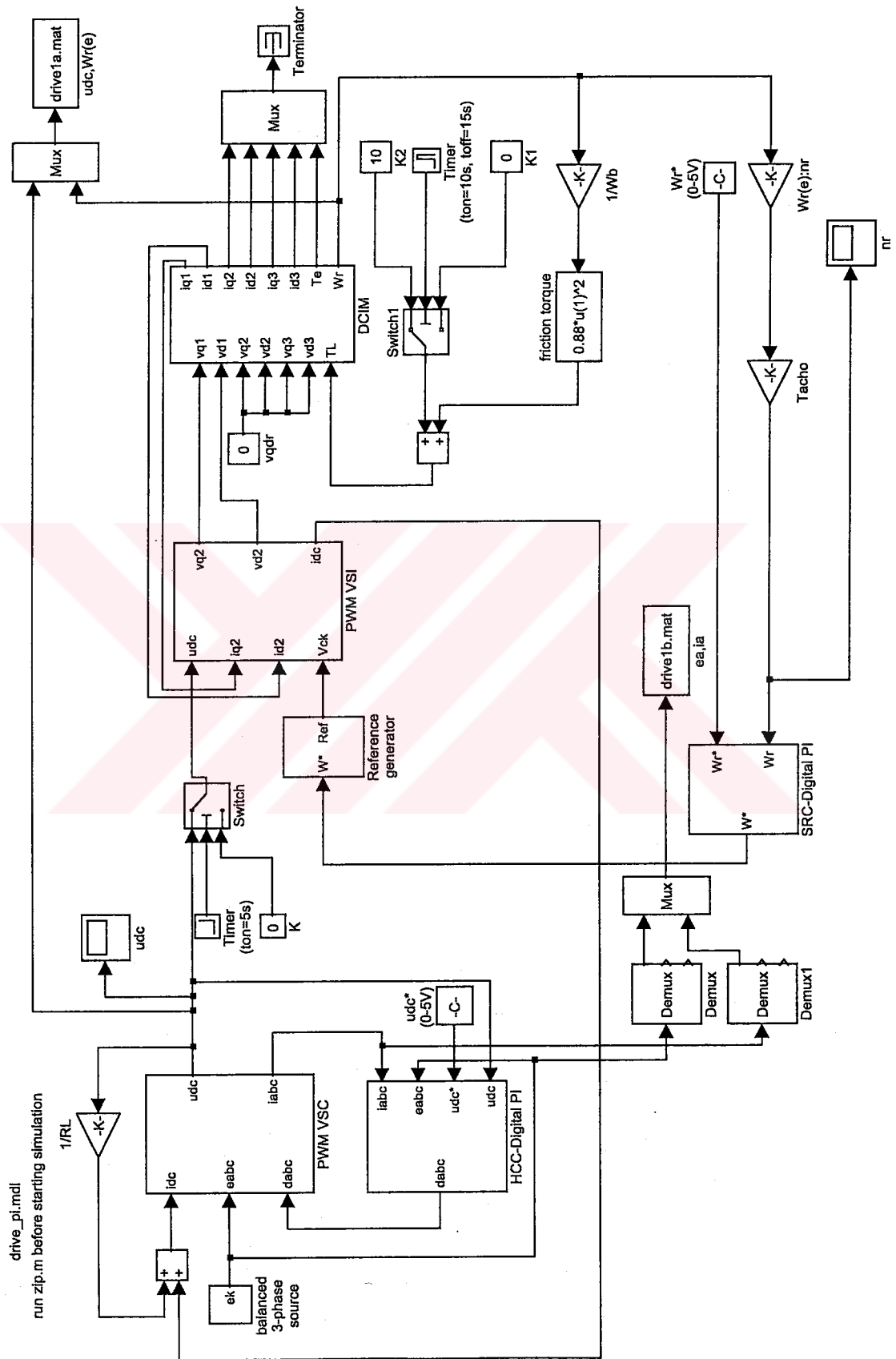
```


APPENDIX B

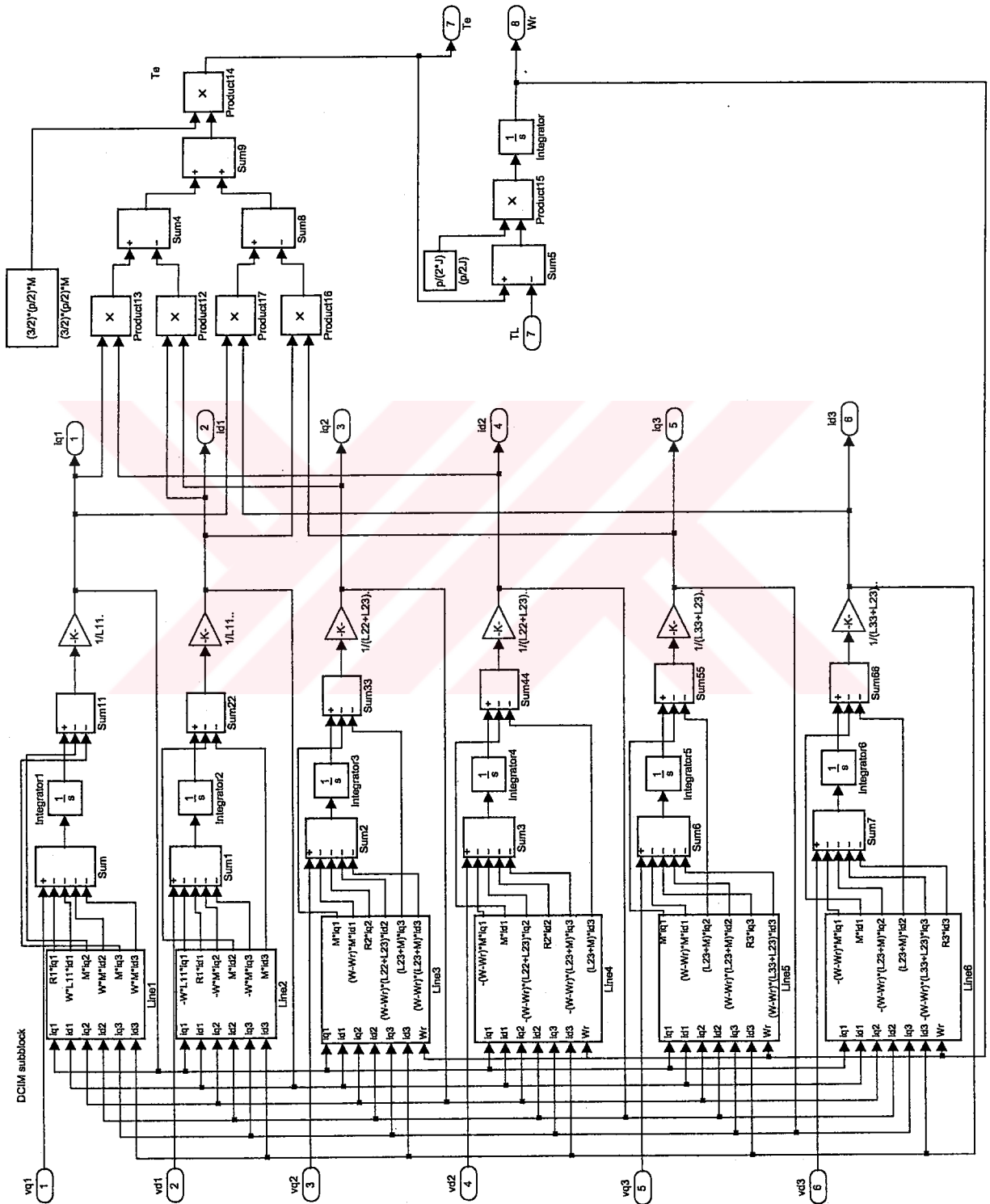
Wind Turbine Model

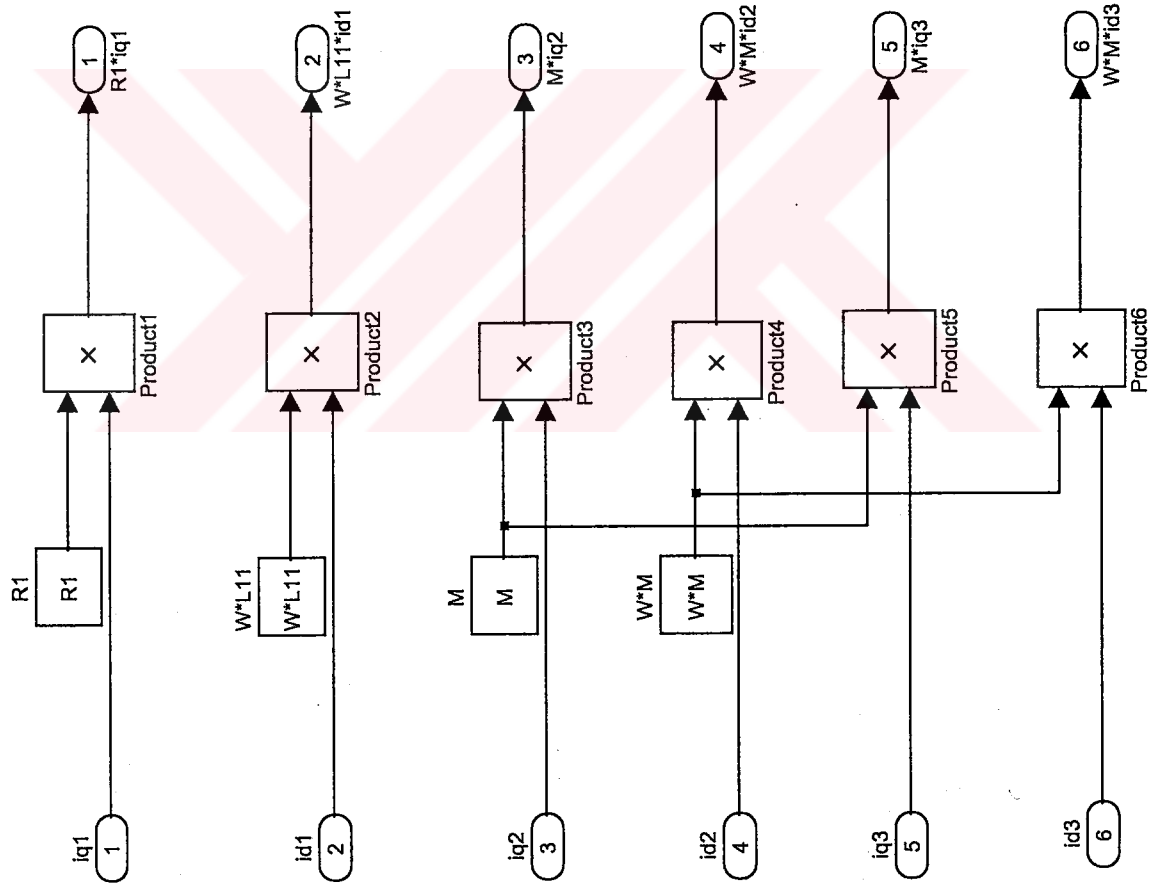


DCIM DRIVE SYSTEM MODEL WITH DIGITAL PI

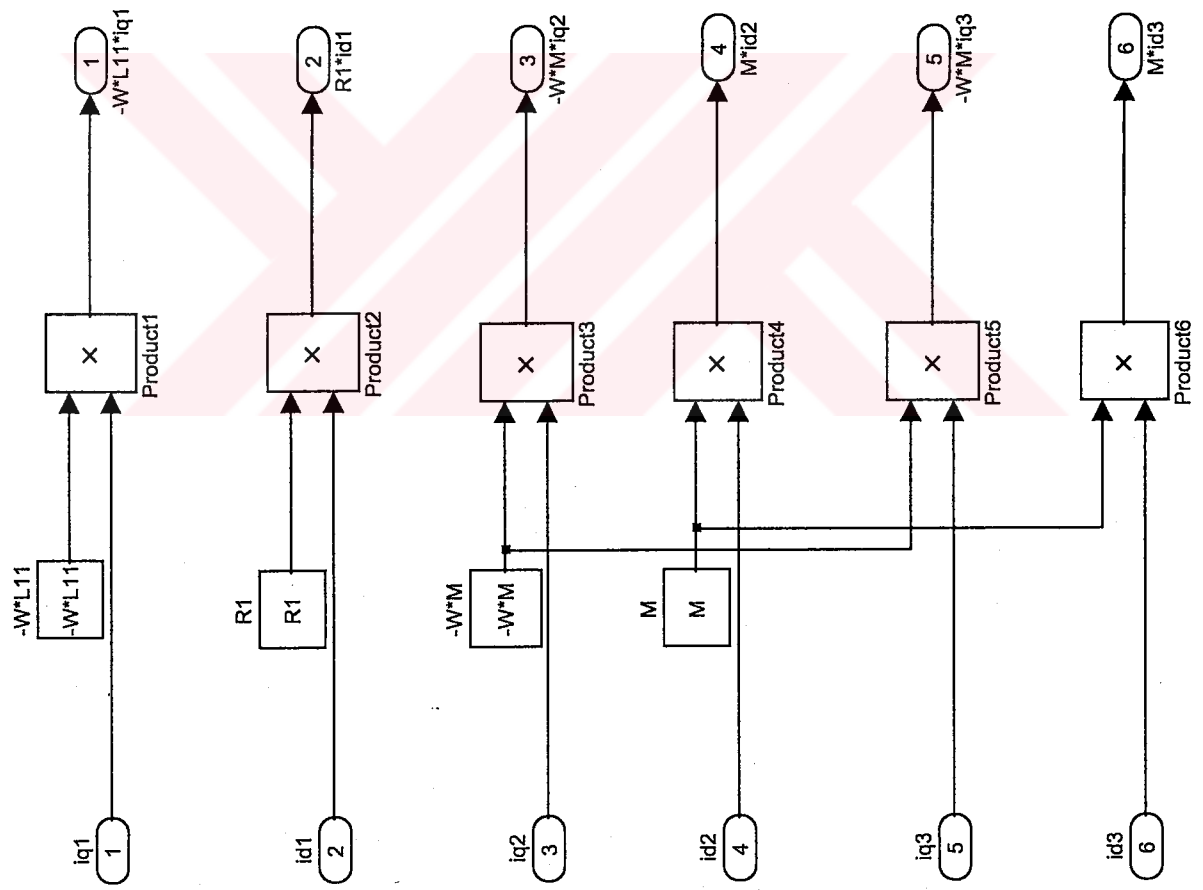


DOUBLE-CAGE INDUCTION MACHINE MODEL



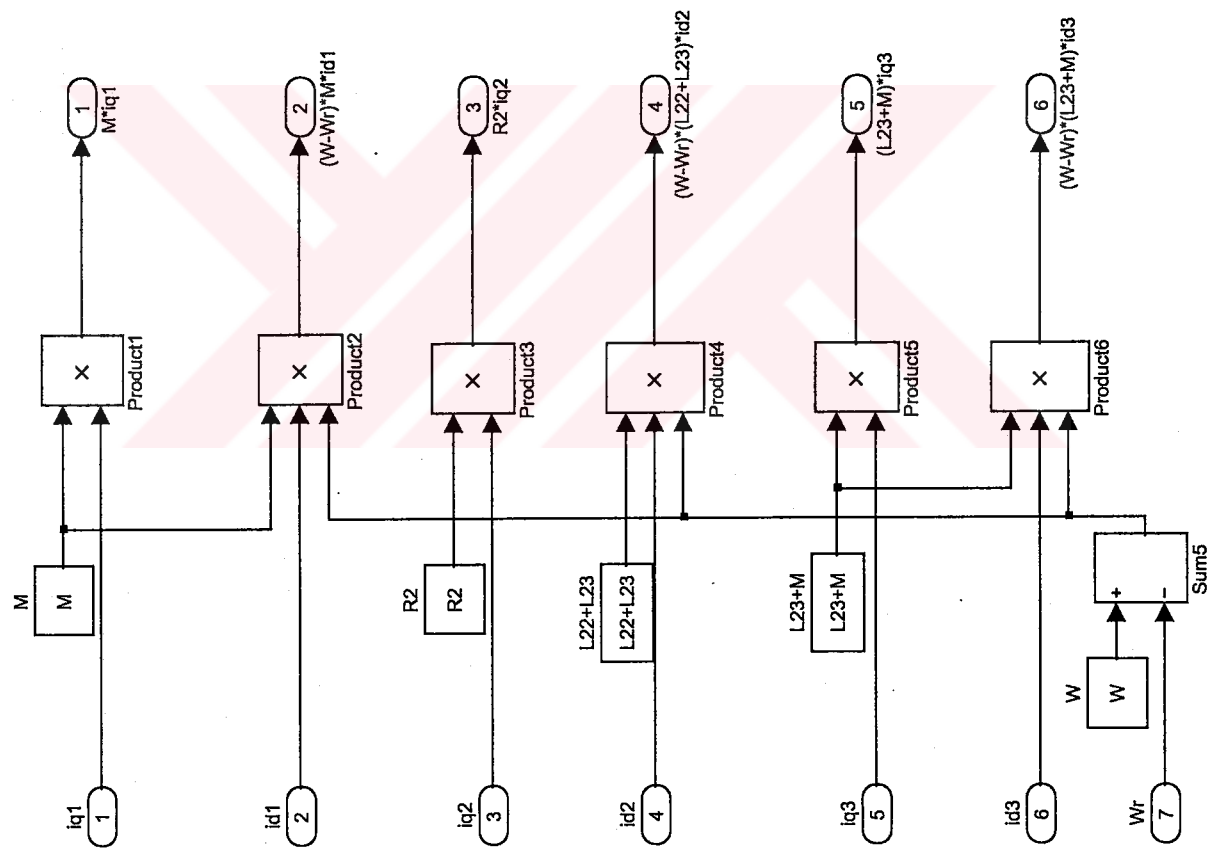


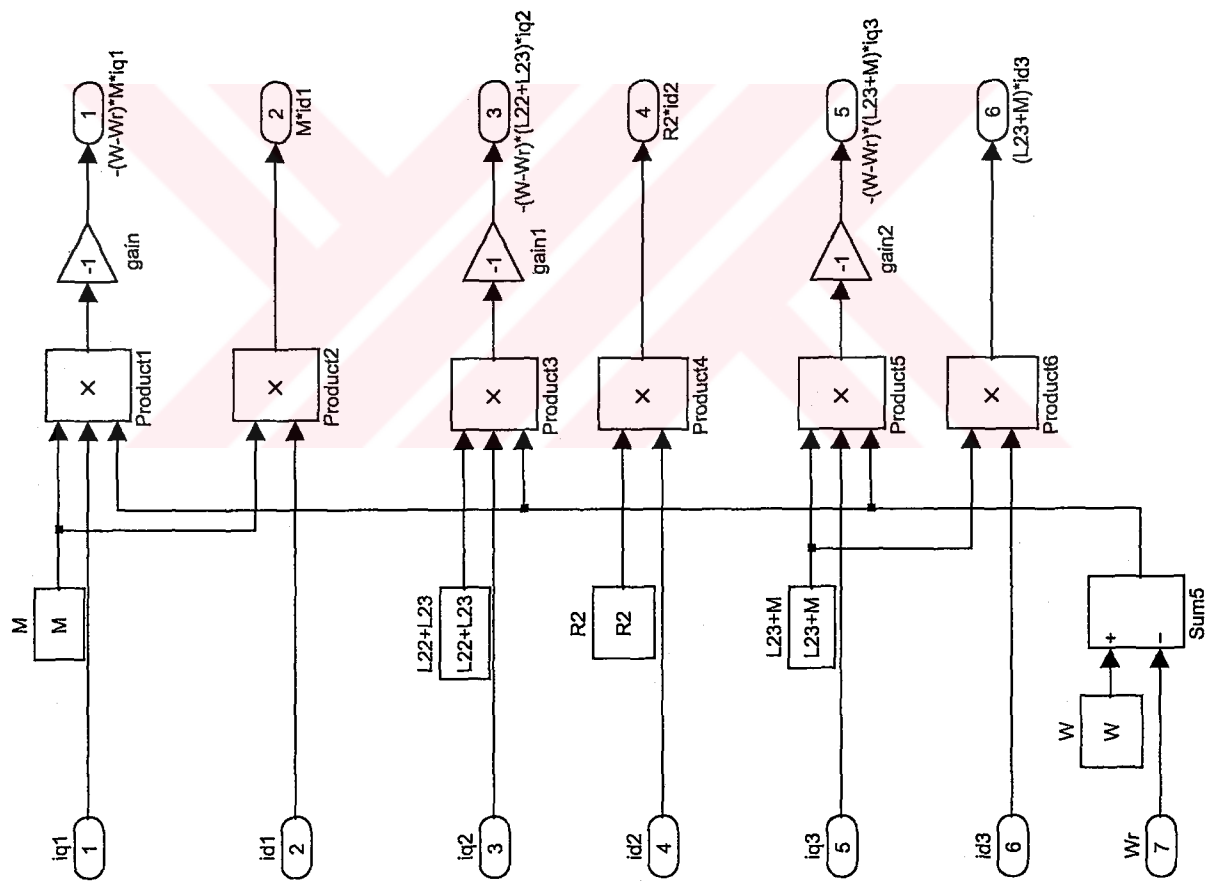
Line1 subblock



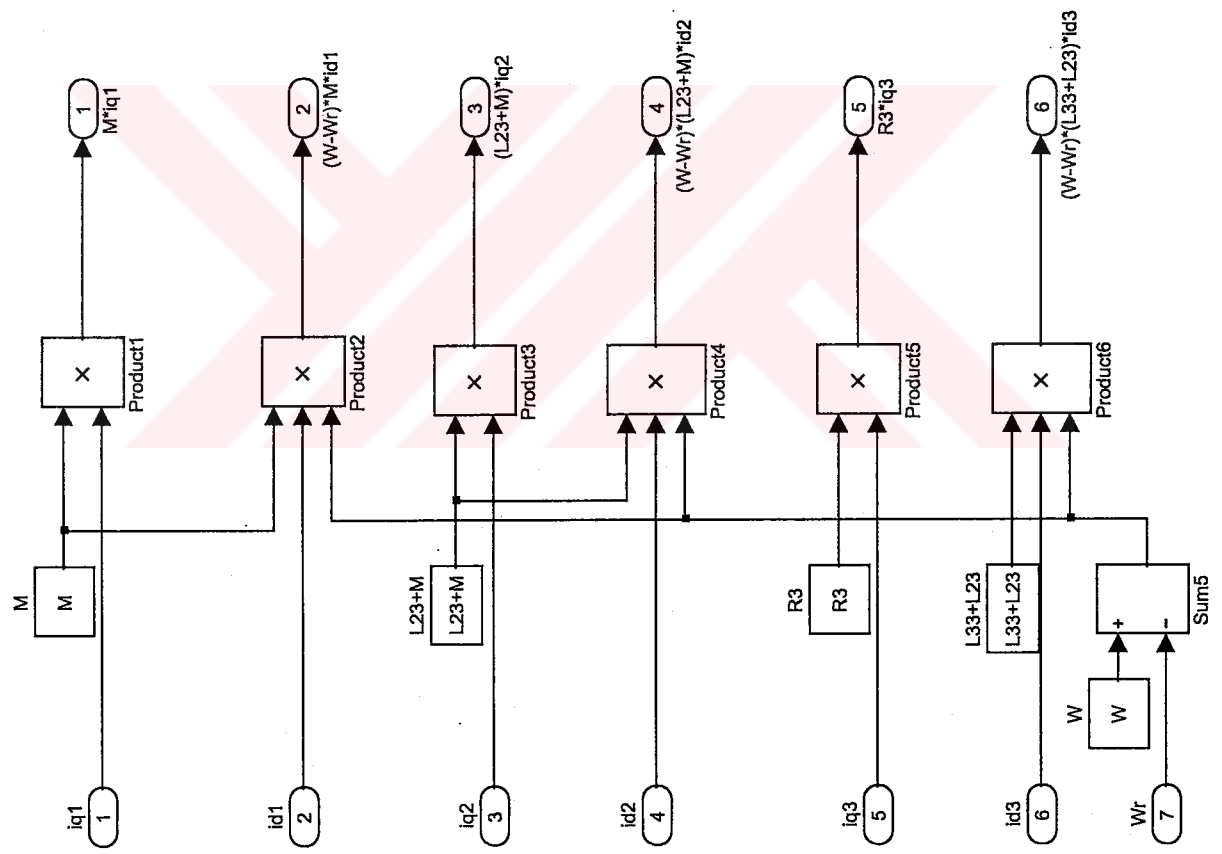
Line2 subblock

Line3 subblock

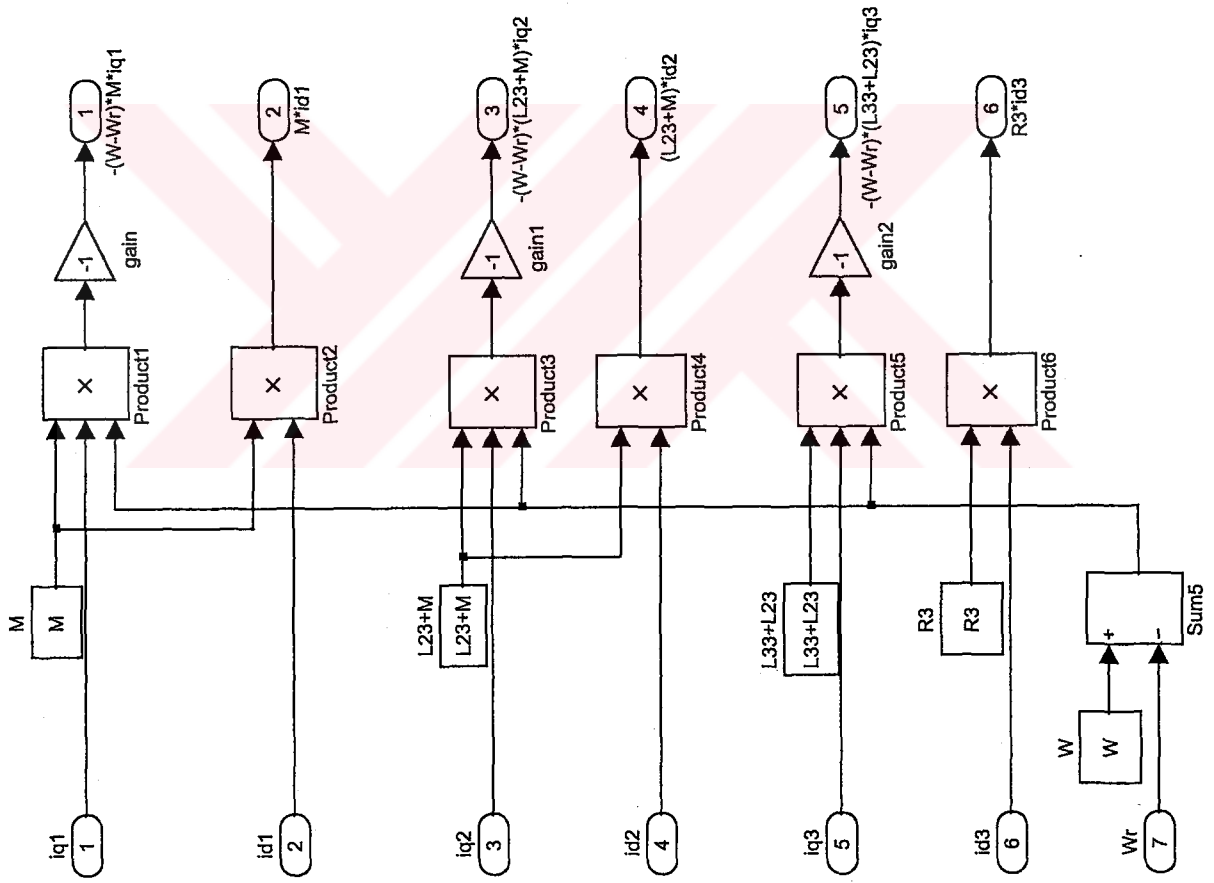




Line4 subblock

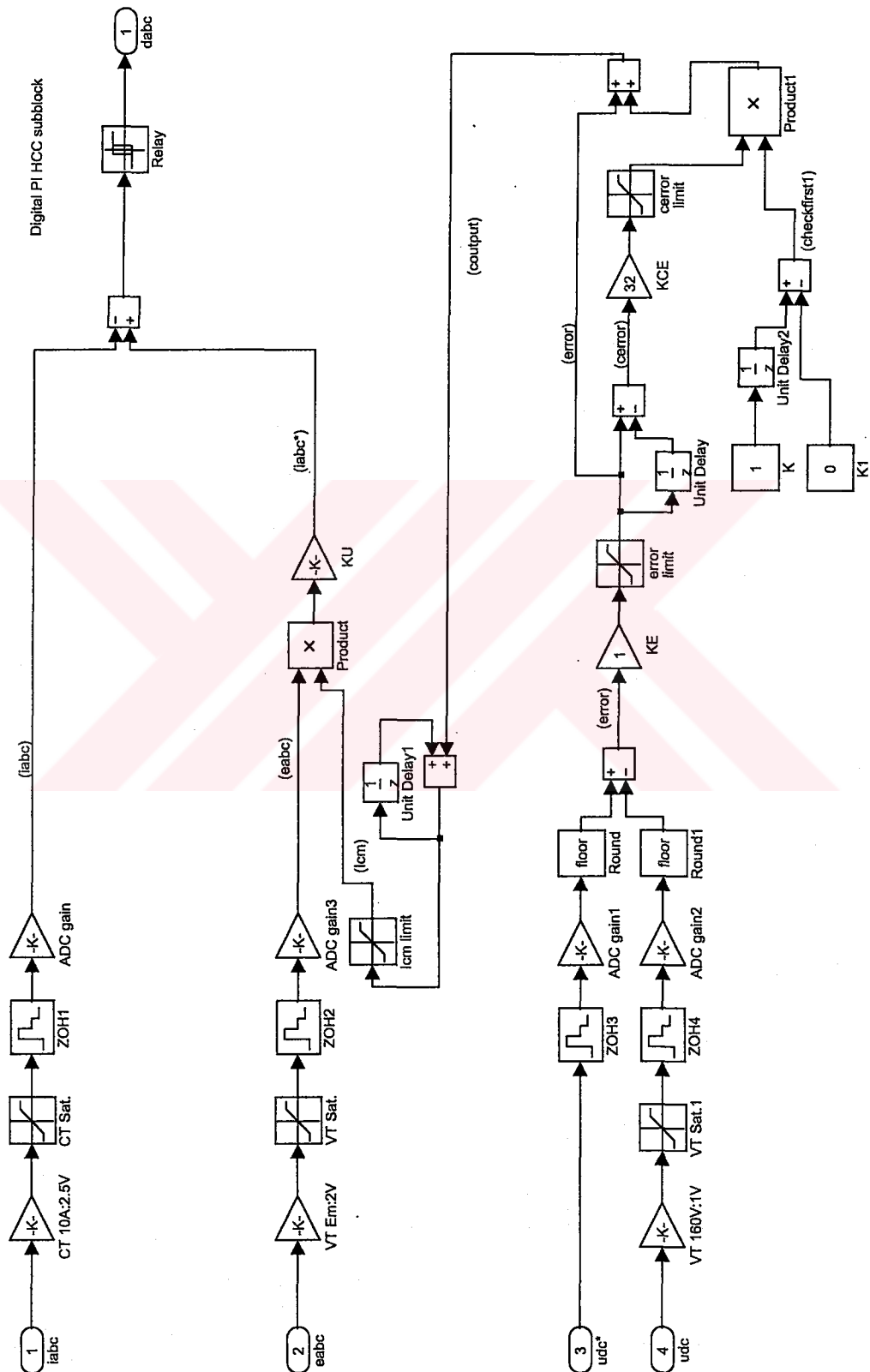


Line5 subblock

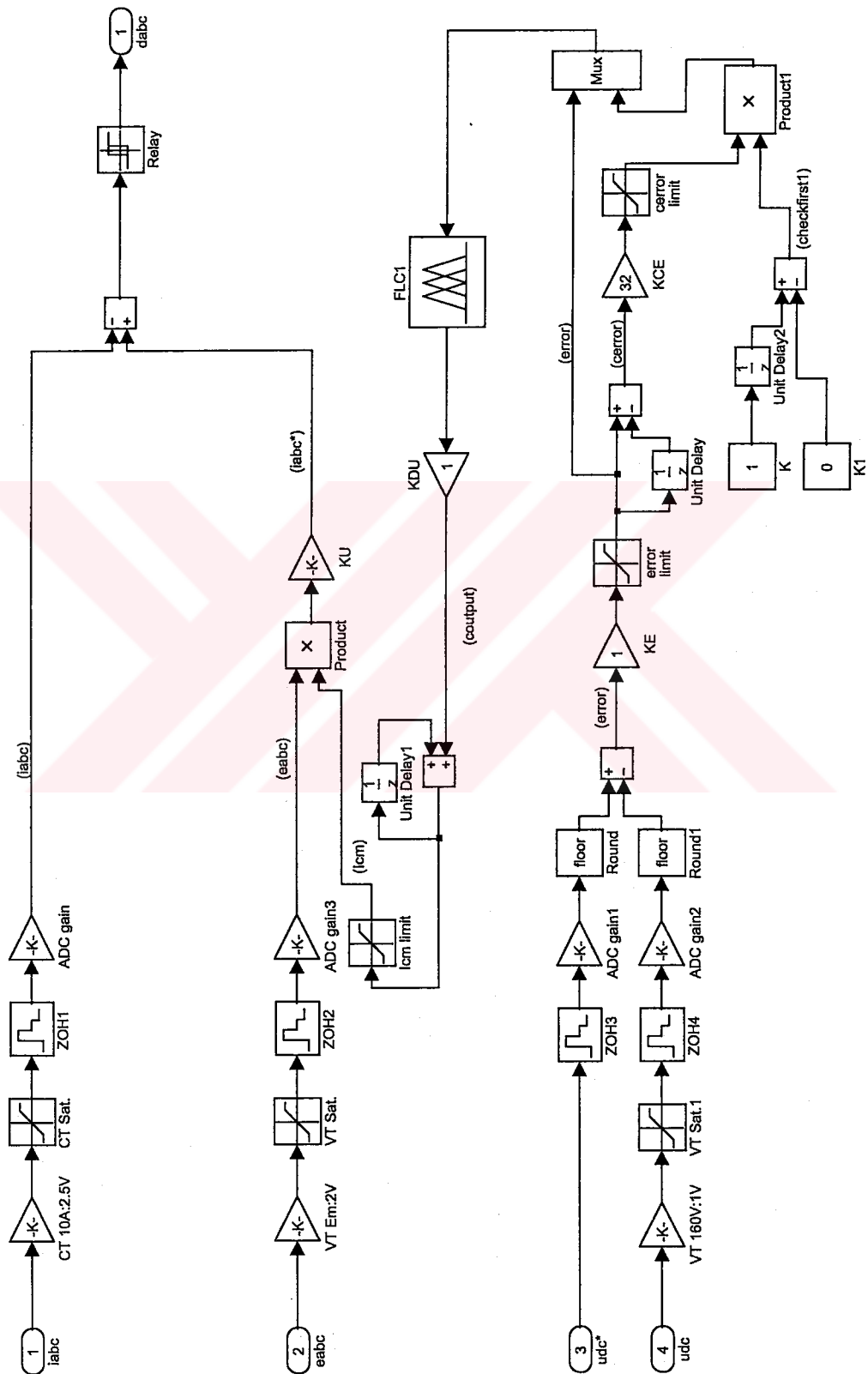


Line6 subblock

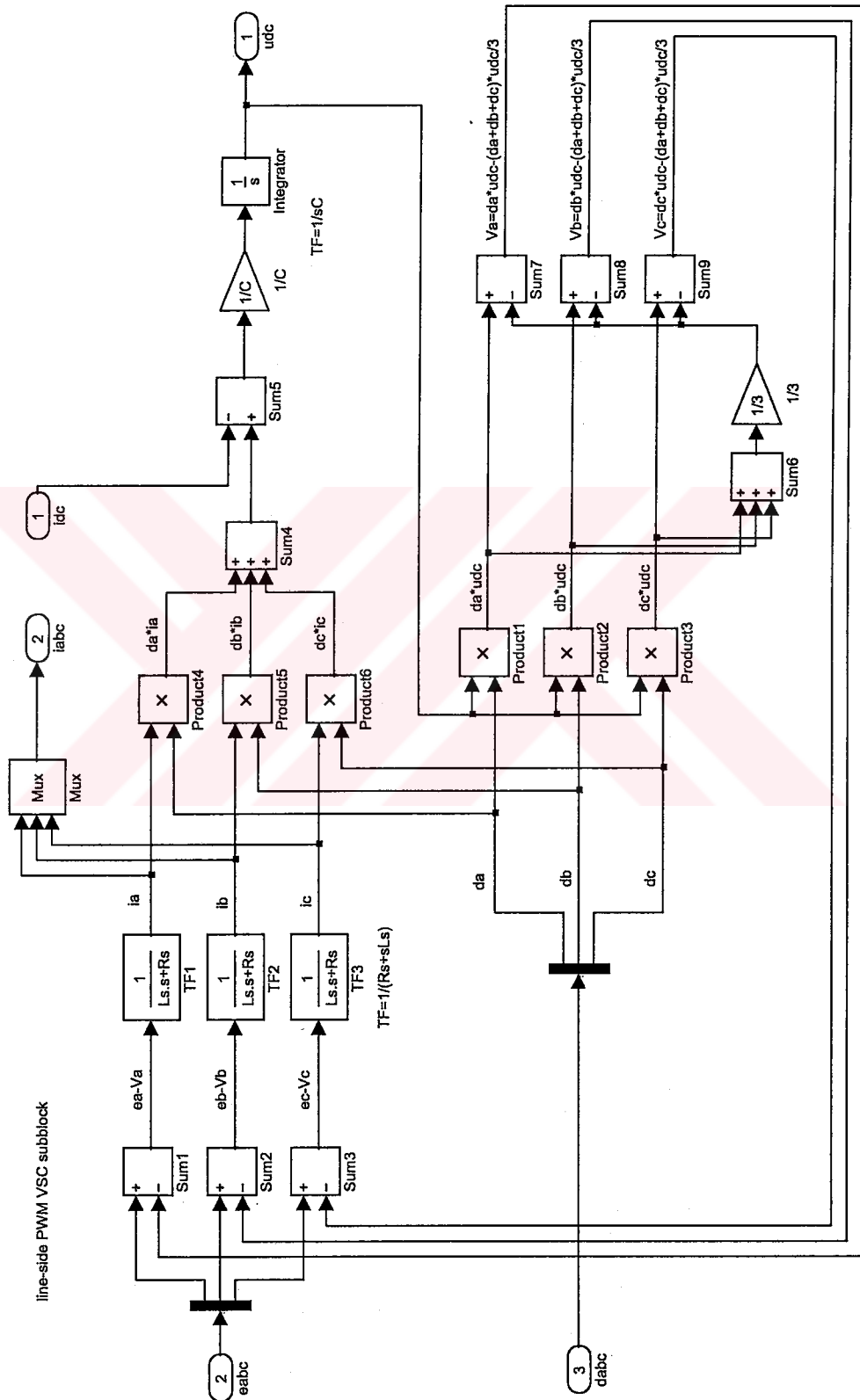
HYSTERESIS CURRENT CONTROL WITH PI CONTROLLER



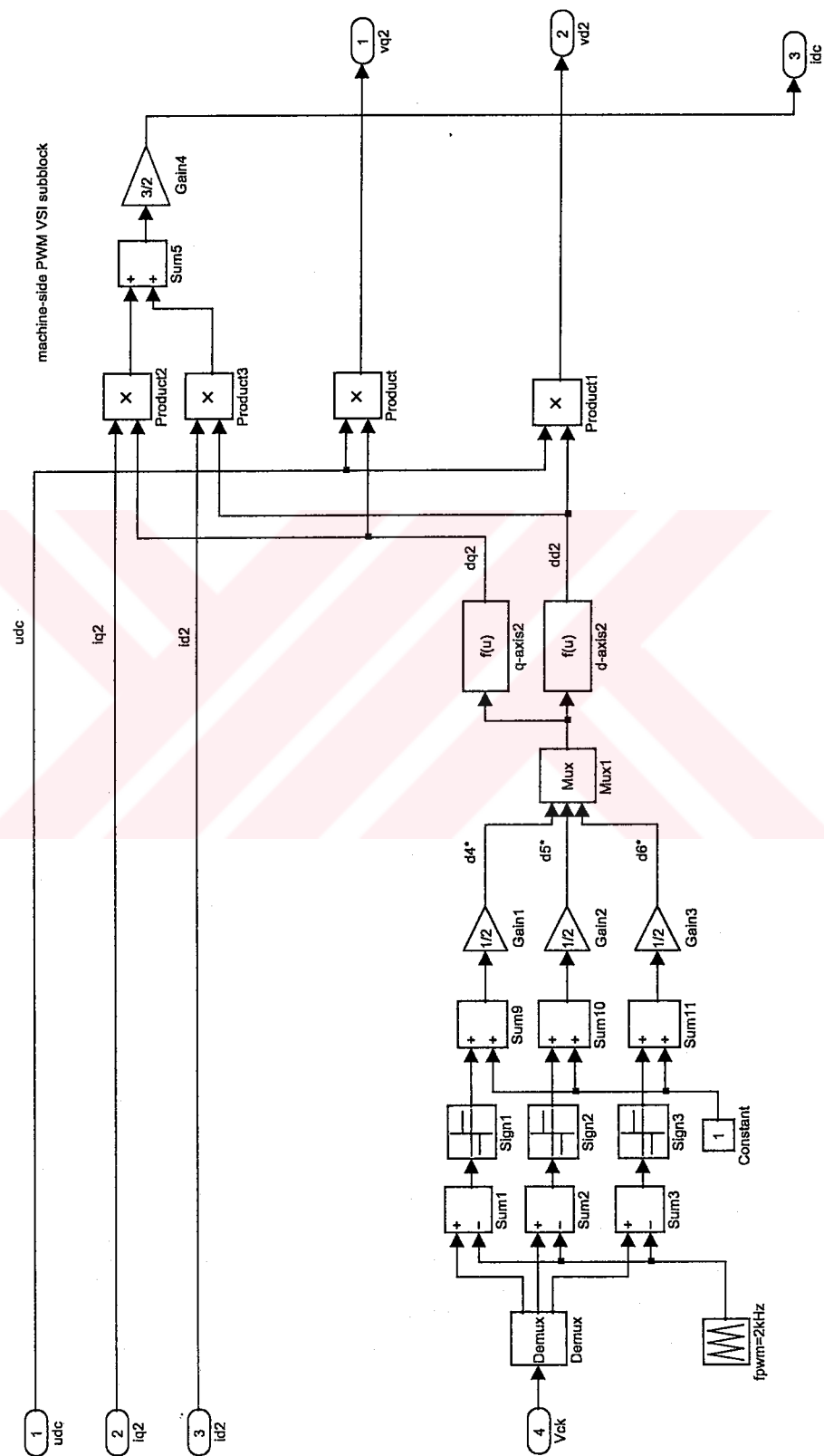
HYSTERESIS CURRENT CONTROL WITH FLC



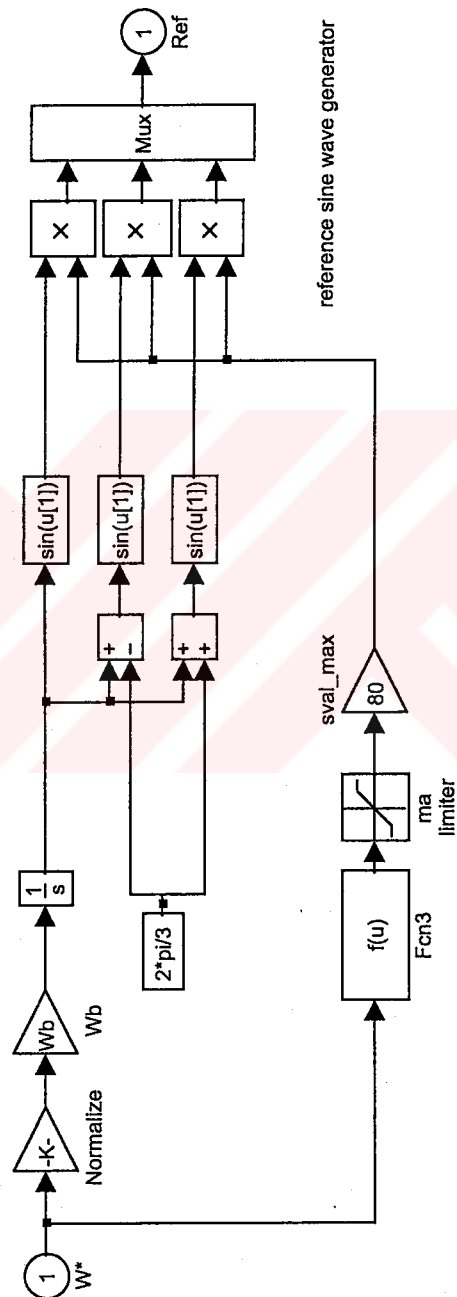
LINE-SIDE PWM CONVERTER MODEL



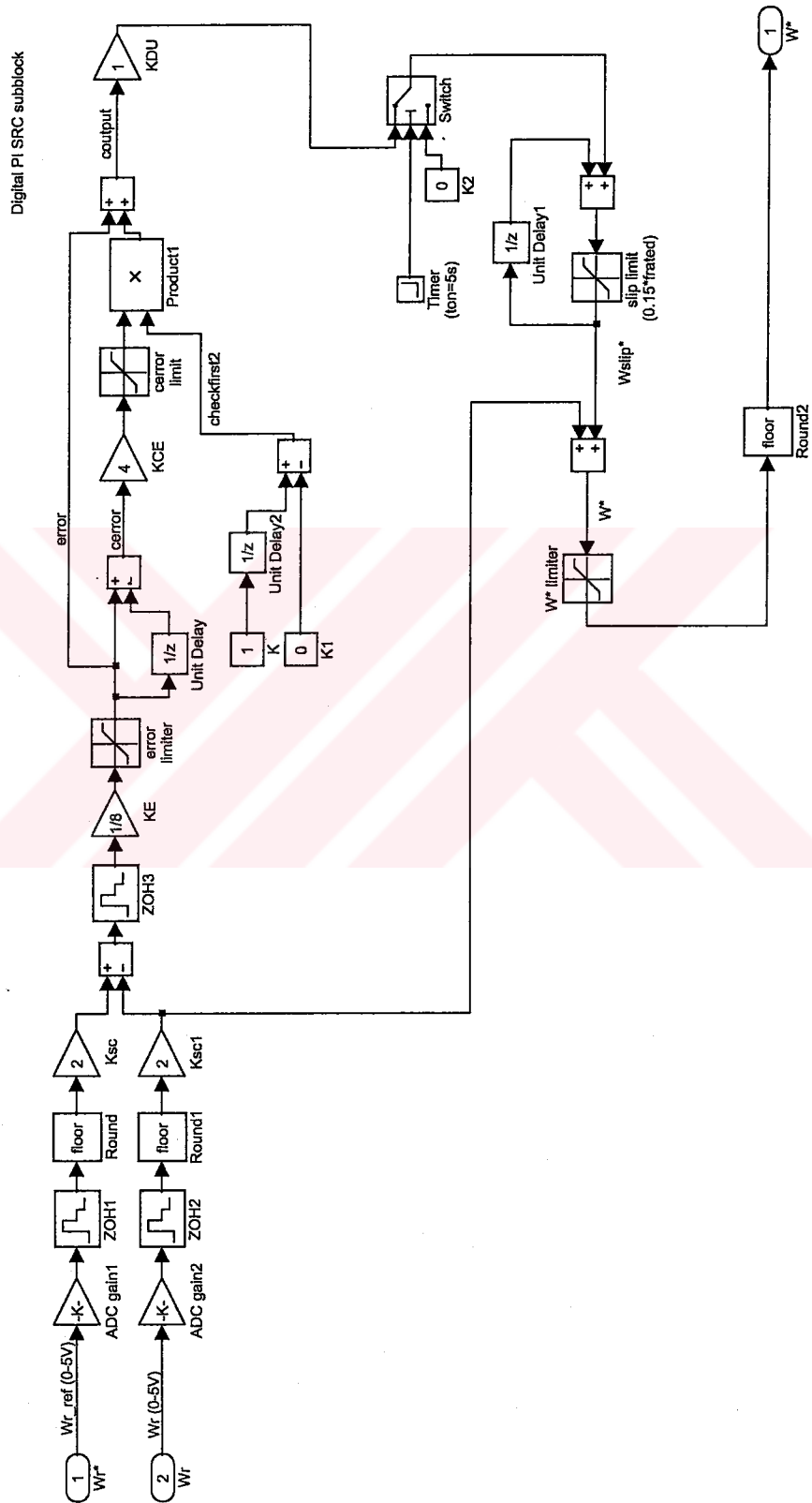
MACHINE-SIDE PWM CONVERTER MODEL



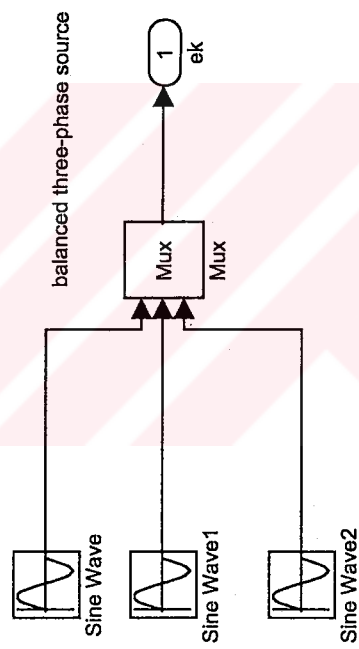
REFERENCE SINE WAVE GENERATOR



SLIP REGULATION CONTROL WITH DIGITAL PI



BALANCED THREE-PHASE SUPPLY



APPENDIX C

Developed DSP Software in Code Composer Environment

The screenshot displays the Code Composer Studio (CCS) environment for the project 'asd240'. The main editor window shows the assembly code for 'asd240.asm', which includes comments in Turkish and assembly instructions. The console window shows the build output, indicating that the software was compiled successfully without errors or warnings. The watch window shows the values of various variables, including registers and memory locations.

File Explorer:

- Files
 - GEL files
 - Project
 - Incremental build
 - asd240.mak
 - asd240.cmd
 - Include
 - Libraries
 - Source
 - adc.c
 - asd240.c
 - Boot.asm
 - ev_pwm.c
 - fault.c
 - hcc.c
 - initvars.c
 - Vectors.asm

Main Editor Window (asd240.asm):

```

/* PWM AC-DC Converter Main Program */
/* Project started on 20/09/2002 */
/*-----*/
/* filename: asd240.c */
/*-----*/

/* asagidaki dosyalar SD nin original kodu yapildi:
/* boot.asm (degisiklikler yapildi, IO port ve i
/* vectors.asm (original)
/* C24Dapp.h (original)
/* asd240.cmd (original, test240.cmd degistirild
/* rts2xx.lib (original, abort function icin ger
/* IMR deki problem cozuldu!*/
/* DAC daki problem cozuldu!*/
  
```

Console Window:

```

Copyright (c) 1987-1999 Texas
PASS 1
PASS 2
No Errors, No Warnings
dsplink asd240.mak
TMS320C1x/C2x/C2x/C5x COFF Lin
Copyright (c) 1987-1999 Texas
Build Complete,
0 Errors, 0 Warnings.
  
```

Watch Window:

```

Tsample = 2741
*T1CNT,x = 0x00000000
*T2CNT,x = 0x00000000
*T3CNT,x = 0x00000000
udc_ref = 53
deneme1 = 0
deneme2 = 0
udc = 53
idc = 462
Icm = 0
configdata = 4
dacdata = 0
swstatus = 1
leddata = 0
GPR0,x = 0x8B84
GPR1,x = 0x0006
  
```

Register Window:

```

PC = 0000 AR0 = 84A8
ACC = 00000000 AR1 = 84AC
PREG = 00007DA0 AR2 = 84AA
TREG = FFFC AR3 = 7032
ST0 = 0600 AR4 = 805D
ST1 = 07FC AR5 = 7FFC
RPTC = 0000 AR6 = 662B
TOS = 0014 AR7 = 005E
IMR = 0006
IFR = 0000
QREG = 0000
  
```

IGBT IPM Data Sheets

FUJI
ELECTRIC

6MBP 75RA-120

IGBT IPM
1200V
6x75A

Intelligent Power Module (R-Series)

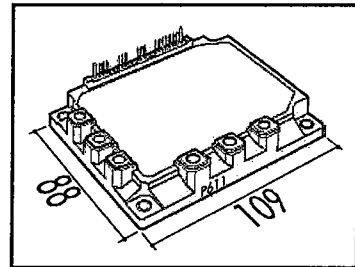
■ Maximum Ratings and Characteristics

• Absolute Maximum Ratings ($T_c=25^{\circ}\text{C}$)

Items	Symbols	Ratings		Units
		Min.	Max.	
DC Bus Voltage	V_{DC}	0	900	V
DC Bus Voltage (surge)	$V_{DC(Surge)}$	0	1000	
DC Bus Voltage (short operating)	V_{SC}	200	800	
Collector-Emitter Voltage	V_{CES}	0	1200	
Inverter	Continuous	I_C	75	A
Collector	1ms	I_{CP}	150	
Current	Duty=62.6%	$-I_C$	75	
Collector Power Dissipation One Transistor	P_C		595	W
Voltage of Power Supply for Driver	V_{CC}	0	20	
Input Signal Voltage	V_{IN}	0	V_Z	V
Input Signal Current	I_{IN}		1	
Alarm Signal Voltage	V_{ALM}	0	V_{CC}	V
Alarm Signal Current	I_{ALM}		15	
Junction Temperature	T_J		150	$^{\circ}\text{C}$
Operating Temperature	T_{OP}	-20	100	
Storage Temperature	T_{stg}	-40	125	
Isolation Voltage	A.C. 1min.	V_{iso}	2500	V
Screw Torque	Mounting *1		3.5	Nm
	Terminals *1		3.5	

Note: *1: Recommendable Value; 2.5 - 3.0 Nm (M8)

■ Outline Drawing



• Electrical Characteristics of Power Circuit (at $T_J=25^{\circ}\text{C}$, $V_{CC}=15\text{V}$)

	Items	Symbols	Conditions	Min.	Typ.	Max.	Units
INV	Collector Current At Off Signal Input	I_{CES}	$V_{CE}=1200\text{V}$, Input Terminal Open			1.0	mA
	Collector-Emitter Saturation Voltage	$V_{CE(Sat)}$	$I_C=75\text{A}$			2.6	V
	Forward Voltage of FWD	V_F	$-I_C=75\text{A}$			3.0	V

• Electrical Characteristics of Control Circuit (at $T_J=25^{\circ}\text{C}$, $V_{CC}=15\text{V}$)

	Items	Symbols	Conditions	Min.	Typ.	Max.	Units
	Current of P-Line Side Driver (One Unit)	I_{CCP}	$f_{sw}=0\sim 15\text{kHz}$, $T_c=-20\sim 100^{\circ}\text{C}$	3		18	mA
	Current of N-Line Side Driver (Three Units)	I_{CCN}	$f_{sw}=0\sim 15\text{kHz}$, $T_c=-20\sim 100^{\circ}\text{C}$	10		85	
	Input Signal Threshold Voltage	$V_{IN(th)}$	On	1.00	1.35	1.70	V
			Off	1.25	1.60	1.95	
	Input Zener Voltage	V_Z	$R_{IN}=20\text{k}\Omega$		8.0		
	Over Heating Protection Temperature Level	T_{COH}	$V_{DC}=0\text{V}$, $I_C=0\text{A}$, Case Temp.	110		125	$^{\circ}\text{C}$
	Hysteresis	T_{CH}			20		
	IGBT Chips Over Heating Protec. Temp. Level	T_{JOH}	Surface Of IGBT Chip	150			$^{\circ}\text{C}$
	Hysteresis	T_{JH}			20		
	Inverter Collector Current Protection Level	I_{OC}	$T_J=125^{\circ}\text{C}$	113			A
	Over Current Detecting Time	t_{OOC}	$T_J=25^{\circ}\text{C}$		10		μs
	Alarm Signal Hold Time	t_{ALM}		1.5	2		ms
	Limiting Resistor for Alarm	R_{ALM}		1425	1500	1575	Ω
	Under Voltage Protection Level	V_{UV}		11.0		12.5	V
	Hysteresis	V_H		0.2			

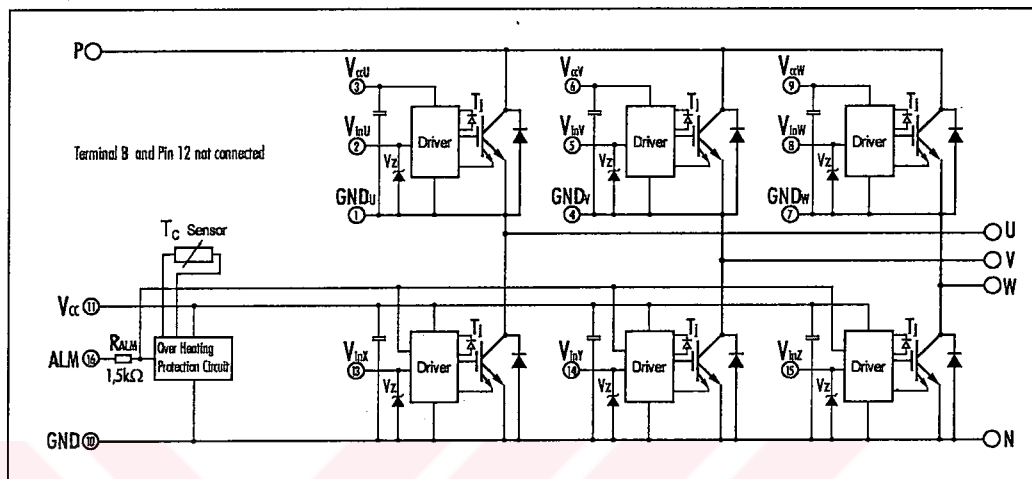
• Dynamic Characteristics (at $T_c=T_J=125^{\circ}\text{C}$, $V_{CC}=15\text{V}$)

	Items	Symbols	Conditions	Min.	Typ.	Max.	Units
Switching Time		t_{ON}	$I_C=50\text{A}$, $V_{DC}=600\text{V}$	0.3			μs
		t_{OFF}				3.6	
		t_{RR}	$I_F=50\text{A}$, $V_{DC}=600\text{V}$			0.4	

• Thermal Characteristics

	Items	Symbols	Conditions	Min.	Typ.	Max.	Units
Thermal Resistance		$R_{th(j-g)}$	Inverter IGBT			0.21	$^{\circ}\text{C/W}$
		$R_{th(j-d)}$	Diode			0.47	
		$R_{th(j-c)}$	With Thermal Compound		0.05		

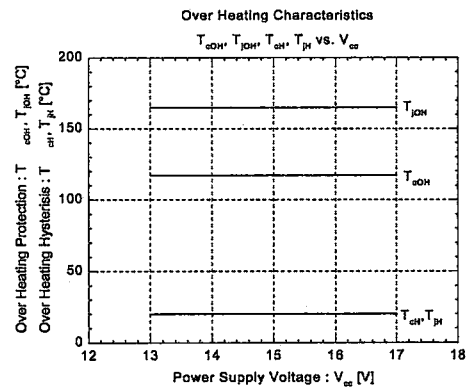
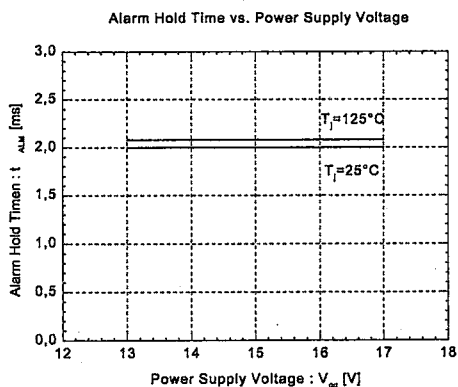
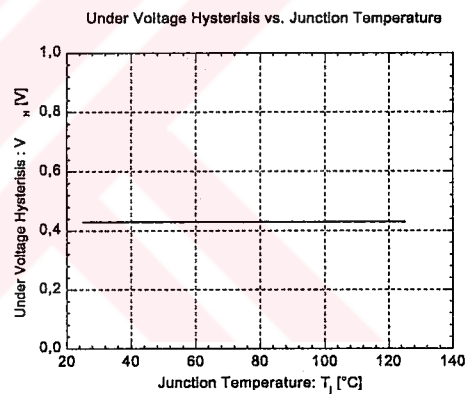
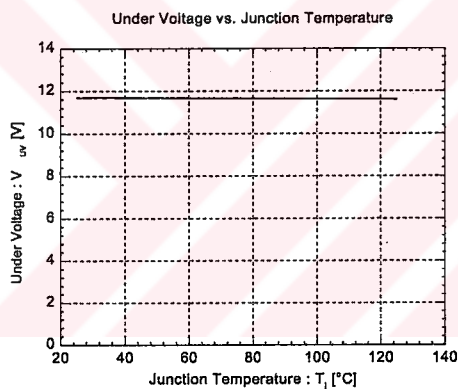
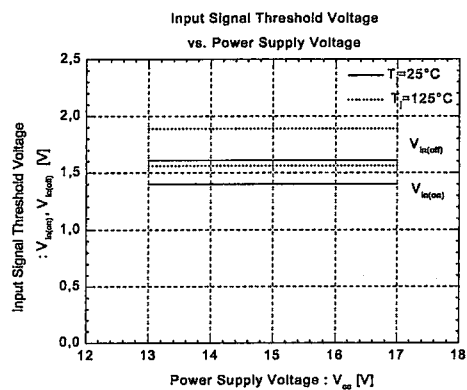
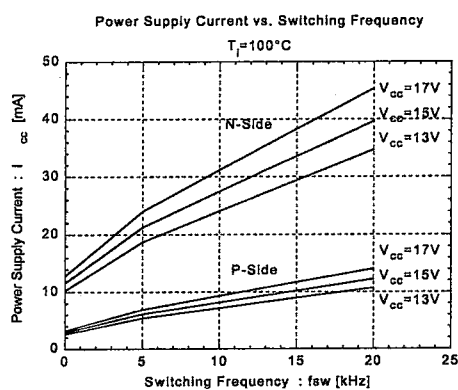
■ Equivalent Circuit



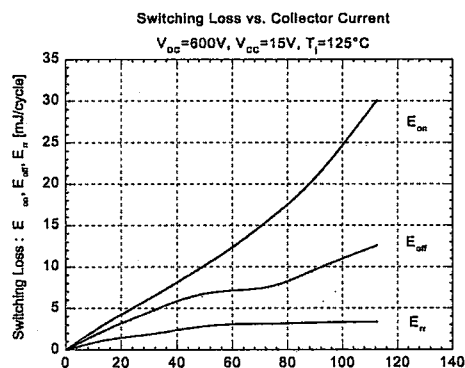
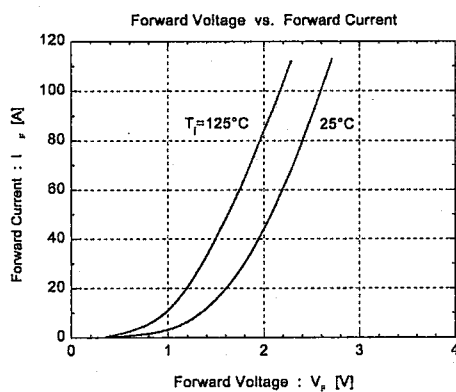
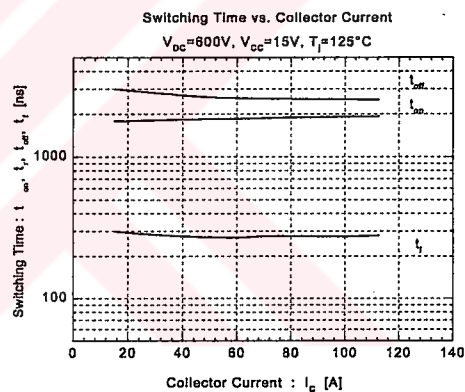
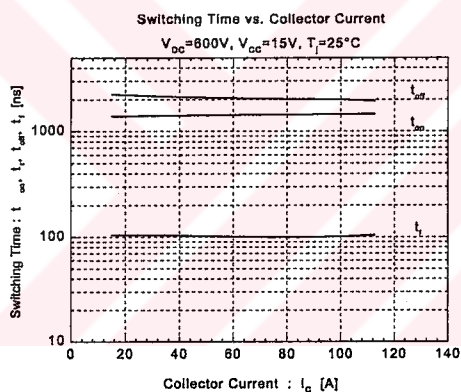
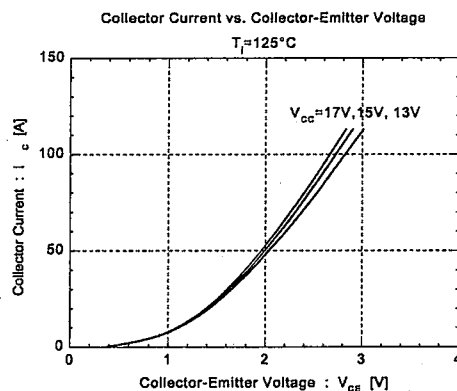
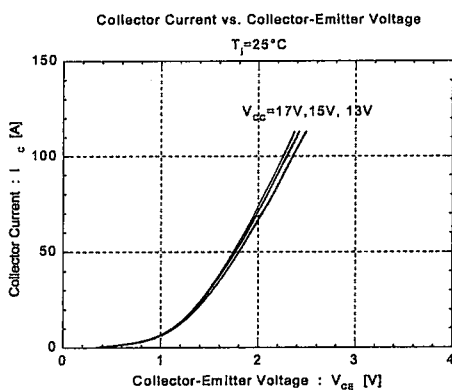
Drivers include following functions

- Short circuit protection circuit
- Amplifier for driver
- Undervoltage protection circuit
- Overcurrent protection circuit
- IGBT Chip overheating protection

■ Control Circuit

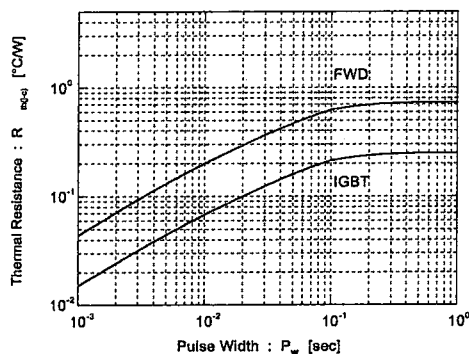


■ Inverter

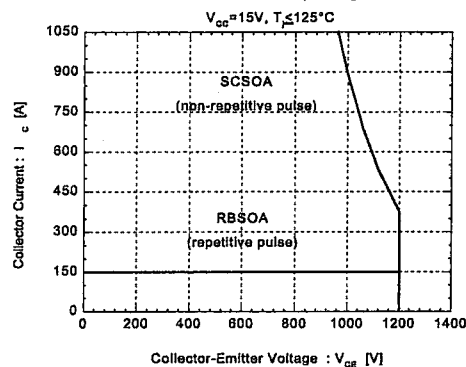


■ Inverter

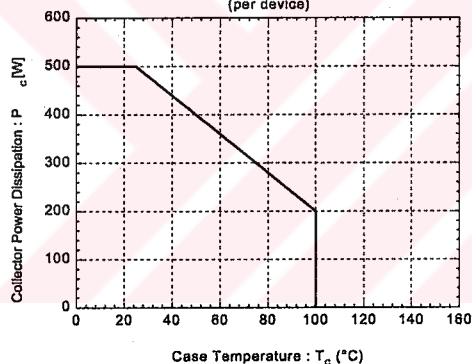
Transient Thermal Resistance



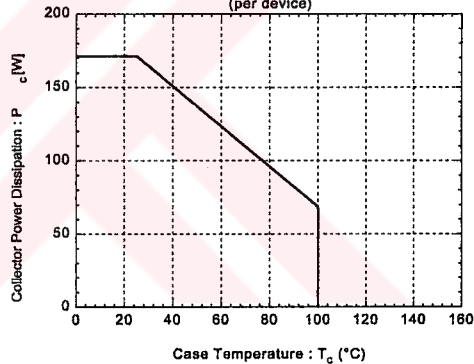
Reverse Biased Safe Operating Area



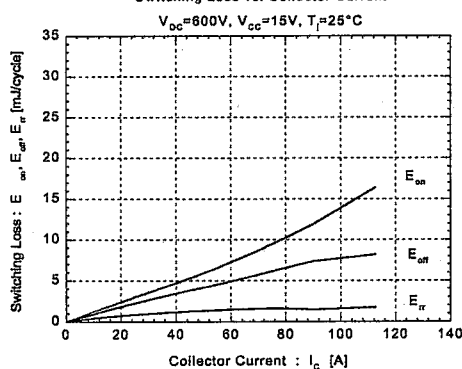
Power Derating For IGBT
(per device)



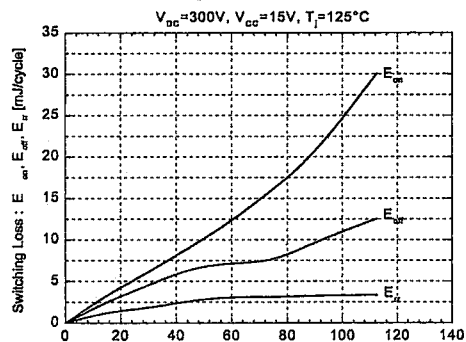
Power Derating For FWD
(per device)



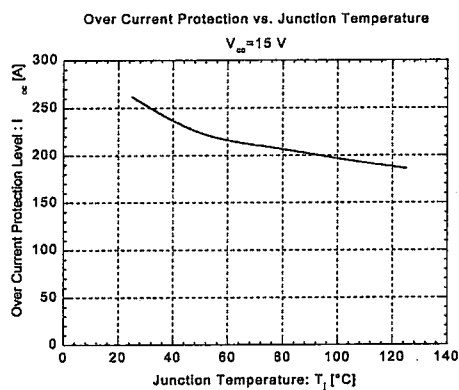
Switching Loss vs. Collector Current



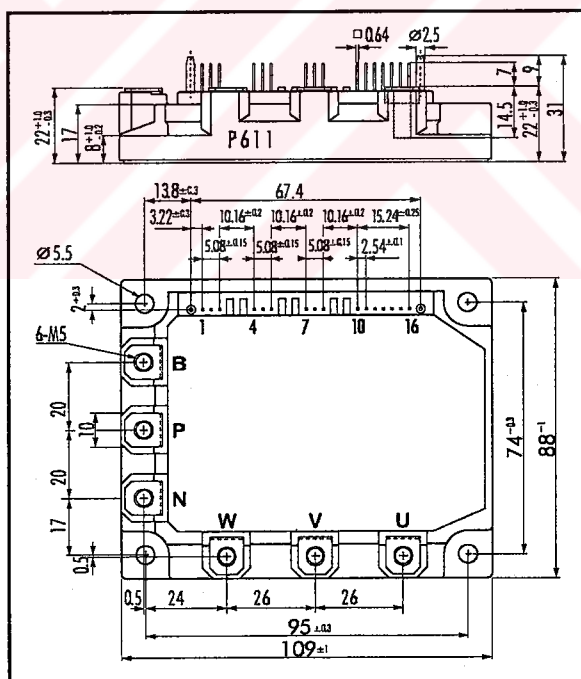
Switching Loss vs. Collector Current



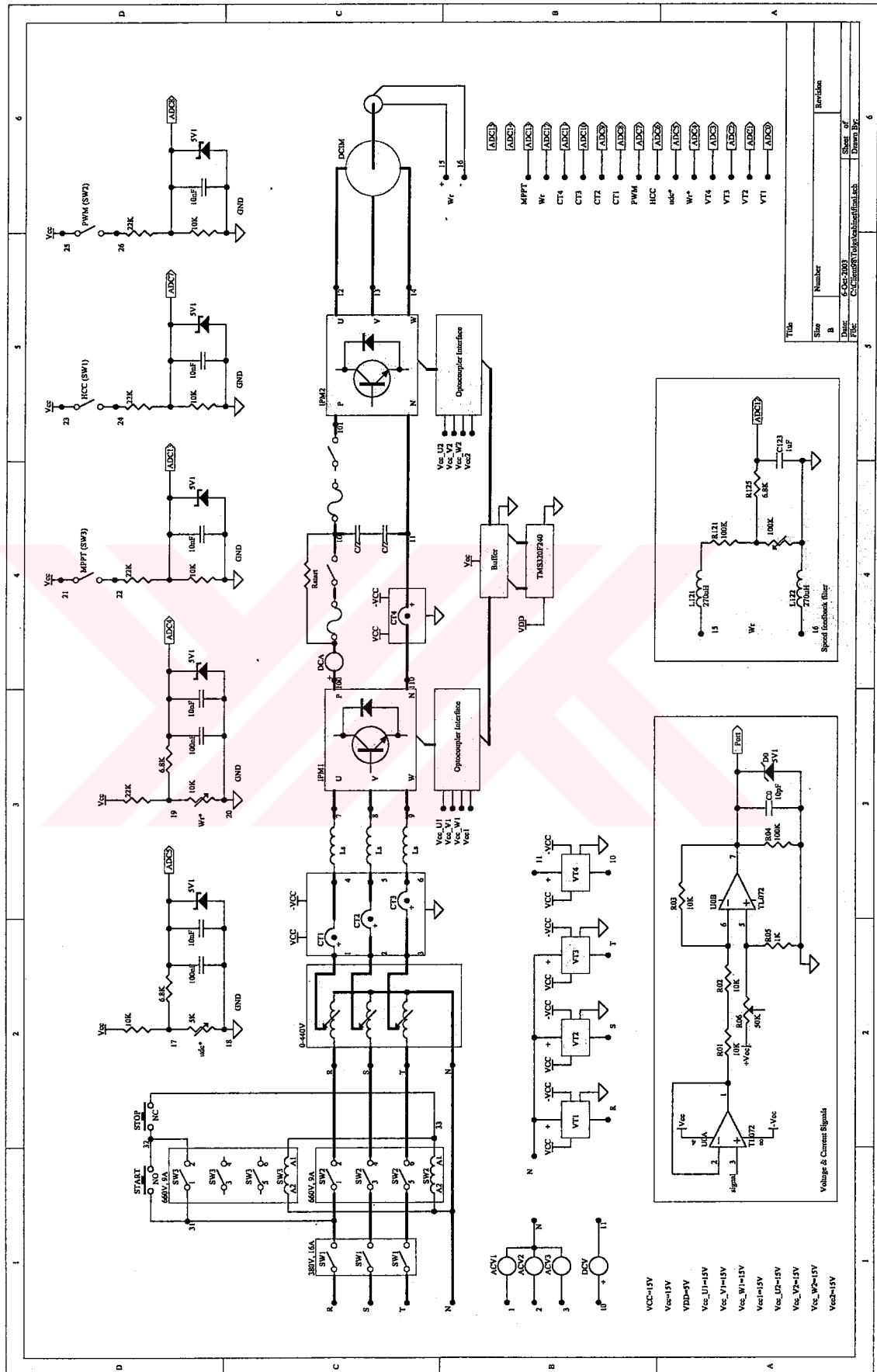
■ Inverter



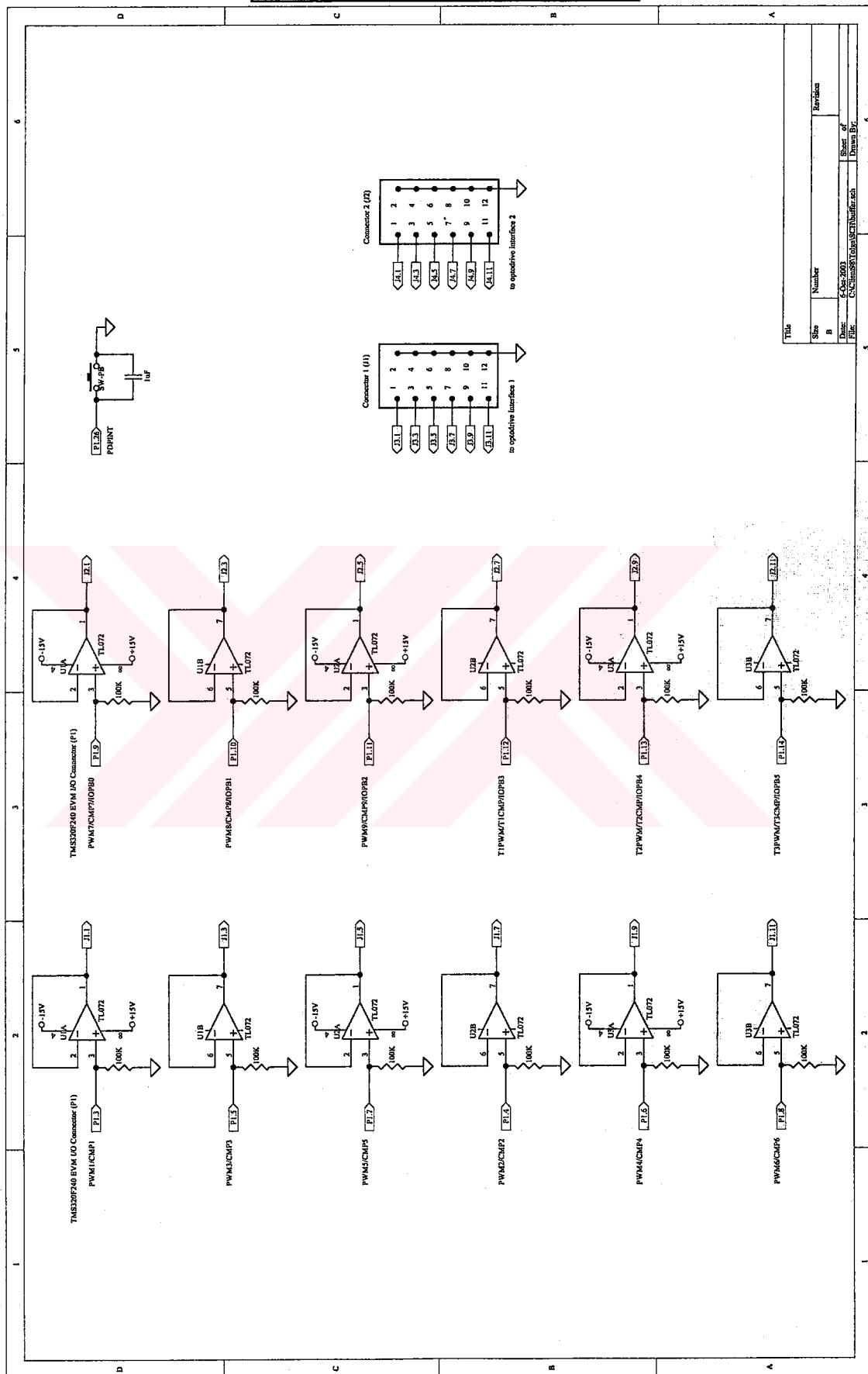
■ Outline Drawing

**Weight: 440g**

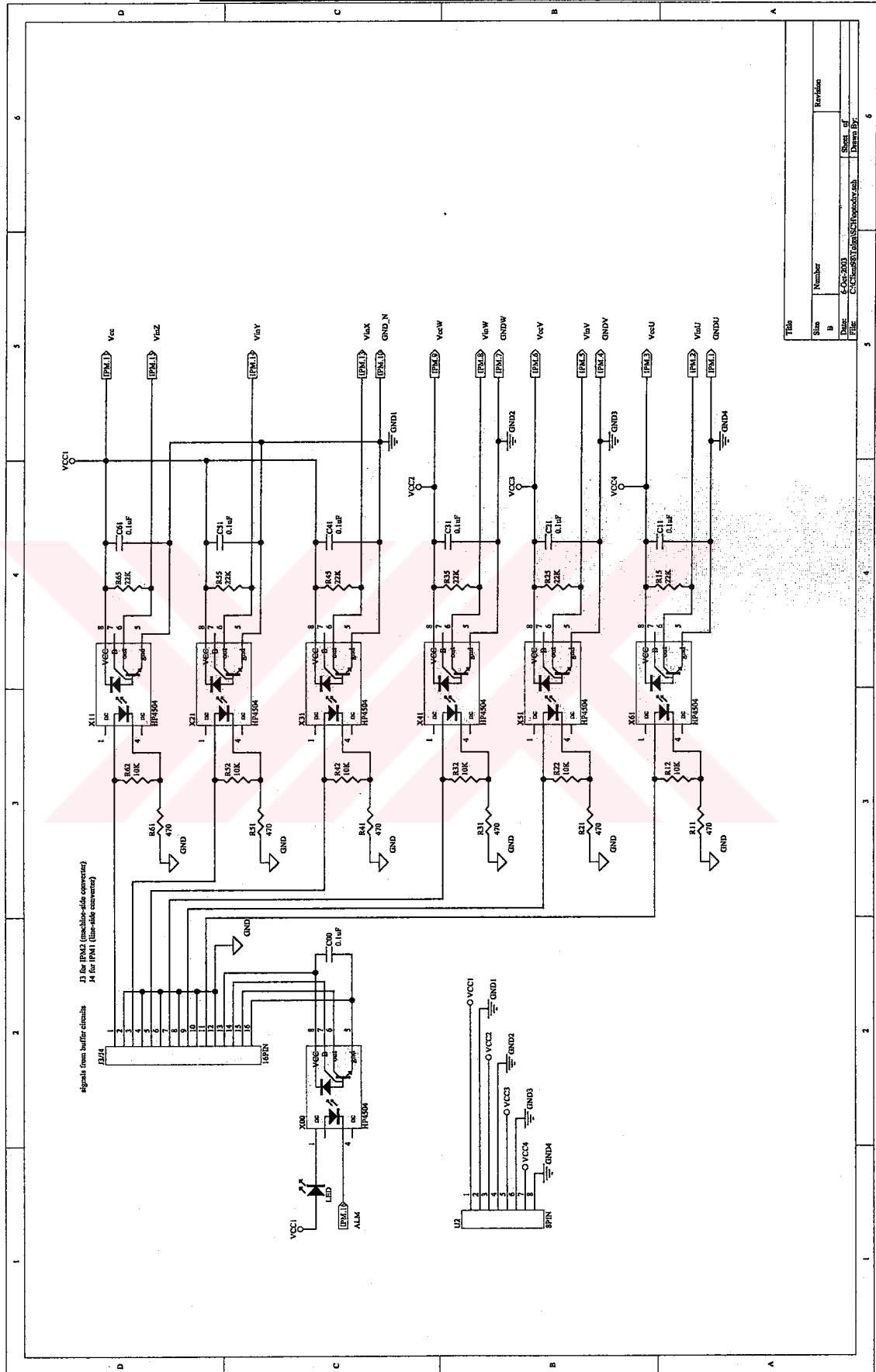
ELECTRIC CIRCUIT SCHEMATICS



BUFFER CIRCUIT SCHEMATICS

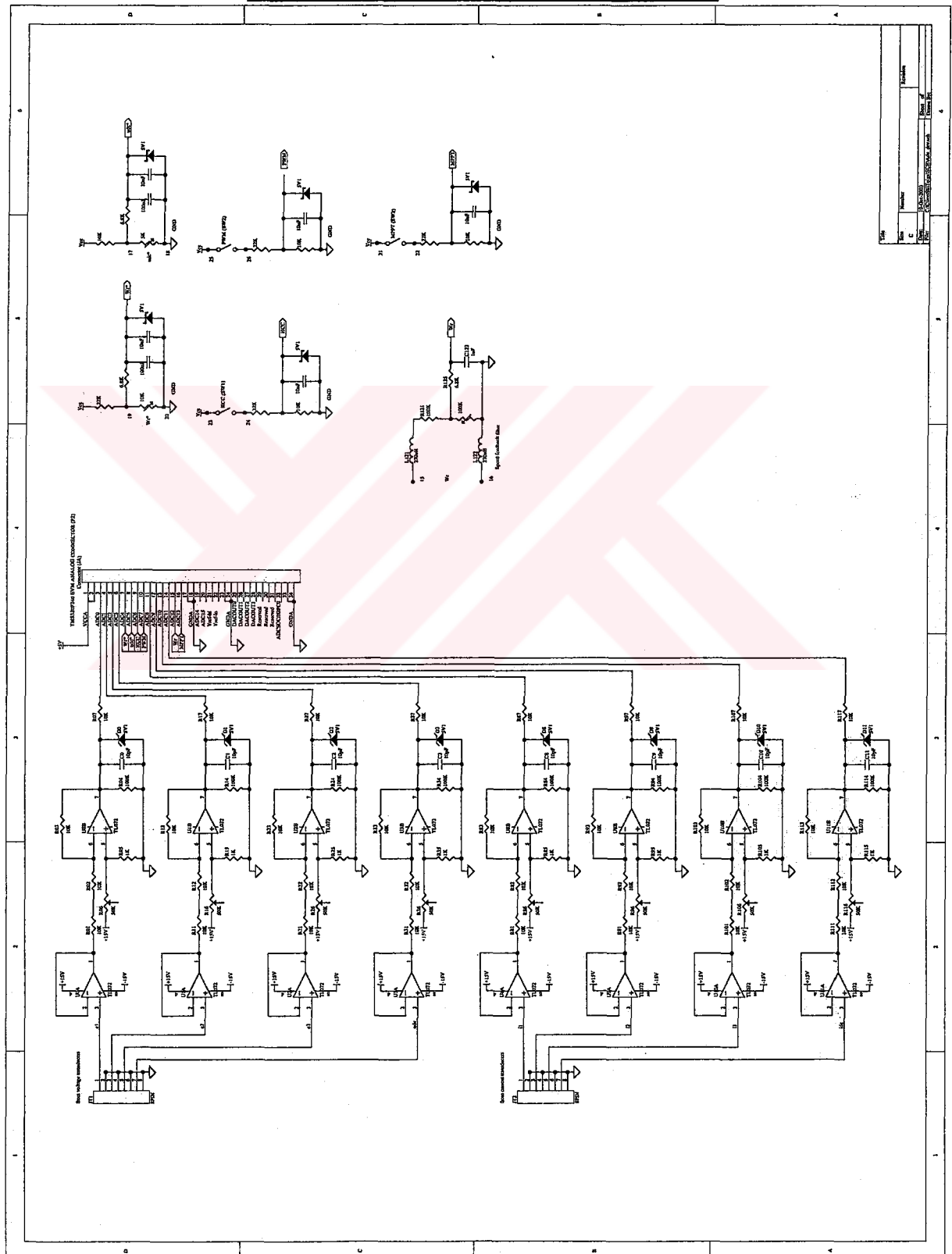


OPTOCOUPLER GATE DRIVE INTERFACE



Title	Size	Number	Revision
	B		
Page	2	2	2
File	C:\Users\j\OneDrive\Documents	Sheet of	6

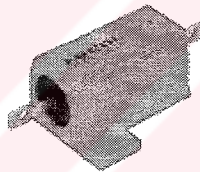
ADC DRIVE INTERFACE SCHEMATICS



NOTES

Practical Considerations

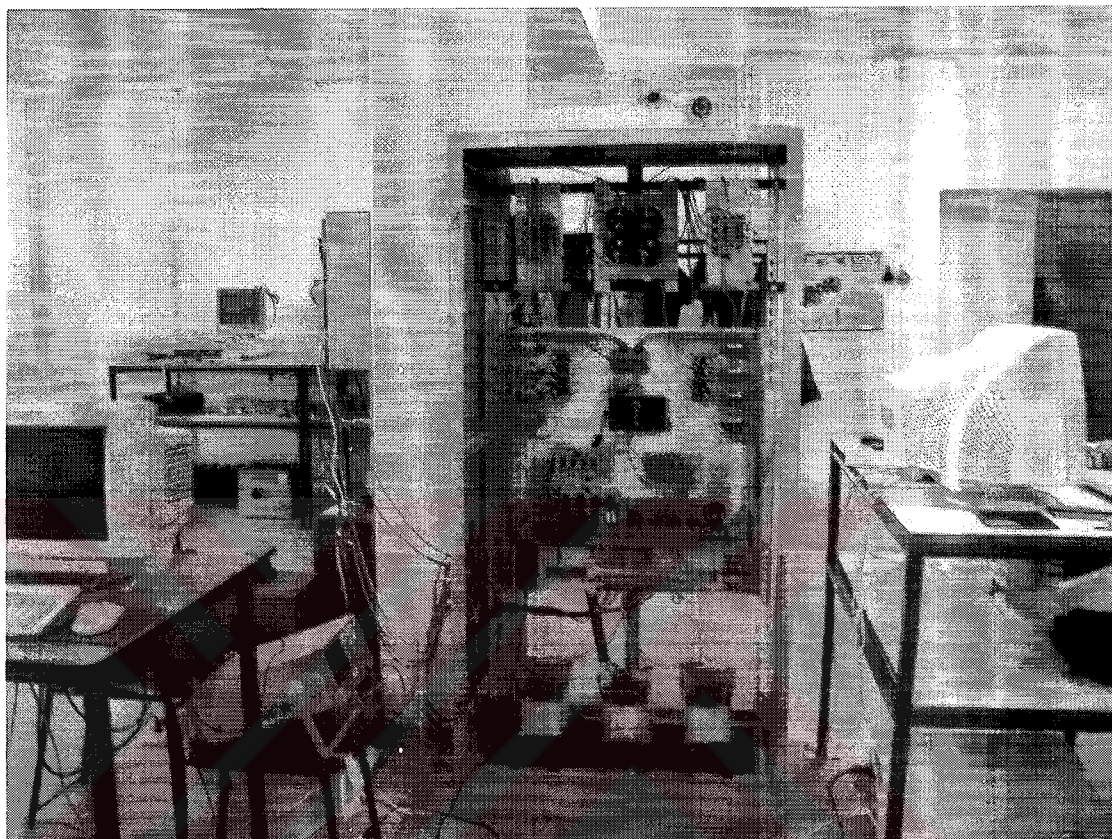
Thermal heating occurs on the resistance which is used for the dc link voltage measurement. This resistance used on the primary side of the hall-effect voltage transducer and should be chosen at higher power rating. An aluminum housed power wire wound resistor as shown in the following figure with heatsink attachment should be used in order to prevent thermal overheating.



The devices and other electronic circuitry, which are connected to the utility line, are affected by electromagnetic interference (EMI) when the drive system is running. In order to prevent conducted EMI, a line filter should be placed before the connection of the drive system to the grid. Radiated EMI due to long motor cables can be suppressed by employing motor filter on the machine side. Also, shielded cabling to the motor is necessary for reducing the EMI.

The printed circuit boards in the system are located in a cabinet as shown in the following figure. However, these are affected by the moisture of the environment. In order to protect the electronic circuitry from climatic conditions, conformal coatings should be applied on PCB surfaces.

NOTES



NOTES

